FACULTY OF SCIENCE
UNIVERSITY OF COPENHAGEN

PhD thesis

This thesis has been submitted to the PhD School of The Faculty of Science, University of Copenhagen

Pseudorapidity Dependence of Anisotropic Azimuthal Flow with the ALICE Detector

Alexander Colliander Hansen
Niels Bohr Institute
University of Copenhagen

CERN-THESIS-2014-204
24/10/2014

Academic Advisor:
Jens Jørgen Gaardhøje
Niels Bohr Institute
University of Copenhagen

October 2014

Contact information:

Institute:	Niels Bohr Institute Blegdamsvej 17 DK-2100 Copenhagen
Phone:	(+45) 20 84 62 64
E-mail:	alexander.c.hansen@gmail.com
Supervisor:	Professor Jens Jørgen Gaardhøje
E-mail:	gardhoje@nbi.dk

Abstract

In ultra-relativistic heavy-ion collisions a new state of matter known as the strongly interacting quark-gluon plasma (sQGP) is produced. A key observable in the study of the sQGP is anisotropic azimuthal flow. The anisotropies are described by flow harmonics, v_n. In this thesis, bias arising from non-uniform azimuthal acceptance and the effect of flow fluctuations are investigated. The main result is an analysis of the pseudorapidity (η) dependence of v_2, v_3 and v_4 over a wide kinematic range: $-3.5 < \eta < 5.0$ in Pb–Pb collisions at $\sqrt{s_{\mathrm{NN}}} = 2.76$ TeV. The analysis is performed using the ALICE Forward Multiplicity Detector and Silicon Pixel Detector at the CERN Large Hadron Collider (LHC). The results are compared to other LHC experiments and previous experiments at lower collision energies.

Contents

Preface

My first real introduction to the CERN Large Hadron Collider came when I did my bachelor project in 2009 in the High Energy Heavy-Ion (HEHI) group at the Niels Bohr Institute (NBI). For this project I analyzed LHC test-beam data from the locally built ALICE Forward Multiplicity Detector (FMD). This was done under the supervision of Professor Jens Jørgen Gaardhøje.

In the following years I regularly went to CERN to take FMD shifts and I wrote my master's thesis on elliptic flow in ALICE, which I defended at the end of September 2011. With the opportunity to delve deeper into the world of heavy-ion physics, I signed up for three more years as a PhD student. Those three years have now passed and the most important results are presented in this thesis. Building on my previous work, this analysis presents a measurement of elliptic (v_2), triangular (v_3) and quadrangular (v_4) flow over a wide pseudorapidity range ($-3.5 < \eta < 5$) in Pb–Pb collisions at $\sqrt{s_{\mathrm{NN}}} = 2.76$ TeV.

Preliminary results for v_2 and v_3 were presented at the Quark Matter 2012 conference in Washington D.C. [1]. In those results, the so-called non-flow was removed using pp collisions at the same collision energy. Rather than go for publication, I chose to further develop the analysis and include a rapidity-gap as a cross-check for the non-flow removal. This proved more difficult than I had first anticipated, and in the process of implementing this, I ended up doing several calculations on biases to the Q-cumulants method - the method used for flow analysis in this thesis. The end result is that the analysis is not yet published. At the time of this writing, a paper draft is being written, and a paper proposal will be presented at a collaboration meeting in October 2014. The hope is to have the results published in the beginning of 2015.

In the first two chapters of this thesis, the theoretical framework is presented. The first chapter presents an overview of the field of heavy-ion physics. The second chapter focuses on relativistic hydrodynamics, the framework used to interpret the results from anisotropic flow analyses. Chapters 3 and 4 are concerning how to measure anisotropic flow and the interpretation of previous measurements. In chapters 5 and 6, the detectors are presented as well as the first part of the data analysis. Chapter 7 describes the various event generators and models necessary to do this analysis. The actual analysis, systematic checks and results are presented in Chapters 8 to 10. In these chapters everything from event selection to cuts and backgrounds are discussed. In particular, the data used for this analysis are not particle tracks, but particle clusters or hits. This means that it is not possible to distinguish between particles originating from interactions with detector material and those originating from the primary collision vertex. This fact presents an extra challenge for the analysis, and a significant amount of the work presented here is regarding the secondary particles produced after the collisions occurred.

Being a PhD student has been an immensely fun and rewarding experience. This is largely due to the many great people I have had a chance to work with. In particular I would like to thank Professor Jens Jørgen Gaardhøje for his supervision of my many projects. Special thanks goes to Kristjan Gulbrandsen for help with everything from calculations, physics interpretations

and understanding, to comments and discussions on various drafts of this thesis. Ante Bilandzic for help with cumulants, flow and comments to my analysis and this thesis. Christian Holm Christensen also deserves thanks for help with coding and a large amount of comments to this text, which greatly improved it. Thanks also to Børge Svane Nielsen and Marek Chojnacki for comments on this text, and, finally, a big thanks to the rest of the HEHI group at NBI for a lot of good times in the past years.

Of course, it is not just the HEHI group that I have had the opportunity to work with, but also the ALICE collaboration. They all deserve thanks. In particular, the conveners of the flow physics analysis group in the past couple of years: Ilya Selyuzhenkov for a lot of help leading up to Quark Matter in 2012 and Alexandru Florin Dobrin and Anthony Robert Timmins for many useful comments during many long meetings. And finally the (past and present) conveners of the correlations and fluctuations working group: Raimond Snellings, Jan Fiete Grosse-Oetringhaus, Michael Weber and Panos Christakoglou.

While being a PhD student has been fun, it has also been a lot of hard work. I would like to thank my friends and family, in particular Ida, for being very understanding about this.

Part I

Theoretical Foundation

Chapter 1

Heavy-Ion Physics

A new state of matter, known as the *strongly interacting quark-gluon plasma* (sQGP) can now be produced in relativistic heavy-ion collisions. The discovery was first made at the Brookhaven Relativistic Heavy Ion Collider by investigating gold–gold (Au–Au) collisions over a wide range of collision energies [2–5]. In 2010, the CERN Large Hadron Collider (LHC) successfully collided lead-ions at center-of-mass energies 14 times higher than RHIC, ushering in a new era in heavy-ion physics. Today, physicists are closer than ever to mapping out the phase diagram of the strong interaction and measuring the properties of the sQGP.

This chapter outlines the basic physics behind heavy-ion collisions. The theory of *quantum chromodynamics* (QCD), which describes the strong nuclear force in the framework of the *standard model* (SM) of particle physics, is introduced. Subsequently, the state of matter known as the *quark-gluon plasma* (QGP) is described. The most important kinematic variables of heavy-ion physics are introduced and finally some of the signals interpreted as a signature for the QGP are presented. The main observable in this thesis - anisotropic flow - is introduced in Chapters 2 to 4.

1.1 Quantum Chromodynamics (QCD)

One of the most successful scientific theories of all time is the SM of particle physics. The model describes a set of fundamental (elementary) particles, and the three forces through which they interact: the electromagnetic force, the weak nuclear force and the strong nuclear force[1]. The electromagnetic and weak forces are described by the electro-weak quantum-field theory. QCD is the quantum field theory describing the strong force. The theory describes the interactions between a group of particles called *quarks* that interact using force-carrying particles called *gluons*. The physical quantity responsible for the interaction is called *color-charge*, hence the name *chromo*dynamics. Color-charge comes in three varieties: blue, red and green, as well as three corresponding anti-colors. The color/anti-color combination can be thought of as the positive and negative charge known from electromagnetism. Indeed combining, for example, blue and anti-blue yields a color-neutral object. However, color-charge has some additional properties: combining one of each of the three (anti-)colors also yields a color-neutral object. The special properties of color-charge is also observed in the gluon, in that it is bi-colored, i.e. has two color charges. Gluons hold quarks together inside hadrons[2]. In a sense, they glue the quarks together, hence the name of gluons. [6]

Two key attributes of QCD are particularly interesting. One is known as *confinement*; it comes from the experimental observation that no free (not bound in a hadron) quark or anti-

[1] The fourth fundamental force, gravity, is not yet described in the SM framework.

[2] A *hadron* is the name given to composite particle made up of quarks (and gluons). They are subsequently divided into *mesons* consisting of a quark and an anti-quark and *baryons* consisting of three quarks

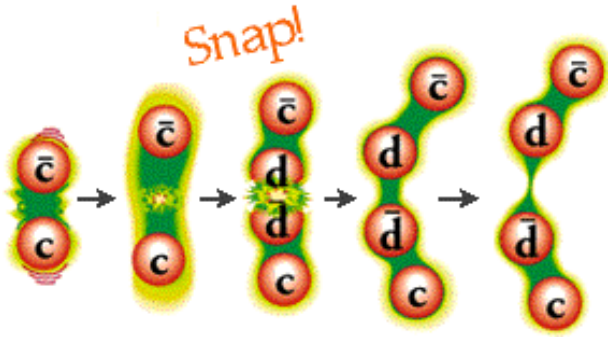

Figure 1.1: Gluon field 'snapping' to produce two new quarks.

quark has ever been observed. Closely related to confinement is the concept of *asymptotic freedom*, which states that quarks interact weakly at short distances. Complementary to this, if two quarks connected by a gluon field move away from each other, the energy stored in the gluon field increases until producing a new pair of quarks becomes energetically favorable. This is illustrated in Fig. 1.1. This behavior is in stark contrast to what is observed in the other three fundamental forces that all become weaker with increasing distance. Not only have free quarks never been observed, but even if two quarks are forced apart, new pairs simply pop into existence. However, asymptotic freedom means that if it is possible to produce a high enough density of quarks, and thus short inter-quark distances, they should interact so weakly with each other that they could be considered *deconfined* or 'free'[3]. Matter consisting of such a high density of quarks and gluons is said to be in a *quark-gluon plasma* state. [7]

The second key attribute of QCD is *chiral symmetry restoration*. Chirality is the *handedness* of a particle. A particle is right-handed if the projection of the spin-vector onto the momentum-vector is positive. Similarly, a particle is left-handed if the projection is negative. Because the quark masses are not zero, chiral symmetry is explicitly broken. When the quarks interact and form hadrons, the chiral symmetry is spontaneously broken. Chiral symmetry *breaking* is responsible for $\sim 99\%$ of hadron masses. In the limit of sufficiently high temperatures and densities, the free quark masses are small enough that chiral symmetry is approximately restored. The theoretical measure of chirality is the vacuum expectation value of the quark/anti-quark system, $\langle q\bar{q}\rangle$. In hadronic matter $\langle q\bar{q}\rangle$ is non-zero, meaning that the vacuum is filled with virtual quarks and anti-quarks. With the onset of deconfinement, $\langle q\bar{q}\rangle \approx 0$ and the symmetry is restored. Thus, creating a deconfined state of quarks and gluons allows for studying unknown and otherwise inaccessible regions of the QCD phase diagram. [8]

Doing calculations within QCD is very difficult. Various techniques are employed for doing the theoretical computations. The most precise method is perturbative QCD. Perturbative QCD only works in the high-momentum limit and consequently has a limited applicability in the study of dense and deconfined matter. To study the non-perturbative regions of QCD an approach treating spacetime as discrete points on a lattice is used - lattice QCD (lQCD). This method is computationally heavy, but allows for insights in otherwise inaccessible regions of the theory. [9]

1.2 Quark-Gluon Plasma (QGP)

T. D. Lee first suggested that the phase transition of hadronic matter into a deconfined state might exist in 1974 [10]. In 1978 Edward Shuryak realized that thermal fluctuations of gauge fields might lead to color screening [11], he then coined the term quark-gluon plasma for describing such matter. This effect is similar to the screening caused by mobile electrical charges

[3] At least free to interact within a small volume.

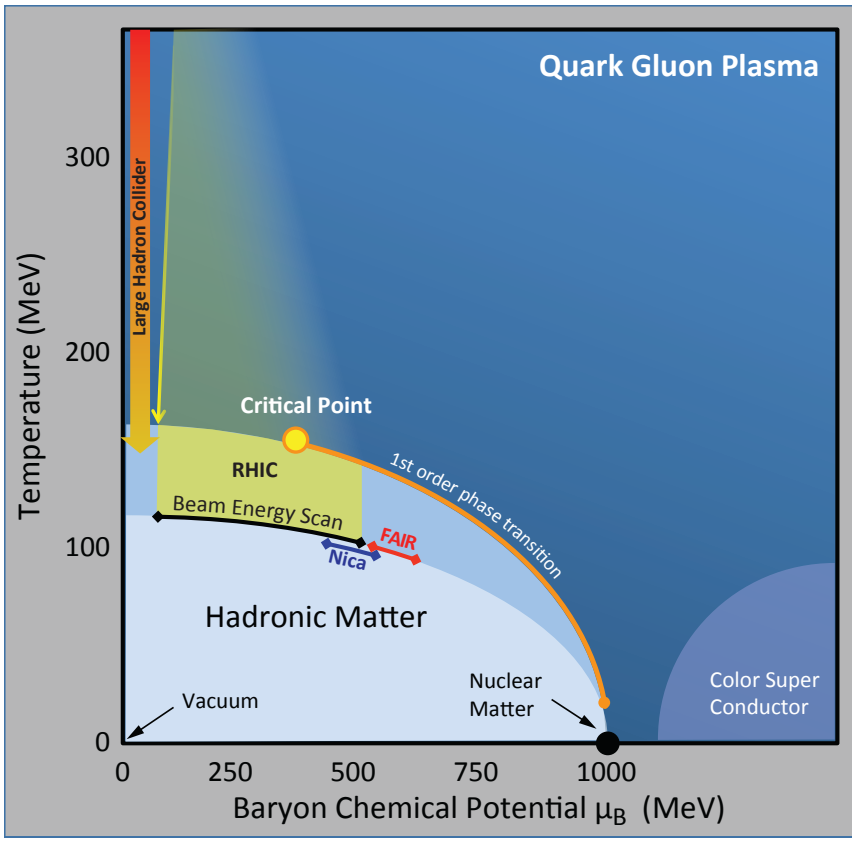

Figure 1.2: The QCD phase diagram and areas explored by RHIC and LHC.

observed in a plasma of ionized gas. Understanding the QGP also has implications for our understanding of the evolution of the Universe. At early times, up to $\sim 10^{-6}$ s after the Big Bang, the Universe was hot and dense enough to be in a QGP state. Thus, understanding the basic properties of the QGP can help understand the evolution of the Universe at early times.

Consequently, there is plenty of motivation to study the QGP phase and corresponding phase transition, but the question is: how to find or produce a QGP? As suggested by Shuryak in his 1978 paper, the density of neutron stars may be high enough for ordinary matter to undergo a phase transition into a QGP. Neutron stars, however, are not readily accessible for these studies. Already in 1974 at the conference in Bear Mountain, it was suggested that collisions of heavy-ions might be used to produce the phase transition [12].

High-energy heavy-ion physics is the study of the QGP and the QGP phase transition. Figure 1.2 shows the QCD phase diagram with the QGP phase at high temperatures and at high baryon chemical potential. Lattice QCD calculations predict that the phase transition occurs at $T_c \simeq 155 \pm 10$ MeV, which is within the range that was first experimentally obtainable [13] at the CERN Super Proton Synchrotron (SPS), and since then at the Brookhaven Relativistic Heavy Ion Collider (RHIC) and CERN Large Hadron Collider (LHC). In Fig. 1.2 the areas of the phase diagram studied at the RHIC and at the LHC are indicated. They are generally at low baryon chemical potential and high temperatures. The early Universe would be positioned at even lower baryon chemical potential, but higher temperature than the LHC [14].

In other words, using relativistic collisions between heavy nuclei makes it possible to study two of the most important properties of the strong interaction: deconfinement and chiral symmetry restoration.

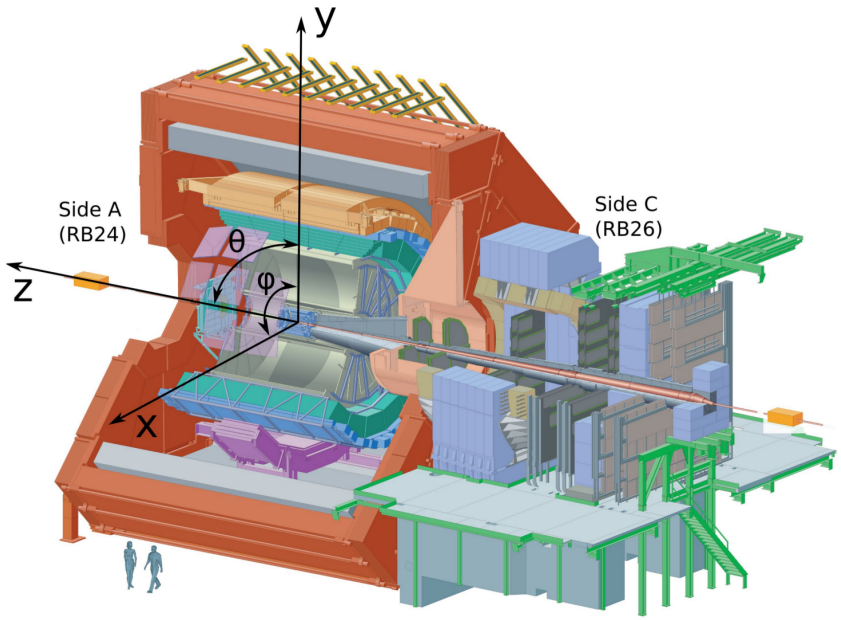

Figure 1.3: A typical example of the coordinate system used in high-energy experiments, here ALICE.

1.3 Kinematic Variables

In order to understand the physics of the collisions it is necessary to define certain variables specific to high-energy physics. In this section the most common kinematic variables are presented.

1.3.1 Collision Energies

The energy in the center-of-mass frame can be calculated using the four-vectors of the colliding beams, $E^\mu = (E, 0, 0, p_z)$, where E is the energy and p_z is the momentum along the beam-pipe. If the particles are of equal mass and energy, it is simply:

$$E_{CM} = \sqrt{(E^\mu + E^\nu)^2} = \sqrt{(2E)^2} = 2E, \tag{1.1}$$

i.e. twice the beam energy. Usually the CM energy is denoted as $\sqrt{s}$ in proton–proton (pp) collisions. When colliding particles consisting of more than one hadron $\sqrt{s_{\mathrm{NN}}}$ is often used, where the 'NN' implies the energy per nucleon pair. Using the available energy per nucleon pair makes it easier to compare heavy-ion experiments with different kinds of nuclei and pp collisions. For the LHC the collision energy is $\sqrt{s_{\mathrm{NN}}} = 2.76$ TeV (5.5 TeV) for the current (design) energy.

1.3.2 Rapidity and Pseudorapidity

The rapidity, y, of a particle is defined as:

$$y \equiv \frac{1}{2} \ln \left(\frac{E + p_z}{E - p_z} \right). \tag{1.2}$$

Rapidity is an important variable in high-energy physics. Moreover, it is additive under Lorentz transformations, which makes it convenient when doing calculations. Of course, to calculate y it is necessary to know the energy of the particle. Sometimes E can be measured directly, but otherwise it is necessary to measure the momentum, p, and mass, m, of the particle, and then use $E = \sqrt{m^2 + p^2}$. In some cases, due to detector limitations, it is not possible to measure

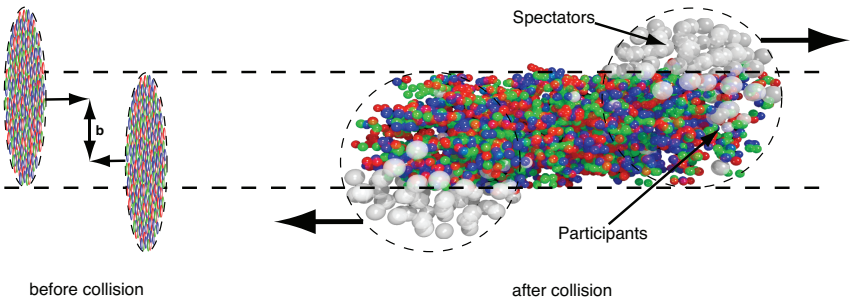

Figure 1.4: Left: The impact parameter of a heavy-ion collision. Right: Spectator and participant nucleons in the collision. Also shown is the so-called *fireball* where the particle production happens. [15]

these properties and calculate y. However, when a particle travels at relativistic speeds, it is a reasonable assumption that $m \ll p \Rightarrow E \to p$. From this follows:

$$y \approx \frac{1}{2}\ln\left(\frac{p+p_z}{p-p_z}\right) = \frac{1}{2}\ln\left(\frac{1+\cos(\theta)}{1-\cos(\theta)}\right) = -\ln[\tan(\theta/2)] \equiv \eta, \tag{1.3}$$

here η is the pseudorapidity and θ is the polar angle as defined in Fig. 1.3. When $p \gg m$ and $\theta \gg 1-\gamma$, where γ is the Lorentz factor, $\eta \approx y$. The pseudorapidity has the advantage that it can be measured when the mass and the momentum of a particle are unknown.

1.3.3 Transverse Momentum

Often the momentum is divided into two terms. A transverse momentum, p_{T}, and a longitudinal momentum, p_z. The transverse momentum has the advantage of being Lorentz invariant. It is defined as:

$$p_{\mathrm{T}} = \sqrt{p_x^2 + p_y^2}. \tag{1.4}$$

1.4 Centrality

The *centrality* of a collision is essential to characterize the hot system that is formed in heavy-ion physics. The nucleus of lead (Pb) has a radius of $R = 1.2 \cdot A^{1/3} \approx 7 \cdot 10^{-15}$ m. When observed from the lab frame, a Pb nucleus traveling at relativistic speeds appear pancake-like because of Lorentz contraction. With at Lorentz factor of 1481 for collisions at $\sqrt{s_{\mathrm{NN}}} = 2.76$ TeV, the length of a Pb nucleus observed from the lab-frame only appears slightly larger than 10^{-19} m. Two of these nuclei colliding will, much like two pancakes colliding, not always have a full overlap. The energy density and consequently the particle production depends on the overlap of the two nuclei. This makes the initial geometry of the collision a very significant observable. The vector connecting the centers of the two nuclei is defined as the *impact parameter*, see the left part of Fig. 1.4. Experimentally it is not feasible to measure b event-by-event, but since the particle production (almost) directly depends on b, the multiplicity can be used as a proxy instead. The experimental measure of the impact parameter is called the *centrality*. The centrality is related to the impact parameter as:

$$c = \frac{\int_0^b \frac{d\sigma}{db'}db'}{\sigma}, \quad b \leq 2R \tag{1.5}$$

where σ is the total nuclear cross section and $\frac{d\sigma}{db'}$ is the differential cross section. For two identical nuclei the differential cross section becomes $\frac{d\sigma}{db'} = 2\pi b' db'$. Using this and the fact that the maximum impact parameter is $b_{max} = 2R$, the total geometric cross section becomes

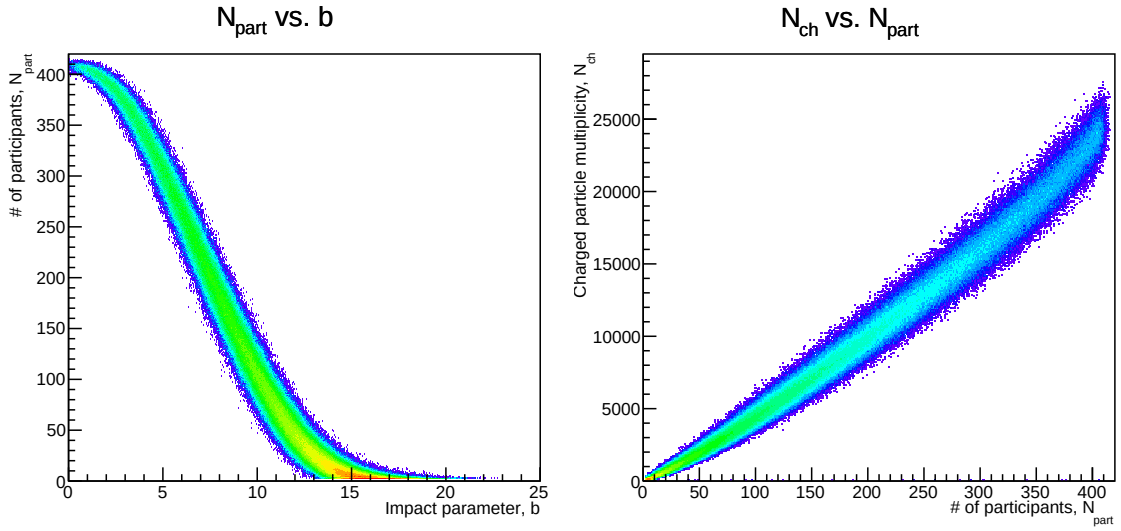

Figure 1.5: Left: Correlation between impact parameter and number of participating nucleons in HIJING. Right: Correlation between total charged particle multiplicity and number of participants.

$\sigma = 4\pi R^2$. Finally the centrality for a given b, assuming the nucleus can be treated as a hard sphere, is:

$$c = \frac{b^2}{4R^2}. \tag{1.6}$$

Equation (1.5) is defined such that c takes a value between 0% and 100%. A collision with a large overlap has a small impact parameter and a small centrality. Such an event is called a *central* event. Similarly a collision with a large b and therefore also large c is called a *peripheral event*.

In general, the colliding nucleons are divided into two different classes: spectators and participants (see Fig. 1.4). The more central a collision is, the more participants and the less spectators it has. The multiplicity depends on the number of participants, N_{part}. This is shown in Figs. 1.5 and 1.6 using the HIJING [16,17] event generator (see Section 7.2). The left plot of Fig. 1.5 shows the correlation between the impact parameter and the total number of nucleons participating. As expected, for a full overlap ($b = 0$) almost all nucleons take part in the collision. The right plot shows the correlation between N_{part} and the charged particle multiplicity. Clearly, the higher multiplicity, the larger the number of participating nucleons. In Fig. 1.6 the left plot shows how a centrality estimator from a detector (in this case the ALICE VZERO, see Section 5.6) is correlated with the total charged particle multiplicity. Finally, the right plot shows how the centrality estimator can be used as a good proxy for the impact parameter.

1.5 QGP Signatures and the Current Status of the Field

Much has happened in heavy-ion physics since the early beginnings in the 1970s. The quark-gluon plasma, as it was originally predicted has not been found. However, it has been experimentally proved that a system with quark-degrees of freedom, now called a strongly interacting QGP (sQGP), is produced. It is the aim of this section to provide an overview of the current understandings in the field, as well as the biggest questions at this time.

One of the more simple and intuitive tests is to look at how many particles are produced per nucleon-nucleon collision, as compared to proton-proton collisions at similar energies. This is done in Fig. 1.7a, where it is clearly seen that the more central a collision is, the more particles

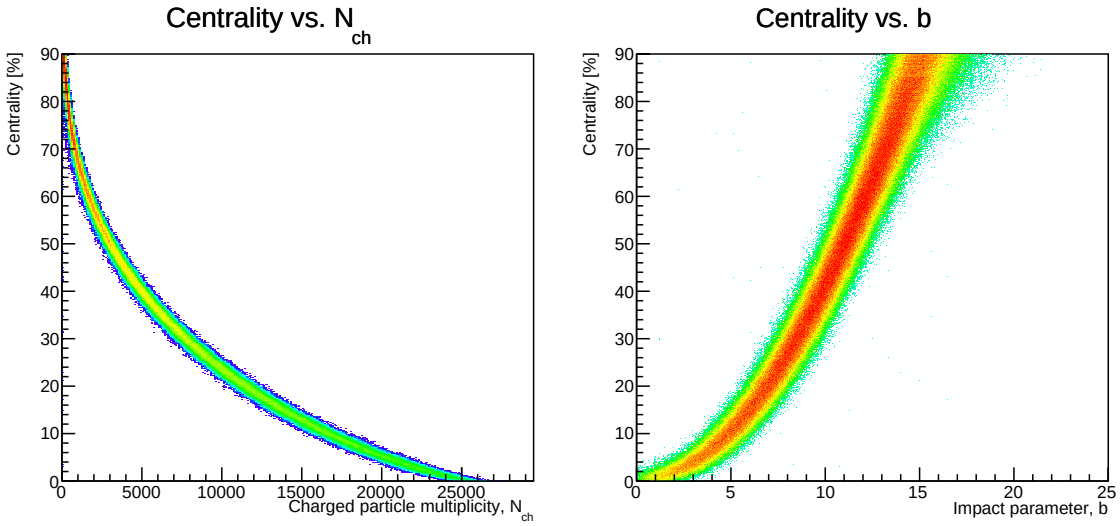

Figure 1.6: Left: Correlation between a centrality estimator (simulation of the ALICE VZERO detector) and total charged particle multiplicity in HIJING. Right: The same centrality estimator used as a proxy for the impact parameter.

are produced per binary collision. This is consistent with a hot lump of QCD matter radiating off quarks and gluons. This system can also be modeled thermodynamically, which is used to predict the relative abundance of particular species of particles. An example of one of these thermal models is shown in Fig. 1.7b, where it is seen that the fit of the thermal model to the data directly yields an estimate on the temperature of the QCD matter at the time where the hadrons are formed. The results of the fits put the temperature close to 160 MeV, which is about the temperature where lattice QCD predicts that the phase transition takes place. If that is the temperature at hadronization, it is likely that it was even hotter in the earlier stages. This suggests that the matter produced may be hot enough to form a QGP.

One of the unique properties of QGP is deconfinement. Deconfinement is expected to set in when a high density of color-charges lead to a screening of long-range interactions [22]. To probe deconfinement the observable must be produced at the early stages of the collision and retain the initial information all the way to the detectors. An example of such observables are the so-called *hard probes*. One example of a hard probe is hard jets. Jets are formed early in the collision when a hard scattering process produces a pair of high-p_{T} quarks or gluons. Due to momentum-conservation the particles in the pair move away from each other and the system undergoes hadronization. The result is two narrow cones of hadrons moving in opposite directions - two jets. If the jets subsequently move through confined matter, only very few gluons will be available to interact with the jets, as they are constrained inside the hadrons. If, on the other hand, the jets move through deconfined matter, there will be many gluons available to interact with the jets. These interactions cause the jets to have a large energy loss per unit length, ultimately leading to jet suppression. Jet suppression was first observed at RHIC [4]. Since then ATLAS has observed events where one of the jets is completely absorbed as it traverses the fireball, thus creating a single jet event [23]. An event-display of one of these events is shown in Fig. 1.8.

Another hard probe is *quarkonia* states. The most famous example of quarkonia in heavy-ion physics is the tightly bound $c\bar{c}$-state - the J/Ψ. The J/Ψ is small, its radius is just $\simeq 0.2$ fm, much less than the normal hadronic scale $\Lambda_{\mathrm{QCD}}^{-1} \simeq 1$ fm. As deconfinement is expected to happen at relatively small length scales, this makes the J/Ψ a good probe. At the same time

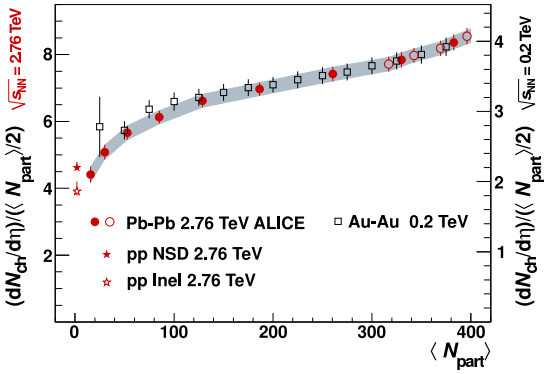

(a) Number of produced particles per binary collision in different collision systems vs. the number of participating nucleons [18].

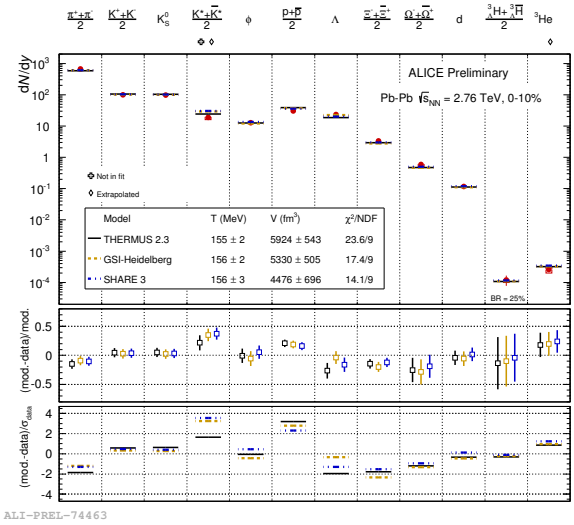

(b) Yields of identified particles with ALICE at LHC. Fits to three thermal models [19–21] are made to estimate the temperature of the medium.

Figure 1.7

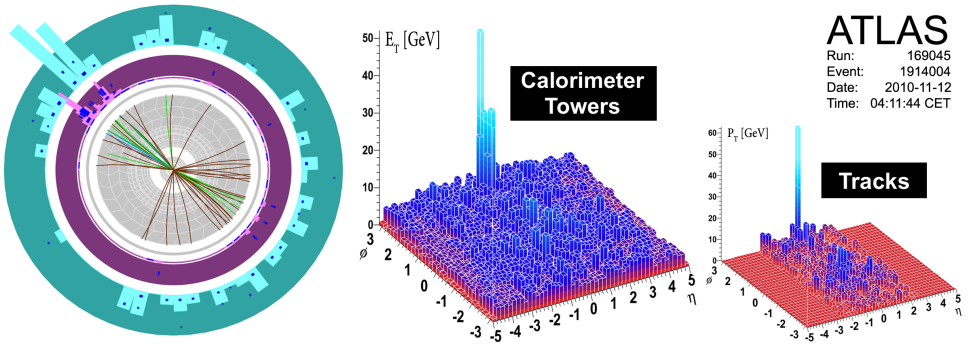

Figure 1.8: ATLAS event-display of a single jet event, where one of the jets is absorbed while traversing the dense medium produced. The middle and right plots show calorimeter towers and tracks, respectively. In both cases a single peak shows the unsuppressed jet, while the signal from the second jet is smeared out over a larger area [23].

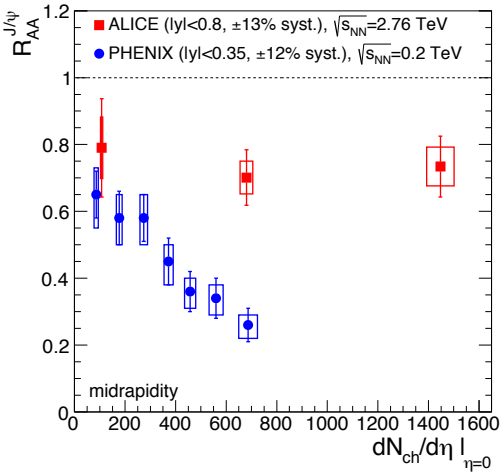

(a) Suppression of J/Ψ-production at RHIC and LHC. At LHC the suppression is smaller, this is expected to be caused by recombination. [29]

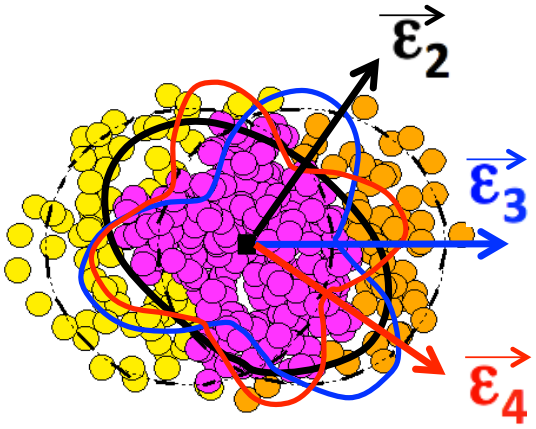

(b) Shapes and symmetry planes in the initial-state geometry giving rise to important observables such as anisotropic flow and correlations.

Figure 1.9

it is a tightly bound state. In a hot QGP, the screening radius is very small. If the screening radius falls below the binding radius of the quarkonium system, the quarks can no longer 'see' each other. This ultimately leads to a suppression in the abundance of quarkonia [24]. Different quarkonium states have different binding radii, making them work almost as a thermometer of the collision [25]. J/Ψ suppression was reported by NA50 at CERN [26] and later by PHENIX at RHIC [27]. For LHC energies it has been suggested that heavy quarks from different nucleus-nucleus collisions may be prevalent enough for quarkonium states to form by coalescence of c and $\bar{c}$ in the sQGP. Thus causing an enhancement of quarkonia [28]. Recent results from LHC seem to support this theory [29]. Figure 1.9a shows the suppression at RHIC and LHC energies. The suppression is clearly smaller at the LHC. Presently, different models describe the data equally well, and there is no final interpretation of the observations at this time. Precision measurements are needed to fully understand the processes involved.

Chiral symmetry restoration is expected to happen, at least approximately, if a QGP phase transition takes place. As the symmetry is restored, the mass of the π and ρ meson changes. The ρ decays into dileptons, which do not interact strongly and should reach the detectors unaffected. A change in mass should be observed as a change or broadening in the dilepton invariant mass spectrum [8]. This has so far not been observed [30], but future precision measurements may show something new.

The main topic of this thesis is anisotropic azimuthal flow, and while it is described in much more detail in the next chapters, it is put here into the general context of heavy-ion physics. The initial-state geometry of the collisions is dominated by the approximately ellipsoidal overlap of the two nuclei. However, it was recently found [31] that other, higher-order shapes also appear due to fluctuations inside the nuclei. A drawing of a collision and the corresponding symmetries is shown in Fig. 1.9b. At RHIC the measurements of the azimuthal anisotropy were for the first time consistent with results from hydrodynamic models, suggesting a strongly interacting medium. This suggests that the quarks and gluons quickly reach a (local) thermal equilibrium, and that the system then behaves as a liquid. It is considered one of the most important results to come out of the early RHIC experiments. For more information on the hydrodynamics used in the models see Chapter 2, for more information on how to measure flow see Chapter 3 and

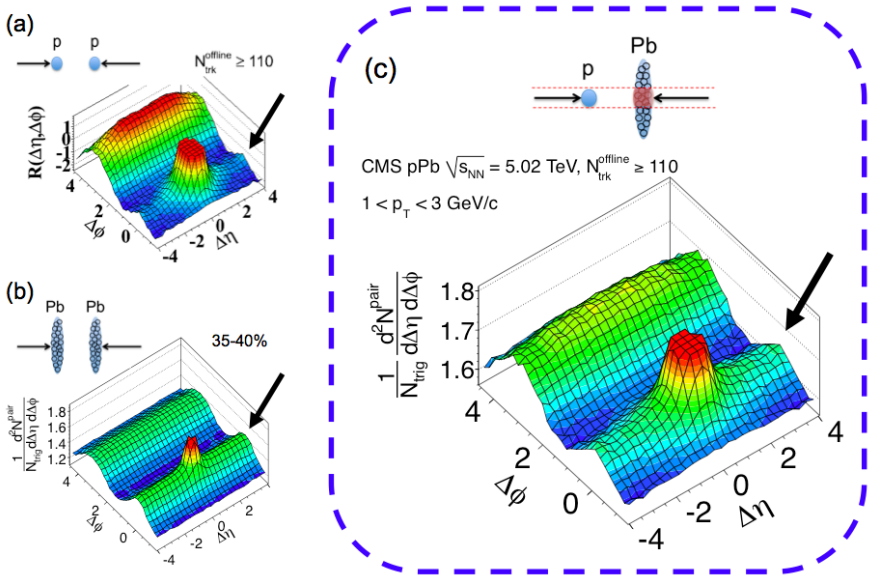

Figure 1.10: CMS observations of two-particle correlation functions. The same structure is observed in Pb–Pb [34] and high-multiplicity p–Pb [35] and pp [36] collisions. [37].

for previous flow measurements and their physical interpretation see Chapter 4.

A consequence of the hydrodynamic evolution of the system is that *collectivity* builds up inside the system. Collectivity means that the bulk of the particles share the same one-particle underlying probability density function. Recent discoveries by CMS [32,33] surprisingly suggest collectivity also in p–Pb collisions. Similarly, results from two-particle correlation analyzes show the same features in Pb–Pb [34] collisions and high-multiplicity p–Pb [35] and pp [36] collisions. These are shown for all three collision systems in Fig. 1.10. The characteristic shape of the 2-dimensional correlation function is associated with collectivity and flow in A–A collisions. With the relatively smaller size of the p–A and pp collision systems it is not yet fully understood what produces these correlations in the smaller systems.

There are many more important observables in heavy-ion physics that have not been covered above [38]. Many observables are found to behave differently in A–A collisions compared to pp or p–A collisions. This behavior can in many cases be understood as a signal of QGP. There are strong suggestions of deconfinement in the early stages, such as the jet-suppression discussed above. The temperature sensitive probes also put the early time temperatures well above the critical temperature for the phase transition found in lQCD calculations. The correlations in the particle spectra observed suggests a strongly interacting system. Some of these observations also appear to a lesser extend in the smaller systems, but there can be little doubt that a system with quark-degrees if freedom is produced in A–A collisions at RHIC and LHC. Although chiral symmetry restoration remains elusive, and with the observation that the system is strongly interacting, asymptotic freedom does not seem to happen either. This means that the 'ideal gas' QGP that was originally expected has not been found, however a sQGP *is* being produced.

It is still not completely understood how the initial state produces the strongly interacting system, some of the initial conditions may be better understood by colliding smaller nuclei, where fluctuations are more dominant. More detailed measurements of heavy quarks and jets may help map out the different stages of the evolution of the system in increasing detail. Finally, the collectivity observed in smaller systems needs to be understood. It is currently not known if these systems are large enough to form a QGP droplet or if some other mechanism can create the same correlations.

Chapter 2

Hydrodynamics

One of the great discoveries at RHIC was that part of the evolution of the fireball produced in heavy-ion collisions could be modeled by relativistic hydrodynamics [2–5]. It is the purpose of this chapter to introduce the basic concepts of relativistic hydrodynamics. This is put in the context of how the system response to an initial spatial anisotropy may lead to an observable anisotropy in momentum space, i.e. the anisotropic azimuthal flow that is the topic of this thesis. For a deeper mathematical treatment of relativistic hydrodynamics or a broader description of hydrodynamic observables in heavy-ion physics, the reader is referred to some of the review papers available on this topic, see Refs. [39–43] and references therein. This chapter begins with a discussion on the applicability of hydrodynamics to describe the evolution of the system produced in heavy-ion collisions.

2.1 Hydrodynamics and Heavy-Ion Collisions

The system goes through a number of different phases in a heavy-ion collision. A schematic of the evolution of the system is shown in Fig. 2.1. First, the initial conditions of the nuclei require knowledge about nuclear structure and the structure of the protons and neutrons. Next is a stage with deconfined quarks in a strongly interacting medium. Then the system undergoes hadronization and kinetic freeze-out.

The application of hydrodynamics relies on local thermal equilibrium. In the very earliest moments after the nuclear impact, when the energy from the participants is converted to new particles with random directions, the system cannot be in thermal equilibrium [40]. This means that the hydrodynamic calculations require some other model to take care of the initial condition calculations. These initial conditions cannot yet be calculated from first principles, but are reasonably well described by various models; The Glauber model [44] (described in Section 7.1) and Color Glass Condensate models [45] are among the most popular. Since many initial state models do not predict a global thermal equilibrium it is important to note that hydrodynamics is also successfully applied to systems near local thermal equilibrium.

Hydrodynamic modeling is applied at early times in the collision, where the quarks are treated as deconfined. At later stages in the collision, when the temperature becomes low enough for hadrons to form again, the mean collision time, τ_{scatt}, becomes larger than the local expansion timescale, τ_{exp}, and the system falls out of equilibrium. This turns it into a gas of free hadrons, a process known as *decoupling*. As the system cools further, the scatterings between the hadrons become too rare for *chemical equilibrium*[1] to be maintained, and the system is said to *freeze out* [40]. As these equilibriums break down, so does the applicability of hydrodynamics. Kinetic-theory models can be applied to describe decoupling and freeze-out [42].

[1] Chemical equilibrium is when the relative abundances of different particle species remain constant.

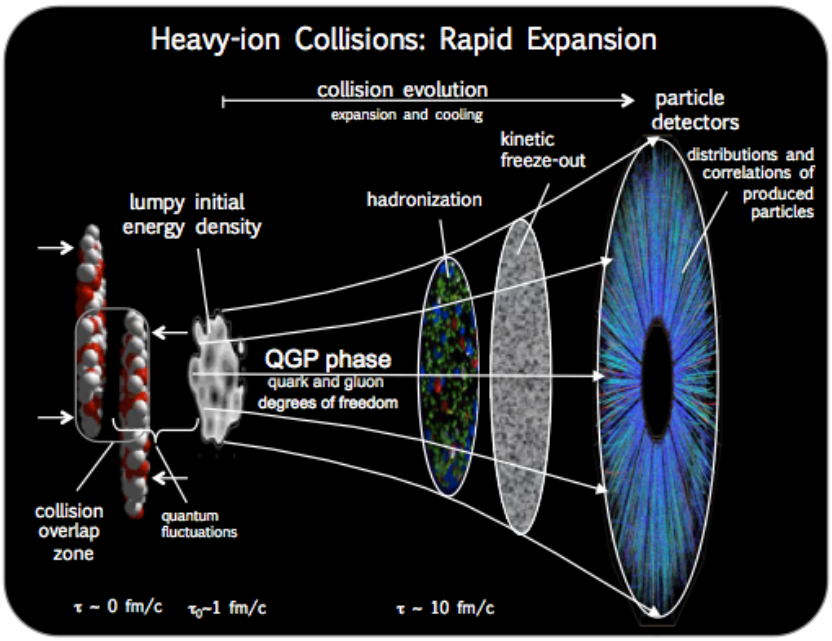

Figure 2.1: Evolution of a heavy-ion collision.

So while hydrodynamics is only one piece of the puzzle, it remains a very important one. This is because it is the description applied while the system is thought to be in the QGP state, from which it follows naturally that many of the most significant observables today in heavy-ion physics have their root in hydrodynamics.

2.2 Ideal Hydrodynamics

An important concept in hydrodynamics is that of fluid elements. A fluid element does not have a specific size, but in the context of hot QCD matter a fluid element contains many more particles than one. All thermodynamic quantities associated with a fluid element are defined in its local rest frame (LRF) [39]. The basic assumption in ideal hydrodynamics is that of local thermal equilibrium. This implies isotropic properties for the fluid elements in their LRF. The basic equations of hydrodynamics are energy-momentum conservation and current conservation:

$$\partial_\mu T^{\mu\nu} = 0, \tag{2.1}$$

$$\partial_\mu N_i^\mu = 0. \tag{2.2}$$

Here $T^{\mu\nu}$ is the energy-momentum tensor and N_i^μ represents any conserved current, typically net baryon number current [41]. The different components of $T^{\mu\nu}$ can be described as [39]:

- T^{00} is the energy density, ϵ.
- T^{0j} is the j^{th} component of the momentum, $j = 1, 2, 3$.
- T^{i0} is the energy flux along the i^{th} axis.
- T^{ij} is the flux along axis i of the j^{th} component of the momentum.

This means that the energy-momentum tensor and current can be decomposed into:

$$T^{\mu\nu} = (\epsilon + p)u^\mu u^\nu - pg^{\mu\nu}, \tag{2.3}$$

$$N_i^\mu = n_i u^\mu, \tag{2.4}$$

where u^μ is the flow vector, $g^{\mu\nu} \equiv diag(1,-1,-1,-1)$ is the Minkowski metric tensor, p is the hydrostatic pressure and n is a current density. For these equations and the rest of this chapter, the notation where repeat indices indicate summation is used. Like any other thermodynamic system, it must also obey the second law of thermodynamics:

$$\partial_\mu S^\mu \geq 0, \tag{2.5}$$

with S^μ being the entropy current, which is just the entropy density, s, times the flow vector: $S^\mu = su^\mu$ [41]. In fact, in ideal hydrodynamics S^μ is a conserved quantity. Only in viscous hydrodynamics does the entropy rise.

For the next calculation a bit of notation needs to be defined. First the tensor

$$\Delta^{\mu\nu} \equiv g^{\mu\nu} - u^\mu u^\nu, \tag{2.6}$$

which in the fluid element's LRF takes the form $diag(0,-1,-1,-1)$ since $u^\mu = (1,0,0,0)$ in the LRF. The substantial time derivative[2],

$$D \equiv u_\mu \partial^\mu, \tag{2.7}$$

is the time derivative along a comoving fluid element, and thus reduces to the regular time derivative, ∂_t, in the LRF. Finally

$$\nabla^\mu = \Delta^{\mu\nu}\partial_\nu, \tag{2.8}$$

which in the fluid element's LRF is simply the gradient [41]. It is also worth noting that [39]:

$$u_\mu u^\mu = 1 \Rightarrow u_\mu \partial_\nu u^\mu = 0, \tag{2.9}$$

$$u_\mu \Delta^{\mu\nu} = 0. \tag{2.10}$$

Contracting Eq. (2.1) with $\Delta_{\alpha\nu}$ and using Eq. (2.3) yields [39]:

$$\partial_\mu T^{\mu\nu} = (\epsilon + p)u^\mu \partial_\mu u^\nu + \partial_\mu((\epsilon+p)u^\mu)u^\nu - \partial^\nu p = 0, \tag{2.11}$$

$$\Delta_{\alpha\nu}\partial_\mu T^{\mu\nu} = (\epsilon+p)(u^\mu \partial_\mu u_\alpha + u_\alpha u^\mu \underbrace{u_\nu \partial_\mu u^\nu}_{=0}) + \underbrace{\Delta_{\alpha\nu}\partial_\mu((\epsilon+p)u^\mu)u^\nu}_{=0} - \Delta_{\alpha\nu}\partial^\nu p \Rightarrow \tag{2.12}$$

$$(\epsilon+p)Du_\alpha = \nabla_\alpha p, \tag{2.13}$$

where Eqs. (2.9) and (2.10) are used to identify the terms equal to 0 in Eq. (2.12). In the LRF this is simply:

$$(\epsilon+p)\partial_t \overline{v} = -\overline{\nabla} p, \tag{2.14}$$

where the bar over the velocity and gradient indicates that they are 3-dimensional spatial vectors. Notice the sign change on the RHS due to the form of $\Delta^{\mu\nu}$ in the local rest frame. This equation states that a pressure gradient (e.g. an external force) accelerates the fluid element. This is Newton's second law and is of great importance in this chapter. It is revisited in Section 2.4.

2.3 Viscous Hydrodynamics

Any deviation from local thermodynamic equilibrium generates additional terms to the decomposition of $T^{\mu\nu}$, N^μ and S^μ [40]:

$$T^{\mu\nu} \rightarrow T^{\mu\nu}_{eq} + \delta T^{\mu\nu} = (\epsilon + p + \Pi)u^\mu u^\nu - (p+\Pi)g^{\mu\nu} + W^\mu u^\nu + W^\nu u^\mu + \pi^{\mu\nu}, \tag{2.15}$$

$$N^\mu_i \rightarrow N^\mu_{i,eq} + \delta N^\mu_i = n_i u^\mu + V^\mu_i, \tag{2.16}$$

$$S^\mu \rightarrow S^\mu_{eq} + \delta S^\mu = su^\mu + \Phi^\mu, \tag{2.17}$$

[2]Sometimes called material derivative or derivative following the motion.

where subscript *eq* denotes the parts from ideal hydrodynamics described above. Π is the bulk pressure, W^μ is the energy flow, $\pi^{\mu\nu}$ is the viscous shear pressure tensor, V_i^μ is the charge (e.g., baryon) flow in the LRF and Φ^μ is the entropy flow vector in the LRF [40].

At this point there is an ambiguity as to which reference frame to choose. The so-called *Eckart frame* has $V^\mu = 0$, i.e. the reference frame is chosen such that there is no baryon flow. This frame is not very well defined for systems with a small net baryon number, such as relativistic heavy-ion collisions. For this reason the so-called *Landau frame* is chosen for the remaining calculations. In the Landau frame there is no energy flow in the LRF, this corresponds to eliminating W^μ (and W^ν) from Eq. (2.15) [41].

As with ideal hydrodynamics the equations of motions are obtained by contracting Eq. (2.1) with $\Delta^{\alpha\nu}$. Defining the total pressure, P, as the sum of hydrostatic and bulk pressure i.e. $P = p + \Pi$ this yields [40]:

$$\partial_\mu T^{\mu\nu} = (\epsilon + P)u^\mu \partial_\mu u^\nu + \partial_\mu((\epsilon + P)u^\mu)u^\nu - \partial^\nu P + \partial_\mu \pi^{\mu\nu} = 0, \tag{2.18}$$

$$\Delta_{\alpha\nu}\partial_\mu T^{\mu\nu} = 0 \Rightarrow$$

$$(\epsilon + P)Du_\alpha = \nabla_\alpha P - \Delta_{\alpha\nu}\nabla_\mu \pi^{\mu\nu} + \pi_{\alpha\nu} Du^\nu. \tag{2.19}$$

Here it is seen that the shear pressure tensor plays a role for the acceleration of the fluid in viscous hydrodynamics. The shear pressure tensor can be written in terms of the shear viscosity η [41]:

$$\pi^{\mu\nu} = 2\eta\langle\nabla^\mu u^\nu\rangle. \tag{2.20}$$

The shear viscosity provides information about the resistance to deformations. A low shear viscosity means a low resistance to deformations. As deformations are exactly what is measured in anisotropic flow analyzes, there is hope of eventually determining the shear viscosity to entropy density ratio, η/s, experimentally, see Section 2.4 and Chapter 4 for further discussion. Just as there is a shear pressure and a bulk pressure, there is also a bulk viscosity. The bulk viscosity determines the resistance to volume changes.

Equation (2.19) is the relativistic version of the famous Navier-Stokes equations from classical fluid dynamics. It does not alway preserve causality and is generally referred to as first order theory. Second order relativistic viscous hydrodynamics does exist, for example in the popular Israel-Stewart version [46, 47]. A more detailed discussion on the shortcomings of first order theory and how to formulate second order theory can be found in Refs. [40, 41, 48]. However, the purpose here is to show how anisotropic flow develops, and Eq. (2.19) is sufficient to show how shear viscosity plays an important role in the evolution of the system.

It has been found that for a strongly coupled N = 4 super-symmetric Yang Mills theory[3], the ratio of shear viscosity to entropy density can be calculated and is found to be $1/4\pi$ [15]. Using the AdS/CFT correspondence[4] [49], it has been suggested that $1/4\pi$ is the lower bound of η/s for all fluids.

2.4 Anisotropic Flow

Anisotropic flow is the measurement of preferred directions of the flow in the fluid. This is a consequence of a non-isotropic pressure gradient, $\nabla^\mu p$ in Eq. (2.13) or Eq. (2.19). The question is how such an anisotropic pressure gradient might come about? To answer this, is it necessary to look at some of the thermodynamic properties of the system. First the thermodynamic identity:

$$dU = -pdV + TdS + \sum_i \mu_i dN_i, \tag{2.21}$$

[3]The standard model is based on Yang Mills theory.

[4]A mathematical duality between conformal field theories (e.g. Yang Mills) and anti-de Sitter spaces used in quantum gravity.

where U is the internal energy, V is the volume, T is the temperature, μ_i is the chemical potential for the conserved current N_i. It can be shown that for an ideal fluid entropy is conserved [41]. This is known as an isentropic process. In such a process only the volume changes, this means that [39]:

$$\frac{ds}{s} = -\frac{dV}{V}. \tag{2.22}$$

Recalling that $\epsilon \equiv U/V$ it follows that:

$$dU = \epsilon dV + V d\epsilon = -pdV. \tag{2.23}$$

Leading to [39]:

$$\frac{d\epsilon}{\epsilon + p} = \frac{ds}{s}. \tag{2.24}$$

Sound is defined as a small perturbation propagating through a uniform fluid at rest. It is possible to define the speed of sound as [39]:

$$c_s \equiv \sqrt{\frac{\partial p}{\partial \epsilon}} \tag{2.25}$$

Using all of the above in Eq. (2.14) yields (in one spatial dimension, x, for simplicity):

$$\begin{aligned}(\epsilon + p)\frac{dv_x}{dt} = -\frac{dp}{dx} \Leftrightarrow \frac{dv_x}{dt} = -\frac{ds}{sd\epsilon}\frac{dp}{dx} = -\frac{dp}{d\epsilon}\frac{d\ln s}{dx} \Leftrightarrow \\ \frac{dv_x}{dt} = c_s^2 \frac{d\ln s}{dx},\end{aligned} \tag{2.26}$$

which states that an initial anisotropy in pressure is equivalent to an initial anisotropy in the entropy density profile. An anisotropic entropy density profile is a natural consequence of the fluctuations inside each of the colliding nuclei, and will, according to Eq. (2.26), accelerate the fluid elements. The actual entropy density profile in a relativistic heavy-ion collision has various theoretical and experimental constraints, and its exact shape depends on the initial conditions. For simplicity it can be assumed initially to be Gaussian [39]:

$$s(x, y, z) \propto \exp\left(-\frac{x^2}{2\sigma_x} - \frac{y^2}{2\sigma_y} - \frac{z^2}{2\sigma_z}\right). \tag{2.27}$$

Figure 2.2a shows the characteristic almond-shaped overlap zone of two spherical nuclei in a non-central collision. In this case, the width in the x-direction is smaller than the width in the y-direction, $\sigma_x < \sigma_y$. Inserting Eq. (2.27) into Eq. (2.26) and integrating over time, for a small time-step δt yields [39]:

$$v_x = \frac{c_s^2 x}{\sigma_x^2}\delta t, \qquad v_y = \frac{c_s^2 y}{\sigma_y^2}\delta t, \tag{2.28}$$

from which it is seen that $\sigma_x < \sigma_y$ implies $v_x > v_y$, this is illustrated by the width of the arrow in Fig. 2.2b. This particular behavior is known as *elliptic flow*, (v_2), due to its shape, and is one of the most important observables in heavy-ion physics.

In reality, as is discussed in Sections 4.1 and 7.1, the nucleons are randomly distributed inside the nuclei, which affects the entropy density profile. This can give rise to higher order shapes, which again gives rise to more complex velocity fields. The acceleration that the fluid elements experience in these situations are equivalent to the elliptic flow example discussed here, but does not decompose as well into v_x and v_y.

In the case of viscous hydrodynamics the assumption made above that the system is isentropic does not strictly hold, as the entropy increases as a function of time in viscous hydrodynamics.

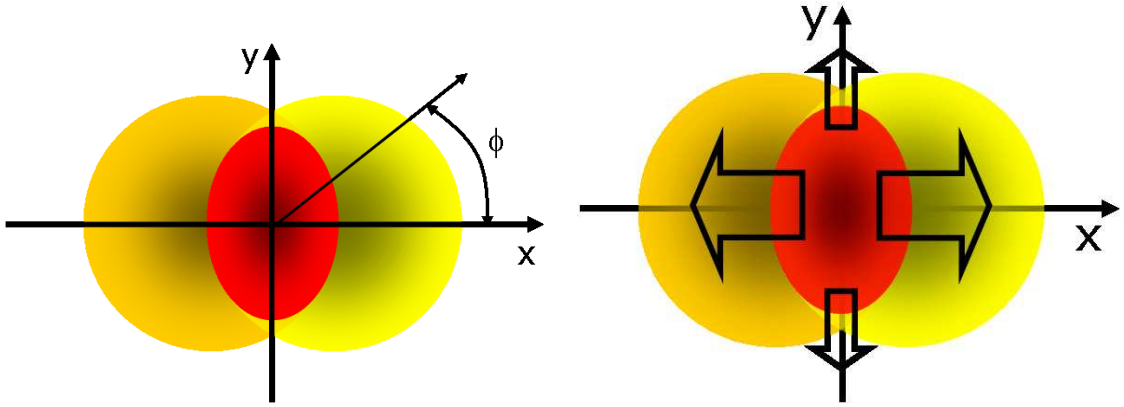

(a) Initial spatial anisotropy.

(b) Momentum-space anisotropy.

Figure 2.2: Anisotropies in a non-central heavy-ion collision. [41]

Moreover, in the derivation of Eq. (2.26) it would be necessary to take into account the shear viscosity, introduced by the shear pressure tensor in Eq. (2.19). The shear viscosity causes diffusion, which dampens the final momentum-space anisotropy as compared to the ideal case. The main conclusion of Eq. (2.28) still holds though, and both elliptic and higher-order flows develop as a consequence of fluctuations in the initial entropy density profile.

As mentioned, the assumption behind the hydrodynamical approach is that the particles interact due to having a small mean free path. For ideal hydrodynamics, this mean free path is zero. Non-zero values means adding viscous effects. As long as the mean free path is very small compared to the system size, hydrodynamics is applicable. Figure 2.3 shows the two extremes. In the left plot, the mean free path is much larger than the system size and the particles move out in their original directions, interacting a little or not at all. The initial anisotropy is not observable in the final particle distributions and the system behaves like a gas. In the right plot, the mean free path is small compared to the system size, the particles interact strongly and the anisotropy is conserved. This is as above, where hydrodynamics works and anisotropic flow can develop. In a sense, this means that the measurement of anisotropic flow is also a measurement of the mean free path of the quarks in the QGP [41].

Treating the particles produced in the collisions with hydrodynamics suggests collective behavior. This means that the particles are emitted independently according to an underlying one-particle probability density function. [50]. While that may be true initially, by the time the particles have gone through hadronization and freeze-out, other correlations are also present. The most dominant of which are:

- Resonance decays: When a particle decays, the azimuthal angles of the decay products are highly correlated.
- Jets: Many particles that are highly correlated, often shows back-to-back structure with two jets shifted in azimuthal angle by π.
- Bose-Einstein correlations: Correlations between identical bosons. The azimuthal angles of these particles are also highly correlated.

In general, few-particle correlations are referred to as *non-flow*. These non-flow correlations are a source of bias in anisotropic flow measurements, as is shown in the next chapter.

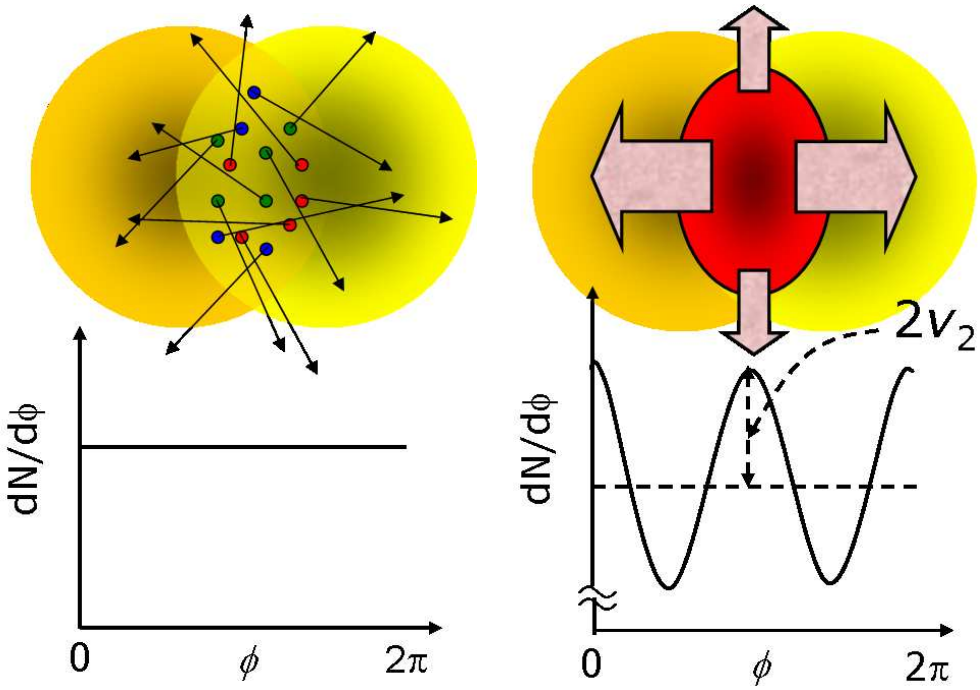

(a) Large mean free path, like a gas.

(b) Small mean free path, like a fluid.

Figure 2.3: Azimuthal particle distributions, $dN/d\varphi$, for systems with different mean free path lengths. [41]

Part II

Anisotropic Azimuthal Flow

Chapter 3

Methods for Measuring Flow

The field of anisotropic flow analysis is characterized by experimentalists and theorists employing a large number of different methods to estimate the flow observables. This chapter presents some of the currently used methods and algorithms for estimating the flow harmonics. The main focus is on the Q-cumulants method which is the method used for this thesis. During this work it has also been improved upon. First, some other methods for measuring flow are discussed in order to motivate the introduction of the Q-cumulants. At the end of the chapter, the current challenges and the future of flow methods are discussed.

The basic principle in flow analysis is to quantify the azimuthal anisotropies via Fourier coefficients obtained through a decomposition of the measured azimuthal yields in a Fourier series:

$$\frac{dN}{d\varphi} \propto f(\varphi) = \frac{1}{2\pi}\left[1 + 2\sum_{n=1}^{\infty} v_n \cos\left(n[\varphi - \Phi_n]\right)\right], \tag{3.1}$$

where Φ_n is the n-th order symmetry plane (or event plane), φ is the azimuthal angle of the produced particles and the coefficient v_n is the n-th order flow harmonic. v_1 is usually referred to as directed flow, v_2 as elliptic flow and v_3 as triangular flow. From Eq. (3.1) by using the orthogonality properties of the trigonometric functions, the coefficients can be found [51]:

$$v_n = \langle \cos(n[\varphi - \Phi_n]) \rangle, \tag{3.2}$$

where the brackets $\langle \ldots \rangle$ denote an average over all particles in an event.

3.1 The Event Plane Method

One of the first - and the most intuitive - method applied in flow analyzes is the *event plane method*, introduced by Voloshin and Zhang in Ref. [51]. First, the symmetry plane is estimated as [52]:

$$\Psi_n = \frac{1}{n}\tan^{-1}\left(\frac{\sum_i w_i \sin(n\varphi_i)}{\sum_i w_i \cos(n\varphi_i)}\right), \tag{3.3}$$

where w_i are weights to correct for e.g. p_{T} efficiency. Here the estimate of the symmetry plane is written as Ψ_n, the reason is that this is only an estimate of the true underlying symmetry plane. Only with an infinite number of particles is the observed symmetry plane the same as the true symmetry plane: $\Psi_n \to \Phi_n$. An inaccurate determination of Φ_n lowers the determination of v_n. It can be shown that v_n is lowered by [50]:

$$R = \langle \cos\left[n(\Psi_n - \Phi_n)\right] \rangle, \tag{3.4}$$

which is known as the *event plane resolution*. In the limit of an infinite number of particles, the resolution factor approaches unity: $R \to 1$. In the low resolution limit, where $v_n/\sqrt{M} \ll 1$, with M representing the number of particles, $R \to kv_n$. Here k is an independent factor that scales as $1/\sqrt{M}$ [50].

Since Φ_n is not known, it is necessary to estimate the resolution in Eq. (3.4) with a different approach. The two most intuitive approaches to estimating the event plane resolution both utilize the division of the particles in a single event into so-called *sub-events*. By dividing the particles into two sub-events with equal multiplicity and measuring Ψ_n for each of them, the event plane resolution is found to be [52]:

$$\left\langle \cos\left[n(\Psi_n^A - \Phi_n)\right]\right\rangle = \sqrt{\langle \cos\left[n(\Psi_n^A - \Psi_n^B)\right]\rangle}, \tag{3.5}$$

where Ψ_n^A and Ψ_n^B denote the event plane *estimate* from sub-event A and B respectively. Sometimes it is not straightforward to divide the event into two equal-sized sub-events. In those cases the three-sub-event method can be utilized [52]:

$$\left\langle \cos\left[n(\Psi_n^A - \Phi_n)\right]\right\rangle = \sqrt{\frac{\langle \cos\left[n(\Psi_n^A - \Psi_n^B)\right]\rangle \langle \cos\left[n(\Psi_n^A - \Psi_n^C)\right]\rangle}{\langle \cos\left[n(\Psi_n^B - \Psi_n^C)\right]\rangle}}, \tag{3.6}$$

which is independent of sub-event multiplicity. Other methods and approximations are discussed in Ref. [52]. Taking into account the event plane resolution, the flow harmonic, v_n, estimated with the event plane method is simply:

$$v_n\{EP\} = \frac{\langle w \cos(n[\varphi - \Psi_n])\rangle}{\langle \cos\left[n(\Psi_n - \Phi_n)\right]\rangle}. \tag{3.7}$$

To reduce bias from non-flow effects it is possible to select particles in different rapidity regions for Ψ_n and v_n. This works because non-flow correlations are often highly correlated in η as well as φ. In general, selecting particles from different rapidity regions is referred to as using η-gaps.

Although the method is very intuitive, it is not without issues. The method was developed at a time where flow fluctuations were expected to be negligible - i.e. the flow being approximately the same every event - which is now known to be wrong.

Furthermore, recent studies reveal that Φ_n may depend on both the rapidity and momentum of the particles, see Section 4.4. If the symmetry plane of the particles of interest (POIs) is not the same as the symmetry plane of the particles used to determine Ψ_n, the measurement will be biased. It may not always be straightforward to correct for this bias

The main issue with the event plane method is best seen by introducing the flow-vector, Q_n:

$$Q_n = |Q_n| e^{in\Psi_n} \equiv \frac{1}{M} \sum_j e^{in\varphi_j}. \tag{3.8}$$

Using this notation, Eq. (3.7) can be written as [50]:

$$v_n\{EP\} = \frac{\left\langle Q_n \frac{Q_{n,A}^*}{|Q_{n,A}|} \right\rangle}{\sqrt{\left\langle \frac{Q_{n,A}}{|Q_{n,A}|} \frac{Q_{n,B}^*}{|Q_{n,B}|} \right\rangle}}, \tag{3.9}$$

where the subscripts A and B denote different sub-events, as for Ψ_n above. In the high resolution case Eq. (3.9) becomes [50]:

$$v_n\{EP\} \to \frac{\langle v_n \cdot 1\rangle}{\sqrt{\langle 1^2\rangle}} = \langle v_n\rangle, \tag{3.10}$$

whereas in the low resolution case,

$$v_n\{EP\} \to \frac{\langle v_n \cdot k v_n \rangle}{\sqrt{\langle k^2 v_n^2 \rangle}} = \sqrt{\langle v_n^2 \rangle}. \tag{3.11}$$

When $v_n\{EP\} = \sqrt{\langle v_n^2 \rangle}$ it is enhanced by flow fluctuations. When $v_n\{EP\} = \langle v_n \rangle$ it is not affected by flow fluctuations. This kind of bias is dangerous when comparing results from different experiments or models. Moving from RHIC energies to LHC energy, the increase in multiplicity yields a higher resolution. This makes comparison of event plane method results between RHIC and LHC experiments difficult. In Ref. [50] Luzum and Ollitrault estimate the bias to be a few percent for v_2 and as much as 10% for v_3 due to moving from a low-resolution case to a high-resolution case. In general, estimating the symmetry planes is cumbersome and comes with an unnecessary uncertainty. Since the introduction of the event plane method many other methods have been introduced that do not require symmetry plane estimation.

3.2 Scalar Product Method

The scalar product method was introduced as an alternative to the event plane method by providing a simpler way to calculate the flow harmonics without as many assumptions [53]. Compared to the event plane method, the scalar product method removes the explicit dependence on symmetry planes and effectively looks at two-particle correlations. It utilizes the notation of flow-vectors, and its simplest form is obtained by simply removing the factors of $|Q_n|$ in Eq. (3.9) [50]:

$$v_n\{SP\} = \frac{\left\langle Q_n \cdot Q_{n,A}^* \right\rangle}{\sqrt{\left\langle Q_{n,A} \cdot Q_{n,B}^* \right\rangle}}, \tag{3.12}$$

where $Q_{n,A}$ and $Q_{n,B}$ is the flow-vector from sub-event A and B, respectively, and Q_n is a differential flow-vector. The particles contributing to each vector can be chosen such that $Q_{n,A}$ and $Q_{n,B}$ contain many particles, thereby yielding statistically stable results. Q_n can then be chosen in a narrow range to measure, for example, the p_{T}- or η-dependence. Under the assumption that Φ_n is the same for the particles in all three flow-vectors, Eq. (3.12) does not require any symmetry plane estimation. It should be noted, that like with the two-sub-event version of the event plane method, Eq. (3.12) requires sub-event A and B to have equal multiplicity. If two equal multiplicity sub-events cannot be made, a three sub-event method can be defined as [50]:

$$v_n\{SP\} = \left\langle Q_n Q_{n,A}^* \right\rangle \sqrt{\frac{\left\langle Q_{n,B} Q_{n,C}^* \right\rangle}{\left\langle Q_{n,A} Q_{n,B}^* \right\rangle \left\langle Q_{n,A} Q_{n,C}^* \right\rangle}}. \tag{3.13}$$

The scalar product method also allows for non-flow removal by introducing a rapidity-gap between the sub-events and the particles of interest. The advantage is that there is no resolution factor to create a bias. It can be shown that $v_n\{SP\}$ yields [54]:

$$v_n\{SP\} = \sqrt{\langle v_n^2 \rangle}, \tag{3.14}$$

independent of any resolution factor. This property makes it directly comparable between different experiments and theoretical models.

The scalar product method is very similar to the two-particle cumulant as it is defined in the Q-cumulants method discussed in Section 3.4.

3.3 Cumulants

A correlation between two particles does not require collectively, e.g. the decay of an unstable particle into two particles also contains correlations. In such cases, the correlation may be from an underlying two-particle probability density function (p.d.f.) instead of the one-particle p.d.f. required for collectivity. Moreover, in the case of collectivity, all particles must have the same symmetry planes. Consequently, all two-particle methods are to some degree affected by non-flow (see Section 3.4.5 for a discussion on the non-flow bias to measurements and Section 2.4 for some of the physical sources of non-flow). As mentioned above, non-flow may be greatly reduced by introducing rapidity-gaps. However, it is not always possible to introduce gaps, and even when it is, it can be difficult to estimate how much of the non-flow is removed. This led to the development of multi-particle techniques (meaning more than two particles), which systematically suppress unwanted few-particle non-flow correlations as the number of particles in the correlator increases.

The first paper on multi-particle correlations by use of cumulants was by Borghini *et al.* in Ref. [55]. In this paper, the cumulants were defined in terms of the amplitude of the flow-vector, but in such a way that an interference between the harmonic of interest, v_n, and higher order harmonics, v_{2n}, would bias the estimate of v_n. In subsequent papers by Borghini *et al.* [56, 57] this bias was removed. These papers introduced the formalism of generating functions.

3.3.1 Multi-Particle Azimuthal Correlations

All cumulant methods used for flow analysis follows the same general formalism. In the following, the single-event average two- and four-particle azimuthal correlations are *defined* as [58]:

$$\langle 2\rangle \equiv \left\langle e^{in(\varphi_1-\varphi_2)}\right\rangle = \frac{1}{\binom{M}{2}2!}\sum_{\substack{i,j=1\\(i\neq j)}}^{M} e^{in(\varphi_i-\varphi_j)}, \tag{3.15}$$

$$\langle 4\rangle \equiv \left\langle e^{in(\varphi_1+\varphi_2-\varphi_3-\varphi_4)}\right\rangle = \frac{1}{\binom{M}{4}4!}\sum_{\substack{i,j,k,l=1\\(i\neq j\neq k\neq l)}}^{M} e^{in(\varphi_i+\varphi_j-\varphi_k-\varphi_l)}, \tag{3.16}$$

which can be generalized to six-, eight- or higher-particle correlations. The averages over all events are then [58]:

$$\langle\langle 2\rangle\rangle \equiv \left\langle\left\langle e^{in(\varphi_1-\varphi_2)}\right\rangle\right\rangle = \frac{\sum_{i=1}^{N}(w_{\langle 2\rangle})_i\langle 2\rangle_i}{\sum_{i=1}^{N}(w_{\langle 2\rangle})_i}, \tag{3.17}$$

$$\langle\langle 4\rangle\rangle \equiv \left\langle\left\langle e^{in(\varphi_1+\varphi_2-\varphi_3-\varphi_4)}\right\rangle\right\rangle = \frac{\sum_{i=1}^{N}(w_{\langle 4\rangle})_i\langle 4\rangle_i}{\sum_{i=1}^{N}(w_{\langle 4\rangle})_i}, \tag{3.18}$$

where $w_{\langle 2\rangle}$ and $w_{\langle 4\rangle}$ are event weights and $\langle\langle\ldots\rangle\rangle$ is the average over all particles in each event and then an average over the events. The expectation values of these observables are [58]:

$$E\left[e^{in(\varphi_1-\varphi_2)}\right] = E\left[e^{in(\varphi_1)}\right]E\left[e^{in(\varphi_2)}\right] + E_c\left[e^{in(\varphi_1-\varphi_2)}\right], \tag{3.19}$$

where E_c is the cumulant containing the genuine correlation. For a detector with perfect acceptance the first two terms on the right-hand-side vanish when averaged over many events. For the four-particle correlator:

$$\begin{aligned} E\left[e^{in(\varphi_1+\varphi_2-\varphi_3-\varphi_4)}\right] &= E\left[e^{in(\varphi_1-\varphi_3)}\right] E\left[e^{in(\varphi_2-\varphi_4)}\right] \\ &+ E\left[e^{in(\varphi_1-\varphi_4)}\right] E\left[e^{in(\varphi_2-\varphi_3)}\right] \\ &+ E_c\left[e^{in(\varphi_1+\varphi_2-\varphi_3-\varphi_4)}\right], \end{aligned} \tag{3.20}$$

from which the cumulants can be isolated and determined by [58]:

$$c_n\{2\} \equiv \langle\langle 2\rangle\rangle, \tag{3.21}$$

$$c_n\{4\} \equiv \langle\langle 4\rangle\rangle - 2\langle\langle 2\rangle\rangle^2, \tag{3.22}$$

using that in the absence of non-flow:

$$\langle\langle 2\rangle\rangle = \left\langle v_n^2 \right\rangle, \tag{3.23}$$

$$\langle\langle 4\rangle\rangle = \left\langle v_n^4 \right\rangle, \tag{3.24}$$

which are estimates of v_n^2 and v_n^4 averaged over *all* events. From these, the two- and four-particle cumulant estimates can be obtained through [56]:

$$v_n\{2\} = \sqrt{c_n\{2\}}, \tag{3.25}$$

$$v_n\{4\} = \sqrt[4]{-c_n\{4\}}. \tag{3.26}$$

3.3.2 Generating Functions

The first attempt at using cumulant for flow estimates, defined the cumulants in terms of flow-vectors. Note that the flow-vector below is defined with a $\sqrt{M}$ prefactor instead of M as in Eq. (3.8) as [55]:

$$Q_n \equiv \frac{1}{\sqrt{M}} \sum_{j=1}^{M} e^{in\varphi_j}. \tag{3.27}$$

Using this definition, the two- and four-particle cumulants were defined as [55]:

$$c_n\{2\} = \left\langle |Q_n|^2 \right\rangle, \tag{3.28}$$

$$c_n\{4\} = \left\langle |Q_n|^4 \right\rangle - 2\left\langle |Q_n|^2 \right\rangle^2, \tag{3.29}$$

which was susceptible to contamination from v_{2n} due to autocorrelations, as the authors also noted in the series of papers.

Consequently, the improved version of the generating functions was proposed by the same authors, which did not have this contamination. One of the main advantages of using cumulants for multi-particle correlation measurements is that they only require a single loop over the particles. The brute-force approach to evaluating Eq. (3.16) requires four nested loops, which is not feasible in an event with thousands of particles due to the necessary large CPU consumption. The generating functions maintain the advantage of doing the analysis in a single loop, as well as introducing a way of correcting for non-uniform azimuthal acceptance (NUA). The main idea is to expand the following complex, real valued function [56]:

$$G_n(z) \equiv \prod_{j=1}^{M} \left(1 + \frac{z^* e^{in\varphi_j} + z e^{-in\varphi_j}}{M}\right), \tag{3.30}$$

in series of $(z^*)^k z^l$, where $k, l = 0, 1, 2, ..., M$. Averaging over many events yields the generating function for the cumulants, $\mathcal{C}_n(z)$ [57]:

$$\langle\langle G_n(z)\rangle\rangle = \left(1 + \frac{\mathcal{C}_n(z)}{M}\right)^M. \tag{3.31}$$

By expanding the generating function for the cumulants in a series of $|z|^{2k}$, the $2k$-particle cumulant can be obtained [58]:

$$\mathcal{C}_n(z) = \sum_{k=1}^{M/2} \frac{|z|^{2k}}{(k!)^2} c_n\{2k\}. \tag{3.32}$$

Expanding the generating function is cumbersome, consequently it is done in practice using numerical interpolation. This need for interpolation is also the weakness of the generating functions approach, as it introduces numerical uncertainties and requires tuning of the interpolation parameters [59].

Borghini *et al.* also introduced the concept of differential flow, where particles from a large part of the phase-space are utilized for a reference measurement. The particles are then divided into smaller bins in e.g. p_T and the correlations with respect to the reference particles are measured. Combined with the reference flow measurement, this can be used to estimate the flow in small differential bins. This allows for statistically stable results, even in areas of the phase-space with relatively few particles that would otherwise be inaccessible to measurements. The calculations are done such that the flow in the reference particles cancel, and only the differential flow remains. This only works if the particles used for the references flow are from the same underlying p.d.f. as the particles used for the differential flow.

3.4 Q-Cumulants

The Q-cumulants were introduced by Bilandzic *et al.* [59] to calculate the cumulants directly and without the use of approximations by making use of Q-vectors. Unlike the original cumulants [55], the Q-cumulant method removes autocorrelations.

The method also includes removal of bias from NUA as well as the possibility to add particle weights to remove reconstruction inefficiencies. Finally, differential flow calculations with respect to a reference flow measurement are also possible. The most important equations and assumptions are outlined below - for detailed calculations, see Ref. [58]. An important note is yet another redefinition of the flow-vector in the following equations:

$$Q_n \equiv \sum_{j=1}^{M} e^{in\varphi_j}. \tag{3.33}$$

3.4.1 Reference Flow

The goal of this section is to determine Eqs. (3.15) to (3.18) by using only the Q-vector defined in Eq. (3.33) and the multiplicity, M.

Two-Particle Reference Flow

As the two sums in Eq. (3.15) are over the same particles, it follows that it can be expressed using Q-vectors:

$$Q_n Q_n^* = |Q_n|^2 = \sum_{i,j=1}^{M} e^{in(\varphi_i - \varphi_j)} = M + \sum_{\substack{i,j=1 \\ (i \neq j)}}^{M} e^{in(\varphi_i - \varphi_j)}, \tag{3.34}$$

thus $\langle 2 \rangle$ can be calculated with a single loop over data [59]:

$$\langle 2 \rangle = \frac{|Q_n|^2 - M}{M(M-1)}. \tag{3.35}$$

The next step is to average $\langle 2 \rangle$ over N events. To minimize effects from multiplicity fluctuations, the following choice of event-weight is chosen for the two-particle reference correlator [59]:

$$w_{\langle 2 \rangle} \equiv M(M-1). \tag{3.36}$$

This is the number of different particle combinations available. If different weights are chosen and the event-by-event multiplicity fluctuations are sufficiently large, there is a risk of the correlators being biased towards higher flow values [58]. Computing Eq. (3.35) and using Eqs. (3.17), (3.21) and (3.25) then yields the reference two-particle cumulant $v_n\{2\}$:

$$\langle\langle 2 \rangle\rangle \equiv \left\langle\left\langle e^{in(\varphi_1 - \varphi_2)} \right\rangle\right\rangle = \frac{\sum_{i=1}^{N} (w_{\langle 2 \rangle})_i \langle 2 \rangle_i}{\sum_{i=1}^{N} (w_{\langle 2 \rangle})_i}, \tag{3.17}$$

$$v_n\{2\} = \sqrt{\langle\langle 2 \rangle\rangle}. \tag{3.37}$$

Four-Particle Reference Flow

The four-particle equations are in general more complicated than the two-particle equations, but the principle is the same. The starting point is the same as before:

$$|Q_n|^4 = Q_n Q_n Q_n^* Q_n^* = \sum_{i,j,k,l=1}^{M} e^{in(\varphi_i + \varphi_j - \varphi_k - \varphi_l)}, \tag{3.38}$$

the combinatorics in this case are a lot more complicated than before, and going from $\sum_{i,j,k,l=1}^{M}$ to $\sum_{i,j,k,l=1,(i \neq j \neq k \neq l)}^{M}$ is not trivial. It can be shown analytically that [59]:

$$\begin{aligned} \langle 4 \rangle = {} & \frac{|Q_n|^4 + |Q_{2n}|^2 - 2 \cdot \mathfrak{Re}\left[Q_{2n} Q_n^* Q_n^*\right]}{M(M-1)(M-2)(M-3)} \\ & - 2 \frac{2(M-2) \cdot |Q_n|^2 - M(M-3)}{M(M-1)(M-2)(M-3)}. \end{aligned} \tag{3.39}$$

The event weight $w_{\langle 4 \rangle}$ is again defined to minimize effects from multiplicity fluctuations [59]:

$$w_{\langle 4 \rangle} \equiv M(M-1)(M-2)(M-3). \tag{3.40}$$

The four-particle cumulant $v_n\{4\}$ result is then obtained by using Eqs. (3.17), (3.18), (3.22) and (3.26):

$$\langle\langle 4 \rangle\rangle \equiv \left\langle\left\langle e^{in(\varphi_1 + \varphi_2 - \varphi_3 - \varphi_4)} \right\rangle\right\rangle = \frac{\sum_{i=1}^{N} (w_{\langle 4 \rangle})_i \langle 4 \rangle_i}{\sum_{i=1}^{N} (w_{\langle 4 \rangle})_i}, \tag{3.18}$$

$$v_n\{4\} = \sqrt[4]{-\langle\langle 4 \rangle\rangle + 2\langle\langle 2 \rangle\rangle^2}. \tag{3.41}$$

3.4.2 Differential Flow

The differential flow is calculated in narrow bins of the observable of interest, e.g. in p_{T} or η. In this case, the initial reference flow measurement is just a tool to get statistically stable results, when measuring in narrow regions of phase-space where only very few particles are present. In general, differential quantities are denoted with a prime ($'$). It is necessary to keep track of which particles are used for the reference flow measurement and which are used for the differential measurement. All particles used for the reference flow are marked as reference particles (RPs). There are M reference particles each event. Particles used for the differential flow are marked as particles of interest (POIs). There are m_p POIs in an event. It is possible to have an overlap between the RPs and the POIs, i.e. a particle can be marked as both POI and RP. In general there are m_q of these particles in an event. It is necessary to keep track of these, as they are used to remove autocorrelations. The two- and four-particle correlators for differential flow (also called the reduced two- and four-particle correlations) are then:

$$\langle 2' \rangle \equiv \left\langle e^{in(\psi_1 - \varphi_2)} \right\rangle = \frac{1}{m_p M - m_q} \sum_{i=1}^{m_p} \sum_{\substack{j \\ (i \neq j)}}^{M} e^{in(\psi_i - \varphi_j)}, \tag{3.42}$$

$$\langle 4' \rangle \equiv \left\langle e^{in(\psi_1 + \varphi_2 - \varphi_3 - \varphi_4)} \right\rangle = \frac{1}{(m_p M - 3m_q)(M-1)(M-2)} \sum_{i=1}^{m_p} \sum_{\substack{j,k,l=1 \\ (i \neq j \neq k \neq l)}}^{M} e^{in(\psi_i + \varphi_j - \varphi_k - \varphi_l)}, \tag{3.43}$$

where ψ_i denotes the azimuthal angle of the i'th POI.

These calculations can be made simpler by introducing the p- and q-vectors:

$$p_n \equiv \sum_{j=1}^{m_p} e^{in\psi_j}, \tag{3.44}$$

$$q_n \equiv \sum_{j=1}^{m_q} e^{in\psi_j}, \tag{3.45}$$

where the sum in p_n is over all POIs and the sum in q_n is over those POIs that are also RPs.

Two-Particle Differential Flow

Using p- and q-vectors in can be shown that Eq. (3.42) can be expressed as [59]:

$$\langle 2' \rangle = \frac{p_n Q_n^* - m_q}{m_p M - m_q}. \tag{3.46}$$

And, as for the reference flow, it can be averaged over N events to:

$$\langle \langle 2' \rangle \rangle = \frac{\sum_{i=1}^{N} (w_{\langle 2' \rangle})_i \langle 2' \rangle_i}{\sum_{i=1}^{N} (w_{\langle 2' \rangle})_i}, \tag{3.47}$$

where the event weight $w_{\langle 2' \rangle}$ is defined as:

$$w_{\langle 2' \rangle} \equiv m_p M - m_q. \tag{3.48}$$

The second order differential Q-cumulant is then:

$$d_n\{2\} = \langle\langle 2' \rangle\rangle. \tag{3.49}$$

And finally, since $\langle e^{in(\psi-\varphi)} \rangle = v_n' v_n$, where v' is the differential flow and v is the reference flow, the flow estimate using the differential two-particle cumulant is [58]:

$$v_n'\{2\} = \frac{d_n\{2\}}{\sqrt{c_n\{2\}}} = \frac{\langle v_n' v_n \rangle}{\sqrt{\langle v_n^2 \rangle}}, \tag{3.50}$$

which in the ideal case with no fluctuation ($\langle v_n^2 \rangle = \langle v_n \rangle^2$) reduces to $v_n'\{2\} = \langle v_n' \rangle$.

Four-Particle Differential Flow

The reduced four-particle cumulant can be written in a similar form:

$$\begin{aligned}\langle 4' \rangle = \Big[& p_n Q_n Q_n^* Q_n^* - q_{2n} Q_n^* Q_n^* - p_n Q_n Q_{2n}^* - 2 \cdot M p_n Q_n^* - 2 \cdot m_q \left| Q_n \right|^2 \\ & + 7 \cdot q_n Q_n^* - Q_n q_n^* + q_{2n} Q_{2n}^* + 2 \cdot p_n Q_n^* + 2 \cdot m_q M - 6 \cdot m_q \Big] \\ & / \Big[(m_p M - 3 m_q)(M-1)(M-2) \Big].\end{aligned} \tag{3.51}$$

This is averaged over N events to:

$$\langle\langle 4' \rangle\rangle = \frac{\sum_{i=1}^{N} (w_{\langle 4' \rangle})_i \langle 4' \rangle_i}{\sum_{i=1}^{N} (w_{\langle 4' \rangle})_i}, \tag{3.52}$$

where the event weight is defined as:

$$w_{\langle 4' \rangle} \equiv (m_p M - 3 m_q)(M-1)(M-2). \tag{3.53}$$

The fourth order differential Q-cumulant is obtained as:

$$d_n\{4\} = \langle\langle 4' \rangle\rangle - 2 \cdot \langle\langle 2' \rangle\rangle \langle\langle 2 \rangle\rangle. \tag{3.54}$$

Using $\langle e^{in(\psi+\varphi_1-\varphi_2-\varphi_3)} \rangle = v_n' v_n^3$ the final result for the four-particle differential cumulant is then [58]:

$$v_n'\{4\} = -\frac{d_n\{4\}}{(-c_n\{4\})^{3/4}} = \frac{-\langle v_n' v^3 \rangle + 2 \left\langle v^2 \right\rangle \langle v' v \rangle}{\langle v_n^4 \rangle^{3/4}}, \tag{3.55}$$

which, when there are no fluctuations, reduces to $v_n'\{4\} = \langle v_n' \rangle$. Section 3.4.4 covers how this changes when flow fluctuations are present.

3.4.3 Rapidity-Gaps

The two-particle cumulant equations presented above are subject to bias from non-flow correlations. It is the same bias that is present when using the scalar product method or the event plane method. These few-particles correlations can be reduced by introducing rapidity-gaps between the flow-vectors. When introducing a rapidity-gap, Eq. (3.50) becomes:

$$v_n'\{2, |\Delta\eta| > x\} = \frac{\langle v_n' v_{n,C} \rangle}{\sqrt{\langle v_{n,A} v_{n,B} \rangle}}, \tag{3.56}$$

where there is a rapidity gap between the two reference flows, $v_{n,A}$ and $v_{n,B}$. In addition, there is a rapidity-gap between v'_n and $v_{n,C}$. The value x states the smallest of the rapidity-gaps in units of η. The particles used for $v_{n,C}$ may overlap with (or equal) $v_{n,A}$ or $v_{n,B}$. Furthermore, in order to get $\langle v' \rangle$, the reference flows must cancel: $v_{n,A} = v_{n,B} = v_{n,C}$, even though they are selected from different regions, in order to satisfy (ignoring flow fluctuations):

$$v'_n\{2, |\Delta\eta| > x\} = \frac{\langle v'_n v_{n,C} \rangle}{\sqrt{\langle v_{n,A} v_{n,B} \rangle}} = \frac{\langle v'_n v_n \rangle}{\sqrt{\langle v_n^2 \rangle}} = \langle v'_n \rangle. \tag{3.57}$$

Equation (3.46) for the differential cumulant, $d_n\{2\}$, is unchanged in the rapidity-gap version, although m_q must be 0 due to no overlap between RPs and POIs. However, in Eq. (3.21) for the reference cumulant, $c_n\{2, |\Delta\eta| > x\}$, there are now two Q-vectors, $Q_{n,A}$ and $Q_{n,B}$, which requires a rewrite of Eq. (3.35) to:

$$\langle 2 \rangle = \frac{Q_{n,A} Q^*_{n,B}}{M_A M_B}, \tag{3.58}$$

and the event weights are similarly changed to $w_{\langle 2 \rangle} = M_A M_B$.

It is not always feasible to choose the reference particles such that $v_{n,A} = v_{n,B}$, in such cases a differential two-particle cumulant with three sub-events may be an alternative [50]:

$$v'_n\{2, |\Delta\eta| > x\} = \sqrt{\frac{d_{n,A}\{2, |\Delta\eta| > x\} \cdot d_{n,B}\{2, |\Delta\eta| > x\}}{c_n\{2, |\Delta\eta| > x\}}} = \sqrt{\frac{\langle v'_n v_{n,A} \rangle \langle v'_n v_{n,B} \rangle}{\langle v_{n,A} v_{n,B} \rangle}}, \tag{3.59}$$

in this case there must be a rapidity gap of at least x units of rapidity between all of v'_n, $v_{n,A}$ and $v_{n,B}$. The denominator is estimated using Eq. (3.58). Furthermore, there are two independent differential cumulants: $d_{n,A}\{2, |\Delta\eta| > x\}$ and $d_{n,B}\{2, |\Delta\eta| > x\}$. The differential cumulants are estimated using Eq. (3.49) with RPs from $v_{n,A}$ and $v_{n,B}$ respectively.

It is worth noticing that using Eq. (3.58) for the reference flow makes $v'_n\{2\}$ identical to the scalar-product method defined in Eq. (3.12). Furthermore, Eq. (3.59) is very similar to Eq. (3.13).

3.4.4 Selection Criteria and Fluctuations

The original event plane method was derived under the assumption that flow fluctuations are negligible. It is now known that this assumption does not hold. Consequently there have been several studies on how fluctuations bias the measurements [50, 54]. However, for this work the bias was studied for differential flow. The findings were published in Ref. [60]. An overview of the findings is presented here, with more detailed calculations given in Appendix A.

It has previously been shown (for a detailed derivation see Appendix A in Ref. [58]) that the reference two-particle cumulant is enhanced by flow fluctuations, while the reference four-particle cumulant is suppressed by flow fluctuations. The reference two- and four-particle cumulant estimates, $v_n\{2\}$ and $v_n\{4\}$, are:

$$v_n\{2\} \equiv \left\langle v_n^2 \right\rangle^{1/2} \approx \langle v_n \rangle + \frac{1}{2} \frac{\sigma^2_{v_n}}{\langle v_n \rangle}, \tag{3.60}$$

$$v_n\{4\} \equiv \left(- \left\langle v_n^4 \right\rangle + 2 \left\langle v_n^2 \right\rangle^2 \right)^{1/4} \approx \langle v_n \rangle - \frac{1}{2} \frac{\sigma^2_{v_n}}{\langle v_n \rangle}, \tag{3.61}$$

where $\langle v_n \rangle$ is the mean value of the flow harmonic of interest and σ_{v_n} the variance of the average. In the last equation it is assumed that $\sigma_{v_n} \ll \langle v_n \rangle$. However, in the more generally applied case, where the reference flow is used to obtain a differential flow, the situation becomes more complicated.

Fluctuations and $v_n'\{2\}$

The differential two-particle cumulant estimate, $v_n'\{2\}$, is obtained using Eq. (3.50). By using $\langle v_n' v_n \rangle = \langle v_n' \rangle \langle v_n \rangle + \rho\, \sigma_{v_n'} \sigma_{v_n}$, where ρ is the correlation coefficient between the reference flow and the differential flow and is by definition in the range $[-1, 1]$. Here $\rho = 1$ when v_n and v_n' are perfectly correlated, $\rho = 0$ when they are uncorrelated, and $\rho = -1$ when they are anti-correlated. Using the assumption $\sigma_{v_n}^2 / \langle v_n \rangle^2 \ll 1$:

$$v_n'\{2\} \approx \langle v_n' \rangle \left(1 + \rho \frac{\sigma_{v_n'} \sigma_{v_n}}{\langle v_n' \rangle \langle v_n \rangle} - \frac{1}{2} \frac{\sigma_{v_n}^2}{\langle v_n \rangle^2}\right), \tag{3.62}$$

from which it is seen that $v_n'\{2\}$ can be *suppressed* by flow fluctuations.

Fluctuations and $v_n'\{4\}$

The differential four-particle cumulant estimate, $v_n'\{4\}$, is obtained as in Eq. (3.55). Using Eq. (3.61) and using that for the variance, $\mathrm{Var}\left[f(x)\right] \approx \left(f'\left(E[x]\right)\right)^2 \mathrm{Var}[x]$:

$$v_n'\{4\} \approx \langle v_n' \rangle \left(1 - \rho \frac{\sigma_{v_n'} \sigma_{v_n}}{\langle v_n' \rangle \langle v_n \rangle} + \frac{1}{2} \frac{\sigma_{v_n}^2}{\langle v_n \rangle^2}\right). \tag{3.63}$$

This is very similar to Eq. (3.62). Once again it is clear that the bias to the differential flow may not be the same as for the reference flow, an enhancement *or* a suppression is possible for both the two- and four-particle differential cumulants. Three specific cases are explored in more detail below.

Specific Cases:

v_n' and v_n are perfectly correlated ($\rho = 1$) and $\sigma_{v_n'}/v_n' = \sigma_{v_n}/v_n$. For this case, RPs and POIs can have a full overlap, but it is not required. Eq. (3.62) can be written as:

$$v_n'\{2\} \approx \langle v_n' \rangle \left(1 + \frac{\sigma_{v_n'}^2}{\langle v_n' \rangle^2} - \frac{1}{2} \frac{\sigma_{v_n'}^2}{\langle v_n' \rangle^2}\right) = \langle v_n' \rangle \left(1 + \frac{1}{2} \frac{\sigma_{v_n'}^2}{\langle v_n' \rangle^2}\right). \tag{3.64}$$

This case reduces to the regular case where the two-particle cumulant is systematically *enhanced* by flow fluctuations, just as for the reference flow. Since $v_n'\{4\}$ simply has opposite signs on the fluctuation terms (Eq. (3.63)), it follows that in this case it is *suppressed*:

$$v_n'\{4\} \approx \langle v_n' \rangle \left(1 - \frac{\sigma_{v_n'}^2}{\langle v_n' \rangle^2} + \frac{1}{2} \frac{\sigma_{v_n'}^2}{\langle v_n' \rangle^2}\right) = \langle v_n' \rangle \left(1 - \frac{1}{2} \frac{\sigma_{v_n'}^2}{\langle v_n' \rangle^2}\right). \tag{3.65}$$

The same as what is found for the reference flow.

v_n' and v_n are uncorrelated ($\rho = 0$). In reality this covers a case where the RPs and POIs are chosen from two groups of particles that do not overlap and do not contain the same underlying correlations. For this case $\rho = 0$ and Eq. (3.62) trivially turns into:

$$v_n'\{2\} \approx \langle v_n' \rangle \left(1 - \frac{1}{2} \frac{\sigma_{v_n}^2}{\langle v_n \rangle^2}\right). \tag{3.66}$$

This means the differential two-particle cumulant is systematically *suppressed* by the flow fluctuations in the reference flow, and that the four-particle differential cumulant is systematically *enhanced*.

$$v_n'\{4\} \approx \langle v_n' \rangle \left(1 + \frac{1}{2} \frac{\sigma_{v_n}^2}{\langle v_n \rangle^2}\right). \tag{3.67}$$

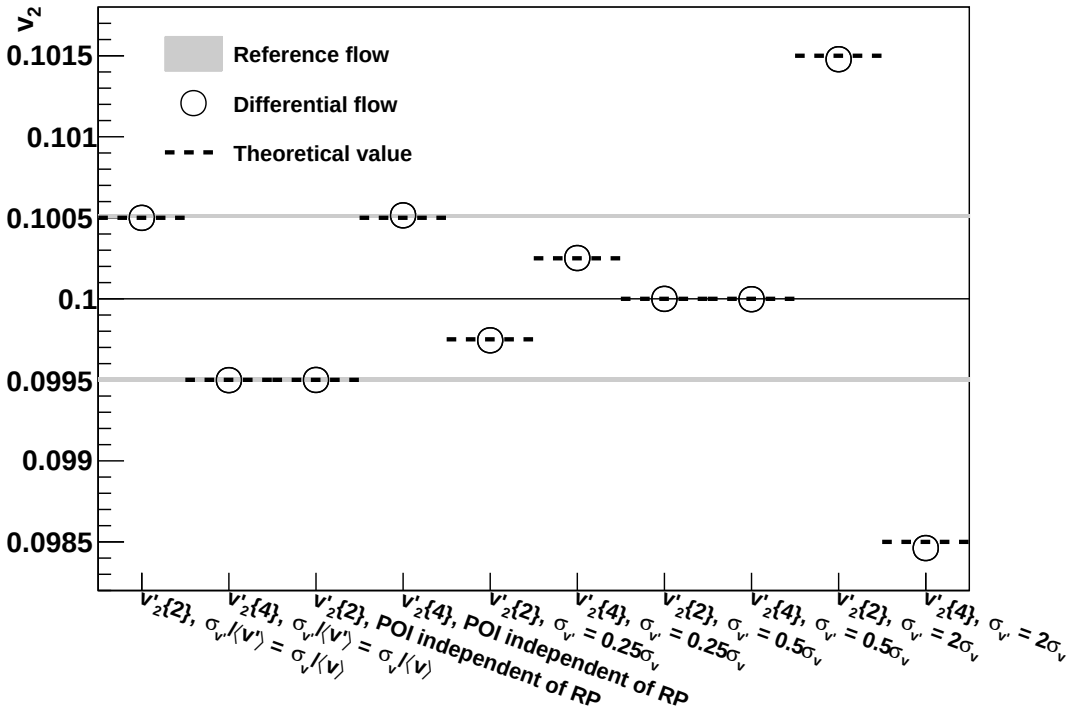

Figure 3.1: 10^6 events with 10000 RPs and 1000 POIs. Input flow is $v_2 = 0.1$, reference flow fluctuations have $\sigma_{v_2} = 0.01$. Depending on the choice of particles for differential flow and the differential flow fluctuations, it is possible to get very different biases to the two- and four-particle cumulants.

Fluctuations from the POIs do not play any role.

v'_n and v_n are correlated, but the relative fluctuations are different. Once again the RPs and POIs may have a full overlap, but it is not required. In this case it is assumed that $\rho \approx 1$, leading to:

$$v'_n\{2\} \approx \langle v'_n \rangle \left(1 + \frac{\sigma_{v'_n}\sigma_{v_n}}{\langle v'_n \rangle \langle v_n \rangle} - \frac{1}{2}\frac{\sigma^2_{v_n}}{\langle v_n \rangle^2}\right), \tag{3.68}$$

and the observed bias for the two-particle (four-particle) differential cumulant is an *enhancement* (*suppression*) as long as $2\frac{\sigma_{v'_n}}{\langle v'_n \rangle} > \frac{\sigma_{v_n}}{\langle v_n \rangle}$. In general the bias observed in the differential flow is influenced by the fluctuations in the reference flow.

To illustrate the different cases a simulation of 10^6 events with 10000 RPs and 1000 POIs is run. The results are shown in Fig. 3.1 with input values, $v_2 = 0.1$ and $\sigma_{v_2} = 0.01$. In the figure, Gaussian fluctuations are used, but other fluctuations, e.g. uniform fluctuations, would yield similar results. The gray lines indicate the reference flow of $v_2\{2\}$ and $v_2\{4\}$, calculated with Eqs. (3.60) and (3.61) respectively, showing the usual enhancement and suppression. The first two data-points are from a simulation illustrating the first case above, where the POIs and RPs are perfectly correlated and share the same relative fluctuations. The dotted lines are calculated using Eq. (3.64) for $v'_2\{2\}$ and the corresponding equation for $v'_2\{4\}$. For the next two data-points the POIs and RPs are chosen with independent fluctuations and no overlap. In this case $v'_2\{2\}$ and $v'_2\{4\}$ are swapped, as expected from Eqs. (3.66) and (3.67). The last six points show cases where the relative fluctuations in the POIs differ from those in the RPs. This can cause the usual enhancement and suppression to be larger, swapped or even be removed completely,

depending on how the relative fluctuations are chosen. In the example simulations shown here, RPs and POIs do not overlap. For the case where $\sigma_{v'_n} = 0.25\sigma_{v_n}$ Eqs. (3.62) and (3.63) yields:

$$v'_n\{2\} = \langle v'_n \rangle \left(1 - \frac{1}{4}\frac{\sigma^2_{v_n}}{\langle v_n \rangle^2}\right), \quad v'_n\{4\} = \langle v'_n \rangle \left(1 + \frac{1}{4}\frac{\sigma^2_{v_n}}{\langle v_n \rangle^2}\right). \tag{3.69}$$

For $\sigma_{v'_n} = 0.5\sigma_{v_n}$, Eqs. (3.62) and (3.63) yields:

$$v'_n\{2\} = v'_n\{4\} = \langle v'_n \rangle, \tag{3.70}$$

and finally for $\sigma_{v'_n} = 2\sigma_{v_n}$:

$$v'_n\{2\} = \langle v'_n \rangle \left(1 + \frac{3}{2}\frac{\sigma^2_{v_n}}{\langle v_n \rangle^2}\right), \qquad v'_n\{4\} = \langle v'_n \rangle \left(1 - \frac{3}{2}\frac{\sigma^2_{v_n}}{\langle v_n \rangle^2}\right). \tag{3.71}$$

It is tempting to use Eqs. (3.60) and (3.61) to estimate the magnitude of the flow fluctuations. However, when doing differential flow analysis with cumulants it is clear from Eqs. (3.62) and (3.63) that it may not be feasible. In fact, any analysis using differential flow should be very careful to describe the choice of RPs and POIs in great detail, such that comparison between different experiments and theoretical models is not biased by mixing two or more of the cases shown in Fig. 3.1 and described above. The potential bias can easily be tested by using different regions for several reference measurements. Then, if the differential measurement changes with the different reference regions, it is possible that a bias from the particle selection is present.

3.4.5 Non-Flow

Non-flow is an important source of bias to any two-particle flow measurement. The main sources for non-flow are described in Section 2.4. Therefore its effect on various flow methods has previously been studied, e.g. in Ref. [54]. In Ref. [58] it is shown that $c_n\{2\}$ receives a bias from non-flow that scales as $\delta_n \propto 1/M$. Whereas $c_n\{4\}$ gets a contribution proportional to $1/M^3$, which is essentially negligible. Although jets and other many-particle correlations may also bias the four-particle results, it is considered to be negligible. When removing non-flow from the two-particle cumulant, the usual approach is to do it by:

$$v_n\{2\}^{nf\text{-}corr} = \sqrt{v_n^2\{2\}^{obs} - \delta_n}, \tag{3.72}$$

where $v_n^2\{2\}^{obs}$ is the measured value of the two-particle cumulant and $v_n^2\{2\}^{nf\text{-}corr}$ is the non-flow corrected value. As with the fluctuations, the calculation has only been done for the reference flow. Below the bias to the two-particle differential flow is studied. The case of differential flow is clearly more complicated as non-flow can be partially removed by not having (or at least minimizing) the overlap between RPs and POIs. Equation (3.72) was obtained assuming that all particles are counted twice. In these calculation a more general case is considered for both the reference and differential flow.

Reference Flow

As mentioned above, the Q-cumulants are based on the use of the flow-vector, Eq. (3.33). To estimate the effect of few-particle correlations, the flow-vector is modified to assume that each particle, j, is counted k_j times. In reality the non-flow correlations will likely have a small difference in φ-angle, but that is neglected in these calculations. The modified flow-vector is then:

$$Q_n = \sum_j k_j e^{in\varphi_j}. \tag{3.73}$$

With this, a number of additional multiplicities become relevant, namely the number of particles that are counted k times, which is denoted as M_k. This means that M_1 particles are counted once, M_2 particles are counted twice, and so on. The total multiplicity is then:

$$M_{tot} = \sum_{k=1} k \cdot M_k. \tag{3.74}$$

Using combinatorics:

$$E\left[|Q_n|^2\right] = v_n^2 \left(\sum_k kM_k \left(M_{tot} - k\right) \right) + \sum_k k^2 M_k, \tag{3.75}$$

$$\begin{aligned} \langle 2 \rangle &= \frac{v_n^2 \left(\sum_k kM_k \left(M_{tot} - k\right)\right) + \sum_k k^2 M_k - M_{tot}}{M_{tot}(M_{tot} - 1)} \\ &= \frac{v_n^2 \left(\sum_k kM_k \left(M_{tot} - k\right)\right)}{M_{tot}(M_{tot} - 1)} + \frac{\sum_k kM_k(k-1)}{M_{tot}(M_{tot} - 1)}, \end{aligned} \tag{3.76}$$

while this expression is not directly useful from an experimental viewpoint, it does show where the $\delta_n \propto 1/M$ scaling comes from. In the limit of $M_{tot} \gg k$ Eq. (3.76) reduces to:

$$\langle 2 \rangle \approx \frac{v_n^2 M_{tot}^2}{M_{tot}^2} + \frac{\sum_k kM_k(k-1)}{M_{tot}^2} = v_n^2 + \frac{\sum_k kM_k(k-1)}{M_{tot}^2}, \tag{3.77}$$

which in the case where all particles are counted twice yields the same results as was found in [58] (where a case where each particle was counted k times was also studied). This shows that the reference flow is biased in such a way that applying Eq. (3.72) will remove the non-flow contribution properly, assuming δ_n is correctly determined. Determination of δ_n is discussed in Chapter 8.

Differential Flow

The differential flow using two-particle cumulants is given by Eq. (3.50), where the bias to the denominator is described above. Focus in this section is therefore on the numerator. There are two flow-vectors associated with the differential flow, as given by Eqs. (3.44) and (3.45). To simplify the calculations, the particles are chosen such that all POIs are also RPs (but not all RPs are POIs), i.e. $m_q = m_p$ and $q_n = p_n$. To estimate non-flow effects, RPs can still be counted k times, but each RP can then be counted as a POI $k_{p,j}$ times, where $k_{p,j} \leq k_j$. The flow-vectors are then:

$$p_n = \sum_{j=1} k_{p,j} e^{in\psi_j} = q_n. \tag{3.78}$$

The multiplicities must fulfill:

$$m_{p,tot} = \sum_{k_p=1} k_p \cdot m_{p,k}. \tag{3.79}$$

As before, $m_{p,1}$ are the particles counted once ($k_p = 1$) in the differential flow, $m_{p,2}$ are the particles counted twice ($k_p = 2$) in the differential flow, and so on. Using Eq. (3.46) yields:

$$E\left[p_n Q_n^*\right] = v_n' v_n \left(\sum_k k_p m_{p,k} \left(M_{tot} - k\right) \right) + \sum_k k k_p m_{p,k}, \tag{3.80}$$

$$\langle 2' \rangle = \frac{v_n' v \left(\sum_k k_p m_{p,k} \left(M_{tot} - k\right)\right) + \sum_k k k_p m_{p,k} - m_{p,tot}}{m_{p,tot}(M_{tot} - 1)} \tag{3.81}$$

$$= \frac{v_n' v_n \left(\sum_k k_p m_{p,k} \left(M_{tot} - k\right)\right)}{m_{p,tot}(M_{tot} - 1)} + \frac{\sum_k k_p m_p(k-1)}{m_{p,tot}(M_{tot} - 1)}, \tag{3.82}$$

in the limit of $M_{tot} \gg k$ this can be approximated as:

$$\langle 2' \rangle \approx \frac{v_n' v_n m_{p,tot} M_{tot}}{m_{p,tot} M_{tot}} + \frac{\sum_k k_p m_{p,k}(k-1)}{m_{p,tot} M_{tot}} = v_n' v_n + \frac{\sum_k k_p m_{p,k}(k-1)}{m_{p,tot} M_{tot}}. \tag{3.83}$$

Denoting the non-flow contribution to the differential flow as δ_n' the total bias to the observed two-particle differential cumulant is:

$$v_n'\{2\}^{obs} = \frac{\langle v_n' v_n \rangle + \delta_n'}{\sqrt{\langle v_n^2 \rangle + \delta_n}}. \tag{3.84}$$

Thus, the differential flow and reference flow need to be corrected individually:

$$v_n'\{2\}^{nf\text{-}corr} = \frac{d_n\{2\}^{obs} - \delta_n'}{\sqrt{c_n\{2\}^{obs} - \delta_n}} = \frac{d_n\{2\}^{nf\text{-}corr}}{v_n\{2\}^{nf\text{-}corr}}. \tag{3.85}$$

The main outcome of these calculations is that in order to efficiently remove non-flow from a differential flow measurement, it is necessary to remove the non-flow contributions from the reference flow and differential flow separately.

3.4.6 Non-Uniform Acceptance

The Q-cumulants are also capable of correcting for bias caused by non-uniform acceptance (NUA). Originally, the NUA correction was found by looking at the expectation value in Eq. (3.19). In this case the two single-particle terms are non-zero only when there is a NUA. Subtracting these terms from $\langle\langle 2 \rangle\rangle$ yields a modified version of Eq. (3.21):

$$c_n\{2\} = \langle\langle 2 \rangle\rangle - \langle\langle \cos n\varphi_1 \rangle\rangle^2 - \langle\langle \sin n\varphi_1 \rangle\rangle^2. \tag{3.86}$$

Using flow-vectors, they are analytically calculated as:

$$\langle\langle \cos n\varphi_1 \rangle\rangle \equiv \frac{\sum_{i=1}^{N} (\mathfrak{Re}[Q_n])_i}{\sum_{i=1}^{N} M_i}, \tag{3.87}$$

and

$$\langle\langle \sin n\varphi_1 \rangle\rangle \equiv \frac{\sum_{i=1}^{N} (\mathfrak{Im}[Q_n])_i}{\sum_{i=1}^{N} M_i}. \tag{3.88}$$

Using similar arguments, the correction to the fourth order cumulant is found to be [58]:

$$\begin{aligned} c_n\{4\} = {} & \langle\langle 4 \rangle\rangle - 2\langle\langle 2 \rangle\rangle^2 - 4 \cdot \langle\langle \cos n\varphi_1 \rangle\rangle \langle\langle \cos n(\varphi_1 - \varphi_2 - \varphi_3) \rangle\rangle \\ & + 4 \cdot \langle\langle \sin n\varphi_1 \rangle\rangle \langle\langle \sin n(\varphi_1 - \varphi_2 - \varphi_3) \rangle\rangle - \langle\langle \cos n(\varphi_1 + \varphi_2) \rangle\rangle^2 - \langle\langle \sin n(\varphi_1 + \varphi_2) \rangle\rangle^2 \\ & + 4 \cdot \langle\langle \cos n(\varphi_1 + \varphi_2) \rangle\rangle \left[\langle\langle \cos n\varphi_1 \rangle\rangle^2 - \langle\langle \sin n\varphi_1 \rangle\rangle^2 \right] \\ & + 8 \cdot \langle\langle \cos n(\varphi_1 - \varphi_2) \rangle\rangle \left[\langle\langle \cos n\varphi_1 \rangle\rangle^2 + \langle\langle \sin n\varphi_1 \rangle\rangle^2 \right] \\ & + 8 \cdot \langle\langle \sin n(\varphi_1 + \varphi_2) \rangle\rangle \langle\langle \sin n\varphi_1 \rangle\rangle \langle\langle \cos n\varphi_1 \rangle\rangle - 6 \cdot \left[\langle\langle \cos n\varphi_1 \rangle\rangle^2 + \langle\langle \sin n\varphi_1 \rangle\rangle^2 \right]^2, \end{aligned} \tag{3.89}$$

where everything but the first two terms are to correct for bias from NUA. The additional terms are defined as:

$$\langle\langle\cos n(\varphi_1+\varphi_2)\rangle\rangle \equiv \frac{\sum_{i=1}^{N}(\mathfrak{Re}[Q_nQ_n-Q_{2n}])_i}{\sum_{i=1}^{N}M_i(M_i-1)}, \tag{3.90}$$

$$\langle\langle\sin n(\varphi_1+\varphi_2)\rangle\rangle \equiv \frac{\sum_{i=1}^{N}(\mathfrak{Im}[Q_nQ_n-Q_{2n}])_i}{\sum_{i=1}^{N}M_i(M_i-1)}, \tag{3.91}$$

$$\langle\langle\cos n(\varphi_1-\varphi_2-\varphi_3)\rangle\rangle \equiv \frac{\sum_{i=1}^{N}(\mathfrak{Re}[Q_nQ_n^*Q_n^*-Q_nQ_{2n}^*]-2(M-1)\mathfrak{Re}[Q_n^*])_i}{\sum_{i=1}^{N}M_i(M_i-1)(M_i-2)}, \tag{3.92}$$

$$\langle\langle\sin n(\varphi_1-\varphi_2-\varphi_3)\rangle\rangle \equiv \frac{\sum_{i=1}^{N}(\mathfrak{Im}[Q_nQ_n^*Q_n^*-Q_nQ_{2n}^*]-2(M-1)\mathfrak{Im}[Q_n^*])_i}{\sum_{i=1}^{N}M_i(M_i-1)(M_i-2)}. \tag{3.93}$$

Similarly for differential flow, the second order differential cumulant is found to be [58]:

$$d_n\{2\} = \langle\langle 2'\rangle\rangle - \langle\langle\cos n\psi_1\rangle\rangle\langle\langle\cos n\varphi_2\rangle\rangle - \langle\langle\sin n\psi_1\rangle\rangle\langle\langle\sin n\varphi_2\rangle\rangle, \tag{3.94}$$

where the last two terms are the added terms, which can be calculated using flow-vectors:

$$\langle\langle\cos n\psi_1\rangle\rangle \equiv \frac{\sum_{i=1}^{N}(\mathfrak{Re}[p_n])_i}{\sum_{i=1}^{N}(m_p)_i}, \tag{3.95}$$

$$\langle\langle\sin n\psi_1\rangle\rangle \equiv \frac{\sum_{i=1}^{N}(\mathfrak{Im}[p_n])_i}{\sum_{i=1}^{N}(m_p)_i}, \tag{3.96}$$

For the four-particle differential cumulant [58]:

$$
\begin{aligned}
d_n\{4\} &= \langle\langle 4' \rangle\rangle - 2 \cdot \langle\langle 2' \rangle\rangle \langle\langle 2 \rangle\rangle \\
&- \langle\langle \cos n\psi_1 \rangle\rangle \langle\langle \cos n(\varphi_1 - \varphi_2 - \varphi_3) \rangle\rangle + \langle\langle \sin n\psi_1 \rangle\rangle \langle\langle \sin n(\varphi_1 - \varphi_2 - \varphi_3) \rangle\rangle \\
&- \langle\langle \cos n\varphi_1 \rangle\rangle \langle\langle \cos n(\psi_1 - \varphi_2 - \varphi_3) \rangle\rangle + \langle\langle \sin n\varphi_1 \rangle\rangle \langle\langle \sin n(\psi_1 - \varphi_2 - \varphi_3) \rangle\rangle \\
&- 2 \cdot \langle\langle \cos n\varphi_1 \rangle\rangle \langle\langle \cos n(\psi_1 + \varphi_2 - \varphi_3) \rangle\rangle - 2 \cdot \langle\langle \sin n\varphi_1 \rangle\rangle \langle\langle \sin n(\psi_1 + \varphi_2 - \varphi_3) \rangle\rangle \\
&- \langle\langle \cos n(\psi_1 + \varphi_2) \rangle\rangle \langle\langle \cos n(\varphi_1 + \varphi_2) \rangle\rangle - \langle\langle \sin n(\psi_1 + \varphi_2) \rangle\rangle \langle\langle \sin n(\varphi_1 + \varphi_2) \rangle\rangle \\
&+ 2 \cdot \langle\langle \cos n(\varphi_1 + \varphi_2) \rangle\rangle \left[\langle\langle \cos n\psi_1 \rangle\rangle \langle\langle \cos n\varphi_1 \rangle\rangle - \langle\langle \sin n\psi_1 \rangle\rangle \langle\langle \sin n\varphi_1 \rangle\rangle \right] \\
&+ 2 \cdot \langle\langle \sin n(\varphi_1 + \varphi_2) \rangle\rangle \left[\langle\langle \cos n\psi_1 \rangle\rangle \langle\langle \sin n\varphi_1 \rangle\rangle + \langle\langle \sin n\psi_1 \rangle\rangle \langle\langle \cos n\varphi_1 \rangle\rangle \right] \\
&+ 4 \cdot \langle\langle \cos n(\varphi_1 - \varphi_2) \rangle\rangle \left[\langle\langle \cos n\psi_1 \rangle\rangle \langle\langle \cos n\varphi_1 \rangle\rangle + \langle\langle \sin n\psi_1 \rangle\rangle \langle\langle \sin n\varphi_1 \rangle\rangle \right] \\
&+ 2 \cdot \langle\langle \cos n(\psi_1 + \varphi_2) \rangle\rangle \left[\langle\langle \cos n\varphi_1 \rangle\rangle^2 - \langle\langle \sin n\varphi_1 \rangle\rangle^2 \right] \\
&+ 4 \cdot \langle\langle \sin n(\psi_1 + \varphi_2) \rangle\rangle \langle\langle \cos n\varphi_1 \rangle\rangle \langle\langle \sin n\varphi_1 \rangle\rangle \\
&+ 4 \cdot \langle\langle \cos n(\psi_1 - \varphi_2) \rangle\rangle \left[\langle\langle \cos n\varphi_1 \rangle\rangle^2 + \langle\langle \sin n\varphi_1 \rangle\rangle^2 \right] \\
&- 6 \cdot \left[\langle\langle \cos n\varphi_1 \rangle\rangle^2 - \langle\langle \sin n\varphi_1 \rangle\rangle^2 \right] \left[\langle\langle \cos n\psi_1 \rangle\rangle \langle\langle \cos n\varphi_1 \rangle\rangle - \langle\langle \sin n\psi_1 \rangle\rangle \langle\langle \sin n\varphi_1 \rangle\rangle \right] \\
&- 12 \cdot \langle\langle \cos n\varphi_1 \rangle\rangle \langle\langle \sin n\varphi_1 \rangle\rangle \left[\langle\langle \sin n\psi_1 \rangle\rangle \langle\langle \cos n\varphi_1 \rangle\rangle + \langle\langle \cos n\psi_1 \rangle\rangle \langle\langle \sin n\varphi_1 \rangle\rangle \right], \qquad (3.97)
\end{aligned}
$$

where everything except the first line is to correct for non-uniform azimuthal acceptance. The additional correction terms are calculated as:

$$\langle\langle \cos n(\psi_1 + \varphi_2) \rangle\rangle = \frac{\sum_{i=1}^{N} \left(\mathfrak{Re} \left[p_n Q_n - q_{2n} \right] \right)_i}{\sum_{i=1}^{N} \left(m_p M - m_q \right)_i}, \qquad (3.98)$$

$$\langle\langle \sin n(\psi_1 + \varphi_2) \rangle\rangle = \frac{\sum_{i=1}^{N} \left(\mathfrak{Im} \left[p_n Q_n - q_{2n} \right] \right)_i}{\sum_{i=1}^{N} \left(m_p M - m_q \right)_i}, \qquad (3.99)$$

$$\langle\langle \cos n(\psi_1 + \varphi_2 - \varphi_3) \rangle\rangle = \frac{\sum_{i=1}^{N} \left(\mathfrak{Re} \left[p_n \left(|Q_n|^2 - M \right) \right] - \mathfrak{Re} \left[q_{2n} Q_n^* + m_q Q_n - 2q_n \right] \right)_i}{\sum_{i=1}^{N} \left[(m_p M - 2m_q)(M - 1) \right]_i}, \qquad (3.100)$$

$$\langle\langle \sin n(\psi_1 + \varphi_2 - \varphi_3) \rangle\rangle = \frac{\sum_{i=1}^{N} \left(\mathfrak{Im} \left[p_n \left(|Q_n|^2 - M \right) \right] - \mathfrak{Im} \left[q_{2n} Q_n^* + m_q Q_n - 2q_n \right] \right)_i}{\sum_{i=1}^{N} \left[(m_p M - 2m_q)(M - 1) \right]_i}, \qquad (3.101)$$

$$\langle\langle \cos n(\psi_1 - \varphi_2 - \varphi_3) \rangle\rangle = \frac{\sum_{i=1}^{N} \left(\mathfrak{Re} \left[p_n Q_n^* Q_n^* - p_n Q_{2n}^* \right] - \mathfrak{Re} \left[2m_q Q_n^* - 2q_n^* \right] \right)_i}{\sum_{i=1}^{N} \left[(m_p M - 2m_q)(M - 1) \right]_i}, \qquad (3.102)$$

$$\langle\langle \sin n(\psi_1 - \varphi_2 - \varphi_3) \rangle\rangle = \frac{\sum_{i=1}^{N} \left(\mathfrak{Im} \left[p_n Q_n^* Q_n^* - p_n Q_{2n}^* \right] - \mathfrak{Im} \left[2m_q Q_n^* - 2q_n^* \right] \right)_i}{\sum_{i=1}^{N} \left[(m_p M - 2m_q)(M - 1) \right]_i}. \qquad (3.103)$$

3.4.7 Removing Cross-Harmonic Bias from Non-Uniform Acceptance

An assumption in the derivation of the NUA correction terms in [58] is that the p.d.f. is completely described by a *single* Fourier component. At LHC and RHIC, the first six coefficients have been measured as non-zero. A study of bias stemming from NUA-effects caused by other harmonics was first studied in [61]. Below, the same method is applied to the two-particle Q-cumulant, and a correction for bias from other harmonics is proposed. Detailed calculations are found in Appendix B.

One of the basic assumptions used in multi-particle flow analysis is that multi-particle p.d.f.'s factorize into the products of single particle p.d.f.'s. The underlying p.d.f.'s are described by

the Fourier series:

$$f(\varphi, \bar{\Psi}) = \frac{1}{2\pi}\left(1 + 2\sum_n v_n \cos(n(\varphi - \Psi_n))\right), \tag{3.104}$$

where $\bar{\Psi} = (\Psi_1, \Psi_2, ..., \Psi_n)$ is the n-dimensional symmetry plane vector, which are unknown parameters. So the expectation value evaluated in Eq. (3.17) is:

$$\langle\langle 2\rangle\rangle = \langle\langle e^{in(\varphi_i - \varphi_j)}\rangle\rangle = \frac{1}{2\pi(\varphi_b - \varphi_a)^2}\int_0^{2\pi} d\bar{\Psi}\int_{\varphi_a}^{\varphi_b} d\varphi_i \int_{\varphi_a}^{\varphi_b} d\varphi_j e^{in(\varphi_i - \varphi_j)} f(\varphi_i, \bar{\Psi}) f(\varphi_j, \bar{\Psi}), \tag{3.105}$$

where φ_i and φ_j are random observables. In addition, the coefficients v_n are also unknown parameters, but assumed fixed in all events, unlike Ψ_n. In the case of uniform acceptance, $\varphi_a = 0$ and $\varphi_b = 2\pi$. In case of a NUA, φ_a and φ_b are given by the coverage of the detector. In case the detector has more than a single non-uniform sector in azimuthal acceptance, the right side of Eq. (3.105) should be changed to a sum over the coverages. The equation assumes that factorization works, i.e., there are only flow correlations present. The product $f(\varphi_i, \bar{\Psi}) f(\varphi_j, \bar{\Psi})$ can be written as:

$$\begin{aligned} f(\varphi_i, \bar{\Psi}) f(\varphi_j, \bar{\Psi})(4\pi^2) = 1 &+ 2\sum_n v_n \cos(n(\varphi_i - \Psi_n)) \\ &+ 2\sum_m v_m \cos(m(\varphi_j - \Psi_m)) \\ &+ 4\sum_k v_k^2 \cos(k(\varphi_i - \Psi_k))\cos(k(\varphi_j - \Psi_k)) \\ &+ 4\sum_{\substack{j,l \\ j\neq l}} v_j v_l \cos(j(\varphi_i - \Psi_j))\cos(l(\varphi_j - \Psi_l)). \end{aligned} \tag{3.106}$$

In order to evaluate Eq. (3.105) it is convenient to divide it into the following five (un-normalized) integrals:

$$\textcircled{1} = \int_0^{2\pi} d\bar{\Psi}\int_{\varphi_a}^{\varphi_b} d\varphi_i \int_{\varphi_a}^{\varphi_b} d\varphi_j e^{in(\varphi_i - \varphi_j)} \cdot 1, \tag{3.107}$$

$$\textcircled{2} = \int_0^{2\pi} d\bar{\Psi}\int_{\varphi_a}^{\varphi_b} d\varphi_i \int_{\varphi_a}^{\varphi_b} d\varphi_j e^{in(\varphi_i - \varphi_j)} \cdot 2\sum_n v_n \cos(n(\varphi_i - \Psi_n)), \tag{3.108}$$

$$\textcircled{3} = \int_0^{2\pi} d\bar{\Psi}\int_{\varphi_a}^{\varphi_b} d\varphi_i \int_{\varphi_a}^{\varphi_b} d\varphi_j e^{in(\varphi_i - \varphi_j)} \cdot 2\sum_m v_m \cos(m(\varphi_j - \Psi_m)), \tag{3.109}$$

$$\textcircled{4} = \int_0^{2\pi} d\bar{\Psi}\int_{\varphi_a}^{\varphi_b} d\varphi_i \int_{\varphi_a}^{\varphi_b} d\varphi_j e^{in(\varphi_i - \varphi_j)} \cdot 4\sum_k v_k^2 \cos(k(\varphi_i - \Psi_k))\cos(k(\varphi_j - \Psi_k)), \tag{3.110}$$

$$\textcircled{5} = \int_0^{2\pi} d\bar{\Psi}\int_{\varphi_a}^{\varphi_b} d\varphi_i \int_{\varphi_a}^{\varphi_b} d\varphi_j e^{in(\varphi_i - \varphi_j)} \cdot 4\sum_{\substack{j,l \\ j\neq l}} v_j v_l \cos(j(\varphi_i - \Psi_j))\cos(l(\varphi_j - \Psi_l)). \tag{3.111}$$

The task is then to evaluate ①–⑤, which is first done in the case of uniform acceptance and then in the case of NUA. In order to solve these equations, the orthogonality relations between

the sine and cosine functions are heavily used:

$$\int_{-\pi}^{\pi} \sin(mx)\sin(nx)dx = \pi\delta_{mn}, \tag{3.112}$$

$$\int_{-\pi}^{\pi} \cos(mx)\cos(nx)dx = \pi\delta_{mn}, \tag{3.113}$$

$$\int_{-\pi}^{\pi} \sin(mx)\cos(nx)dx = 0, \tag{3.114}$$

where δ_{mn} is the Kronecker delta function.

Uniform Acceptance

In the case of uniform acceptance $\varphi_a = 0$ and $\varphi_b = 2\pi$. In this case (1)–(3) are trivially 0. For (4) two cases are considered. First the case where $k = n$:

$$(4\text{a}) = \int_0^{2\pi} d\bar{\Psi} \int_0^{2\pi} d\varphi_i \int_0^{2\pi} d\varphi_j e^{in(\varphi_i - \varphi_j)} \tag{3.115}$$

$$\cdot\, 4v_n^2 \cos(n(\varphi_i - \Psi_n))\cos(k(\varphi_j - \Psi_n)) = (2\pi)^3 v_n^2, \tag{3.116}$$

which, when normalized, is equal to v_n^2 as expected. In the case where $k \neq n$:

$$(4\text{b}) \propto \int_0^{2\pi} d\varphi_i e^{in\varphi_i} \sum_k v_k^2 \cos(k(\varphi_i - \Psi_k)) \propto \int_0^{2\pi} d\varphi_i \cos(n\varphi_i)\sin(k\varphi_i) = 0, \tag{3.117}$$

by making use of $\cos(x - y) = \cos(x)\cos(y) + \sin(x)\sin(y)$. Finally in (5) using either the integral over φ_i or φ_j it is always possible to get proportionality to a term similar to Eq. (3.117) and so (5) = 0 for a uniform acceptance. In conclusion, for a uniform acceptance, evaluating Eq. (3.105) yields:

$$\langle\langle e^{in(\varphi_i - \varphi_j)}\rangle\rangle = \langle v_n^2\rangle, \tag{3.118}$$

as expected.

Non-Uniform Acceptance

In this section a non-uniform acceptance is assumed. This means that, at least, either $\varphi_a \neq 0$ or $\varphi_b \neq 2\pi$. Both may also be true, and in case the detector used has more than one hole, it is possible to do:

$$\int_0^{2\pi} d\bar{\Psi} \int_{\varphi_a}^{\varphi_b} d\varphi_i \int_{\varphi_a}^{\varphi_b} d\varphi_j \to \sum_\alpha \left(\int_0^{2\pi} d\bar{\Psi} \int_{\varphi_{a,\alpha}}^{\varphi_{b,\alpha}} d\varphi_i \int_{\varphi_{a,\alpha}}^{\varphi_{b,\alpha}} d\varphi_j \right). \tag{3.119}$$

For simplicity, the summation is not explicitly written below. In Appendix B it is shown that (2), (3) and (5) are all zero, even when there is a NUA. Integral (1), when normalized, is found to be:

$$(1)_{norm} = \langle\langle\cos(n\varphi_1)\rangle\rangle\langle\langle\cos(n\varphi_2)\rangle\rangle + \langle\langle\sin(n\varphi_1)\rangle\rangle\langle\langle\sin(n\varphi_2)\rangle\rangle. \tag{3.120}$$

This term is the correction derived in [58] and shown in Eq. (3.86), which only depends on n (and the detector acceptance). (4) is once again divided into two cases. The normalized results for the case where $n = k$ it is found to be:

$$(4\text{a})_{norm} = v_n^2 \left(1 + \langle\langle\cos(2n\varphi_1)\rangle\rangle\langle\langle\cos(2n\varphi_2)\rangle\rangle + \langle\langle\sin(2n\varphi_1)\rangle\rangle\langle\langle\sin(2n\varphi_2)\rangle\rangle\right), \tag{3.121}$$

which shows an extra bias from terms with $2n$. The case with $n \neq k$ is where a real bias from other harmonics shows up:

$$\begin{aligned}\text{(4b)}_{norm} = \sum_{\substack{k \\ k\neq n}} v_k^2 &(\langle\langle\cos((k-n)\varphi_1)\rangle\rangle\langle\langle\cos((k-n)\varphi_2)\rangle\rangle \\ &+\langle\langle\sin((k-n)\varphi_1)\rangle\rangle\langle\langle\sin((k-n)\varphi_2)\rangle\rangle \\ &+\langle\langle\cos((k+n)\varphi_1)\rangle\rangle\langle\langle\cos((k+n)\varphi_2)\rangle\rangle \\ &+\langle\langle\sin((k+n)\varphi_1)\rangle\rangle\langle\langle\sin((k+n)\varphi_2)\rangle\rangle).\end{aligned} \tag{3.122}$$

It is important to note, that the bias from other harmonics has a factor v_k^2 in front. This means that when $v_k > v_n$ it may contribute more to the uncorrected $v_n\{2\}$ measurement than v_n. In conclusion, evaluating Eq. (3.105) in the case of a NUA yields:

$$\begin{aligned}\langle\langle e^{in(\varphi_1-\varphi_2)}\rangle\rangle &= v_n^2 + \langle\langle\cos(n\varphi_1)\rangle\rangle\langle\langle\cos(n\varphi_2)\rangle\rangle + \langle\langle\sin(n\varphi_1)\rangle\rangle\langle\langle\sin(n\varphi_2)\rangle\rangle \\ &+ v_n^2\big[\langle\langle\cos(2n\varphi_1)\rangle\rangle\langle\langle\cos(2n\varphi_2)\rangle\rangle + \langle\langle\sin(2n\varphi_1)\rangle\rangle\langle\langle\sin(2n\varphi_2)\rangle\rangle\big] \\ &+ \sum_{\substack{k \\ k\neq n}} v_k^2\big[\langle\langle\cos((k-n)\varphi_1)\rangle\rangle\langle\langle\cos((k-n)\varphi_2)\rangle\rangle \\ &+ \langle\langle\sin((k-n)\varphi_1)\rangle\rangle\langle\langle\sin((k-n)\varphi_2)\rangle\rangle \\ &+ \langle\langle\cos((k+n)\varphi_1)\rangle\rangle\langle\langle\cos((k+n)\varphi_2)\rangle\rangle \\ &+ \langle\langle\sin((k+n)\varphi_1)\rangle\rangle\langle\langle\sin((k+n)\varphi_2)\rangle\rangle\big].\end{aligned} \tag{3.123}$$

All of the above terms need to be subtracted from the measurement. This means that all the non-zero harmonics are coupled. To correct for this it is advantageous to first correct for the terms that are coming from the same harmonics:

$$c_n^{\mathrm{NUA}}\{2\} = \frac{\langle\langle 2\rangle\rangle - \langle\langle\cos(n\varphi_1)\rangle\rangle\langle\langle\cos(n\varphi_2)\rangle\rangle - \langle\langle\sin(n\varphi_1)\rangle\rangle\langle\langle\sin(n\varphi_2)\rangle\rangle}{1 + \langle\langle\cos(2n\varphi_1)\rangle\rangle\langle\langle\cos(2n\varphi_2)\rangle\rangle + \langle\langle\sin(2n\varphi_1)\rangle\rangle\langle\langle\sin(2n\varphi_2)\rangle\rangle}. \tag{3.124}$$

Since the terms are coupled, an n-dimensional vector containing the non-zero coefficients of Eq. (3.124) is constructed. It is written as $\overline{c_n^{\mathrm{NUA}}\{2\}}$. Similarly a vector is constructed containing the fully corrected values of interest, $c_n\{2\}$, in the case of reference flow. This vector is written as $\overline{c_n\{2\}}$ and:

$$\overline{c_n\{2\}} = \begin{pmatrix} c_1\{2\} \\ c_2\{2\} \\ \vdots \\ c_n\{2\} \end{pmatrix}. \tag{3.125}$$

Then:

$$\overline{c_n^{\mathrm{NUA}}\{2\}} = \mathfrak{M}\cdot\overline{c_n\{2\}} \Rightarrow \overline{c_n\{2\}} = \mathfrak{M}^{-1}\cdot\overline{c_n^{\mathrm{NUA}}\{2\}}, \tag{3.126}$$

where $\mathfrak{M}$ is a $n \times n$ matrix containing the cross-harmonic bias terms:

$$\mathfrak{M} = \begin{pmatrix} 1 & \mathrm{NUA}_{1,2} & \dots & \mathrm{NUA}_{1,n} \\ \mathrm{NUA}_{2,1} & 1 & & \mathrm{NUA}_{2,n} \\ \vdots & & \ddots & \vdots \\ \mathrm{NUA}_{n,1} & \mathrm{NUA}_{n,2} & \dots & 1 \end{pmatrix}, \tag{3.127}$$

$$\begin{aligned}\mathrm{NUA}_{n,m} = &\frac{\langle\langle\cos\left[(m-n)\varphi_1\right]\rangle\rangle\langle\langle\cos\left[(m-n)\varphi_2\right]\rangle\rangle + \langle\langle\sin\left[(m-n)\varphi_1\right]\rangle\rangle\langle\langle\sin\left[(m-n)\varphi_2\right]\rangle\rangle}{1 + \langle\langle\cos(2n\varphi_1)\rangle\rangle\langle\langle\cos(2n\varphi_2)\rangle\rangle + \langle\langle\sin(2n\varphi_1)\rangle\rangle\langle\langle\sin(2n\varphi_2)\rangle\rangle} \\ &+ \frac{\langle\langle\cos\left[(m+n)\varphi_1\right]\rangle\rangle\langle\langle\cos\left[(m+n)\varphi_2\right]\rangle\rangle + \langle\langle\sin\left[(m+n)\varphi_1\right]\rangle\rangle\langle\langle\sin\left[(m+n)\varphi_2\right]\rangle\rangle}{1 + \langle\langle\cos(2n\varphi_1)\rangle\rangle\langle\langle\cos(2n\varphi_2)\rangle\rangle + \langle\langle\sin(2n\varphi_1)\rangle\rangle\langle\langle\sin(2n\varphi_2)\rangle\rangle}.\end{aligned} \tag{3.128}$$

A toy model of the cross-harmonic bias, and how to properly correct for it using Eq. (3.126) is shown in Fig. 3.2. The figure shows an example with only elliptic and triangular flow present, with input values $v_2 = 0.1$ and $v_3 = 0.02$. A detector with acceptance from $0° < \varphi < 60°$ and $120° < \varphi < 360°$ is simulated. The black circles show the uncorrected $v_n\{2\}$. The red circles show what happens when the standard NUA correction is applied, i.e. the correction in Eq. (3.120). For v_2 it sufficiently corrects for the bias. This is because $v_2 \gg v_3$ in this example. For v_3 a remaining bias of almost 50% is observed. Applying the full coupled correction method from Eq. (3.126) yields the blue circles. For v_2 there is basically no change, but for v_3 the remaining bias is removed and the measured value is now consistent with the true value.

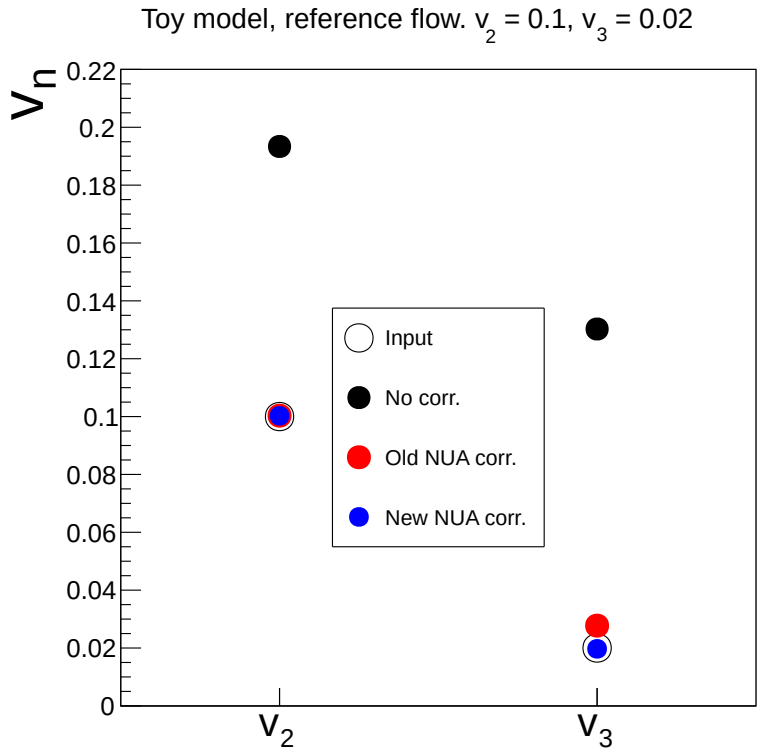

Figure 3.2: Toy model with non-uniform acceptance. It is shown that the bias to v_3 is not fully corrected using the old approach to NUA (red circles), while the new equations derived in the text (blue circles) does remove the bias.

With this, the NUA correction to the two-particle Q-cumulants also removes bias from other harmonics. In the case of very large acceptance gaps, the extracted v_n is also rescaled, which the above does not correct for. Finally, similar calculation can be done for the four-particle cumulant, but have not been completed at this time. Consequently, the results presented here for $v_n\{4\}$ are corrected using Eq. (3.97), and thus not corrected for cross harmonic bias. However, since only results for $v_2\{4\}$ are presented, and v_2 is the dominant harmonic for almost all centralities, the remaining bias should be negligible. For the two-particles measurements presented here, the full correction derived above is applied.

3.4.8 Finite Azimuthal Segmentation

Not all detectors are tracking detectors. Some may have clusters or pads with limited azimuthal resolution. This reduces the measured v_n by a small amount [60]. When $0 < n < N/2$, where

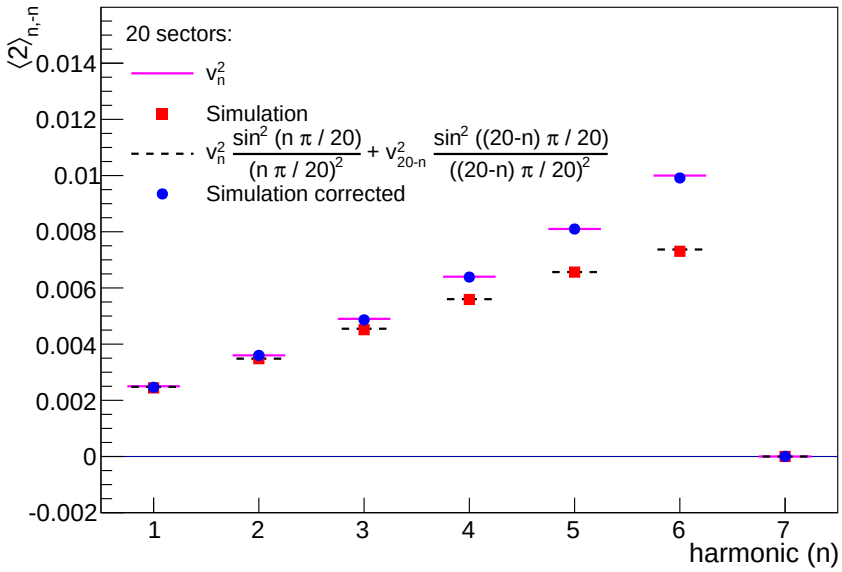

Figure 3.3: Effect on the flow harmonics v_n^2 for $n = 1, 2, ..., 7$ of having 20 φ-sectors [60]. Magenta lines are input flow, red squares are observed values with 20 φ-sectors and blue circles are corrected using Eq. (3.129)

N is the number of φ-sectors, the bias is approximately given by:

$$E\left[\langle v_n \rangle\right] \approx \langle v_n \rangle \cdot \frac{\sin\left(\frac{n}{N}\pi\right)}{\frac{n}{N}\pi}. \tag{3.129}$$

The effect is shown using a toy model in Fig. 3.3, where the effect of having an azimuthal resolution of 18° (20 φ-sectors) is shown on v_n^2 for $n = 1, 2, ..., 7$. In the toy model $v_7 = 0$, and consequently it is unaffected by the suppression. All other harmonics, however, are suppressed as explained by Eq. (3.129).

In a more general case, where the n of the highest non-zero harmonic is larger than N/2, the expectation value of $\langle 2 \rangle$ is [60]:

$$E\left[\langle 2 \rangle_n\right] = v_n^2 \frac{\sin^2\left(\frac{n}{N}\pi\right)}{\left(\frac{n}{N}\pi\right)^2} + v_{N-n}^2 \frac{\sin^2\left(\frac{(n-N)}{N}\pi\right)}{\left(\frac{(n-N)}{N}\pi\right)^2} = E\left[\langle 2 \rangle_{N-n}\right], \tag{3.130}$$

which shows that for detectors with low segmentation there will be interference between harmonics, and the observed values will be mirrored around $v_{N/2}$.

3.4.9 Mixed Harmonic Correlations

Already in Ref. [58] it was suggested that the Q-cumulants framework could be expanded to multi-particle correlations in mixed harmonics. This was recently achieved in [60], where Q-vectors are used to calculate the average m-particle correlation in harmonics $n_1, n_2, \ldots, n_m$

given by [60]:

$$\begin{aligned}\langle m\rangle_{n_1,n_2,\ldots,n_m} &\equiv \langle e^{i(n_1\varphi_{k_1}+n_2\varphi_{k_2}+\cdots+n_m\varphi_{k_m})}\rangle \\ &\equiv \frac{\sum\limits_{\substack{k_1,k_2,\ldots,k_m=1\\ k_1\neq k_2\neq\ldots\neq k_m}}^{M} w_{k_1}w_{k_2}\cdots w_{k_m}\, e^{i(n_1\varphi_{k_1}+n_2\varphi_{k_2}+\cdots+n_m\varphi_{k_m})}}{\sum\limits_{\substack{k_1,k_2,\ldots,k_m=1\\ k_1\neq k_2\neq\ldots\neq k_m}}^{M} w_{k_1}w_{k_2}\cdots w_{k_m}},\end{aligned} \tag{3.131}$$

where w_{k_i} are particle weights that may depend on e.g. p_T or φ. This allows for calculations of mixed harmonic correlations [62]:

$$\mu_{\langle m\rangle_{n_1,n_2,\ldots,n_m}} \equiv \left\langle e^{i(n_1\varphi_1+\cdots+n_m\varphi_m)}\right\rangle = v_{n_1}\cdots v_{n_m}e^{i(n_1\Psi_{n_1}+\cdots+n_m\Psi_{nm})}, \tag{3.132}$$

where μ is the mean. The inclusion of particle weights allows for corrections for p_{T} dependent efficiency or even cases with only partial φ-acceptance. It is, however, not possible to correct for holes with completely missing φ acceptance using these weights. In Ref. [60] a recursive algorithm for deriving any m-particle correlator from the $m-1$ correlator is also presented. Since the number of distinct terms per correlator grows with m following a Bell sequence, a recursive relation is a great advantage when considering more than three- or four-particle correlators.

This improved framework for the Q-cumulants allows for access to new observables. Some of these have been dubbed the *Standard candles*. An example is the following generic four-particle correlation:

$$\langle\langle\cos(m\varphi_1+n\varphi_2-m\varphi_3-n\varphi_4)\rangle\rangle\,, \tag{3.133}$$

with the constraint $m \neq n$. The isotropic part of the corresponding four-particle cumulant is given by:

$$\begin{aligned}\langle\langle\cos(m\varphi_1+n\varphi_2-m\varphi_3-n\varphi_4)\rangle\rangle_c =& \langle\langle\cos(m\varphi_1+n\varphi_2-m\varphi_3-n\varphi_4)\rangle\rangle \\ &- \langle\langle\cos[m(\varphi_1-\varphi_2)]\rangle\rangle\langle\langle\cos[n(\varphi_1-\varphi_2)]\rangle\rangle \\ =& \langle v_m^2 v_n^2\rangle - \langle v_m^2\rangle\langle v_n^2\rangle.\end{aligned} \tag{3.134}$$

This equation tests correlations in fluctuations between v_n and v_m. Only if the fluctuations in v_n are correlated (or anti-correlated) to those of v_m will Eq. (3.134) be non-zero. A range of these observables can also be constructed from for example three- or five-particle correlators. The hope is that measuring these mixed harmonic correlations will allow for much stronger constraints on theoretical models as they directly probe the fluctuations in the underlying p.d.f.

3.4.10 Symmetry Plane Fluctuations

All of the above methods, $v_n\{EP\}$, $v_n\{SP\}$, $v_n\{2\}$ and $v_n\{4\}$, are built around one or more reference measurements, which are used to measure v_n differentially versus e.g. p_{T} or η. These approaches all have a built in assumption that Ψ_n is a global observable, independent of p_{T} and η. Recent findings point to the fact that this assumption does not completely hold [63]. The consequence for the cumulants is that factorization breaks down, such that the results become slightly biased. Therefore it was suggested in Ref. [64] to apply the equations for the reference flow to the differential measurements. The idea is that instead of using Eq. (3.50) for a differential flow analysis, simply use Eq. (3.25) but choose only POIs and let that be the result. The notation for this method is $v_n[2]$. While it certainly has the advantage of being insensitive to symmetry plane fluctuations - and indeed in Ref. [64] a small difference between $v_n\{2\}(p_{\mathrm{T}})$

and $v_n[2](p_{\mathrm{T}})$ is found due to symmetry plane fluctuations - it also severely limits the number of particles that can be used. The introduction of differential flow, as it is defined in Eq. (3.50), was exactly to reduce issues caused by a lack of particles. Consequently, $v_n[2]$ does not seem like the final solution to the problem.

3.4.11 Unresolved Issues

With precision measurements becoming more and more important in heavy-ion physics, it is also increasingly important to understand the potential sources of bias to the measurements performed. Some of these biases have been studied in some detail above, and yet, there are still certain unresolved issues.

Bias from non-flow: It is shown in Section 3.4.5 how the non-flow contribution to the two-particle cumulant scales with the number of RPs and POIs. But since the non-flow correlations can be difficult to estimate experimentally, the equations cannot be directly utilized for an analytical correction. Currently, the best known method of correcting for non-flow is to estimate δ_n and δ'_n using either a Monte Carlo generator without collective flow or a smaller collision system, e.g. pp collisions, where no collectivity is assumed. The estimate is then subtracted from the observed value of $v_n\{2\}$ in heavy-ion collisions. Using correlation techniques with more particles suppresses the issue, but as they require more statistics they are not always a feasible solution.

Bias from multiplicity fluctuations: The event weights, $w_{\langle\rangle}$ are derived in [58] to minimize bias from multiplicity fluctuations. However, in the presence of non-flow they do not fully work. For example, biases show up when using the Q-cumulants on p–Pb collisions, where multiplicities are on the order of some hundred particles and there are large amounts of non-flow. These can at the moment only be removed by doing the calculations in multiplicity bins of width 1. This issue is also pointed out in Ref. [58].

Remaining bias from NUA: In the case of an extremely limited coverage, there is a remaining bias after correcting for NUA. This is observed both when there is only a single harmonic present and the correction derived in [58] is applied, and in the more realistic case with many non-zero harmonics where the equations derived in Section 3.4.7 are applied. Furthermore, at the time of this writing, only the two-particle cumulant can be corrected for bias from other harmonics. The optimal solution would be to find a recursive relation for the NUA correction as was done for the calculations in [60] and understand the rescaling observed in very low-acceptance detectors.

Bias from symmetry plane fluctuations: Recent studies indicate that Ψ_n may depend on both p_{T} and η. While the cumulants do not directly rely on Ψ_n, they do assume that the particles are correlated to the same symmetry planes. If the RPs are chosen over a sufficiently large range of p_{T} or η, this assumption may be violated. The magnitude of this bias is not known for the cumulants. Calculations should be done, and different cases should be studied.

3.5 The Future of Flow Algorithms

Several methods for measuring v_n are presented in this chapter and more can be found in the literature. The fitted q-distributions [51] and the Lee-Yang Zeroes methods [65–68] are noteworthy examples. What all of these methods have in common is that the flow is measured over many events. In some cases biases are introduced during the averaging over events. More

importantly, with the discovery of higher order harmonics and significant flow fluctuations - all induced by initial-state fluctuations - precision measurements become increasingly important.

As collision energy goes up, so does the particle multiplicity. Increased particle multiplicity translates to increased resolution. The natural next step for flow analysis is a move to event-by-event measurements. Some methods are already being suggested. One example is the application of the spherical harmonics analysis tools used in cosmology to study the cosmic microwave background to allow for event-by-event measurements of flow in high-multiplicity events [69]. Another approach to event-by-event flow analysis, involving measuring and unfolding $P(v_n)$ distributions, has already seen published results [70]. However, new methods entail new possible biases that need to be studied. Non-flow and symmetry plane fluctuations may play an even more important role when the measurements are not averaged over many events.

In the low-multiplicity region, application of flow analysis methods to p–Pb and even pp collisions are starting to emerge. In these systems non-flow plays a much larger role. In those cases multi-particle-correlation techniques may be non-zero even in the absence of collectivity. Event-by-event measurements do not seem feasible in events with so few particles, and biases from non-flow and multiplicity fluctuations need to be studied in great detail before any conclusions are drawn.

Not only are there many ways to measure v_n, a lot of information can also be obtained from these measurements. The next chapter covers some of the previous flow measurements.

Chapter 4

Flow in Heavy-Ion Collisions

This chapter contains an overview of current experimental anisotropic azimuthal flow results. The first part of the chapter presents results of the flow harmonics, v_1 to v_6, and how they are interpreted. In this thesis v_2 to v_4 are measured as a function of pseudorapidity, see Chapters 8 to 10. The rest of the chapter shows recent results from analyses of event-by-event flow measurements, correlations between the flow harmonics and p_{T}- and η-dependent symmetry planes.

4.1 v_n Measurements

In Section 2.4 it is shown how an initial elliptical anisotropy containing the interacting matter, caused by the overlap of two nuclei in a non-central collision, may lead to momentum anisotropies. On top of this, initial-state fluctuations from the random positions of nucleons inside the nuclei may lead to complex energy density distributions in the developing fireball. Chapter 2 discusses how the evolution of the system at early times can be described with (viscous) relativistic hydrodynamics. A direct probe of this is anisotropic azimuthal flow, which contains information on the degree of thermalization of the initial system, and is an indirect probe of the systems transport properties, such as viscosity.

As discussed in Chapter 3, in heavy-ion physics these anisotropies are quantified via Fourier coefficients obtained through a decomposition of the measured azimuthal yields in a Fourier series, see Eq. (3.1). Harmonics from v_1 up to and including v_6 (hexagonal flow) have so far been measured to be non-zero [71, 72].

In this section, measurements of the anisotropic flow harmonics are presented as a function of various observables, such as p_{T}, η and centrality, with a focus on RHIC and LHC measurements.

4.1.1 $\sqrt{s_{\mathrm{NN}}}$-Dependence

In Fig. 4.1a the integrated elliptic flow over a large range of collision energies is shown. At the very lowest energy a positive signature is observed. This is, however, not to be confused with a sign of hydrodynamical flow. The in-plane motion is observed because when two colliding nuclei bounce off each other, at very low energies, they pull the produced particles in their respective directions, thus creating the observed v_2 anisotropy. For slightly larger energies and up to $\sqrt{s_{\mathrm{NN}}} \lesssim 5$ GeV the spectator nucleons are moving slow enough to influence the produced particles via shadowing effects - effectively the opposite of the bounce-off. This causes an out-of-plane motion and the elliptic flow is observed to be negative. As the energy goes up and the spectators no longer affect the system evolution, v_2 becomes positive. This was first suggested as being a sign of collectivity by Ollitrault in Ref [73]. At low energies, the observed anisotropy is well described by models for a hadron gas undergoing hadronic scatterings [43], i.e. there

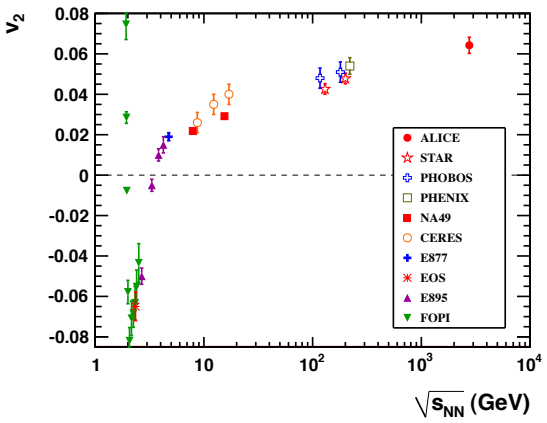

(a) Collision energy dependence of integrated elliptic flow in the 20–30% centrality class at mid-rapidity. At the lower energy, first a bounce-off and then a shadowing from the spectators is observed. At the highest available energies, the flow is well described by hydrodynamic models [74].

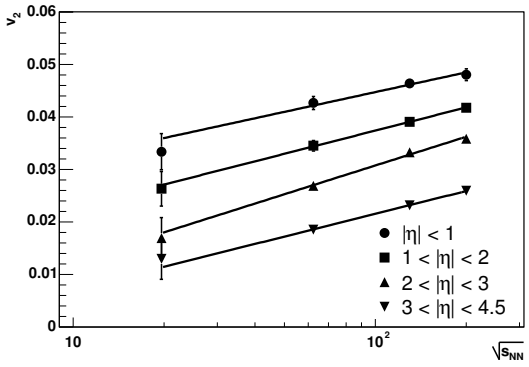

(b) Energy dependence at different pseudorapidity intervals. At forward rapidity the same scaling with $\sqrt{s_{\mathrm{NN}}}$ is observed as at mid-rapidity. PHOBOS data from RHIC [75].

Figure 4.1

is still an anisotropy caused by the initial ellipsoidal deformation, but it is not so large as to require hydrodynamic behaviour to describe it. Only at the highest energies is a hydrodynamic transport approach necessary to describe the observed flow, see [43] and references therein. This is interpreted as a possible QGP signal due to the underlying collective behaviour associated with hydrodynamics. The increase in integrated flow from top RHIC energy to LHC energy is attributed to a larger mean p_{T} at the LHC (v_2 generally increases with p_{T}) [74]. Fig. 4.1b shows the energy dependence at different rapidity intervals. The same scaling with collision energy that is shown in Fig. 4.1a at mid-rapidity is observed at forward rapidities.

4.1.2 Centrality-Dependence

Figure 4.2a shows the centrality-dependence of all moments from v_2 to v_6 at the LHC. v_2 is observed to have a very strong centrality dependence, while the higher harmonics show comparatively small changes with centrality. The initial rise with centrality is understood as a consequence of the ellipsoidal overlap in non-central collisions of identical nuclei. The subsequent fall is because the system becomes to small to thermalize. And indeed, for many years, only v_2 was seriously considered in anisotropic flow analysis (although v_4 and v_6 were also reported on, see the next subsection). In Ref. [31] it was proposed to also look at v_3 and other higher-order harmonics. They were predicted to be non-zero due to initial-state fluctuations. It turns out that the simple picture of the nuclear overlap suggested in Fig. 2.2b is not realistic. Models taking into account quantum fluctuations inside the nuclei predict a much more complex initial energy density profile, which fluctuates from event to event. An example of this is shown in Fig. 4.3, where the left most plot shows the initial energy density distribution in a simulated Au–Au collision. The middle and right plot shows the system after some time, with and without a small η/s. The blurring effect of the shear viscosity (see Section 2.3) is clearly seen. Such an initial distribution may cause v_3, v_5, etc. to be non-zero. As these higher-order harmonics originate from fluctuations around the ellipsoidal overlap, they are much less sensitive to the centrality of the collision, which is indeed what is observed in Fig. 4.2a.

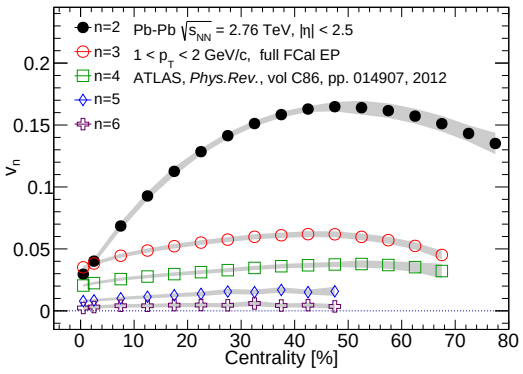

(a) Centrality dependence of v_2–v_6 in Pb–Pb collisions at $\sqrt{s_{NN}} = 2.76$ TeV as observed by ATLAS. Adapted from: [71].

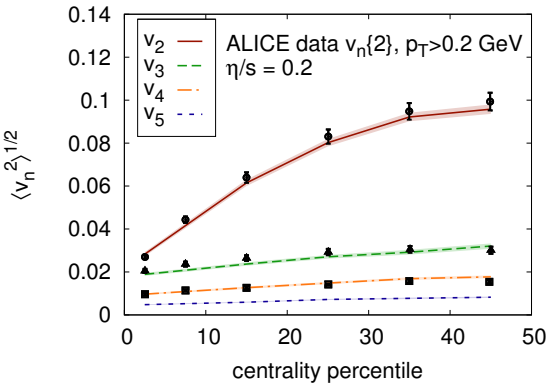

(b) Fit of the event-by-event viscous hydrodynamics models IP-Glasma and MUSIC to ALICE data. A value of η/s is extracted from the fit, see text for discussion. From [76].

Figure 4.2

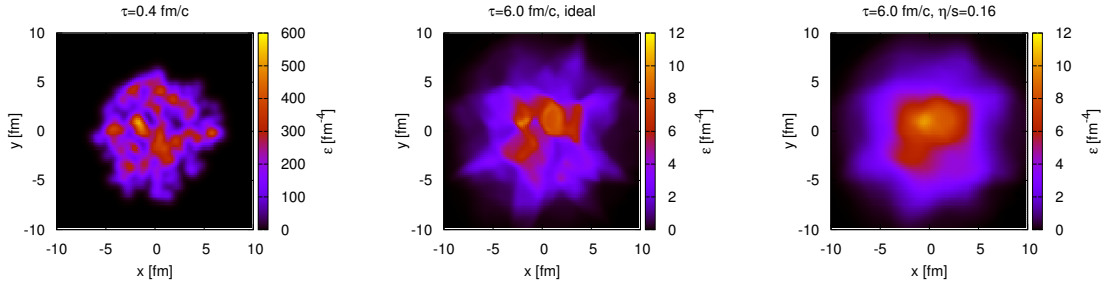

Figure 4.3: Energy density distributions for an Au–Au collision with $b = 2.4$ fm. Left: initial distribution, middle: after $\tau = 6$ fm/c for ideal hydrodynamics, right: same τ but with $\eta/s = 0.16$. (3+1)D hydro from [79].

An example of how these higher harmonics can be used to measure the transport properties of the sQGP is seen in Fig. 4.2b, where event-by-event viscous hydrodynamics is used to extract a value of η/s. In Ref. [76] a value of $\eta/s = 0.2$ is found to give good agreement with the current experimental results. Typically, the values obtained are in the range of $0.07 < \eta/s < 0.43$ for LHC [77]. However, as noted in Refs. [43, 78], the hadronic stage in the modelling changes the flow values significantly. So changing parameters for the hadronic stage also affects the η/s value in the hydrodynamic stage necessary to reproduce data. This means that obtaining a precise value for the shear viscosity to entropy density ratio in the sQGP stage depends on models being able to describe the hadronic stage accurately.

4.1.3 p_{T}-Dependence

The transverse momentum dependence of the anisotropic flow probes another aspect of the hydrodynamical picture. Generally, high-momentum particles spend less time inside the dense medium, and thus cannot be expected to reach equilibrium with the slower particles, and therefore cannot be modelled by hydrodynamics. Measuring the p_{T}-dependence and comparing with hydrodynamic models makes it possible to estimate at which p_{T} hydrodynamics no longer pro-

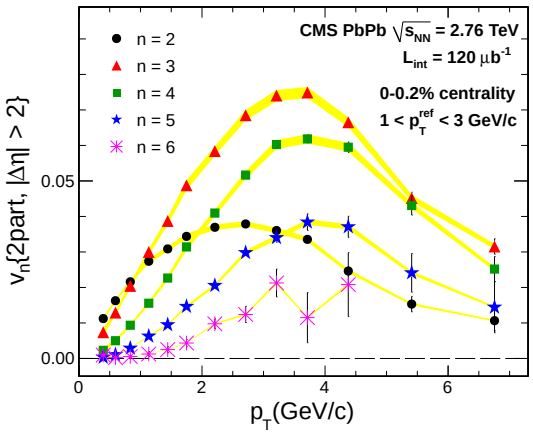

(a) v_2–v_6 in ultra-central (0.0–0.2%) Pb–Pb collisions at $\sqrt{s_{NN}} = 2.76$ TeV collisions observed by CMS [72]. v_3, v_4 and even v_5 are in some cases larger that v_2, suggesting a spherical overlap dominated by initial-state fluctuations.

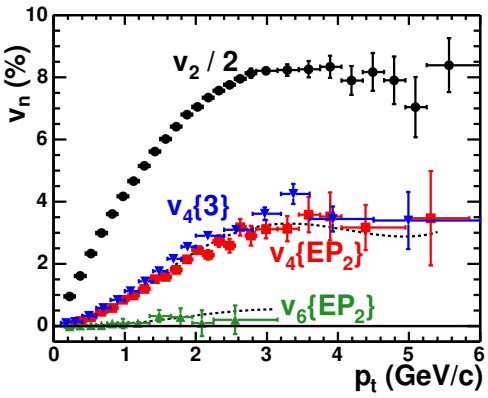

(b) v_2, v_4 and v_6 in minimum-bias Au–Au collisions at $\sqrt{s_{NN}} = 200$ GeV observed by STAR [80]. The measurement suggests that v_4 and v_6 are correlated to the second-order symmetry plane. The dashed lines are $1.2 \cdot v_2^2$ and $1.2 \cdot v_2^3$ respectively.

Figure 4.4

vide a feasible description. Generally it is found that the hydrodynamics picture breaks down for particles with $p_T > 2$ GeV/c [39]. Figure 4.4a shows the p_T dependence of v_2–v_6 for Pb–Pb collisions at the LHC as observed by CMS in ultra-central collisions (0.0–0.2% centrality). The reason for the initial rise with p_T is described in the next section. For $p_T \simeq 4$ GeV/c the anisotropies flatten and become smaller at higher p_T. This indicates that hydrodynamics no longer completely describes the behaviour of those particles. Another interesting observation in this measurement is that v_3 is the dominant harmonic. The selected collisions are so central that the ellipsoid is no longer the most significant geometric feature, and the observed elliptic flow is attributed only to geometric fluctuations. The observation that $v_3 > v_2$ for $p_T > 1$ GeV/c, $v_4 > v_2$ for $p_T > 2$ GeV/c and $v_5 > v_2$ for $p_T > 3$ GeV/c makes this measurement ideal for comparisons to models describing the initial conditions, such as Glauber and CGC-based models.

Figure 4.4b shows one of the first measurements of harmonics higher than v_2, reported by STAR for Au–Au collisions at $\sqrt{s_{NN}} = 200$ GeV in minimum-bias collisions. An important detail in this measurement is that v_4 and v_6 are measured with respect to the second-order symmetry plane, Ψ_2, suggesting that the observed values for v_4 and v_6 are also partly related to the ellipsoidal anisotropy.

4.1.4 Flow of Identified Particles

The flow of identified hadrons provides one of the most significant insights into the hydrodynamic origin of anisotropic azimuthal flow. Fig. 4.5a shows the elliptic flow vs. p_T of various identified hadrons in Pb–Pb collisions at the LHC. In Fig. 4.5b some of the results are compared to a CGC-based hydrodynamic model. The model correctly reproduces the observed difference in v_2 of the different species, an effect known as *mass ordering*. Mass ordering can be interpreted as a consequence of hadronization, as is shown with the following equations. It is assumed that when the hydrodynamic picture breaks down at late stages of the collision, the particles have the same momentum distributions as they had in the fluid, but they can be considered independent particles (an ideal gas basically). This is known as the *Cooper-Frye freeze-out picture* [81].

Furthermore it is assumed that the fluid has a zero net baryon number and that the momentum distributions follow Boltzmann statistics [39]:

$$\frac{d^3N}{d^3xd^3p} = \frac{2S+1}{(2\pi\hbar)^3}\exp\left(-\frac{E^*}{T}\right), \tag{4.1}$$

where $2S+1$ is the number of spin degrees of freedom and E^* is the energy of the particle in the fluid rest frame. Assuming the fluid velocity is parallel to the particle velocity and that the fluid momentum in the z-direction $p_z = 0$, the energy is [39]:

$$E^* = p^\mu u_\mu = m_\mathrm{T}u^0 - p_\mathrm{T}u. \tag{4.2}$$

where the same notation as in Chapter 2 is used, $u^0 = \sqrt{1+u^2}$, and $m_\mathrm{T} = \sqrt{p_\mathrm{T}^2 + m_0^2}$ is called the *transverse mass*. Inserting Eq. (4.2) into Eq. (4.1) and rewriting to polar coordinates using $dp_xdp_y = p_\mathrm{T}dp_\mathrm{T}d\varphi$ yields [39]:

$$\frac{dN}{p_Tdp_Td\varphi} \propto \exp\left(\frac{-m_tu_0(\varphi) + p_Tu(\varphi)}{T}\right). \tag{4.3}$$

Here the idealized picture, as in Section 2.4, with the ellipsoid entropy density distribution is assumed. In that case, the fluid velocity is larger in the x-direction than in the y-direction, i.e. $v_x > v_y$. The particle velocity can then be parametrized as [39]:

$$u(\varphi) = u + 2\alpha\cos(2\varphi), \tag{4.4}$$

where α is a positive coefficient which depends on the magnitude of the (elliptic) flow. Using $u^0 = \sqrt{1+u^2}$ and expanding to first order in α yields:

$$u^0(\varphi) = u^0 + 2v\alpha\cos(2\varphi), \tag{4.5}$$

with $v \equiv u/u^0$. Inserting Eqs. (4.4) and (4.5) into Eq. (4.3) and using using $dN/d\varphi \propto 1 + 2v_2\cos(2\varphi)$ shows how the mass ordering comes about [39]:

$$v_2 = \frac{\alpha}{T}(p_T - vm_T). \tag{4.6}$$

Here it is important not to be confused by the different notation: v_2 is the elliptic anisotropy and v is the velocity. Equation (4.6) implies that v_2 scales linearly with p_T for particles with $p_\mathrm{T} \simeq m_\mathrm{T}$, such as pions. While heavier particles such as protons generally have a lower v_2 at low p_T. The m_T-scaling is often removed by plotting the flow vs. the transverse kinetic energy $\mathrm{KE}_\mathrm{T} = m_\mathrm{T} - m_0$.

The hadron mass however is only one important parameter for the final particle spectra. The quark coalescence model postulates that, at intermediate p_T, hadron production proceeds through coalescence of valence quarks. This happens in a p_T-regime in which hydrodynamics alone cannot describe the system [40]. The model predicts that v_n of hadrons scale with the number of valence quarks, n_q, i.e. $v_n^{hadron}(p_\mathrm{T}) = n_q v_n^{quark}\left(\frac{p_\mathrm{T}}{n_q}\right)$. Thus, both axes are often rescaled with $1/n_q$, this is done in Fig. 4.6. When plotted this way all the scaled v_2 values of the different particle species end up on one universal curve, which is known as *quark number scaling*. However, recently this scaling has been shown to break for non-central events. At RHIC, deviations of up to 10% are observed [82]. At the LHC deviations of up to 20% are observed [83].

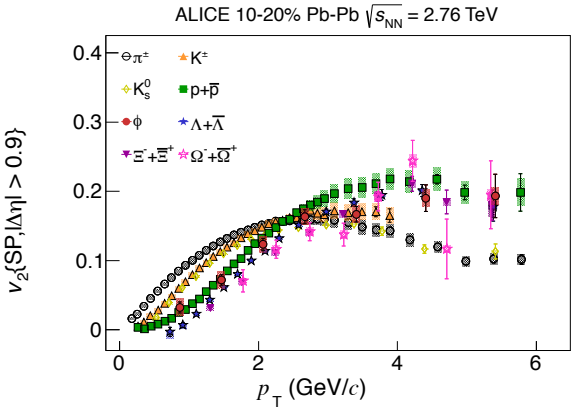

(a) v_2 vs. p_T for identified hadrons in Pb–Pb collisions at $\sqrt{s_{NN}}$ = 2.76 TeV as observed by ALICE [83].

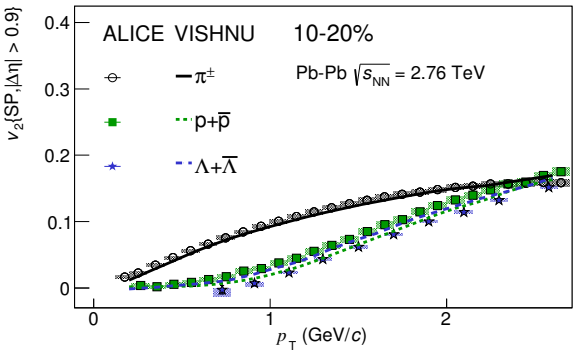

(b) v_2 vs. p_T for identified hadrons in Pb–Pb collisions at $\sqrt{s_{NN}}$ = 2.76 TeV compared to a hydrodynamical model [83].

Figure 4.5

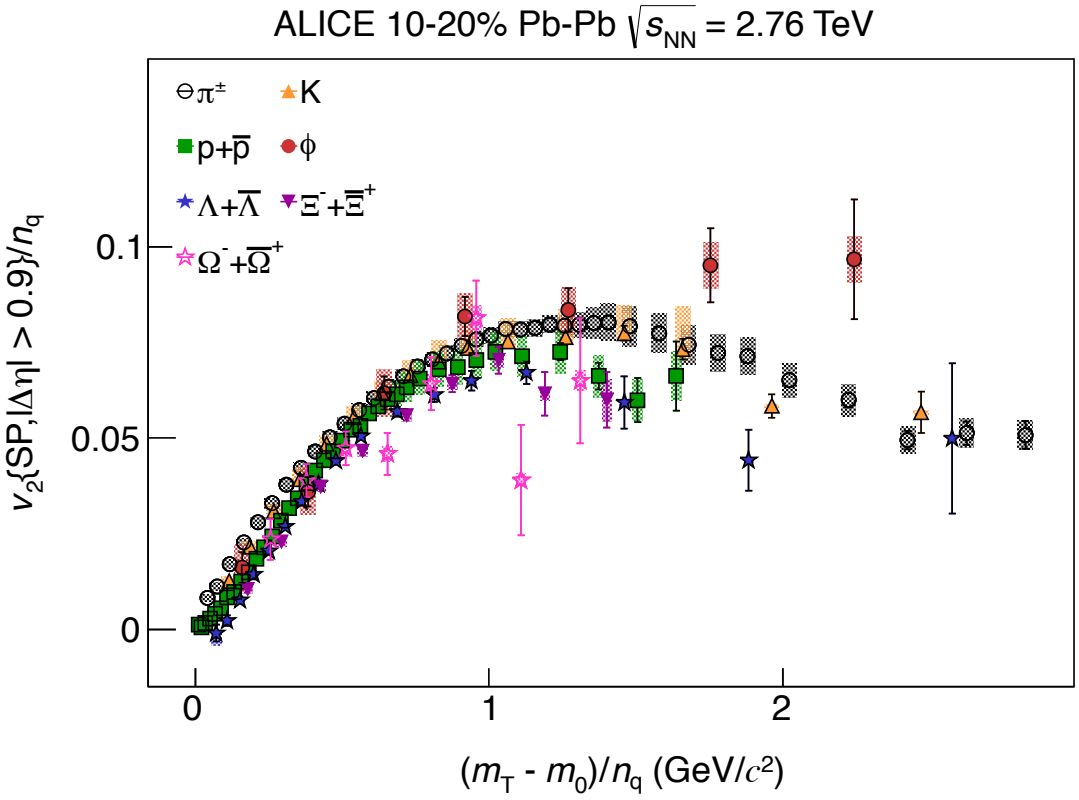

Figure 4.6: v_2/n_q vs. KE_T/n_q in Pb–Pb collisions at $\sqrt{s_{NN}}$ = 2.76 TeV as observed by ALICE. n_q is number of valence quarks and KE_T is transverse kinetic energy [83].

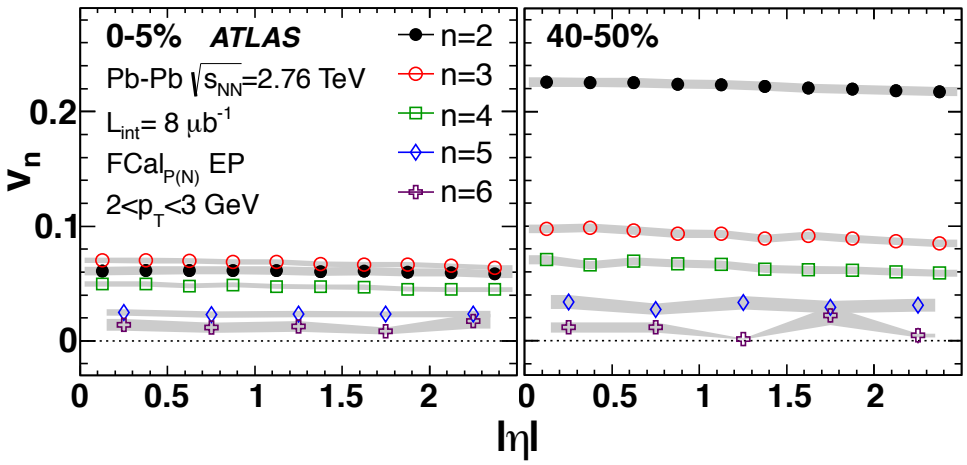

Figure 4.7: v_2–v_6 in Pb–Pb collisions at the LHC, measured by ATLAS. All measured flow harmonics have a very weak η-dependence. Adapted from [71].

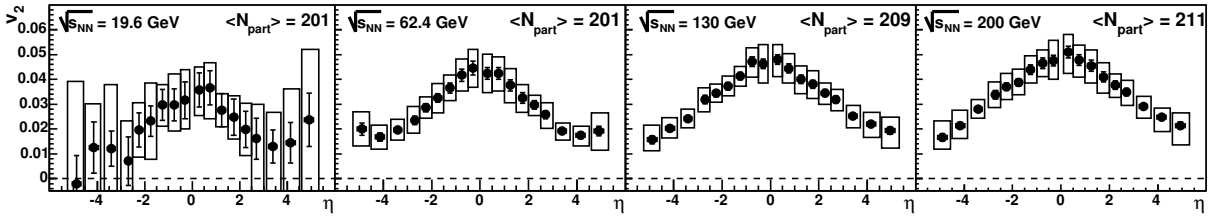

Figure 4.8: Pseudorapidity dependence of the elliptic flow in Au–Au collisions at $\sqrt{s_{\mathrm{NN}}}$ = 19.6 GeV , 62.4 GeV, 130 GeV and 200 GeV. For all energies the elliptic flow exhibits a strong rapidity dependence. PHOBOS [75].

4.1.5 η-Dependence

This section presents previous measurements of the pseudorapidity dependence of v_n. They are of special importance since it is such a measurement that is reported on in this thesis. At the LHC, ATLAS [71] (and CMS [84]) has reported on v_2 to v_6 (v_2 to v_4) vs. η for $|\eta| < 2.5$ ($|\eta| < 2.4$) respectively. As seen in Fig. 4.7, in this range all of the measured flow moments exhibit very little pseudorapidity dependence. This is in contrast to what was observed at RHIC, where PHOBOS observed an almost triangular distribution of v_2 vs. η [75], see Fig. 4.8. Although both STAR [85] and BRAHMS [86] reported a flattening around $\eta \approx 0$, the variation within this region is still stronger than what is observed by ATLAS and CMS.

At forward rapidity the multiplicity density becomes smaller. This corresponds to a smaller initial entropy density, which in turn means that the system undergoes the phase transition to the hadronic stage sooner. This makes it more sensitive to viscous effects in the hadronic phase [40], making the understanding of flow at forward rapidities very important, as it can help to estimate flow contributions from the different stages.

Another study that is often done, when measuring the rapidity dependence of flow, is to plot the observable as it is seen in the rest frame of one of the colliding nuclei. The shift is approximated by $\eta - y_{beam}$, with y_{beam} being the beam rapidity. In this shifted frame, many observables related to particle production are found to be independent of $\sqrt{s_{\mathrm{NN}}}$, an effect known as *longitudinal scaling* or *limiting fragmentation*. At RHIC this scaling was found to hold over an order of magnitude in collision energy for v_1, v_2 [87] and $(dN_{ch}/d\eta)/(\langle N_{part}\rangle/2)$. More recently it was found to hold over one more order of magnitude in collision energy, all the way to the

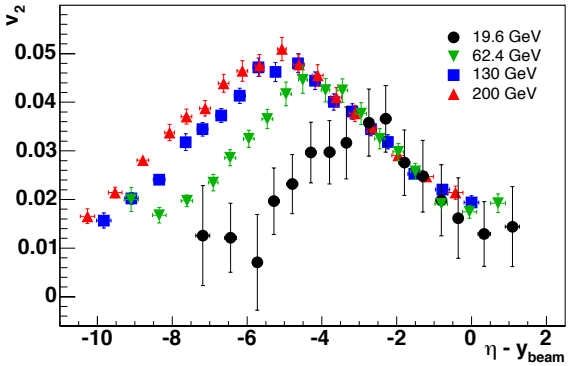

(a) Longitudinal scaling for v_2 as observed by PHOBOS from $\sqrt{s_{\mathrm{NN}}} = 19.6$ GeV to 200 GeV [75].

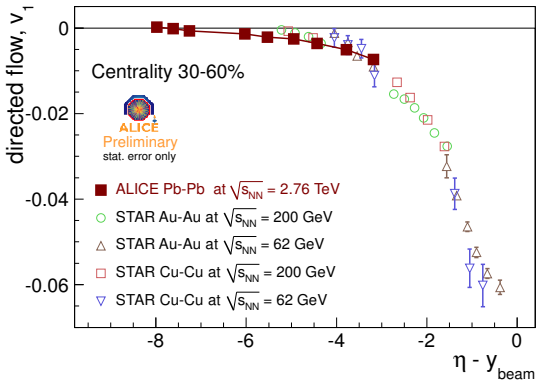

(b) Longitudinal scaling for v_1 as observed by ALICE and STAR from $\sqrt{s_{\mathrm{NN}}} = 62$ GeV to 2.76 TeV [88].

Figure 4.9

LHC [88, 89], see Figs. 4.9 and 4.10.

Figure 4.9b is the first directed flow result presented here. While v_2 is motivated by the almond shaped overlap zone of the colliding nuclei and the higher harmonics from fluctuations, v_1 arises a bit differently. To understand how directed flow develops, it is necessary to look at the system, not in the transverse (x, y)-plane, but in the longitudinal (z, x)-plane (or (z, y)). This is shown in Fig. 4.11a, which is a schematic of a non-central collision just after it has happened. The two nuclei are moving away from each other. The nuclei are moving along the z-direction, but their centers are offset in the x-direction. This means that the tip of one nucleus hit the center of the other nucleus, and vice-versa. Once again the entropy density profile of the initial system has an anisotropy, and as a response to this anisotropy, the fluid elements are accelerated with a preferential direction. The response to the situation in Fig. 4.11a is shown in Fig. 4.11b, where the system for negative (positive) z develops a preferred direction of negative (positive) x. Translated into the transverse plane where the measurement is done, it is observed as a $\cos(1(\varphi - \Psi_1))$ periodicity which is asymmetric around $\eta = 0$.

4.2 Event-by-Event Measurements

One of the very promising new developments in flow analysis is the observation of flow harmonics on an event-by-event (EbE) basis. While tried before [90], most recently ATLAS has had great success with a new method involving disentangling contamination effects from e.g. the finite number of particles and non-flow [70]. EbE measurements allow access to not just $\langle v_n \rangle$ (or an approximation thereof) like standard analyses, but makes it possible to measure the probability distribution of the flow harmonics, $P(v_n)$. Figure 4.12 shows the measured distributions for $P(v_2)$ to $P(v_4)$, with the v_3 and v_4 distributions fitted with Bessel-Gaussian functions, which have been suggested as being the underlying probability distribution function of the flow harmonics [91]. They provide a good fit for the most central events. Although recently, it has been suggested that so-called *elliptic power* distributions provide a better description [92].

The EbE measurement also provide an almost independent test to the initial geometry [42]. This is shown in Fig. 4.13a, where both the Glauber and MC-KLN initial conditions are found to completely describe the v_3 distribution, but have some issues in the tails where non-linearities in hydrodynamic effects play an important role. Similar agreements have been found using the

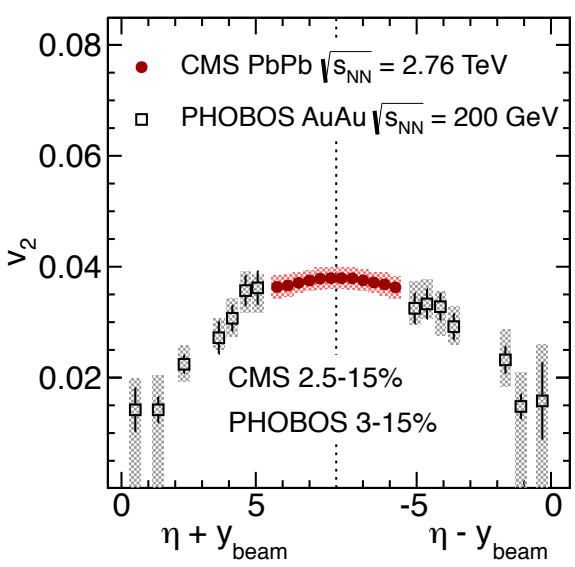

(a) Longitudinal scaling for v_2 between top RHIC energy with PHOBOS (black) and LHC with CMS (red) [87].

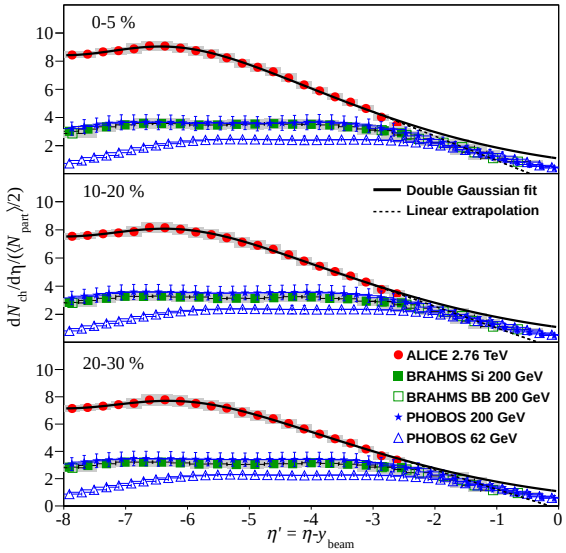

(b) Longitudinal scaling in pseudorapidity density analysis from $\sqrt{s_{\mathrm{NN}}} = 62$ GeV to 2.76 TeV, BRAHMS, PHOBOS and ALICE [89].

Figure 4.10

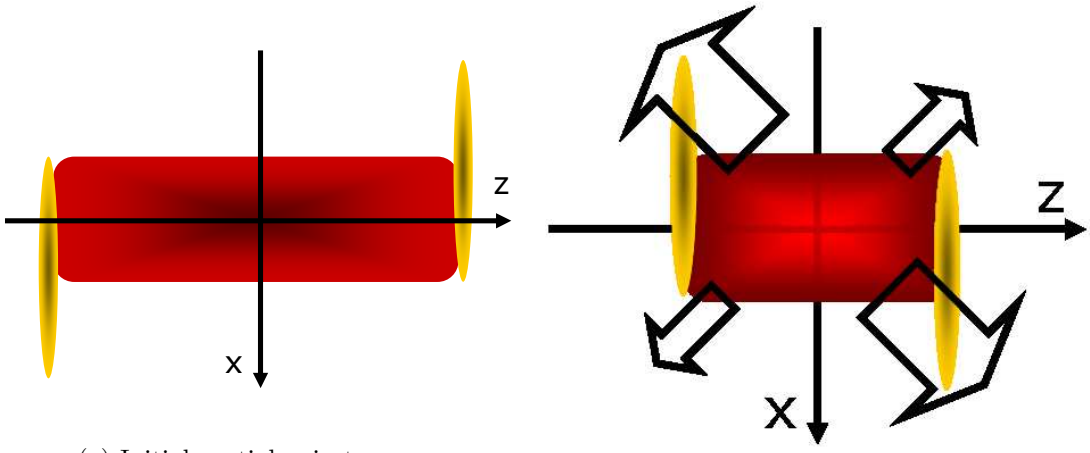

(a) Initial spatial anisotropy.

(b) Momentum-space anisotropy.

Figure 4.11: v_1 anisotropy in a non-central heavy-ion collision. [41]

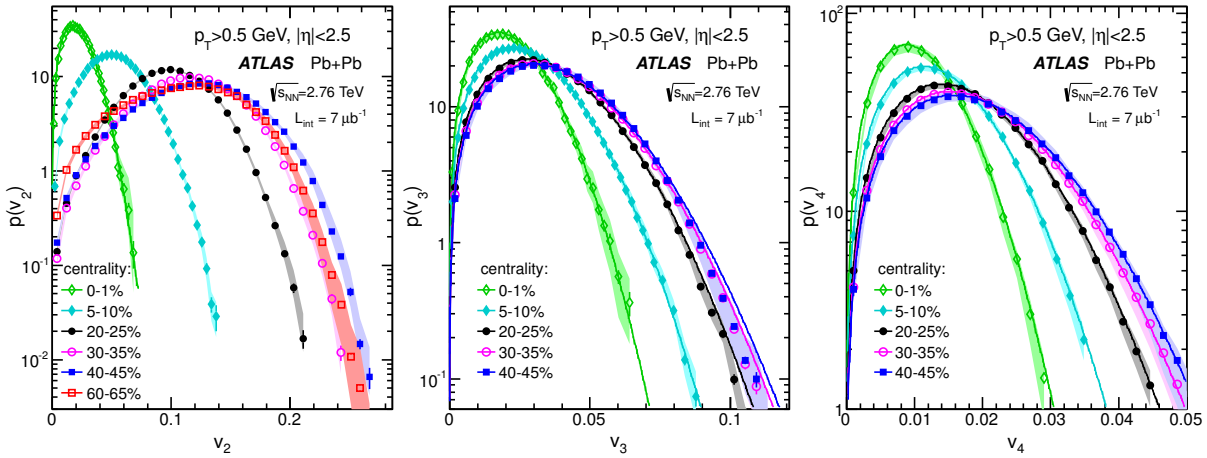

Figure 4.12: Probability distribution, $P(v_2)$ to $P(v_4)$ for various centralities. By ATLAS at $\sqrt{s_{\rm NN}} = 2.76$ TeV. Solid lines are Bessel-Gaussian fits to the data [70].

IP-GLASMA initial-state model [93].

Finally the $P(v_n)$ measurement allow for a direct determination of the widths of the distributions, σ_{v_n}. These are often approximated through the difference between two- and multi-particle correlations, see Section 3.4.4 for a discussion on this method. The scaling of σ_{v_2} to σ_{v_4} with centrality is shown in Fig. 4.13b.

4.3 Correlations Between Fluctuations of Different Harmonics

To completely understand the underlying p.d.f., it is necessary to not only look at flow fluctuations, but also the correlations between flow fluctuations of different harmonics. As suggested recently in [60, 93, 94] and discussed in Section 3.4.9 a new generic framework for exact and efficient calculations of all multi-particle correlations makes it possible to construct a set of so-called standard candles. An example is the following four-particle cumulant (with $m \neq n$):

$$\langle\langle\cos(m\varphi_1 + n\varphi_2 - m\varphi_3 - n\varphi_4)\rangle\rangle_c = \langle v_m^2 v_n^2\rangle - \langle v_m^2\rangle\langle v_n^2\rangle, \tag{4.7}$$

which is zero by definition if v_n and v_m are fixed or uncorrelated. Dependence on symmetry planes also cancel, which means that if the observable above is non-zero, then the EbE fluctuations of v_n and v_m must be correlated (or anti-correlated). At the moment there are no observation from experiments, but AMPT shows a correlation between v_2 and v_4 and an anti-correlation between v_2 and v_3 at both LHC and RHIC energies for non-central events, see Fig. 4.14. Utilizing a wide range of these inter-harmonic correlations, it should be possible to completely identify the underlying p.d.f.

4.4 Symmetry Plane Fluctuations

Another recent development in flow analyses is the suggestion of symmetry plane fluctuations [63, 95]. The hypothesis is that the participant planes may depend on $p_{\rm T}$ and η, i.e., $\Phi_n \to \Phi_n(p_{\rm T}, \eta)$. A way to understand the $p_{\rm T}$-dependence is to look at the results shown in Section 4.1.3, where it was found that hydrodynamics only describes the low $p_{\rm T}$ particles. The high $p_{\rm T}$ particles are often associated with jet-production, which does not have to be correlated with the symmetry planes of the other particles. Consequently Φ_n at high $p_{\rm T}$ may be jet dominated, while Φ_n at low $p_{\rm T}$ is dominated by collective effects.

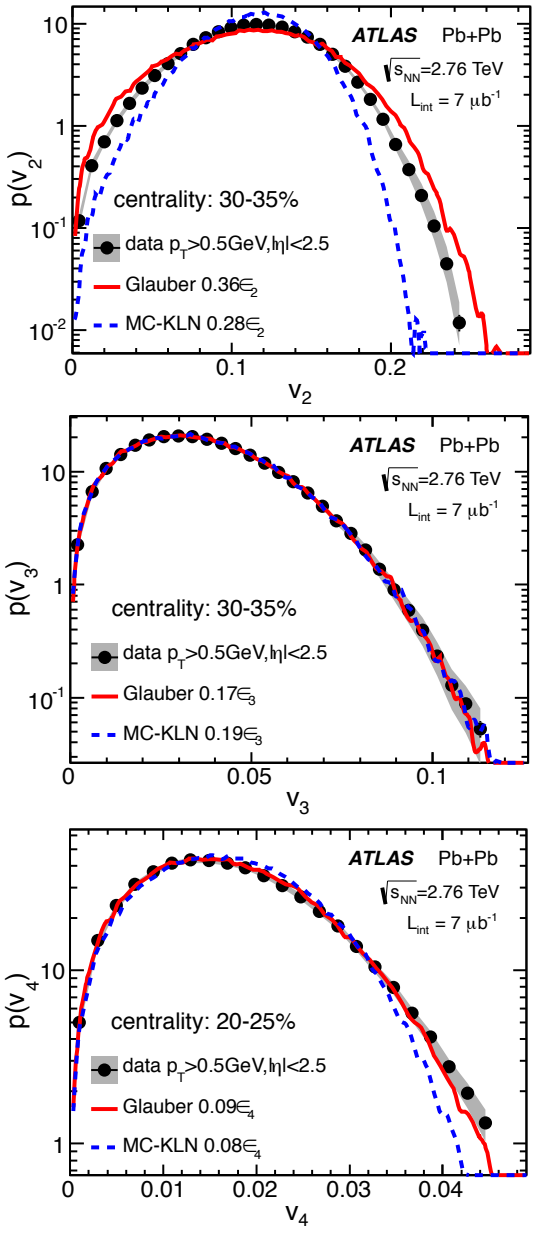

(a) $P(v_n)$ comparisons to initial state models. Generally the models fail at describing the tails for v_2 and v_4, this is an indication of non-linear hydrodynamic effects.

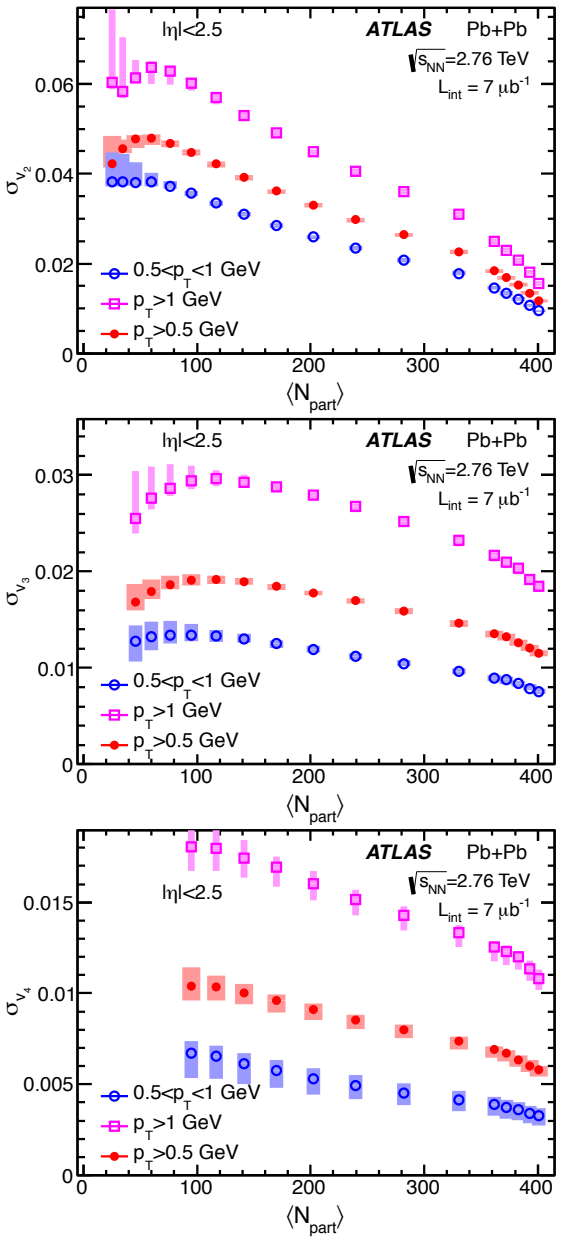

(b) Flow fluctuations, σ_{v_n}, measurements extracted directly from the event-by-event $P(v_n)$ distributions.

Figure 4.13: ATLAS at $\sqrt{s_{\mathrm{NN}}} = 2.76$ TeV. Adapted from [70]

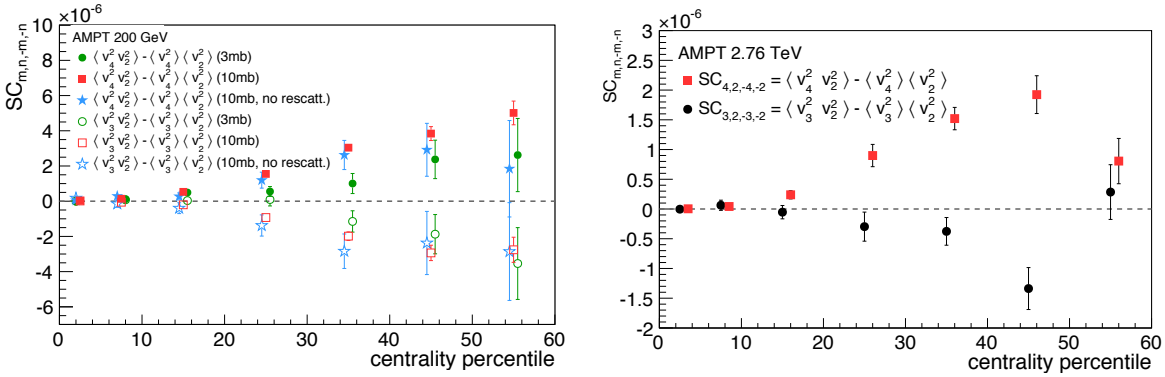

(a) Au–Au at $\sqrt{s_{\mathrm{NN}}} = 2.76$ GeV with various settings.

(b) Pb–Pb at $\sqrt{s_{\mathrm{NN}}} = 2.76$ TeV.

Figure 4.14: Correlations between v_2 and v_4 and anti-correlations between v_2 and v_3 are observed in AMPT at both RHIC and LHC energies with various settings. These observables are among the new suggested standard candles [60].

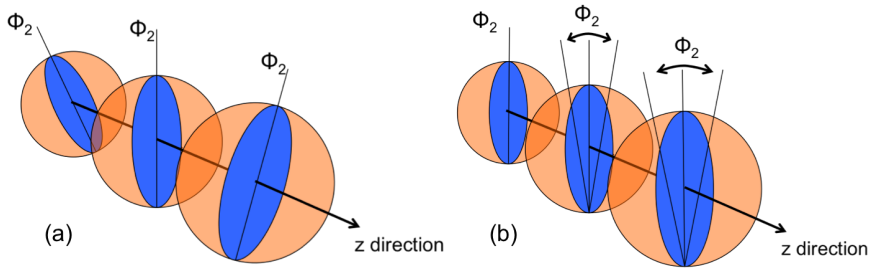

Figure 4.15: Schematic drawing of how a torqued fireball may affect Φ_2, either via a symmetric rotation (left) or randomly fluctuations along η (right) [63].

For the η-dependence, particles produced in the forward- (backward-) directions are mainly produced from participants in the forward- (backward-)going nucleus (this is also where the observed asymmetry in p–Pb collisions comes from). In this case they could be correlated to the fluctuations in the corresponding nucleus. Since the two nuclei fluctuate independently, their symmetry plane angles may not align: $\Phi_n^F \neq \Phi_n^B$, where F (B) denotes the forward- (backward)-going nucleus. This creates a torqued fireball. As the system undergoes hydrodynamic evolution the collective flow is also torqued, leading to symmetry plane angles that rotate with η. A schematic drawing of such a system is shown in Fig. 4.15, where the left plot shows a system with a systematic rotation to Φ_2 and the right plot shows a randomly fluctuating Φ_2. It is not yet clear to what extent these torqued fireballs exist in the collisions, and the consequences may be quite important, not just for symmetry plane measurements, but also multi-particle cumulant methods. For a deeper discussion on the observables sensitivity to symmetry plane fluctuations see Section 3.4.10.

4.5 Flow in p–A and pp Collisions?

At the LHC long-range correlations (the so-called *ridge*) were observed in high multiplicity events in pp collisions at $\sqrt{s} = 7$ TeV by CMS [36], see Fig. 1.10. In heavy-ion collisions very similar correlations are observed, and are understood in terms of the flow harmonics. This means they are typically associated with collectivity and to some extend hydrodynamics. When the p–Pb

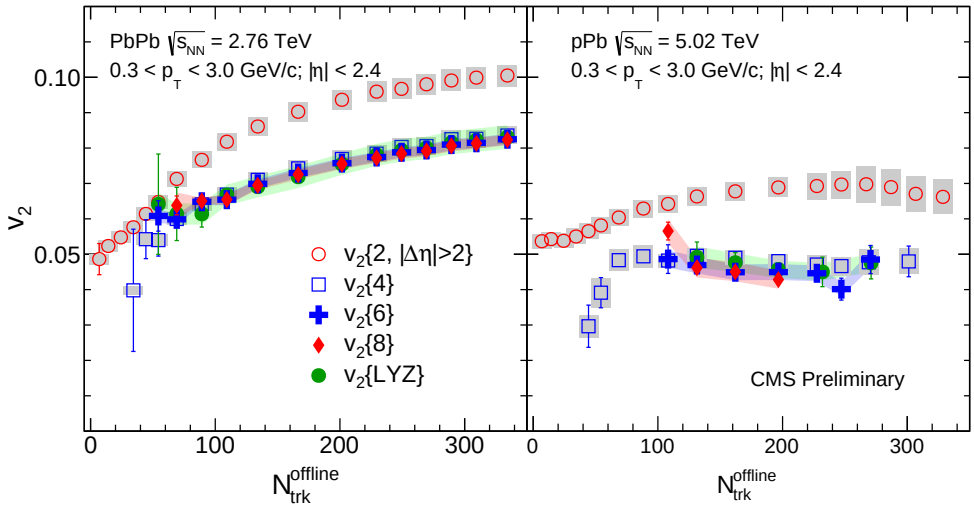

Figure 4.16: Comparison between the multiplicity dependence of $v_2\{2\}$, $v_2\{4\}$, $v_2\{6\}$, $v_2\{8\}$ and $v_2\{LYZ\}$ in p–Pb and Pb–Pb collisions by CMS [32, 33]. Non-zero values for v_2 are observed. The splitting between $v_2\{2\}$ and multi-particle correlation techniques is similar between the two systems. Most importantly, $v_2\{4\}$=$v_2\{6\}$=$v_2\{8\}$=$v_2\{LYZ\}$, which is a strong sign of collectivity.

data was analysed, the same correlation patterns were found in high-multiplicity events. ATLAS reported on non-zero v_2 [96] and CMS reported on non-zero v_2 and v_3 [32] for p–Pb collisions at $\sqrt{s_{\mathrm{NN}}}$ = 5.02 TeV. The ATLAS analysis was done in relatively broad multiplicity-bins, which makes it susceptible to fake flow induced by multiplicity fluctuations, see Chapter 3 in Ref. [58]. The CMS analysis was done in small multiplicity-bins and a comparison between p–Pb and Pb–Pb is shown in Fig. 4.16, which indicates a similar pattern between the hydrodynamical flow in Pb–Pb and the correlations observed in p–Pb. The very interesting results that all the multi-particle measurements ($v_2\{4\}$, $v_2\{6\}$, $v_2\{8\}$ and $v_2\{LYZ\}$) agree is a strong sign of collectivity.

The question is whether or not these correlations are similar to the collective hydrodynamic anisotropic flow observed in heavy-ion collisions, which essentially would suggest a sQGP having formed, or if they stem from some other underlying concept? ALICE later published v_2 for identified particles in p–Pb [97], which exhibits the mass splitting associated with hydrodynamical flow (see Section 4.1.4). These data can be described with a relativistic fluid dynamical approach [98], a test which was considered one of the significant signatures of the sQGP at RHIC in Au–Au collisions. So at this time there are significant results pointing at hydrodynamical flow, and maybe even sQGP in p–A collisions and possibly also pp. If this turns out to hold for such relatively small systems, it will require a rethinking of some of the current ideas about what it takes to produce a sQGP. In any case, there can be no more doubt about the fact that collectivity is present in high-multiplicity p–A collisions.

4.6 Outlook

Currently most direct v_n measurements of many different hadrons and over large ranges of p_{T} have been performed. With this analysis the flow harmonics will also have been measured over a large range in η. At the current LHC energy, most of the interesting future result will come from EbE measurements and a better understanding of the flow fluctuations. Once the new, higher energy, Pb–Pb collisions are made, new v_n measurements will once again put stronger limits

on the models and help determine the shear viscosity. Similarly, at RHIC, a physics program with collisions over a wide range of energies (the energy beam scan program) as well as using different types of nuclei provide a continuous stream of new data. The results of the standard v_n analyses of these collisions are very interesting.

Recently it has been suggested to classify events in terms of the magnitude of the Q-vector, similar to what is done with multiplicity for centrality dependent studies. This is known as *event-shape engineering* and it is quickly becoming an interesting and rich corner of heavy-ion physics on its own, but it is considered beyond the scope of this text. For more information on event-shape engineering see Refs. [94, 99].

Another interesting development is the analysis of symmetry plane correlations [100, 101]. The idea is that due to non-linearities in the hydrodynamical evolution of the system, the initial symmetry planes Φ_n^{in} may be different from the symmetry planes observed in the final particle spectra, Φ_n^{out}. This difference comes about due to correlations between different symmetry planes developing in the early stages of the collision. The ATLAS collaboration recently published results showing correlations between various symmetry planes [102].

Part III

Experimental Setup

Chapter 5

The LHC and the ALICE Detector

This chapter contains an introduction to the experimental apparatus used in this thesis. The chapter starts with the CERN accelerator complex, including the LHC. The ALICE detector is then described. The focus of this chapter is on the detector technologies used and the kinematic regions covered by the sub-systems of ALICE. At the end of the chapter, plans for detectors upgrades are discussed. Signal processing is described in Chapter 6.

5.1 The CERN Accelerator Complex and the LHC

The LHC is the world's largest accelerator. Its measures 27 km in circumference and is located roughly 100 m underground on the border between France and Switzerland. There are four main experiments located around the LHC: ALICE, ATLAS, CMS and LHCb. All four experiments have active pp and p–A programs. Out of the four, ALICE is the only dedicated heavy-ion experiment. ATLAS and CMS are general purpose experiments optimized for discovering the Higgs particle and other new particles. LHCb is focused on b-physics in the forward regions.

The entire CERN accelerator complex is shown in Fig. 5.1. The accelerator providing the collisions analyzed here is the LHC. However, it cannot, by itself, accelerate stationary particles directly to the relativistic speeds at which the collisions take place. Pre-accelerator systems are employed for lower speeds. The lead ions originate from a source of vaporized lead and enter the accelerator complex at Linac 3. From Linac 3 they enter the Low Energy Ion Ring (LEIR) and are then accelerated through LEIR, the Proton Synchrotron (PS) and the Super Proton Synchrotron (SPS) before they are injected into the LHC. Linac 3 is a linear (one-shot) accelerator, while the LEIR, PS and SPS are rings where the particles can be stored and accelerated.

The LHC is also the world's most powerful particle accelerator. It currently holds the world record in pp and heavy-ion (Pb–Pb) collisions, at $\sqrt{s} = 8$ TeV and $\sqrt{s_{\mathrm{NN}}} = 2.76$ TeV respectively. It is designed to collide protons up to $\sqrt{s} = 14$ TeV and lead ions up to $\sqrt{s_{\mathrm{NN}}} = 5.52$ TeV. The difference in energy between pp and Pb–Pb collisions is due to the fact that only the 82 electrically charged protons in the Pb nuclei, out of the 208 nucleons available, feel the acceleration field of the LHC: $82/208 \cdot 14$ TeV $= 5.52$ TeV. The current plan is to collide at maximum energy in 2015 or 2016 for both pp and Pb–Pb. Finally, the LHC has also provided the experiments with proton–lead (p–Pb) collisions at $\sqrt{s_{\mathrm{NN}}} = 5.02$ TeV.

5.2 The ALICE Detector

ALICE (A Large Ion Collider Experiment) is optimized for particle identification (PID) and low-momentum measurements. The most important detector is the Time Projection Chamber

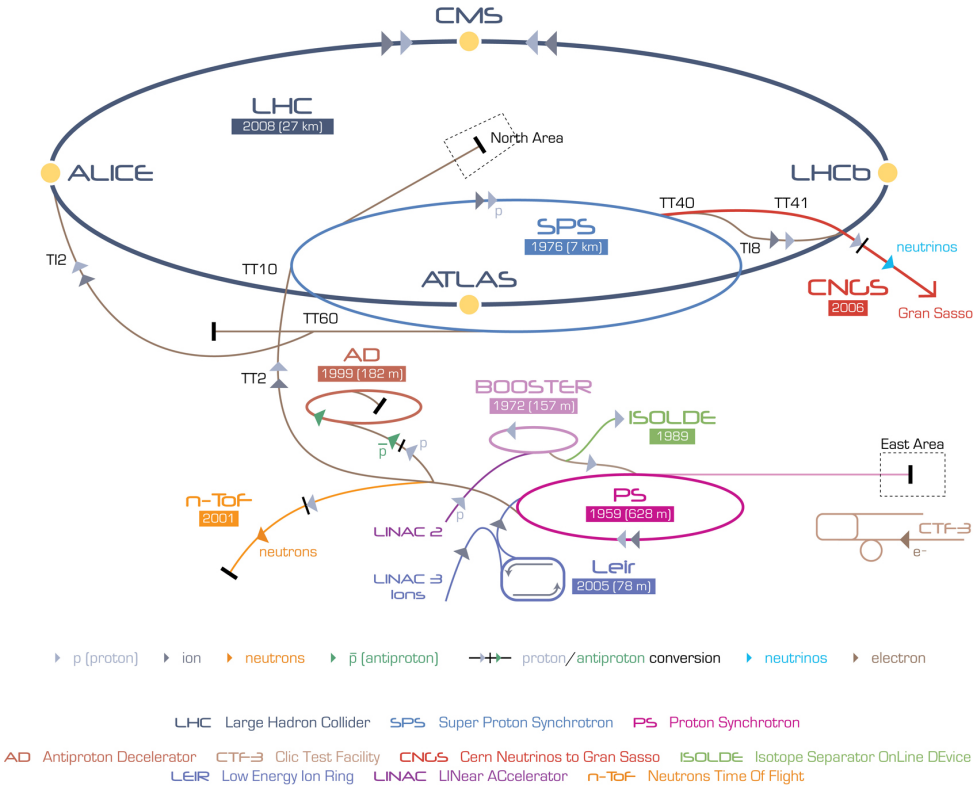

Figure 5.1: The CERN accelerator complex. Credit: CERN.

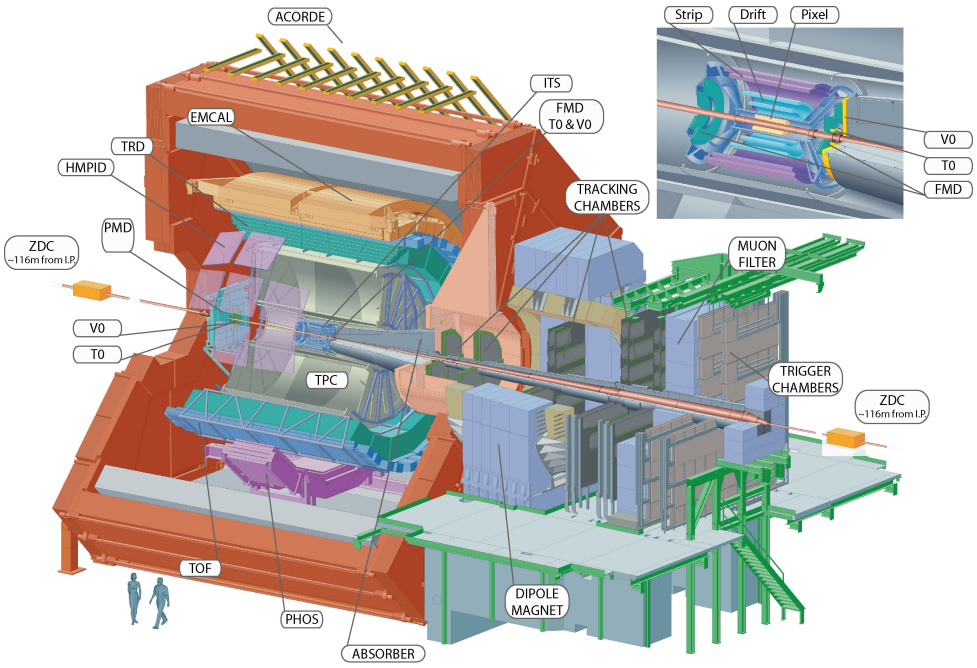

Figure 5.2: The ALICE experiment. The inner-most detectors are shown in a larger version in the top right corner.

Detector	Purpose	Technology
ITS†	Vertex, trigger, tracking	Silicon detectors
TPC	Tracking, PID‡	Gas time projection chamber
TOF	Tracking, PID‡	Photomultipliers
TRD	Electron ID, tracking	Transition radiation
HMPID	Hadron ID, tracking	Cherenkov radiation
PHOS	Photon ID, tracking	Electromagnetic spectrometer
EMCAL	Tracking	Electromagnetic calorimeter
MUON	Muon ID, tracking	Electromagnetic spectrometer
FMD	Charged particle multiplicity	Silicon detector
PMD	Photon multiplicity	Gas proportional counter
ZDC	Trigger, centrality	Hadronic calorimeter
V0	Trigger, centrality	Scintillators
T0	Trigger	Cherenkov radiation

Table 5.1: List of the ALICE sub-detector systems. First the central barrel detectors and then the forward detectors. Each detector's main purpose and primary detector technology is listed. †: The ITS consists of three smaller systems: the SPD, SDD and SSD. ‡: PID = particle identification.

(TPC) designed to track and identify the thousands of particles created in each collision. The Inner Tracking System (ITS) close to the interaction point (IP) determines the vertex position, tracks particles and contributes to triggering. The VZERO detector located at forward rapidity is used for centrality determination and triggering. Surrounding the detectors is the large L3 magnet which provides a 0.5 T magnetic field.

Table 5.1 provides an overview of all of the different sub-detectors, the technologies they use and their main purpose [103]. In general, the *central barrel* is located at mid-rapidity. The central barrel consists of detectors capable of tracking and PID (ITS, TPC, TOF, TRD, HMPID, PHOS and EMCAL). At forward-rapidities, triggering detectors and detectors designed for centrality measurements are positioned (ZDC, V0 and T0). In addition, there are detectors for measuring charged particle multiplicities (FMD) and photon multiplicities (PMD). Finally, there is a muon system to identify and track muons (MUON). A drawing of the experiment is shown in Fig. 5.2. In the following sections the sub-systems used for this work are presented in more detail.

5.3 The Forward Multiplicity Detector (FMD)

The purpose of the FMD is to provide charged particle information in the forward and backward regions. It covers $-3.4 < \eta < -1.7$ and $1.7 < \eta < 5.0$ in pseudorapidity and has full azimuthal acceptance. A large number of radial channels provides high resolution in η, while the azimuthal segmentation provide a φ-resolution good enough for flow analyzes. For this analysis the FMD is the main detector at forward pseudorapidity. The FMD consists of five rings of silicon sensors arranged in three sub-detectors: FMD1, FMD2 and FMD3. Furthermore, FMD2 and FMD3 consist of an inner and an outer ring, while FMD1 only has an inner ring. Table 5.2 shows the parameters of the FMD inner and outer rings. Figure 5.3 shows a drawing of the system, with the individual η-coverage and z-coordinate of the rings. The large η-coverage together with 20 or 40 azimuthal sectors makes it uniquely suited for flow analysis over a large rapidity range.

In each of the FMD channels, the deposited charge is collected and the resultant signal is

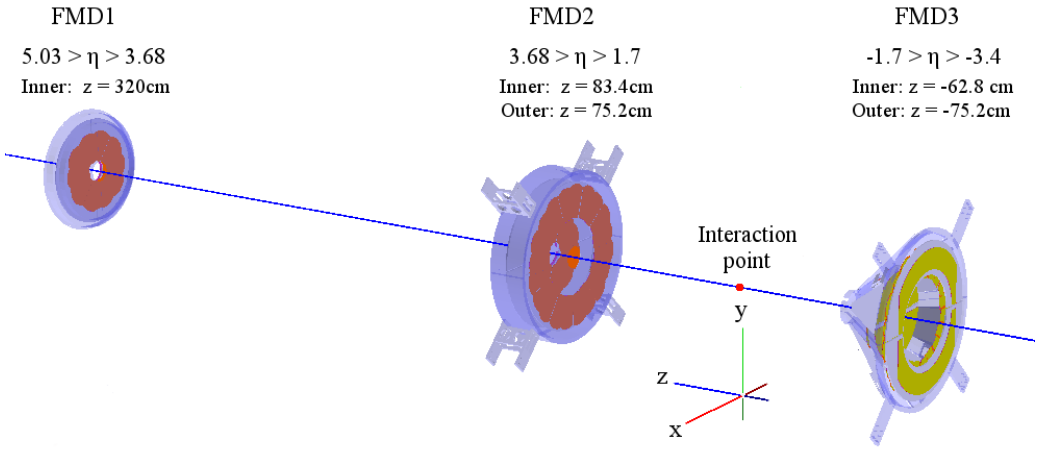

Figure 5.3: The Forward Multiplicity Detector.

	$N_{channels}$	$N_{sectors}$	r_{min}	r_{max}	$\Delta\varphi_{sector}$	$N_{strips/sector}$	Strip pitch
Inner ring:	10240	20	4.2 cm	17.2 cm	18°	512	250 μm
Outer ring:	10240	40	15.4 cm	28.4 cm	9°	256	500 μm

Table 5.2: Parameters for the FMD rings. In total the FMD has 51200 channels.

digitized to a 10 bit ADC value[1] between 0 and 1023 (both included). This makes it possible to estimate, on average, how many particles have hit the FMD. This process is described in more detail in Section 6.2.

The FMD uses silicon sensors to detect the charged particles. When a charged particle traverses silicon it deposits energy in the material. The most probable value (MPV), of the energy deposited by the traversing particle is described by the Bethe-Bloch parametrization curve of charged particles ionization energy loss. Due to noise and the finite binding energy of the electrons, the distribution around this MPV is a Landau distribution convoluted with a Gaussian. [104]

Silicon itself is a semi-conductor material. Semi-conductors can be arranged in so-called *pn-junctions*. When using silicon for particle detection, arranging the sensors in pn-junctions has the advantage of reducing noise due to their intrinsic field. In the FMD there is also a *reverse bias voltage* applied to further reduce noise, by depleting the sensitive area of thermal electrons. When particles traverse the silicon sensors, they interact with the electrons in the material, exciting the electrons in the valence band. They then drift (due to the bias voltage) over the silicon. A signal is induced on strips covering the surface and can be read out and used to obtain information on how many particles hit the sensor. For a more technical description of pn-junctions in particle detectors, see e.g. Ref. [104]. Two pictures of the FMD sensors are shown in Fig. 5.4.

The charge is collected over $\sim 2\mu$s in order to shape the signal. Consequently, the FMD cannot be used as a trigger detector. Although it could provide centrality and symmetry plane determination, it is currently not used for either.

For more information on the FMD detector, electronics and read out, see Refs. [104, 105]. For more information on the signal processing see Section 6.2

[1]ADC stands for Analog to Digital Converter. A device to convert an analog signal to a digital signal. An ADC value is the digitized output signal.

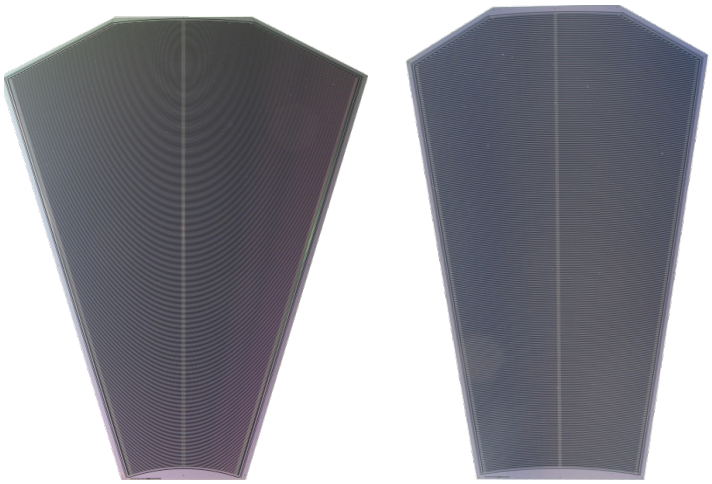

Figure 5.4: Picture of an inner (left) and an outer (right) FMD sensor, each with two azimuthal segments and 512 radial segments for the inner and 256 radial segments for the outer.

Layer	Type	Channels	r (cm)	$\pm z$ (cm)	$\pm\eta$
1	Pixel	3 276 800	3.9	14.1	2.0
2	Pixel	6 553 600	7.6	14.1	1.4
3	Drift	43 008	15.0	22.2	0.9
4	Drift	90 112	23.9	29.7	0.9
5	Strip	1 148 928	38.0	43.1	1.0
6	Strip	1 459 200	43.0	48.9	1.0

Table 5.3: Acceptance and number of channels for each of the six ITS layers [103].

5.4 The Inner Tracking System (ITS)

The ITS consists of three silicon-based sub-detectors. Starting with the innermost detector, they are: the Silicon Pixel Detector (SPD), the Silicon Drift Detector (SDD) and the Silicon Strip Detector (SSD). The SPD is covered in more detail in the next subsection. Each of the sub-detectors are made up of two concentric silicon layers centered at the beam-pipe. Table 5.3 shows the acceptance of each of the ITS layers. Being silicon detectors, basic detection of particles in the three ITS systems is the same as that described above for the FMD.

Combining the three sub-systems allows for low-momentum charged-particle tracking. In this respect the ITS detectors complement the other central barrel detectors by tracking particles with low p_{T} that do not reach the TPC due to deflection from the magnetic field. The SSD is made to match up with the TPC, improving on the precisions of the tracks measured by the TPC by fitting them inwards to the collision vertex. The SSD and SDD read-outs allow for dE/dx measurements for low-momentum PID. For this analysis the TPC tracks refitted with the ITS, so-called *hybrid tracks*, are utilized for systematic checks - see Section 6.6. More details about the ITS detectors and electronics are found in Ref. [106].

5.4.1 The Silicon Pixel Detector (SPD)

The SPD is the main ALICE vertexing detector, including detection of secondary vertices from weak decays. In addition, it has a fast read-out allowing it to act as a Level 0 trigger. The front-end electronics send the trigger information to the Central Trigger Processor (CTP) where

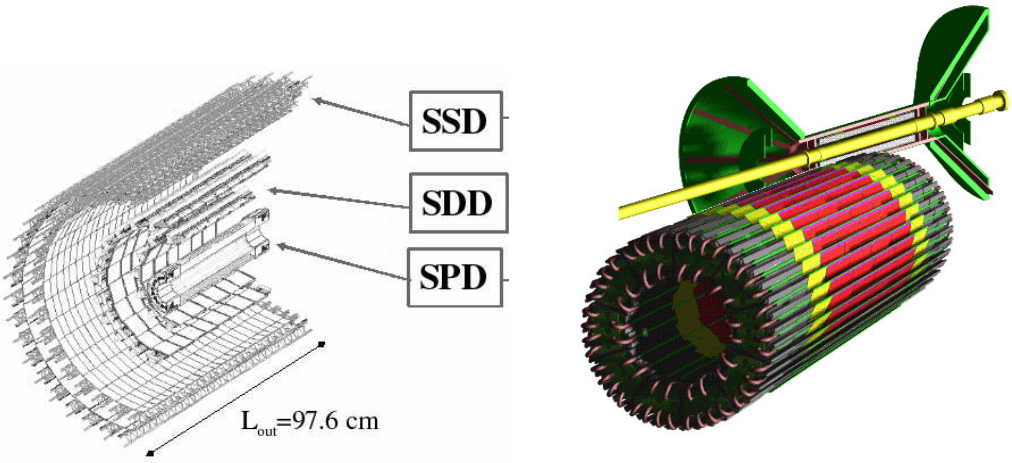

(a) The ALICE Inner Tracking System [103].

(b) The ALICE Silicon Pixel Detector (SPD).

Figure 5.5

a trigger decision is made in less than 800 ns from the collision time.

The SPD has a very high spatial resolution. The two silicon layers consists of $9.8 \cdot 10^6$ cells with a binary read-out. This means it is only possible to tell if a pixel is hit or not, and not how many particles may have hit it. The binary read-out is sufficient because each cell measures just 50 μm ($r\phi$) $\times$ 70 μm (z). Thus, the probability of more than one particle hitting a single cell is very small. The cells are so small that it is necessary to take into account the cases where a single particle leaves a signal in several neighboring channels. To achieve this, a clustering algorithm is applied which is described in detail in Section 6.4. Once the clusters of each of the two layers are found, it is possible to match up the clusters with the primary vertex and obtain a mini-track known as a *tracklet*.

For this analysis the vertex position from the SPD is used for the primary vertex determination. Furthermore, the clusters from the inner layer are used for the charged particle multiplicity information in the range $|\eta| < 2.0$. This provides continuous coverage over a large rapidity range when combined with the FMD or VZERO (see below). Although the SPD is designed to provide full azimuthal coverage, cooling issues prevented some of the sectors from running during the 2009–2011 data taking periods. The SPD is shown in Fig. 5.5b. More details on the SPD are found in Ref. [106].

5.5 The Time Projection Chamber (TPC)

The TPC is the primary tracking detector in ALICE. It consists of an active gas volume of 90 m^3 surrounded by a field cage. A schematic of the TPC is shown in Fig. 5.6. The TPC has a central high-voltage electrode and a potential divider at each end. This provides a uniform electrical field inside the gas volume. When a charged particle traverses the chamber, the gas inside ionizes. The electrons then drift, due to the electrical field, to the read-out chambers at each end of the TPC. The drift time is precisely known due to a laser calibration system[2]. The read-out chambers are multi-wire proportional chambers that amplify the charge. The signal is subsequently read out by a grid of pads. The (x, y) position of the pad together with the difference between the charge arrival time and the trigger time, allows for excellent tracking

[2]The laser system is built at the Niels Bohr Institute.

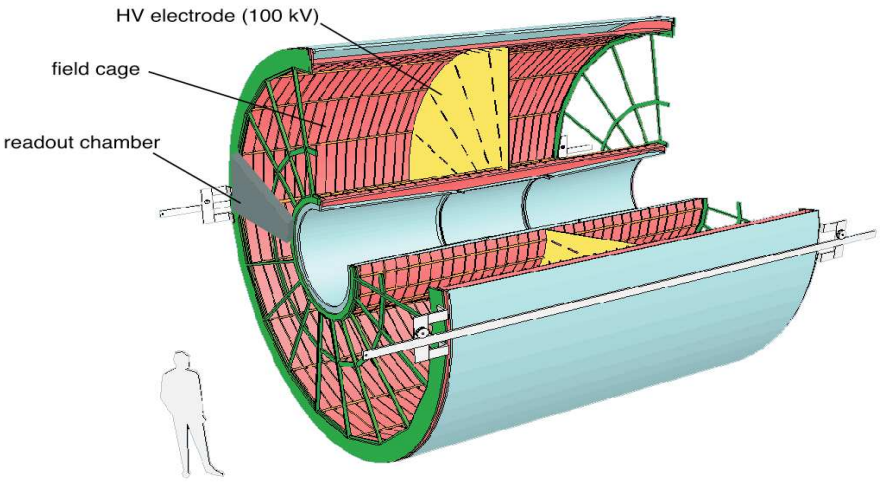

Figure 5.6: The ALICE Time Projection Chamber.

capability. Furthermore, the amplitude of the signal can be used for dE/dx analysis and PID information.

The TPC measurements are used to classify different kinds of tracks: TPC-only (stand-alone) tracks, TPC+ITS hybrid tracks, and global tracks in which as many of the central barrel tracking detectors as possible are included. The coverage allows for full azimuthal tracking within $|\eta| < 0.9$.

For this thesis both TPC-only and hybrid tracks are used. These are described in detail in Section 6.6. More technical details about the detector are found in Ref. [107].

5.6 The VZERO Detector (V0)

The V0 consists of two arrays of scintillators connected to photo multipliers, divided into two sub-detectors: the V0A and V0C[3] - placed on either side of the IP. When a charged particle traverse one of the scintillators, photons are created and sent through fibers to photo multiplier tubes (PMTs). In the PMTs, a shower of electrons is created, thereby amplifying the signal. The signal is subsequently digitized and stored as an ADC value. Two pictures of the V0 with the scintillators visible are shown in Fig. 5.7.

Each V0 is made up of 32 elementary counters arranged in four rings. This provides an angular φ-resolution of 45°. In pseudorapidity the V0 covers $-3.7 < \eta < -1.7$ and $2.8 < \eta < 5.1$ from the nominal vertex position. The individual coverage of each ring is shown in Table 5.4. Consequently, the VZERO does not have a high segmentation in η or φ. It does, however, have a timing resolution which is better than 1 ns. This allows the V0 to serve as an efficient trigger detector. It can be used in either AND or OR mode, where AND requires a coincidence between V0A and V0C while OR requires a detection in either V0A or V0C.

The signal amplitude read out from the PMTs is proportional to the number of charged particles impinging on the scintillator. This allows the VZERO to estimate the centrality, and it is main centrality estimator in ALICE. It provides a good resolution of 0.5% in centrality in the most central events and 2% in the most peripheral. It is also used for symmetry plane determination in the forward regions.

In this analysis it is used as part of the minimum bias (MB) trigger and as the centrality

[3]The A-C naming is from the ALICE naming scheme of A-side and C-side, with A-side being $\eta > 0$ and C-side being $\eta < 0$.

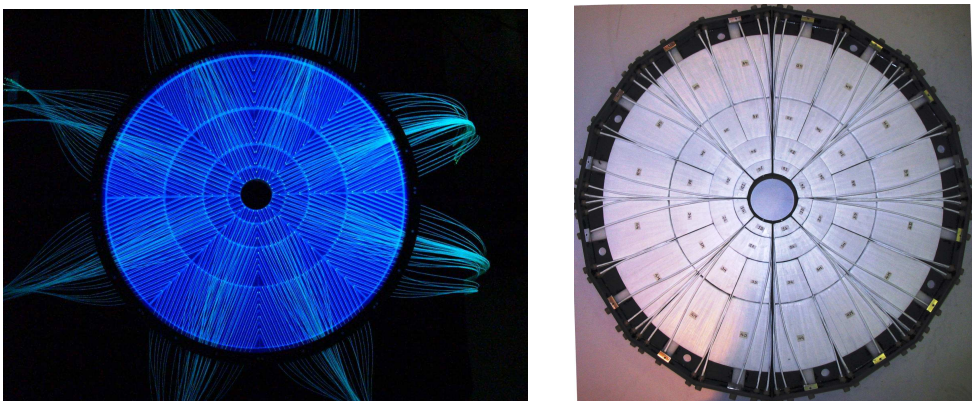

Figure 5.7: Left: front view of the V0A, showing the scintillators. Right: front view of the V0C. [103]

	0	1	2	3
V0A	$4.5 < \eta < 5.1$	$3.9 < \eta < 4.5$	$3.4 < \eta < 3.9$	$2.8 < \eta < 3.4$
V0C	$-3.7 < \eta < -3.2$	$-3.2 < \eta < -2.7$	$-2.7 < \eta < -2.2$	$-2.2 < \eta < -1.7$

Table 5.4: V0 individual ring acceptance at nominal vertex.

estimator. In addition, in spite of its limited spatial granularity, it is also used in the flow analysis presented here as a cross-check of the results obtained with the FMD. The centrality determination is discussed further in Section 8.1.4 and its use in flow analysis is discussed in Section 6.3. The VZERO is described in more detail in Ref. [105].

5.7 Upgrade Plans

The LHC long shutdown 2 is planned to start in 2018. The current plan for 2019 and onwards is to provide the experiments with much higher luminosities. In order to cope with these conditions and to reach new physics observables, a number of upgrades for the ALICE detector are being proposed [108].

- The entire ITS will be replaced with a by high-resolution detector, significantly improving the ITS tracking capabilities as well as timing resolution and η-coverage [109].
- The TPC will have its multi-wire proportional chambers replaced by gas electron multipliers (GEMs) along with new electronics in order to provide continuous readout. This is necessary for running the TPC at the high luminosities proposed [110].
- A new muon forward tracker (MFT) is to be installed in front of the current muon systems [111].
- A new trigger detector to replace the T0 and V0, named the Fast Interaction Trigger (FIT) will be installed [112].
- Upgrades to the TRD, TOF and PHOS detectors are planned, in order to enable high data-taking rates [108].
- Upgrades to the online and offline triggering, data acquisition and data processing facilities to handle the high-rate data-taking are planned [108].

The FMD will be removed and the forward charged-particle estimate will come from either FIT, the MFT or a combination of the two.

Chapter 6

From Signals to Particles

This chapter provides an overview of how the signals from the detectors used in this work (FMD, VZERO, ITS and TPC) are analyzed. The emphasis is on the FMD, since developing and testing the FMD framework has been a large part of this work. Most of the algorithms presented in this chapter allow the user to apply cut values to the data being analyzed. Types of cuts are described in this chapter, while the actual values chosen and uncertainties related to the cuts are discussed in Chapters 8 and 9.

6.1 Data Reconstruction

The data processing for all of the ALICE detector systems follows the same basic scheme. It is shown in Fig. 6.1. The left half of the figure shows how the raw data can either come from the actual detector Data Acquisition (DAQ) system or be generated via Monte Carlo (MC) event generators. The right half of the figure shows the process that happens after the raw data files are created.

In general, data in ALICE comes in three data formats. First, immediately following data collection, data are saved in a raw format. These are big files that are not fit for physics analysis. The first pass on these files is to update system calibration files in the Online Calibration Data Base (OCDB) and quality assurance (QA) analysis. This is to ensure that the data quality is acceptable. A second pass produces Event Summary Data (ESD) files. In the ESD format, the data is ready for analysis. However, the files are still relatively large, making analysis slower and more resource demanding than necessary. A third pass, run on the ESD files, creates Analysis Object Data (AOD) files. These files are optimized for physics analysis. For example, they contain specific cuts applied to ensure high-quality tracks.

6.2 FMD Signal Processing

For some detectors in ALICE, in particular those used for tracks, the main part of the signal analysis is done when the ESD files are created. For the FMD a significant part of the signal analysis is done afterwards. Consequently, this section is divided into two parts. The first part deals with how the raw data is calibrated and stored in ESD files. The second part explains what is done with the information from the ESD files before physics analysis is performed.

6.2.1 Raw FMD Data

Like most other electronics, particle detector electronics contains noise. There can be many sources of the noise, for example power supplies or leakage current. The noise is most often Gaussian. It is important to know the noise, such that it does not get confused with the signal.

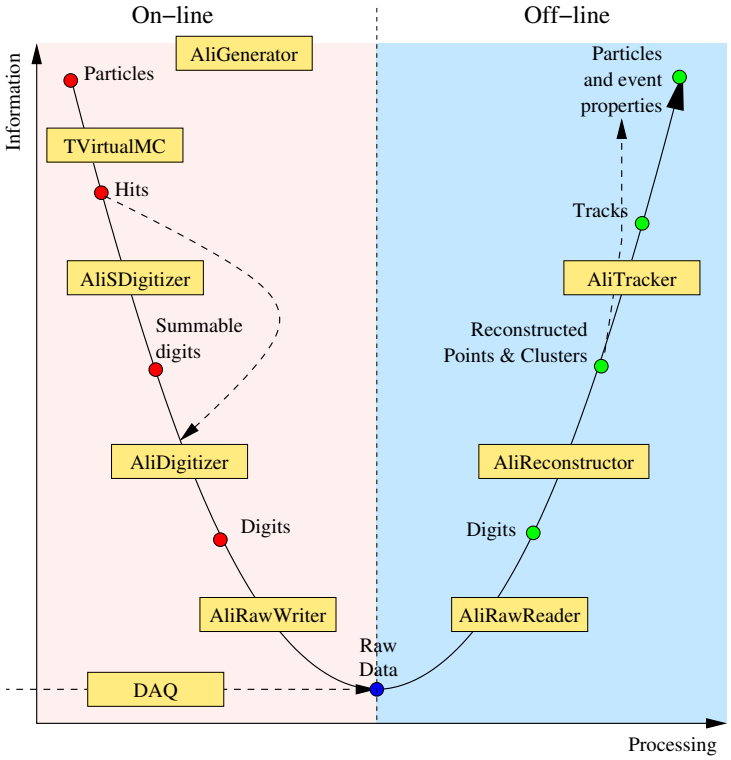

Figure 6.1: Data processing in ALICE. Online either goes through actual detector DAQ system or MC generators. [104]

By measuring the offset and the width of the noise, it is then possible to subtract it from the signal.

In a FMD channel there is a DC voltage offset, referred to as the 'pedestal'. It is the signal offset of the noise in the ADC spectrum. The electronic and thermal noise produce a Gaussian distribution with the pedestal offset as the mean. By measuring the signal in the detector when there are no beams in the accelerator, it is possible to estimate the mean and width of the distribution and subtract it during reconstruction. Figure 6.2 shows the signal and the noise of two FMD sensors during test beam studies. The Gaussian noise distribution is the large structure around the pedestal value of ADC = 100. The signal is several orders of magnitude smaller, but well separated from the noise. The figure shows the importance of knowing the noise of the electronics in order to successfully measure the signal.

The individual channels of the FMD do not have the same pre-amplification due to internal circuitry. This leads to relative shifts in the ADC spectrum between the individual channels. To find the relative gain of each channel, the FMD electronics allows for injecting a predefined charge into the circuitry. Afterwards, the ADC counts are rescaled by an electronics constant and stored in the ESD data format (see Section 6.1) [104].

6.2.2 ESD Processing

The ESD processing in the FMD is done in three steps. First, a sharing (or clustering) algorithm is applied. Second, the estimate of the number of charged particles in a region of the FMD is calculated. Last, the results from the five individual FMD rings are merged into a single 2-dimensional (η, φ)-histogram. Each step is described below.

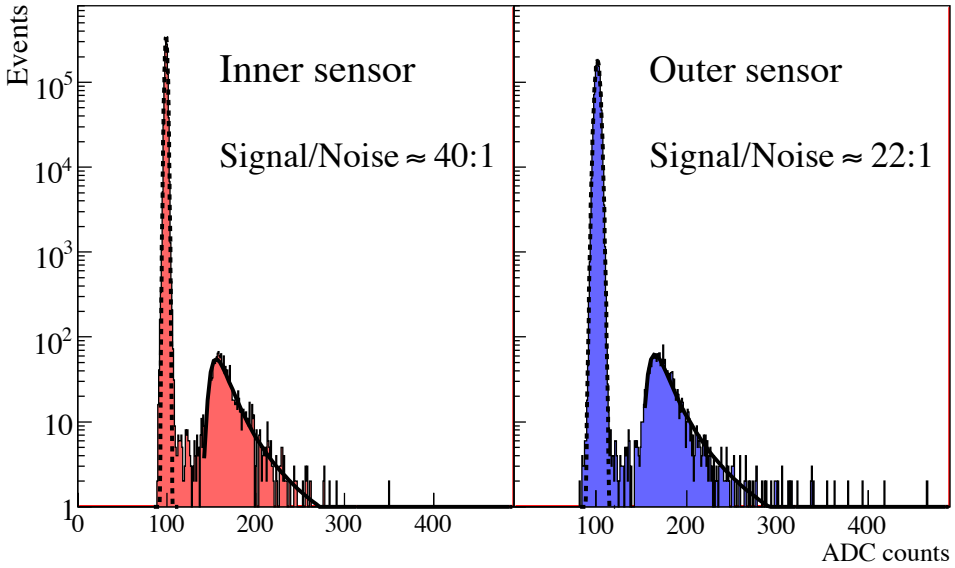

Figure 6.2: Signal-to-noise ratios of two FMD sensors from a 630 MeV e^- test beam [104].

The Sharing Filter

Even though the individual channels in the FMD are thin (300 μm), it is still possible for a single particle impinging on the FMD at an angle to deposit energy in two adjacent strips - the width of a strip is only 250 μm for inner rings and 500 μm for outer. To account for this, a clustering algorithm is applied to group strips that might have shared energy. The algorithm uses two energy cut values: E_{low} and E_{high}, between which the clustering is performed. E_{low} is a cut set to remove any remaining noise. E_{high} is a cut set to minimize the probability of merging the signals from two particles in adjacent strips into a single cluster representing a single particle.

The algorithm loops over all the strips in each FMD ring. If a strip has $E_{strip} < E_{low}$, the energy of that strip is set to 0. If a strip is found to have energy in the range $E_{low} < E_{strip} < E_{high}$, the adjacent strips (in the same sector) are checked for a signal; if an adjacent strip with a signal is found, i.e. $E_{adj.strip} > E_{low}$, the two signals are merged into the strip with higher energy. If a strip has $E_{strip} > E_{high}$ nothing is done. The method is described in more detail in Ref. [113].

Charged Particle Calculation

A third cut is needed to determine above which energy a signal should count as a particle. To find this cut, it is necessary to look a bit more on the energy loss distributions. When more than one particle hits a strip in a single event, the probability distribution of the energy deposited still follows a Landau convoluted with a Gaussian. However, the peak of the Landau distribution is shifted by $n(E_{MPV} + \xi \ln n)$. Where n is the number of particles traversing the strip, E_{MPV} is the value of the single-particle peak and ξ is the width of the Landau distribution. In principle, a complicated fit over data from many events could be used to extract parameters to estimate the most probable number of particles in a strip in a single event. The parameters, however, depends on centrality, rapidity, vertex coordinates and even on φ. The number of parameters to be stored for such calculations would therefore be huge. Due to this, a different approach was taken, in which the fit parameters are only used to estimate values for the three cuts. In this case the cuts should only depend on the position of the first peak of the distribution, which is dominated by the polar angle, η.

To estimate the effect of multiple particles hitting the same strip, a charged particle estimate based on Poissonian statistics is used. The assumption is that the particles traversing a region of the detector are randomly distributed. In that case, the probability, $P(n)$, of finding n particles in a single channel is:

$$P(n) = \frac{\mu^n e^{-\mu}}{n!}, \tag{6.1}$$

where μ is the mean number of charged particles, N_{ch}, in a group of channels, $N_{channels}$. Thus, $\mu = N_{ch}/N_{channel}$. For a channel that is hit, the average number of particles, N_{avg}, is [114]:

$$\begin{aligned} N_{avg} &= \frac{\sum_{n>0}(nP(n))}{\sum_{n>0} P(n)} = \frac{1}{1-P(0)} \sum_{n>0} \frac{n\mu^n}{n!} e^{-\mu} \\ &= \frac{e^{-\mu}}{1-e^{-\mu}} \mu \sum_{n>0} \frac{\mu^{n-1}}{(n-1)!} = \frac{e^{-\mu}}{1-e^{-\mu}} \mu \sum_{m} \frac{\mu^m}{m!} \\ &= \frac{e^{-\mu}}{1-e^{-\mu}} \mu e^{\mu} = \frac{\mu}{1-e^{-\mu}}. \end{aligned} \tag{6.2}$$

The final result of Eq. (6.2) only depends on μ. Although μ also depends on centrality, η, vertex - all of the same things as the fit parameters. By using a large enough number of adjacent channels in a single event to measure μ it is possible to get a good estimate in each event. This is illustrated in Fig. 6.3, where the difference between the analytical solution and a simulation using a given number of channels in a single event is shown. It is found that using 256 or more strips gives a reasonable estimate when dealing with occupancies smaller than 90%.

The algorithm utilizes a single cut: E_{hit}. If, after the sharing algorithm, a strip has energy $E_{strip} < E_{hit}$ it is considered empty. Otherwise it is considered to have been hit by one or more particles. From this, the number of channels hit, N_{hit}, in a region of $N_{channels}$ is used to estimate $P(n > 0)$:

$$N_{hit}/N_{channels} \approx P(n > 0) = 1 - P(0) = 1 - e^{-\mu} \Rightarrow \mu \approx \ln(1 - N_{hit}/N_{channels})^{-1}, \tag{6.3}$$

where the accuracy of the approximation can be estimated using the right plot in Fig. 6.3. It should be noted that the calculations in the figure assumes μ is the same for all channels, which is not necessarily true if the regions are chosen over large ranges in η or φ.

Once N_{avg} in Eq. (6.2) is determined, all non-zero channels in the selected region are set to contain N_{avg} particles.

Merging of Rings

The last task is to use the z-coordinate of the primary vertex and calculate the (η, φ)-coordinate of each channel such that the charged particle estimate can be stored in 2-dimensional (η, φ)-histograms. Finally, all of the individual FMD rings are combined into a single (η, φ)-histogram, which is stored in the AOD files. For the vertices where some of the FMD rings overlap in η, the average N_{ch} of the rings is stored in the histogram. Note that the histogram only contains 20 φ-bins, i.e. it only has the φ-resolution of the inner rings. This means the extra resolution of the outer rings with 40 φ-sectors is lost at this point. However, in Section 8.8 it is shown that this does not have a significant effect on the flow measurement.

6.3 VZERO Amplitudes

The 64 VZERO channels are read out and stored as ADC values. Each V0 channel is calibrated to determine the PMT gain and the light yield of the scintillator and fibers. The gain calibration

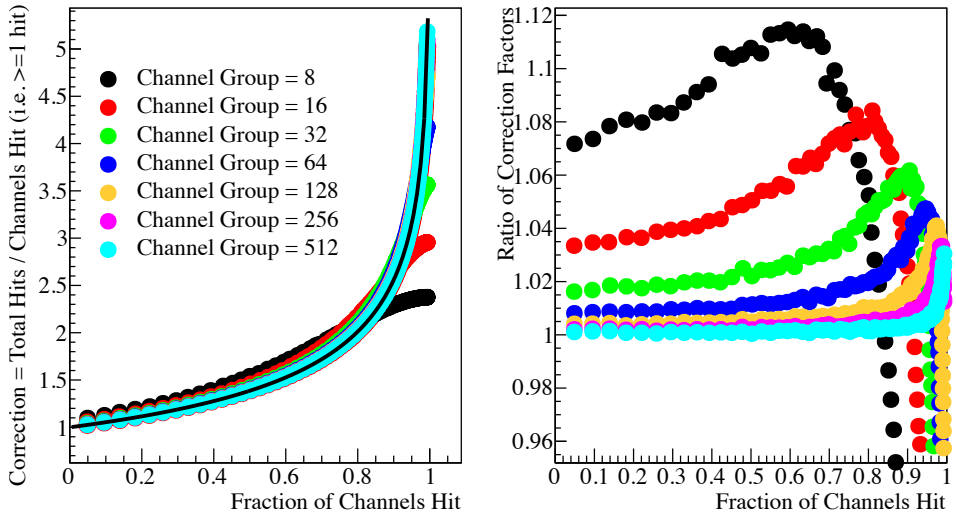

Figure 6.3: Comparison between the analytical value of the Poisson parameter μ, and estimating it by measuring the number of non-zero channels in groups of N channels, for a range of values of N between 8 and 512. For $N \geq 256$ deviations $< 1\%$ are found for occupancies up to 90%. [114]

was done before installation using cosmic muons. The light yield was measured in pp collisions at $\sqrt{s} = 7$ TeV and combined with a simulation and the gain vs. high voltage curve of each PMT. This allows for an estimate of the charged particle multiplicity in each channel. However, the high voltage is adjusted according to beam conditions and particle multiplicities to avoid saturation of the ADCs [115]. This means that in order to get a relative multiplicity estimate, it is necessary to do *gain matching* (equalization) of each channel. To get an absolute estimate, either a MC simulation or a reference measurement using another detector is necessary. The procedure for equalization is shown in Section 8.2.5.

6.4 ITS Clusters and Tracks

The SPD has high granularity and a binary read out. Consequently, the two types of algorithms used to analyze the data are for clustering and tracking. For clustering, neighboring channels, that are hit, are grouped together to form a single cluster. As the SPD has a very fast read out, one particle may be measured in several consecutive time-steps. These time-steps are also grouped into the cluster, counting as a single particle. The various spatial cluster configurations in a MC study is shown in Fig. 6.4, where the very high efficiency of the SPD clusters is also seen. 97% of all SPD clusters are either single-cell clusters or made up of two adjacent clusters. The read-out is sent to the trigger system for fast online triggering and stored in the raw data files. For vertex determination all possible combinations of clusters in the two layers are combined into so-called tracklets. By using a linear fit, the vertex is found where most of the tracklets coincide. For the ESD data format, the tracklets, refitted to the most probable vertex position, are saved along with any remaining unused clusters in the two layers. [116]

Similar to the SPD, the SDD and SSD have high granularity, and both a clustering and a tracking algorithm are run on the output of these detectors. The clusters are used in tracks which are combined with the TPC clusters to make *global tracks* and with the SPD to make ITS stand-alone tracks. There are two sets of ITS stand-alone tracks: one using all available clusters and another only using those not included in global tracks. The tracking is discussed further in Section 6.6.

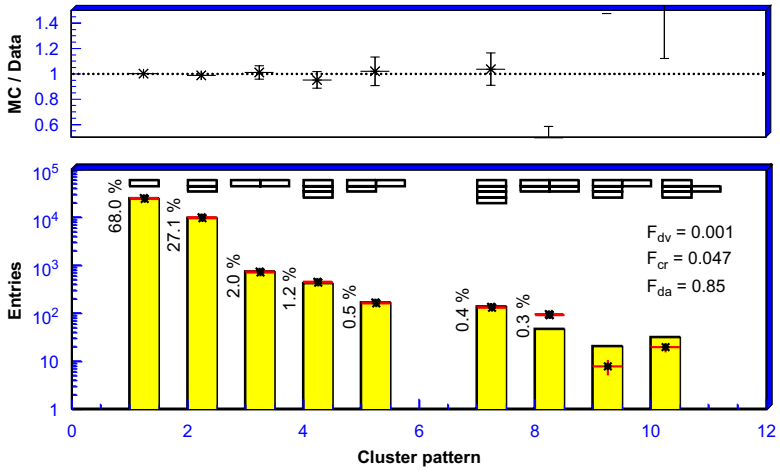

Figure 6.4: Spatial clustering configurations with the SPD compared in a MC model. [116]

6.5 TPC Clusters

As described in Section 5.5, charged particles traversing the TPC ionize the gas in the main chamber. An electric field ensures that electrons drift to the end plates, and are read out by a grid of 560000 channels. This high resolution allows efficient and precise tracking in the momentum region: 0.2 GeV/c < p_{T} < 100 GeV/c. With a resolution better than 2.5% for tracks with p_{T} < 4 GeV/c, the TPC can track and identify up to 20000 charged particles in a single event. The channels are combined in space and time to form clusters in a similar way to what is done in the ITS. A maximum of 159 clusters from the TPC can be associated with each track. [117]

6.6 Tracking with the ALICE Detectors

Tracking is done during the reconstruction phase of the data-flow diagram (see Fig. 6.1). Clusters in the central barrel are combined into tracks, which take into account the curvature caused by the magnetic field as well as the energy loss from interactions with the active detector elements. The tracks are constructed starting with so-called *seeds* in the outermost pads of the TPC, where the track density is smallest. They are propagated inwards following a Kalman filter algorithm [118]. Moving into the ITS, the procedure is the same with the tracks being propagated towards the vertex. The unused clusters in the ITS are then combined for ITS stand-alone tracks. Then the tracking is done from the inner ITS clusters outward. Potentially going all the way out to the TRD, TOF, HMPID and PHOS while performing particle identification (PID). Finally the tracks are refitted to the primary vertex using the PID information, these are called global tracks. [119]

For this analysis, TPC-only tracks and so-called *hybrid tracks* are used. TPC-only tracks use only TPC clusters when the tracks are fitted. The hybrid tracks are a combination of global tracks and TPC-only tracks refitted to the primary vertex. The hybrid tracks are believed to contain fewer secondary particles than the TPC-only tracks, but have slightly more complicated cuts and track definitions. During the tracking, a number of quality parameters are stored along with the track information. These parameters can be used to apply cuts on the track sets. They include the number of clusters in the various detectors, χ^2-values of the fits and rejection (or inclusion) of weak decays, seen as a *kink* on the track. The cuts for both TPC-only and hybrid tracks are discussed in Section 8.2.4.

Chapter 7

Event Generators and Models

To understand what happens in collisions of heavy-ions, it can be beneficial to model all aspects of the collision, both the events and the detector response. As described in Chapter 2, a heavy-ion collision goes through many phases before the particles are finally detected.

The initial stage is where the initial geometry of the collision is produced. It is the eccentricities in the initial geometry that give rise to the anisotropic flow. Then, in the partonic stage, with quark and gluon degrees of freedom, the flow develops. Hadronization is where the particles that are measured in the detectors are produced. In the hadronic stage, further scatterings may change the azimuthal anisotropies, as discussed in Chapter 4. Finally, in the detection of the particles, it is necessary to understand how the particles interact with their surroundings as they move out through the detector as well as how the detectors measure the particles.

Each of these stages has important implications for the flow measurement. Consequently, it is necessary to model each of the stages and understand how the flow measurement is affected by each stage. This chapter describes the various Monte Carlo (MC) event generators used for this analysis. It starts with the Glauber model of the initial conditions and proceeds with full event-based generators. Finally, transport codes and simulated detector response are discussed.

7.1 Glauber Models

Glauber Models [44] are a family of models that describe the scattering of nucleons in nuclear targets. There is a theoretical version based on an optical limit approximation and then there are various MC event based implementations, e.g. Ref. [120]. The underlying assumption is that the collision of two nuclei can be considered as a collective of individual interactions among the constituent nucleons.

While this section mostly covers the MC event based approach, most of the conclusions also apply to the optical limit approach. The MC models construct two nuclei with a collection of nucleons. The nucleons are randomly distributed according to three-dimensional nuclear density distributions, which were measured in electron scattering experiments and are of the Wood-Saxon type. The two nuclei are then placed such that their centers are separated by an impact parameter, b, which can be randomly chosen from the distribution $d\sigma/db = 2\pi b$. A nucleon-nucleon collision then occurs if the distance between two nucleons, d, in the transverse plane is [44]:

$$d \leq \sqrt{\sigma_{inel}^{\mathrm{NN}}/\pi}, \tag{7.1}$$

where $\sigma_{inel}^{\mathrm{NN}}$ is the total inelastic nucleon-nucleon cross-section. As the nuclei are three-dimensional objects, each nucleon can participate in more than one collision. In general, for two identical

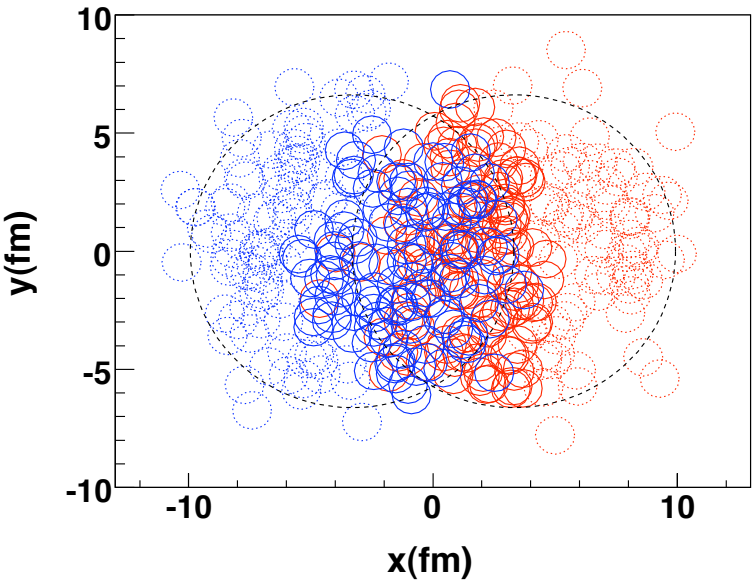

Figure 7.1: A non-central Pb–Pb collisions simulated with the PHOBOS Glauber Monte Carlo [120]. The initial-state fluctuations giving rise to v_3 and higher moments can be seen, as well as the almond shaped overlap responsible for v_2.

nuclei, the number of collisions, N_{coll}, scales as [44]:

$$N_{coll} \propto N_{part}^{4/3}, \tag{7.2}$$

where N_{part} is the number of participating nucleons, which depends on b. [44]

The Glauber model framework is used extensively in modern heavy-ion physics. Glauber models are used to relate the measured multiplicities or signal amplitudes to the single-event centrality and N_{part} estimation. They are often used in flow analyzes to estimate the initial-state eccentricities, ϵ_n. The initial-state fluctuations giving rise to higher harmonic flow effects are also reproduced by the models. See Fig. 7.1 for an example of a non-central Pb–Pb collision simulated with the PHOBOS Glauber Monte Carlo [120], clearly exhibiting initial-state fluctuations around the roughly almond-shaped overlap zone.

7.2 HIJING

HIJING (Heavy Ion Jet INteraction Generator) [16,17] is the most commonly used event generator for heavy-ion physics at the LHC. A Glauber model is used to model the geometry of the collisions. Parton structure functions are included to study nuclear shadowing. PYTHIA [121,122] routines are used for hard interactions and JETSET [123] routines are used for string fragmentation[1]. PYTHIA and JETSET have been used extensively in pp and p$\bar{\text{p}}$ collisions[2]. In HIJING they are used to describe the binary collisions between the nucleons.

Jet quenching is implemented in HIJING as an effective energy loss parameter dE/dz. Finally, mini-jet production is also included. Usually these mini-jets have too little energy to be seen experimentally, but they are well described by perturbative QCD and play an important

[1] One of the possible MC model approaches to hadronization.
[2] From PYTHIA 6.1, JETSET and PYTHIA were merged into PYTHIA.

role in the particle production at high energies. HIJING is designed to simulate events with center-of-mass energies of $\sqrt{s_{\mathrm{NN}}} = 4$ GeV and up for pp, p–A and A–A collisions [16, 17].

Current versions of HIJING describe RHIC data well and were able to predict the mid-rapidity multiplicity at the LHC reasonably well [124]. HIJING is now tuned to the LHC multiplicity measurements at mid-rapidity. While HIJING does include the initial-state anisotropies from the Glauber model, it does not include the interactions necessary to produce collective flow effects. The only correlations present in HIJING are non-flow correlations (See Section 2.4). It is therefore a convenient tool for estimating and removing non-flow effects from a measurement. In this thesis, HIJING is used to estimate and remove the non-flow contribution from the two-particle cumulant measurements.

7.3 AMPT

AMPT (A MultiPhase Transport model) is a prime example of how many different processes are needed to reproduce heavy-ion observables. AMPT consists of four parts: initial conditions, partonic interactions, hadronization and final state hadronic rescatterings. Each of these phases is described by a different model embedded in AMPT.

The initial conditions in AMPT are modeled by HIJING version 1.383. This includes the initial conditions from a Glauber model, spatial and momentum distributions of mini-jet partons and soft string excitations [125]. There are two options: either AMPT uses the Lund string model in which the excited strings are not used in the partonic stage, but only released during hadronization. Otherwise so-called *string melting* is used, in which all of the strings and hadrons produced by HIJING are turned into valence quarks and anti-quarks. It is with the string melting setting turned on that the observed flow is best reproduced.

The partonic stage is described with Zhang's Parton Cascade model (ZPC) [126], which simulates the interactions between the particles with a differential cross section [127]:

$$\frac{d\sigma}{dt} \approx \frac{9\pi\alpha_s^2}{2(t-\mu^2)^2}, \tag{7.3}$$

where t is one of the Mandelstam variables, α_s is the strong coupling constant and μ is the screening mass in the partonic matter. It is in this stage that collective flow develops.

For hadronization, the partons are put through a coalescence model that combines quarks in groups of two and three and converts them into hadrons [128].

Finally, A Relativistic Transport model (ART) [129] is used for the hadronic rescattering phase. This is where the final modifications to the collective flow happens.

AMPT has been tuned to match RHIC data [128, 130] and more recently LHC results [127, 131]. Figure 7.2a shows the modifications of $dN/d\eta$ by including ART with and without final state interactions (FSI). By tuning AMPT to ALICE data in the $40-50\%$ centrality bin, it reproduces the centrality-dependence of the multiplicity reasonably well (see Fig. 7.2b). Figure 7.4 shows how well AMPT reproduces the centrality- and p_{T}-dependence of v_2 to v_5. Generally AMPT reproduces the data well in centrality bins near the one it was tuned to match. However, the resultant multiplicity is too low and the flow is too high in the most central events. Similarly the multiplicity in AMPT is slightly too high in the most peripheral events.

7.4 Model with Parametrization of ALICE Measurements

Parameterizations of ALICE measurements in Pb–Pb collisions have been used to make a simple event generator in the ALICE simulation framework. Here it is referred to as AliGenTunedOnPbPb. It does not contain any initial state model or parton scatterings. Instead it is based

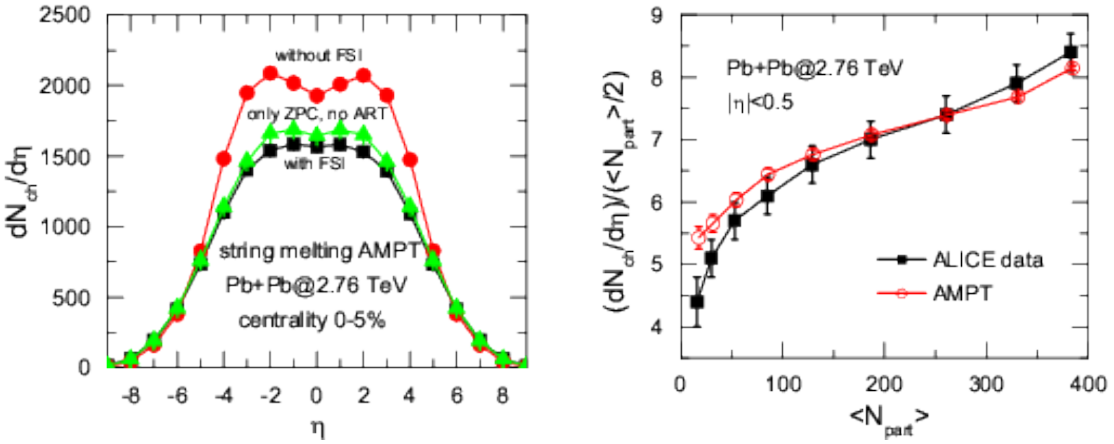

(a) Changes to $dN/d\eta$ predicted by AMPT when final state interactions (FSI) are off in ART (red), or ART is turned off (green). Black is with ART and FSI turned on (default).

(b) AMPT multiplicity densities compared to ALICE results. AMPT is slightly too high in peripheral events and slightly too low in central events.

Figure 7.2: AMPT in Pb–Pb collisions at $\sqrt{s_{\mathrm{NN}}} = 2.76$ TeV, tuned to ALICE data in the 40–50% centrality bin [127].

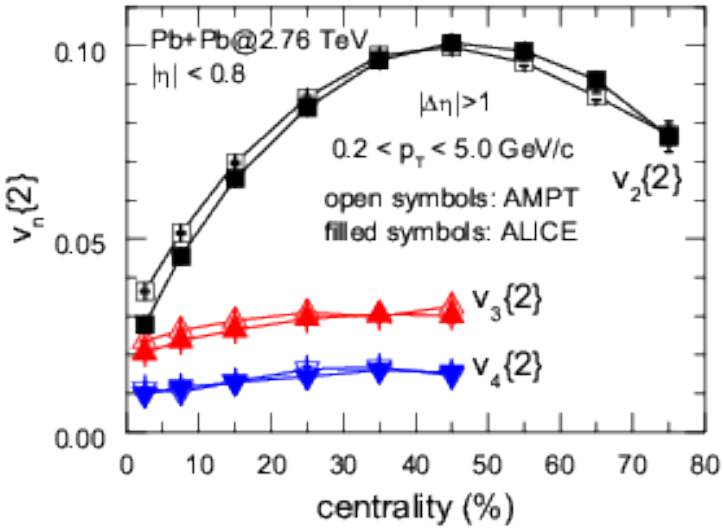

Figure 7.3: Centrality dependence of v_2–v_4. Comparison between AMPT and ALICE. AMPT predicts slightly too high flow values in the most central events. AMPT is tuned to ALICE data in the 40–50% centrality bin [131].

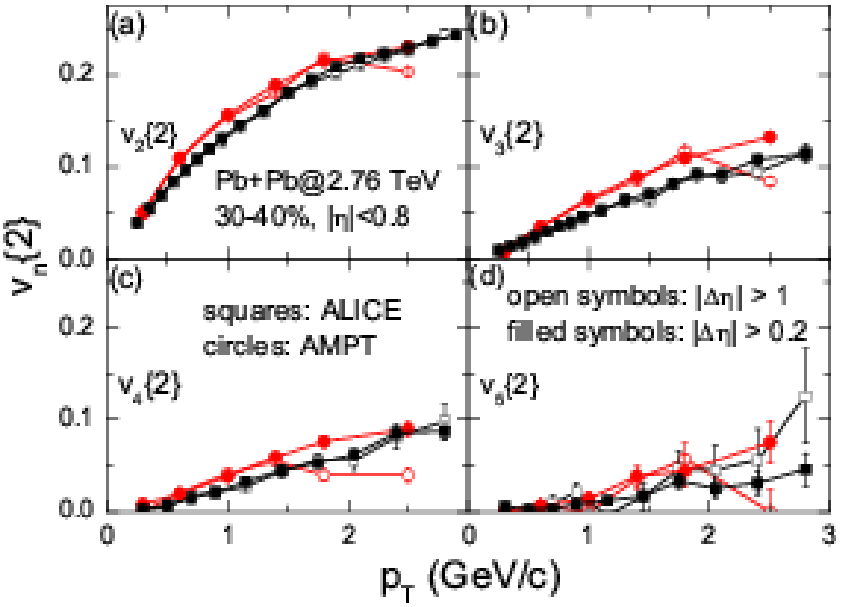

Figure 7.4: p_T dependence of v_2–v_5. Comparison between AMPT and ALICE for 30–40% central events. This is close to the centrality-region AMPT was tuned to match and a good agreement is observed. [131].

Centrality:	$0-5\%$	$5-10\%$	$10-20\%$	$20-30\%$	$30-40\%$
Multiplicity:	2668	2210	1664	1124	735
Centrality:	$40-50\%$	$50-60\%$	$60-70\%$	$70-80\%$	
Multiplicity:	452	258	133	61	

Table 7.1: Base values for multiplicities generated with AliGenTunedOnPbPb.

on parameterizations of ALICE measurements. The event multiplicity is centrality dependent, and the base values for the multiplicity densities are given in Table 7.1. Particles are produced up to a maximum absolute rapidity value, y_{max}. The multiplicity density distribution is flat up to a rapidity value, y_{flat}. After this, the multiplicity density falls of linearly with a factor f_M. All of these parameters must be set externally by the user. For the simulations used in this thesis: $y_{max} = 6.0$, $y_{flat} = 2.0$ and $f_M = 0.2$.

The species of the produced particles are distributed according to Table 7.2. Both multiplicity and the relative abundance of different species are based on ALICE measurements.

Blast-wave fits to the spectra of each particle type are used to assign p_{T} to the particles. Two examples of these fits are given in Fig. 7.5.

Finally, fits to v_2 vs. p_{T} are used to add collective flow effects. Originally the event generator was written and implemented by Francesco Noferini for systematic studies of the ALICE PID v_2 results. It included a v_2 and v_3 amplitude. For this work it was expanded to also include v_4. The φ angles of the produced particles are chosen randomly according to the p.d.f.:

$$f(\varphi) = 1 + 2v_2\cos(2(\varphi - \Psi_2)) + 2v_3\cos(3(\varphi - \Psi_3)) + 2v_4\cos(4(\varphi - \Psi_4)), \tag{7.4}$$

where each Ψ_n is chosen randomly in every event. The v_2 parameter is assigned according to the

$\pi^{\pm}$	π^0	$K^{\pm}$	p, $\bar{p}$	K^0_S	Λ, $\bar{\Lambda}$	ϕ	$\Xi^{\pm}$	$\Omega^{\pm}$
27.5%	27.5%	4.00%	1.35%	4.00%	1.12%	0.440%	0.104%	0.0152%

Table 7.2: Relative abundances of different species in AliGenTunedOnPbPb. Value applies to particle with both positive and negative charge in case of superscript $\pm$. E.g. 27.5% are π^+ and 27.5% are π^-.

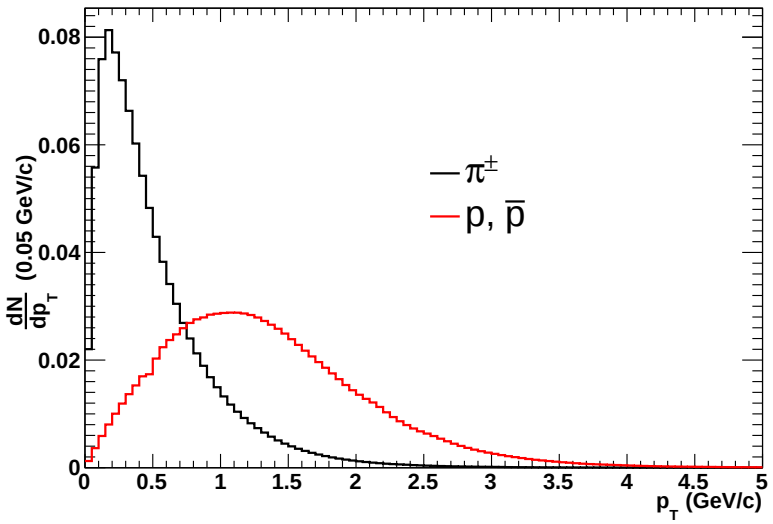

Figure 7.5: Example distributions used for assigning the p_{T} of $\pi^{\pm}$ and $p, \bar{p}$ in AliGenTunedOnPbPb, for the $0-5\%$ centrality bin.

p_{T}, species and y of the particle. The p_{T}- and species-dependence is found using fits to ALICE measurements. At mid-rapidity, there is no η-dependence. For $|y| > y_{flat}$ the flow is linearly reduced by a factor f_{v_n} set externally, here $f_{v_n} = 0.2$. v_3 is determined by multiplying v_2 with a centrality dependent factor: $v_3(p_{\mathrm{T}}) = f_{v_3/v_2} \cdot v_2(p_{\mathrm{T}})$, with the values of f_{v_3/v_2} given in Table 7.3. v_4 is set to be $0.5 \cdot v_3$, which is reasonably close to what is observed in real data. Two examples of fits for v_2 vs. p_{T} are shown in Fig. 7.6.

7.5 Geant

GEometry ANd Tracking (Geant) [132] is a transport code developed at CERN to describe particle interactions with material. It is based on the EGS program originally developed at SLAC. It utilizes a virtual description of the geometry of a particle detector; both the physical size and the material the different parts are made of. When coupled to an event generator, e.g. HIJING or AMPT, Geant tracks the particles as they propagate through the detector. It then uses Monte Carlo methods to model the interactions between the particles and the detector when

Centrality:	$0-5\%$	$5-10\%$	$10-20\%$	$20-30\%$	$30-40\%$
f_{v_3/v_2}	1.200	0.820	0.625	0.500	0.450
Centrality:	$40-50\%$	$50-60\%$	$60-70\%$	$70-80\%$	
f_{v_3/v_2}	0.400	0.370	0.300	0.300	

Table 7.3: Ratios of triangular flow to elliptic flow generated with AliGenTunedOnPbPb.

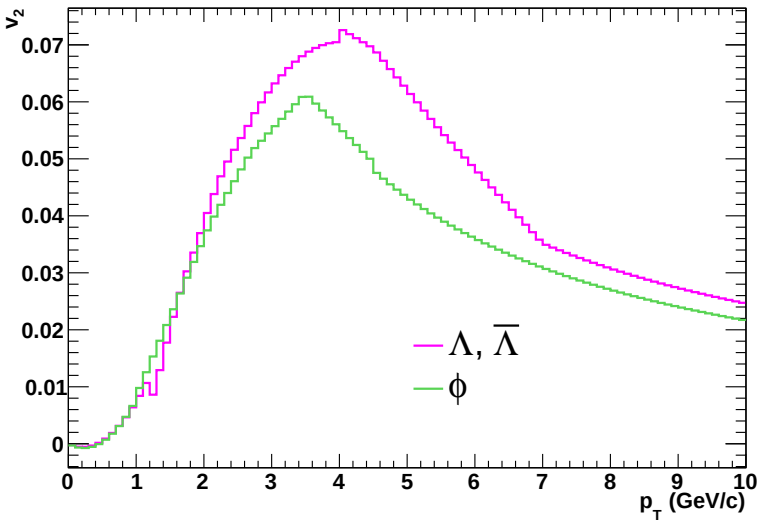

Figure 7.6: Example distributions used for assigning the proper v_2 according to particle p_{T} in AliGenTunedOnPbPb. The distributions for Λ, $\bar{\Lambda}$ and ϕ particles for the 0–5% centrality bin are shown. The distributions are a combination of fits in different p_{T} ranges. Consequently, the regions with overlap between different fits show some discontinuities. The overall effect from this is, however, negligible.

the particles traverse the material. These interactions include: secondary particle production, particle scattering and energy loss. When secondary particles are created Geant also tracks them [132]. In the ALICE simulation framework, a so-called *track reference* is made every time a particle hits a detector element - these are utilized to study the detector response.

The default version of Geant used in ALICE is GEANT3, although Geant 4 is also available [133] and Geant 5 is currently under development. Geant 4 is written in C++, whereas GEANT3 is written in Fortran. In addition, Geant 4 is tuned to newer experimental data. Geant 5 is going to take advantage of the parallelism available in modern CPUs to greatly speed up the simulation process. This is an important development, as currently the transport code is the most resource demanding part of the simulation.

7.5.1 Track References and Their Uses

A track reference contains all of the MC information from the generator as well as information about where the particles hit a detector. This can be utilized for efficiency studies or systematic uncertainty studies; for example how secondary particles are deflected compared to their mother particle. In addition, track references can be used for embedding signals that were not included originally in the simulation. An example is reweighing the track references according to the function:

$$w(\varphi) = \frac{1}{2\pi}\left(1 + \sum_n 2v_n \cos(n(\varphi - \Psi_n))\right), \tag{7.5}$$

which makes it possible to add a flow signal without the need of running a new MC simulation from scratch, simply by counting each track reference $w(\varphi)$ times. Using track references for systematic studies is a way to save computing resources. The reweighing method above is applied for the systematic uncertainty studies in Section 9.3.

7.6 The Virtual ALICE

A transport code such as Geant is not very useful without a complete virtual description of the experiment. This description should contain not only the active elements of the detectors, but also cooling pipes, support structures, wires, etc. The more precise the description is, the better the transport model is to estimate where particles are absorbed, scattered or produced. Part of this detector description is also used to simulate the signals read out by the detectors. See below for an example of how this works for the FMD. The simulated detector responses are then processed through the same algorithms as the real data, providing valuable cross-checks and systematic uncertainty estimates.

As the FMD has no tracking, it relies fully on the MC to subtract secondary particle contributions. Consequently, a wrong estimate of the particle production is a critical issue. In ALICE there has been some issues with inaccuracies in the description of the ITS geometry. This has led to the MC simulations underestimating the number of secondary particles produced in the forward regions, which includes the FMD. It is mainly the ITS support and cooling structures that affect the secondary particle production in the forward regions. Although the geometry description has been continuously improved over the last couple of years, it is still an important issue in FMD analyzes. The study of secondary particles and inaccuracies in the geometry plays a major role for the analysis presented in Chapter 8 and is also discussed there. Further discussion of the ALICE geometry can also be found in the thesis of Hans Dalsgaard [113].

7.6.1 FMD Response and Digitization

This section provides an example of how to simulate the detector response due to a traversing charged particle. The detector used in this is example is the ALICE FMD. The response is simulated by evaluating the energy loss, E_{loss}, of all of the particles that hit a specific channel (provided by the transport code). Noise is added according to real calibration measurements. The signal is then converted into ADC counts or so-called *digits*. The ADC count, c_i, for strip i is then:

$$c_i = p_i + x + g_i E_{loss} C, \tag{7.6}$$

here p_i is a pedestal taken from real pedestal runs, x is a value randomly taken from a Gaussian distribution with a width of the known detector noise, g_i is the gain factor from real gain calibration runs and C is a fixed conversion factor from gain calibrated signals to ADC counts and depends on the response of the $\mathrm{VA1}_3$ pre-amplifier. In this way, the simulated digits represent as closely as possible the real ADC counts found during data-taking [104]. At this point the MC data can be further processed (reconstructed) in the same way as real data. The reconstruction process is described in Chapter 6.

Part IV

Analysis and Results

Chapter 8

Analysis

High-energy physics analyzes contain many complex layers. The previous chapters have already laid the foundations, describing the experimental setup, the motivation for collective flow measurements as well as how to measure the flow. This chapter describes the analysis of Pb–Pb collisions at $\sqrt{s_{\mathrm{NN}}} = 2.76$ TeV with ALICE at the LHC, performing a measurement of $v_2\{2\}$, $v_3\{2\}$, $v_4\{2\}$ and $v_2\{4\}$ (Section 3.4) vs. η. The analysis is done using data from the ALICE Time Projection Chamber (TPC - Section 5.5) for the reference flow. The Forward Multiplicity Detector (FMD - Section 5.3) and Silicon Pixel Detector (SPD - Section 5.4.1) are used for the differential flow measurement. The main topics of this chapter are:

Event selection: To understand triggering, rejection of background events, measuring the vertex position and estimating the centrality.

Selecting the particles: To determine cuts on detector signals and tracking parameters.

Correcting for backgrounds: To estimate effects from secondary particles, non-flow and finite azimuthal resolution.

Two different Monte Carlo (MC) generators are used to estimate effects from secondary particles: AMPT and AliGenTunedOnPbPb (Sections 7.3 and 7.4 respectively). A non-flow correction using HIJING (Section 7.2) is presented. At the end of the chapter, the results, including statistical uncertainties only, are shown. The next chapter contains the systematic checks performed and the final results are presented in Chapter 10.

The main software used for this work is AliROOT [134]. AliROOT is the offline software framework in ALICE, it contains the source code needed for simulation, calibration, data quality monitoring, reconstruction, quality assurance and physics analysis. It is built on ROOT [135], which is a C++ based software developed at CERN. ROOT provides a framework for fast processing of large amounts of data, complex mathematical and statistical tools, as well as a number of different visualization capabilities.

8.1 Event Selection

This section describes the part of the analysis related to the general ALICE analysis software framework. It pertains to general event classification, vertex determination and centrality. The same, common setup is used in all ALICE physics analyzes and maintained by a centrally coordinated working group. In total 10^7 Pb–Pb events were analyzed for this analysis.

8.1.1 Triggering Selection

Each collision is assigned one or more *trigger strings*. Event selection based on these strings is performed by the so-called *physics selection*. The trigger strings contain information on

which conditions were fulfilled for the event to trigger, what type of trigger it is (e.g. collision, background or calibration) and which detectors were read out. The events selected in this analysis are all collision triggers containing a read out of the detectors used for this analysis, i.e.: FMD, ITS, TPC and VZERO. Furthermore, while it is possible to select triggers with a specific requirement for high multiplicity or a specific centrality range, only minimum-bias (MB) triggers are considered here.

The LHC is taking data most of the year. During a year a number of conditions may change, e.g. collision energy, luminosity or the beam type (e.g. proton or lead). To take these changes into account, in ALICE, a year of running is typically divided into certain *periods*. A change of period is typically made to coincide with a longer shut-down of the accelerator, a significant change in luminosity, or a switch from proton physics to heavy-ion physics. The periods are named according to the year with digits and the period of the year with numbers, e.g. the Pb–Pb collision period analyzed here is named LHC10h as it was recorded in the 8^{th} period of 2010.

During a period the accelerator is *fill*ed many times. During a fill the ALICE detectors may start and stop data-taking several times. Sometimes a system needs to be restarted, which requires all of ALICE to stop taking data, and then start again once the system is ready. These intervals of data-acquisition are known as *runs* and are simply numbered from when ALICE first started taking data. They are not reset by any change in period or year. For example, the runs of the LHC10h period analyzed here are numbered from 137135 to 139510. The active detectors, and even the trigger setting, may change from run-to-run, as systems need restarting or the beam-conditions change. This means that even the trigger string of the MB trigger may change from run-to-run. The physics selection makes sure that all of these changes are taken into account. This ensures that comparable events are selected consistently for the physics analysis despite underlying changes to the detector setup.

Table 8.1 summarizes the periods, runs and trigger settings used in the analysis presented here.

Beam info	Period	Basic MB trigger condition	Main MB trigger string†
Pb–Pb @ $\sqrt{s_{\mathrm{NN}}} = 2.76$ TeV	LHC10h	VOA and VOC	CMBACS2-B-NOPF-ALL
pp @ $\sqrt{s} = 2.76$ TeV	LHC11a	SPD or V0A or V0C	CINT1-B-NOPF-ALLNOTRD

Table 8.1: Overview of the data-sets used in this analysis. †: The actual meaning behind each of the words in the trigger string is rather technical and will not be described here - they are included for completeness. ALICE users may find up-to-date information on the string on internal ALICE web-pages [136].

8.1.2 Background Event Rejection

There are several sources of background events that may contaminate the analysis if not properly removed. One of these sources is known as *beam-gas* interactions. These interactions happen because the vacuum inside the LHC is not perfect. Even though the pressure is lower than in outer space, some atmospheric molecules are still present. Similarly, molecules from the inside of the beam-pipe may come loose from the violent forces present when *a bunch* of charged particles pass. The effect is that a very dilute gas of molecules is present in the beam-pipe, and sometimes a particle from one of the beams collides with a molecule from the gas. Many particles can be produced in these events, making them look like beam-beam collisions, although the kinematics are typically different. In addition, the produced particles may flow downstream along the beam

direction and disturb signals from beam-beam collisions. [113]

Over time, the beam structures dilute and prolong as the particles inside each bunch interacts. Some particles may escape the main bunch structure and follow the beam around in a halo. When two beams pass at an interaction point (IP), a particle from the main bunch of one beam may collide with a particle in the halo of the other beam. This type of interaction is called a *beam-halo* interaction and causes the same problems as beam-gas interactions. [113]

Despite the different origins of beam-gas and beam-halo interactions, their signatures a very similar. Consequently they are identified in the same way. Since the probability of the background interactions happening in the range considered for actual collisions is very small ($|v_z| < 10$ cm from nominal IP - 20 cm out of a 27 km circumference), the main contamination is from the downstream flow. This downstream flow can be removed by requiring a coincidence of e.g. the V0A and V0C triggers inside a very limited time window. This removes effects from particles traveling along the beam pipe. [113]

Another source of contamination comes from *pile-up*. Pile-up is when two or more collisions happen during a single bunch-crossing. The amount of pile-up depends heavily on the luminosity. The pile-up collisions are often slightly shifted in vertex position. Precision tracking thus allows for distinguishing between particles from different collisions, even though they happen at approximately the same instant. In Pb–Pb collisions, due to the large number of particles produced in a single collision, it is more difficult to distinguish the different vertices. Consequently, events with suspected pile-up are usually skipped in analyzes. For the Pb–Pb data analyzed here, the luminosities were low enough that no significant bias from pile-up is expected. The amount of pile-up can be roughly estimated by knowing the interaction rate, R, the number of interacting bunches, N_b, and the time it takes a beam to do one full turn around the accelerator, Δt:

$$P(\text{interaction}) = \frac{R}{N_b/\Delta t} = \frac{100 \text{ Hz}}{130/89100 \text{ ns}} \approx 6.5 \cdot 10^{-5}, \tag{8.1}$$

where the numbers are from the highest rate of Pb–Pb collisions obtained during 2010 in ALICE. Using Poisson statistics, the probability of one interaction is: $P(1) \approx 6.5 \cdot 10^{-5}$. The probability of two or more interactions is: $P(\geq 2) \approx 2.9 \cdot 10^{-9}$. This gives a pile-up contamination on the order of 0.003%. Since this was obtained using the highest rate of collisions in the data sample, it serves as an upper bound on the pile-up and shows that it is indeed negligible in this analysis.

8.1.3 Vertex Determination

The main vertex determination in ALICE is performed by the SPD, as described in Section 6.4. As the coverage of the FMD and SPD shifts with the z-coordinate of the vertex, v_z, it is important that the vertex is determined precisely. This is done by imposing a requirement that the error on the z-coordinate cannot be larger than 0.2 cm. To reduce contamination from beam-gas and beam-halo events a further requirement that $|v_z| < 10.0$ cm is imposed. The vertex distribution after the trigger selection for the events analyzed here is shown in Fig. 8.1. The vertex distribution follows a Gaussian distribution with a mean of 0.3 cm. To take into account the shifting coverage with v_z, this analysis is performed in 20 vertex bins of width 1 cm. From the figure it is seen that the total number of events analyzed here in a single vertex-bin is then at least 250000 and at most 780000.

The SPD is also capable of determining the x- and y-coordinates of the collision. This is shown in Fig. 8.2 where a shift in the y-direction of 0.18 cm away from the nominal $(0, 0)$-position is observed. This shift has an effect on the φ-distribution of the measured particles in the FMD and SPD (tracks are not affected by this). The shift causes the φ-distribution to follow a $\sin(\varphi)$-distribution and would be important in a measurement of v_1. For v_2 to v_4 as

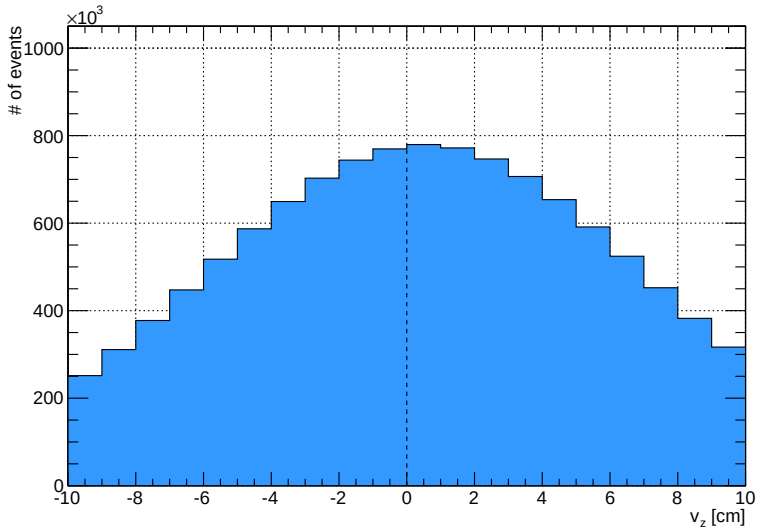

Figure 8.1: v_z-distribution from Pb–Pb collisions at $\sqrt{s_{\rm NN}} = 2.76$ TeV taken during the LHC10h period analyzed here.

measured here the effect is negligible. In addition, the MC samples used for the corrections also include the shift, thus removing any small effect it might contribute with to the flow analysis.

8.1.4 Centrality Estimation

To study the dependence of flow on the centrality (see Section 1.4), the events are divided into centrality bins. The VZERO detector is used to estimate the centrality. The resolution of all the ALICE centrality estimators is shown in Fig. 8.3, where the combined V0A and V0C amplitudes are found to have the best resolution [137]. The resolution is found through a weighted iterative procedure, where each estimator is compared to the (weighted) mean of all the estimators. For the most central events, the resolution is 0.5%. For the most peripheral the resolution is 2%. For a more detailed description of the method used to estimate the centrality resolution see Ref. [137]

The VZERO amplitudes for all the events is shown in Fig. 8.4a, in which a fit based on a Glauber model (Section 7.1) is also shown. For the fit, a Glauber model is used to estimate N_{part} and N_{coll} for a range of b. The particle production is parametrized by a negative binomial distribution, which is the multiplicity distribution observed in pp collisions over a wide range of energies. It is then assumed that soft interactions produce average multiplicities proportional to N_{part} and hard interactions produce multiplicities proportional to N_{coll}. This assumption is inspired by so-called two-component models [137].

The centrality distribution used for this analysis, after trigger and vertex cuts is shown in Fig. 8.4b. Vertical lines indicate the centrality binning chosen for the analysis. The distribution is found to be flat over the measured range, as it should be from the definition of centrality. While the V0 estimator is able to estimate the centrality out to 90%, events more peripheral than 80% are considered to be dominated by non-flow and biased from electromagnetic disassociation (EMD) events[1].

[1]EMD is when one nucleus absorbs a photon from the other nucleus and transitions into an excited state. It then decays and emits one or more nucleons. However, it is not a hadronic nuclear interaction.

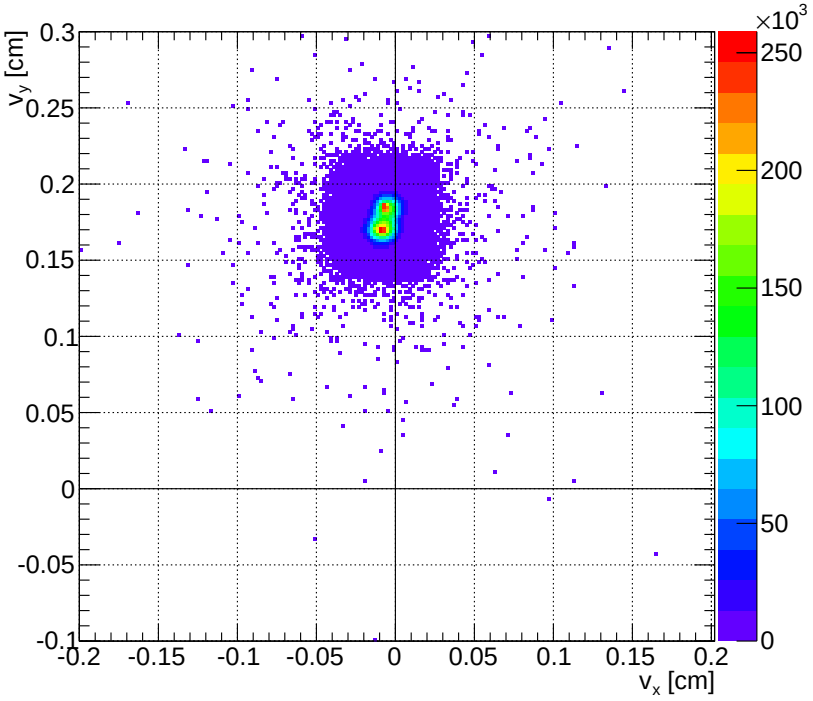

Figure 8.2: (v_x, v_y)-distribution from Pb–Pb collisions at $\sqrt{s_{\mathrm{NN}}} = 2.76$ TeV taken during the LHC10h period analyzed here. A shift away from the nominal $(0, 0)$ IP is observed.

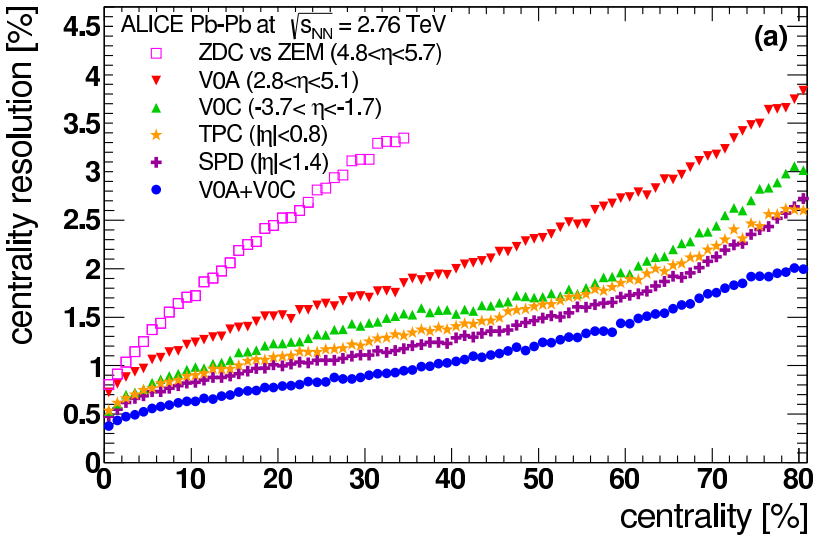

Figure 8.3: Resolution of the various centrality estimators in ALICE vs. centrality. The combined V0 estimator is found to be the most precise, with a resolution down to 0.5% for the most central events. [137]

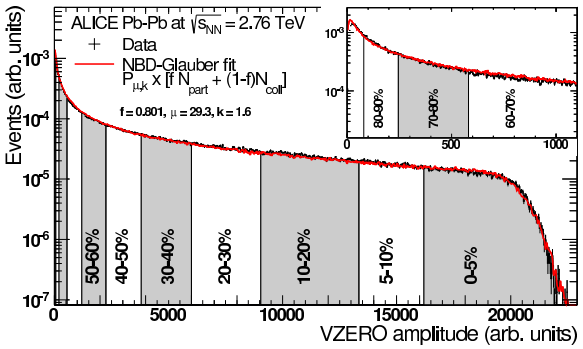

(a) Centrality slices of the summed V0 amplitudes fitted with a two-component Glauber model with negative binomial distributions. A good fit is found. [137]

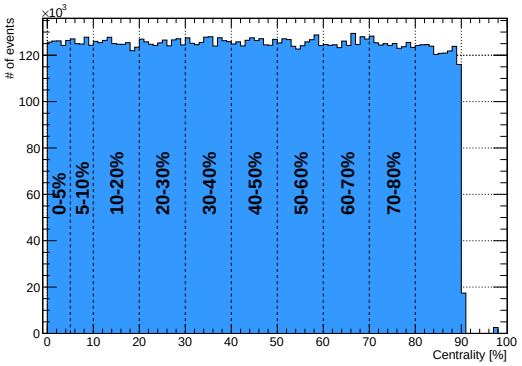

(b) Centrality distribution from Pb–Pb collisions at $\sqrt{s_{\mathrm{NN}}} = 2.76$ TeV with the ALICE V0 as the estimator. The centrality slices considered for this analysis are indicated with the vertical lines.

Figure 8.4

8.2 Detector Cuts

In this section, the cuts applied to the detector signals are presented and discussed. For the FMD, cuts on the energy distributions (see Section 6.2) are presented, as well as a special cut to remove 'bad' events, necessary to get statistically stable results for $v_n\{4\}$. For tracks, the cuts on the fitting parameters and kinematic variables are presented. For the VZERO, the gain matching discussed in Section 6.3 is applied. It should be noted that while results using hybrid tracks and the VZERO are not shown until Chapters 9 and 10, the cuts are still presented here.

8.2.1 FMD Energy Distribution Cuts

The algorithms described in Section 6.2 allow cuts to be made on the energy deposited in the FMD strips. For the sharing filter a low and a high cut are applied. A plot of the energy distributions is shown in Fig. 8.5. In the figure, the colored distributions clearly show a large noise peak at low values, a sharing region for $E_{loss} \lesssim 0.5$ and the convoluted Landau-Gauss function with two peaks visible.

The low cut for the sharing filter, E_{low}, is defined as a hard cut on the energy value, only depending on whether it is an inner or outer ring. This is done to cut away any remaining noise. Everything covered by the yellow region in Fig. 8.5 is removed by the low cut as energy deposits below the low cut are ignored and those channels are considered empty.

The high cut, E_{high} and the cut for the Poisson algorithm, E_{hit}, are set to be identical. The actual values are calculated to be the most probable value, E_{MPV}, minus the width of the Landau distribution, ξ. Both of these parameters are obtained from fits to the observed energy distributions, found during an initial pass over the data. These depend on system size and collision energy and also varies between real data and MC. The fits are done in η-bins with a width of 0.05 units in pseudorapidity, and consequently the cut values also vary by pseudorapidity. These cuts are shown as the light-blue region in Fig. 8.5. For each η-region the value is constant, but as each plot is for an entire ring there is a shift, which makes it appears as a narrow region rather than a specific cut in the figure.

Strips with energy deposits in between the two values (between the yellow and light-blue regions) are considered for merging, while energy deposits above the high cut count as particles and are not merged.

After merging, the high cut is also used for when the Poisson method is applied, defining when a channel is to be considered empty or non-empty for the final N_{ch} estimate. The values of the cuts were checked against MC studies, and are chosen such that the measured multiplicity densities agree best with the input values in the MC. These cuts are shared among all FMD analyzes. The values are given in Table 8.2. In Fig. 8.5, the slightly darker colored regions show the energy loss distributions after the sharing algorithm, and it is clear that many of the signals in the sharing region are merged.

Ring	Sharing E_{low}	Sharing E_{high}	Poisson E_{hit}
FMD1i	0.15	$E_{MPV} - \xi$	$E_{MPV} - \xi$
FMD2i	0.15	$E_{MPV} - \xi$	$E_{MPV} - \xi$
FMD2o	0.18	$E_{MPV} - \xi$	$E_{MPV} - \xi$
FMD3i	0.15	$E_{MPV} - \xi$	$E_{MPV} - \xi$
FMD3o	0.18	$E_{MPV} - \xi$	$E_{MPV} - \xi$

Table 8.2: Cut values for the FMD energy loss.

For the Poisson calculations it is necessary to choose regions in which to calculate the occupancy of Eq. (6.3). Since this analysis is concerning azimuthal anisotropies, the maximum resolutions in φ is desirable. Consequently, only channels within a given sector (see Section 5.3) is considered in the same region. I.e. the φ-width of the region chosen is the same as the φ-resolution of the FMD. This leaves the choice of how many consecutive strips to include, which determines the regions' η-range. From Fig. 6.3 it is seen that with 256 channels, the Poisson parameter deviates less than 0.5% for occupancies smaller than 90% and at most deviates with 4%. Combining more than 256 channels improves the determination of the parameter but is not possible while retaining the requirement of only using a single sector, as the outer rings only contain 256 strips per sector. Using less than 256 channels increases bias in high occupancy events. Therefore, a choice was made to use regions of a single sector and 256 strips for the calculation of N_{ch}. The observed occupancies are shown in Fig. 8.6. In the figure, it is seen that only FMD3 inner has occupancies in the region where the approximation of using just 256 channels has an uncertainty higher than 1%. However, these events are very rare, so no significant bias arises from this choice of region.

As mentioned above, the FMD cuts were found by studying multiplicity densities. To verify that the cuts are also applicable in flow analysis, the measured v_n values in the simulated detector response are compared to the measured v_n values of the track references (see Section 7.5.1). A good agreement is observed for all centralities, see Fig. 8.7 for a representative centrality. More plots are available in Appendix C.1.

8.2.2 Flow Specific Cuts

The four-particle cumulant is sensitive to many-particle correlations. If a many-particle correlation effect comes from a collective phenomenon $c_n\{4\}$ in Eq. (3.26) is negative and $v_n\{4\}$ yields a real number. Non-collective effects generally contribute to $c_n\{4\}$ with positive contributions, potentially making it positive and $v_n\{4\}$ imaginary. However, some non-collective effects do give negative contributions, e.g. fake-flow induced by large multiplicity fluctuations.

$$v_n\{4\} = \sqrt[4]{-c_n\{4\}}. \tag{3.26}$$

Sometimes, in the FMD, a 'hot spot' appears - see inset in Fig. 8.8. If even a few per mil of the events contain a 'hot spot', it is enough to make $c_n\{4\}$ positive, since they have very large multiplicities compared to the rest of the event. As M^4 is included in the event weight, a single

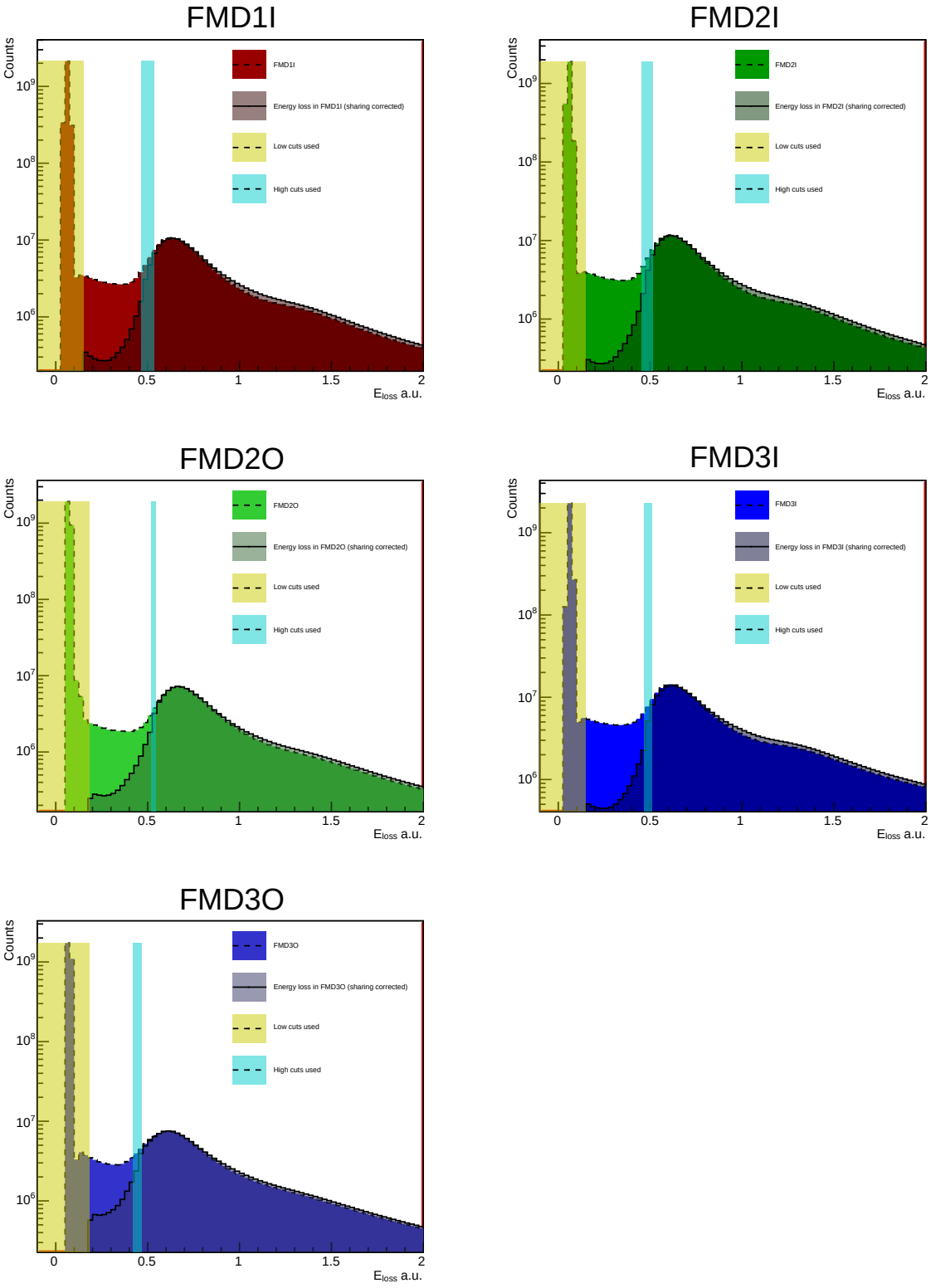

Figure 8.5: Energy loss distributions before and after sharing for each FMD ring. Yellow and light-blue regions show cuts applied. See text for further details. Data is from a single Pb–Pb run at $\sqrt{s_{\mathrm{NN}}} = 2.76$.

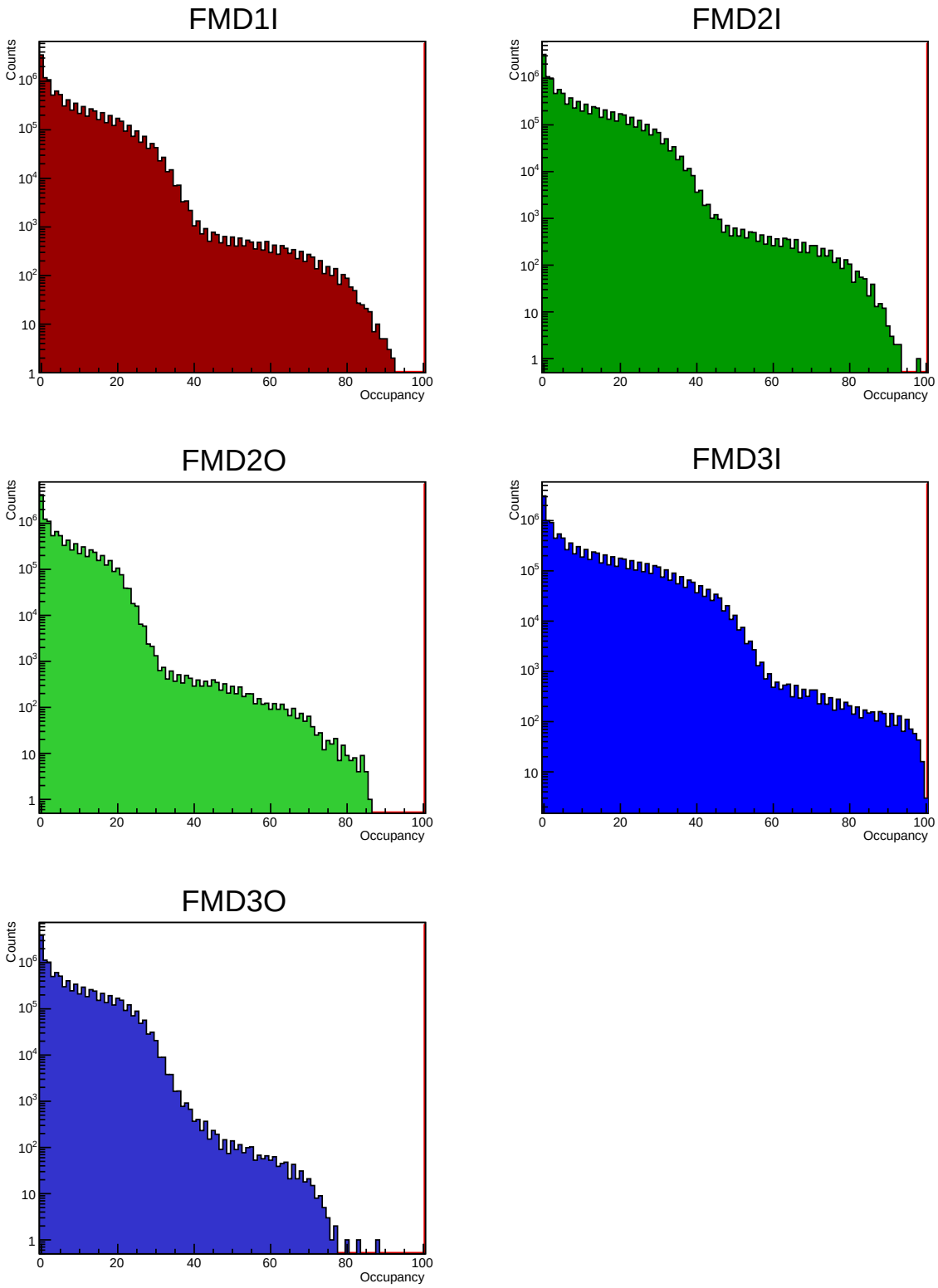

Figure 8.6: Occupancies for each FMD ring in the regions chosen to be considered in the Poisson calculations. For this analysis regions of a single sector and 256 strips are chosen. Data is from a single Pb–Pb run at $\sqrt{s_{\mathrm{NN}}} = 2.76$.

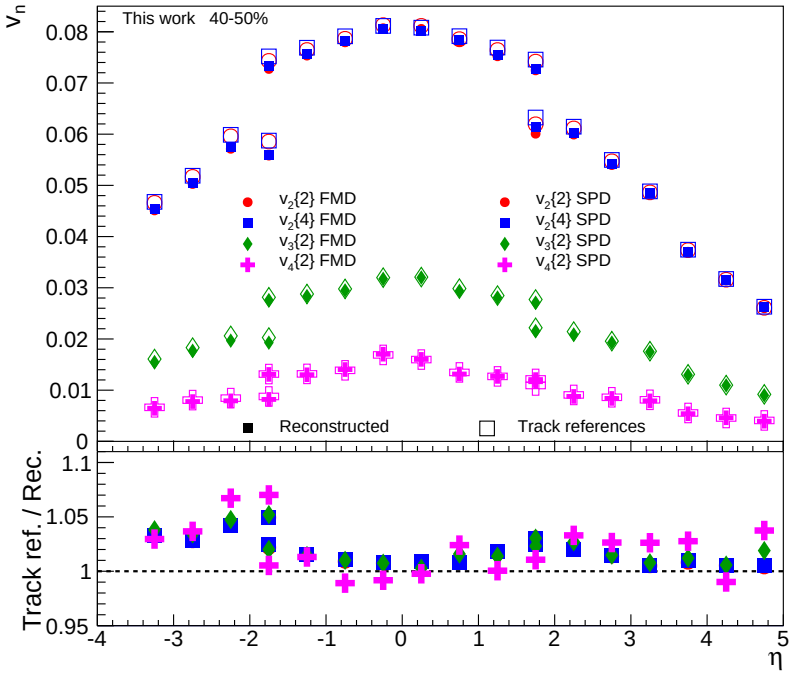

Figure 8.7: Comparison between simulated detector response with cuts applied and using track reference information from the MC generator. The event generator is AliGenTunedOnPbPb with GEANT3 transport code and 40–50% central events. A good agreement is observed.

of these events may count as much as thousands of regular events. Including just a few of such events can completely change $c_n\{4\}$, making $v_n\{4\}$ imaginary (*statistically unstable*).

It is of course important to know what causes the 'hot spots'. Several possible sources were considered: single-event upsets[2], corrupted read-out or data-files, or if the events were read out too close to each other. In the end, the appearance of a 'hot spot' did not seem to be correlated to any of these. It was, however, found that the 'hot spots' also appear in MC simulations. This made it possible to study other sources, as all information about tracks and particles is available in MC data. To do this, an AMPT simulation was used. It turned out that in all events where a 'hot spot' was observed, a slow moving particle (mostly an electron) was scattering (or even stopping) on the FMD. Figure 8.8 shows an example of such an event. Here, a slow moving electron is highlighted in red among the other particles hitting the FMD (green lines). There is a kink in the electrons trajectory as it hits FMD2, and a large signal is observed in the same region of FMD2. While almost all the events investigated had an easily identifiable slow moving particle hitting the detector in the region where the 'hot spot' was observed, it is still a random process; a slow moving particle can hit the FMD and not make a 'hot spot'. Examples of a few more events is shown in Appendix C.2. As the events appear to be unrelated to the underlying physics, it is safe to remove them.

To identify the events with a 'hot spot', the following algorithm is applied for each η-bin in the 2-dimensional (η, φ)-histogram:

1. Calculate the mean multiplicity, $\langle M \rangle$ (loop over φ).

2. Calculate the width of the multiplicity distribution (in the φ-bins), σ.

[2] A single-event upset is when ionizing radiation interferes with detector electronics.

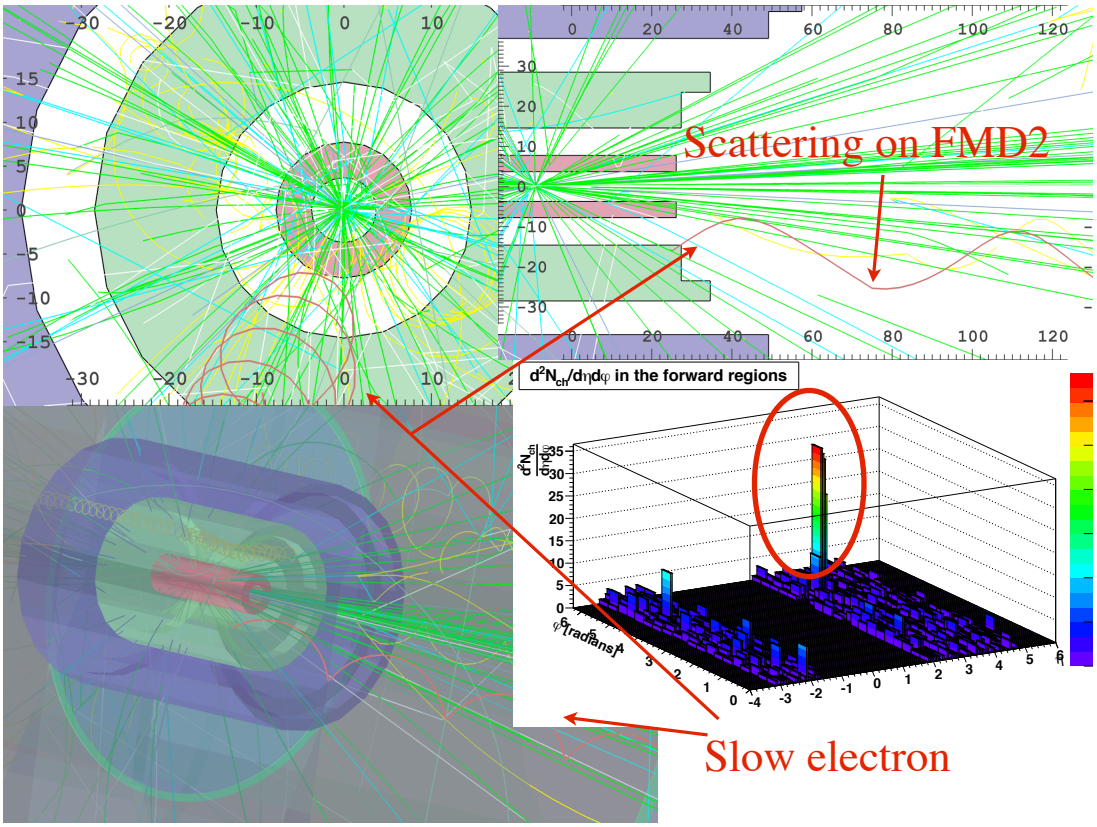

Figure 8.8: Several views of an event where a large signal in the FMD is caused by a single slow moving electron. The bottom right corner shows a very large signal confined to a few strips of the FMD. Looking at event-displays, it is possible to identify the particle responsible for the signal as being a slow electron. In the top right plot a small kink in the electron trajectory is seen where it impinges on FMD2 and produces the signal.

3. If $\frac{M_{max}}{\langle M \rangle} \geq \alpha_c \sigma$, where M_{max} is the maximum multiplicity in a single φ-bin and α_c is some cut value, it is counted as a single *bad* η *bin*.

4. In a loop over the η-bins, if there are four consecutive bad η-bins: *Do not use the event.*

This cut algorithm is very efficient for the 0–60% most central events. For more peripheral ones the 'hot spots' do not seem to be as easy to distinguish from regular fluctuations, and the four-particle cumulant results are not stable for the more peripheral events. Finding the value of α_c is a matter of optimization: making the value too small will cut away a large number of events, while making it too high simply will not fix the problem. Figure 8.9 shows the $v_2\{4\}$ calculation efficiency and event selection efficiency for different values of α_c. The chosen value is $\alpha_c = 4.0$, as the cumulant efficiency seems to stabilize at that point, while the event selection efficiency starts to go down by quite a lot. The chosen value cuts away 0.41% of the events. Applying the same cut to $v_2\{2\}$ does not yield any significant changes to the results, so no extra bias seems to be introduced by this cut. The cut is applied to both data and simulations, so any small bias is corrected with the MC correction (see below).

8.2.3 SPD Cluster Selection

The SPD data in the ESD files is divided into tracklets and unused clusters, i.e. clusters that have fired, but not been associated with a tracklet. For this analysis both the tracklets and the

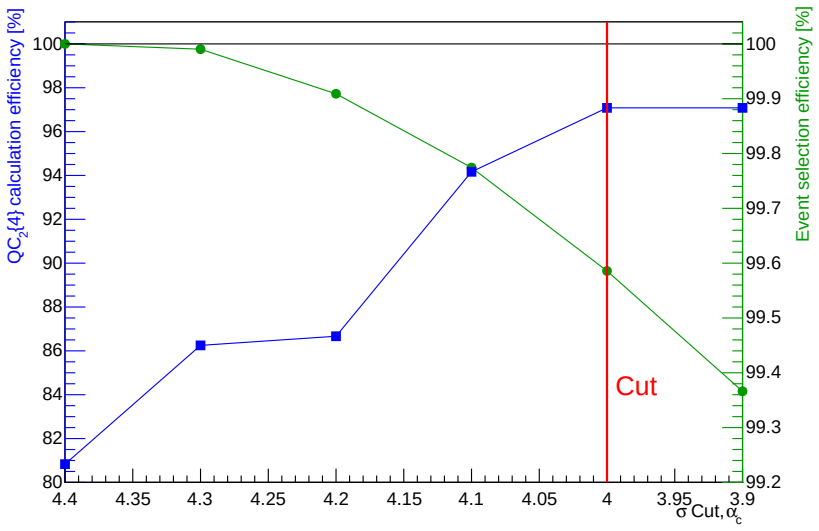

Figure 8.9: Search for a value, α_c, at which to cut away events in the FMD to make the four-particle cumulant stable. Real data is used in these estimates.

unused clusters from the inner layer of the SPD are used equally. The clusters and tracklets are all put into a 2-dimensional (η, φ)-histogram, similar to the one used for the FMD data. This ensures that the analysis of the SPD data is as similar to that of the FMD data as possible. During the recording of the data analyzed here, parts of the SPD were turned off due to cooling issues. Consequently, the SPD has rather large gaps in its azimuthal acceptance, this issue is discussed further in Section 8.4.

8.2.4 Track Cuts

The tracking in ALICE is described in Section 6.6. When the tracks are stored, not only kinematic information such as η or p_{T} is stored, but some of the quality parameters of the fits used to find the tracks are also available. This makes it possible to apply cuts to get a set of high quality tracks to use for physics analysis. Some of the important quality parameters that can be cut on are:

Number of clusters: Typically specified to e.g. number of TPC clusters or ITS clusters, this number contains information on how many clusters have been used to find the track. A large number of clusters signifies that the particle has been tracked in a large part of the detector, which in principle makes the tracking information more precise.

χ^2 per cluster: This number is simply the χ^2 of the fit divided by the number of clusters. A low χ^2 generally means a better fit.

Distance of closest approach (DCA): DCA is how close the track is to the primary vertex of the collision, when extrapolated inwards to the IP. This is usually done either in the z-direction or as a 2D cut in the (x, y)-plane.

Furthermore, it is possible to remove tracks that appear to originate from weak decays by looking for a kink on the track, due to e.g. a kaon decaying to a muon and a neutrino. It is also possible to refit tracks from a single detector (e.g. the TPC) with the primary vertex or constrain them to tracks found with other detectors.

In this thesis, two types of tracks are considered: TPC-only tracks and hybrid tracks (see Section 6.6 for descriptions). The cuts for these two classes of tracks are determined centrally in

Cut parameter	*TPC-only*	*Hybrid tracks*	
p_{T}	0.2–5.0 GeV/c	0.2–5.0 GeV/c	
η	$\lvert\eta\rvert < 0.8$	$\lvert\eta\rvert < 0.8$	
Min. # of TPC clusters	70	Max(70,70 + 1.5 · p_{T})†	
Max. χ^2 per TPC cluster	4	4	
Max. DCA in z-direction	3.2 cm	3.2 cm	
Max. DCA in (x, y)-plane	2.4 cm	2.4 cm	
Max. fraction of shared TPC clusers	N/A	0.4	
Remove decays	yes	yes	
Use only TPC clusters	yes	yes	
Refit to primary vertex	no	yes	
Track combinations	N/A	*Global*	*TPC-only*
Refit to include ITS	no	yes	no
Max. χ^2 per ITS cluster	N/A	36	N/A
Max. χ^2 for TPC constrained to global tracks	N/A	36	N/A
# of SPD clusters required:	N/A	any	N/A

Table 8.3: Comparison of track cuts between TPC-only and hybrid tracks. Since hybrid tracks are a combination of two different selections, the bottom part is split between the global tracks and TPC-only tracks. †: The cut is the highest number of the two inside the function.

ALICE by a dedicated working group and are summarized below. The track cuts may change with period or year due to changes in the detector settings. The track cuts for TPC-only tracks and hybrid tracks are shown and compared in Table 8.3. Most of the cut values used here are the standard cuts, but the p_{T} cuts applied here are slightly more narrow. This is done to avoid contamination from jets and other hard processes.

The hybrid tracks are used as a systematic check (see Section 9.1). Two slightly different track selections are made for the hybrid tracks: one on global tracks and another on TPC-only tracks refitted to the primary vertex. This effectively means that in the areas where the ITS has full azimuthal coverage, the extra information from the ITS is used in the tracking. Whereas in the regions with non-uniform acceptance in the ITS, the standard TPC tracks refitted to the primary vertex is utilized. This ensures full azimuthal acceptance among the hybrid tracks.

In this analysis, tracks are only used for the reference flow measurement.

Extra Cuts for the SPD Cluster Analysis

For the differential flow estimated using SPD clusters, there is an extra cut on the η-coordinate of the tracks used for the reference flow, in order to avoid auto-correlations between clusters and tracks, as it cannot be done in the usual way of the Q-cumulants.

SPD cluster region	Track cut
$\eta < 0$	$\eta > 0$
$\eta > 0$	$\eta < 0$

8.2.5 VZERO Amplitudes

The gains on the VZERO channels are individually set. This means that the same ADC count in two different channels does not correspond to the same number of charged-particle hits. In order to utilize the VZERO information in flow analysis it is necessary for the ADC values to be comparable across channels. To facilitate this, each channel is given an equalization factor.

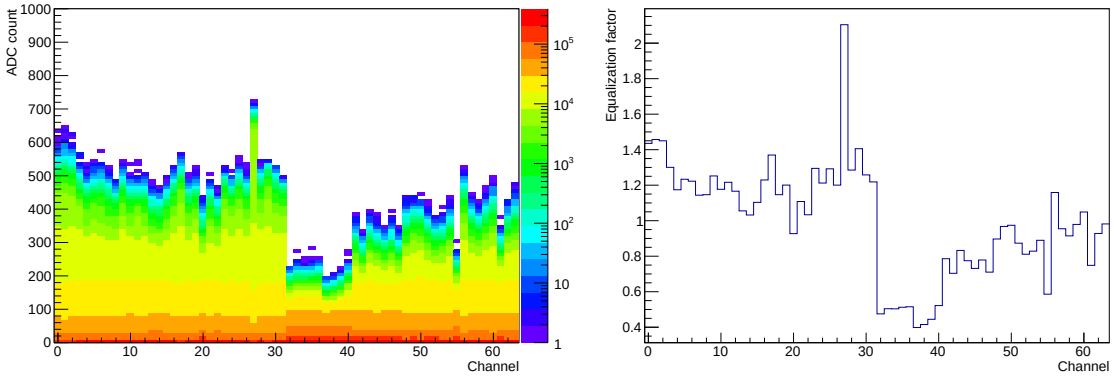

(a) Un-equalized ADC values for each channel in the VZERO for a single run. The color-scale is given in arbitrary units.

(b) Equalization factors for each channel in the VZERO for a single run.

Figure 8.10: Un-equalized signals in the VZERO.

First the raw ADC counts for each channel are plotted, as in Fig. 8.10a. From this, the mean ADC value of all the channels, ADC_{MEAN}, is calculated. Then the average ADC values for each of the 64 channels, $ADC_{mean,i}$ (with i being the channel number), are calculated. From these numbers the equalization factors, $f_{eq,i}$, are calculated as:

$$f_{eq,i} = ADC_{mean,i}/ADC_{\mathrm{MEAN}}. \tag{8.2}$$

The equalization factors are shown in Fig. 8.10b. When using the VZERO information for flow analysis the ADC value of each channel is divided by the corresponding equalization factor for that channel. The result is shown in Fig. 8.11. In general the equalization factors may be run-dependent. However, for this analysis only the set of equalization factors shown in Fig. 8.10b are used. They are from a single run in the LHC10h period. It is shown in Section 8.9 that the VZERO measurements are very consistent for all the analyzed runs, which strongly suggests that it is not causing a significant bias to only apply one set of equalization factors for the entire LHC10h period.

8.3 Statistical Uncertainties

An unresolved issue with the Q-cumulant analysis, which was not discussed in Chapter 3 is that of statistical errors. In Appendix C in Ref. [58] analytical derivations of the statistical errors on the differential measurements of $v_n\{2\}$ and $v_n\{4\}$ are presented. It is, however, under the assumption of perfect azimuthal acceptance. It is shown that the equation to calculate the statistical uncertainty of:

$$v_n'\{4\} = \frac{2\cdot\langle 2\rangle\langle 2'\rangle - \langle 4'\rangle}{[2\cdot\langle 2\rangle - \langle 4\rangle]^{3/4}}, \tag{8.3}$$

contains more than 30 different terms. Consequently, deriving the analytical equations in the case of a NUA - where the equations for $v_n\{2\}$ and $v_n\{4\}$ are already quite complex - is not feasible. The approach used here to estimate the statistical uncertainties is to divide the data-sample into sub-samples, i, and do a weighted average depending on the number of events, $N_{evts,i}$, in each sub-sample:

$$\bar{v}_n = \frac{\sum_i (v_{n,i} N_{evts,i})}{\sum_i N_{evts,i}}. \tag{8.4}$$

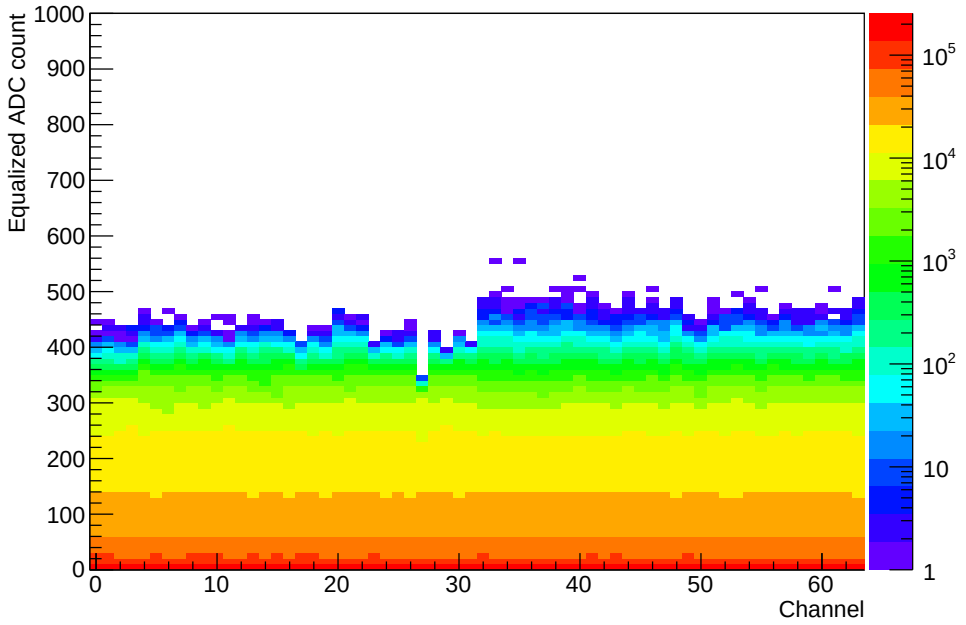

Figure 8.11: Equalized ADC values for each channel in the VZERO for a single run. The color-scale is given in arbitrary units.

The statistical uncertainty is then found as the spread of the sub-samples around $\bar{v}_n$. In Fig. 8.12 a toy model with perfect azimuthal acceptance compares the statistical uncertainties of $v_n\{2\}$ and $v_n\{4\}$ between using the analytically derived equations and simply measuring the spread of v_n from 20 sub-samples. While there are small discrepancies between the two methods, in general they are consistent in the estimate of statistical uncertainties.

The division into sub-samples comes naturally in this analysis. As mentioned in Section 8.1.3, the coverage of the detectors shifts with vertex, and, as is shown in Section 8.4, the acceptance is not uniform in either FMD or SPD. Consequently, in order for the non-uniform acceptance (NUA) corrections derived in Chapter 3 to work as intended, the analysis is done in 20 vertex bins, each with a width of 1 cm to keep the acceptance constant. The mean $\bar{v}_n$ of the vertex bins is then found using Eq. (8.4), and the statistical error is the spread of the individual vertex bin measurements around this mean.

8.4 Acceptance

While both the SPD and FMD were designed will full azimuthal coverage in mind, in reality both suffer from a few gaps, as can be seen in Fig. 8.13. For the FMD, a chip is no longer working in FMD1. In FMD2i a chip is masked out as its signal is getting closer and closer to the pedestal noise. In addition, a few single channels are no longer working, but those are far enough apart not to be clearly visible in the figure. For the 2010 and 2011 data-taking periods, the SPD suffered from having some of its cooling pipes blocked by deposits in inaccessible regions. The issue is now fixed by a complex procedure involving inserting drilling rods in the pipes. For the data analyzed here, several sections were turned off due to not being cooled down, and thus risking overheating if turned on. Figures similar to Fig. 8.13 in 2 cm v_z ranges from -10 cm to $+10$ cm are shown in Appendix C.3, where the shift in coverage with v_z is clearly visible.

When Eqs. (3.97) and (3.126) are applied to $v_n\{2\}$ and $v_n\{4\}$ respectively (in vertex-bins of

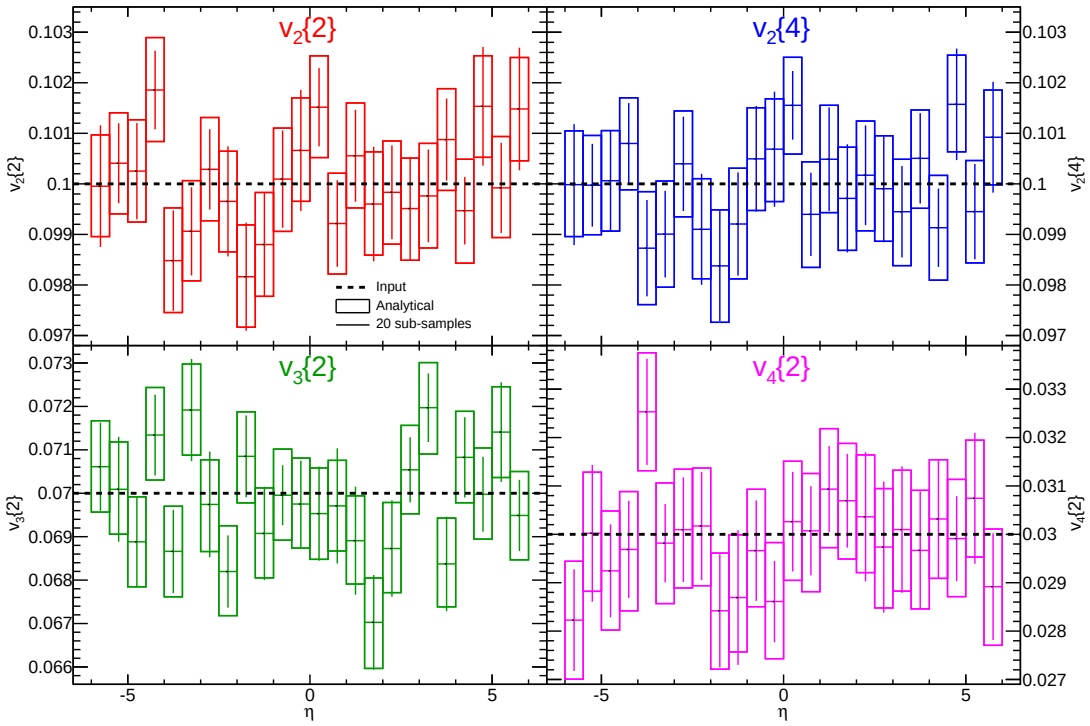

Figure 8.12: A comparison between the analytical equations for statistical uncertainties (boxes) and a method where the data is divided into 20 samples and the error is estimated from the spread of these (lines). Input values are given by the dotted lines ($v_2 = 0.10$, $v_3 = 0.07$ and $v_4 = 0.03$). The two approaches to estimating the statistical uncertainties approximately agree.

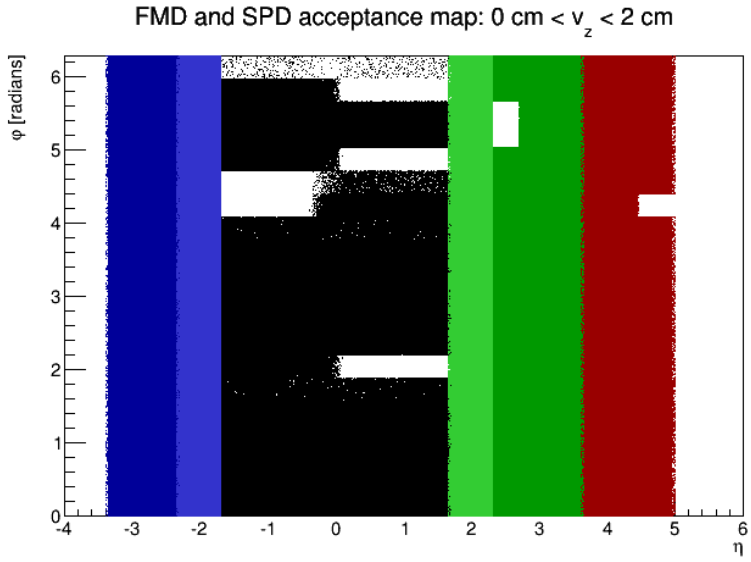

Figure 8.13: (η, φ)-coverage of the FMD and SPD for vertices in the range 0 cm $< v_z <$ 2 cm. Blue colors are FMD3 inner and outer, black is SPD, green are FMD2 inner and outer, and red is FMD1. For more vertex ranges see Appendix C.3.

1 cm) all effects from the NUA are removed and no acceptance-related issues are observed in the final results.

8.5 Secondary Particles in ALICE

This analysis utilizes several detectors that are not capable of tracking particles. In particular, the FMD and the VZERO cannot track particles since they are single layer detectors, and there are no other detectors in ALICE with similar coverage that can do tracking. For the SPD it is possible to use tracklets because of its two layers of silicon. However, in order to get a wide enough η-coverage to match up with the FMD or VZERO, only the inner layer provides enough coverage, which also removes the tracking options when using the SPD. Consequently, all of the detectors used for the differential flow analysis rely on measurements of charged-particle hits. This means that it is not possible to find the origin of the particles detected and thus it is not possible to distinguish secondary particles, created from particle interactions with material or decays, from the primary particles of interest for the flow analysis.

While the most central region of ALICE is designed with a low material density, many of the cooling and support structures for the central detectors are placed in front of the FMD and VZERO. This has the consequence that both detectors are hit by a large number of secondary particles. In Fig. 8.14 a MC generator with GEANT3 as the transport code has been used to estimate the origins of the secondary particles hitting the FMD. In the figure it is seen that the six ITS layers and corresponding support structures are relatively big contributors. Similarly, the beam-pipe and support structures on the beam-pipe are responsible for a large fraction of the secondary particles hitting the FMD.

It should be noted that Fig. 8.14 does not contain any information on how many secondary particles hit the detector. Figure 8.15 on the other hand shows the multiplicity-densities of charged particles hitting the FMD and SPD in a HIJING simulation with GEANT3 as transport code. The figures shows the 0–5% most central events, but the scale is actually not important. What is important is the relative contributions to the number of observed charged particles. The gray distribution shows the primary charged particles. The other distributions are all secondary particles with various origins. Once again the ITS and the beam-pipe are observed to be the main contributors. At the maximum, there are twice as many secondary particles hitting the FMD, as there are primary particles. For the SPD the situations is less serious, with generally less than 10% of the particles not originating directly from the primary vertex.

For multiplicity analyzes, Fig. 8.15 gives direct information on how the secondary particles are going to affect the measurement. For flow analysis the answer is not as straight forward. If the secondary particles keep the direction of the original (mother) particle, the underlying v_n signal does not change. This means that multi-particle measurements would be completely unaffected by the secondary particles. Two-particle techniques would be sensitive to the non-flow of the secondary particles, as they are sometimes created in pairs. Similarly, the increased multiplicity would rescale the non-flow contribution accordingly. Once again a MC simulation using GEANT3 as transport code is used to estimate what the effects really looks like. The result is shown in Fig. 8.16 for the FMD, where the difference in azimuthal angle of a particle, $\Delta\varphi$ is defined as:

$$\Delta\varphi = \varphi_{hit} - \varphi_{mother}, \tag{8.5}$$

where φ_{hit} is the azimuthal angle where the particle hit the detector and φ_{mother} is the azimuthal angle of the original, primary particle produced in the collision. The distribution is well fitted by a sum of two Lorentzian functions[3] and a constant. The most narrow Lorentzian contains 70.2% of the particles. The second, wider Lorentzian accounts for 25.8% of the particles. Such

[3] A function of the form $f(x) = N/(1 + (x\sigma)^2)$ where N is a normalization factor and σ is a width.

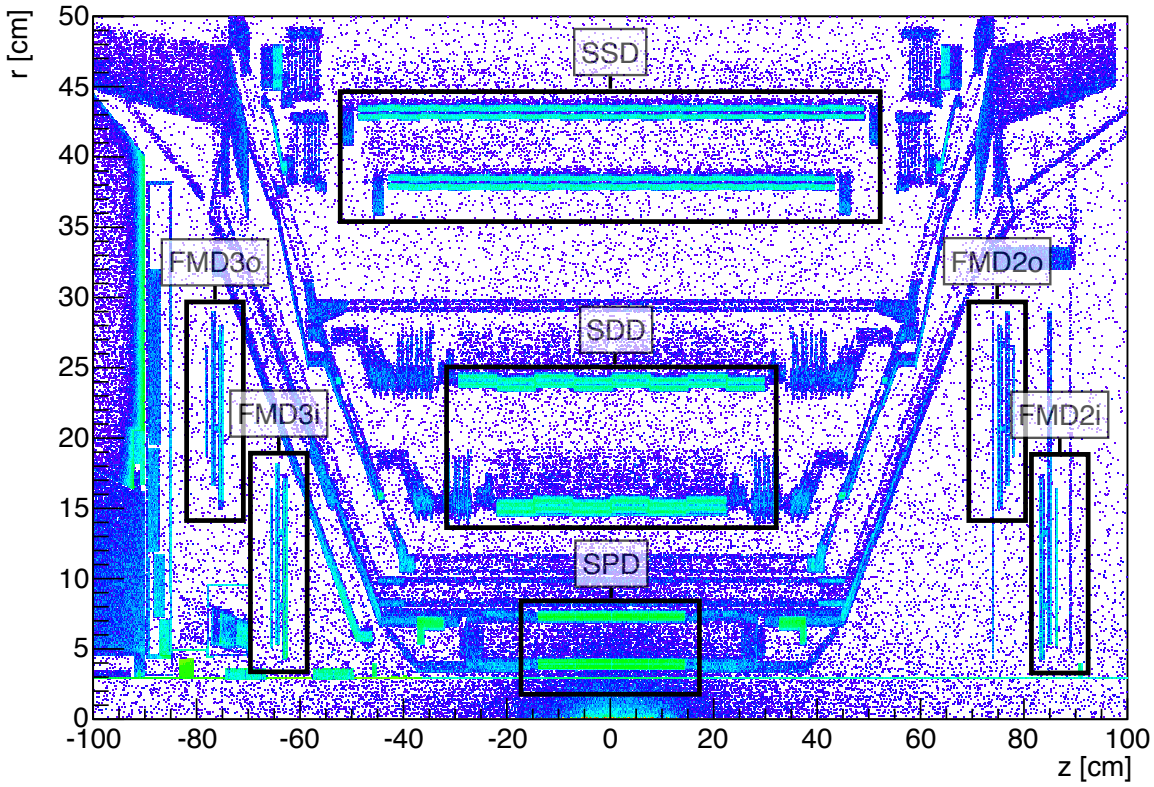

Figure 8.14: Origins of secondary particles hitting FMD2 and FMD3. The six ITS layers at $r = 3.9$, 7.6, 15.0, 23.9, 38.0 and 43.0 cm are clearly visible. The support structure of the ITS is also seen to be a big contributor as well as the beam-pipe and related structures at $r = 3.0$ cm.

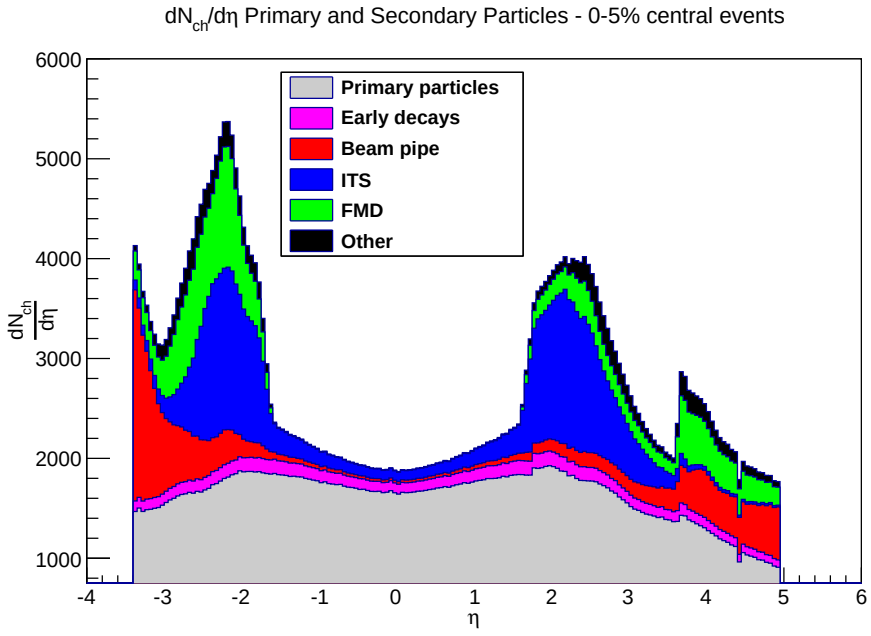

Figure 8.15: Multiplicity densities of charged particles hitting the SPD and FMD in a HIJING simulation with GEANT3 as transport code for 0–5% central events. In some regions there are twice as many secondary charged particles hitting the FMD, as there are primary.

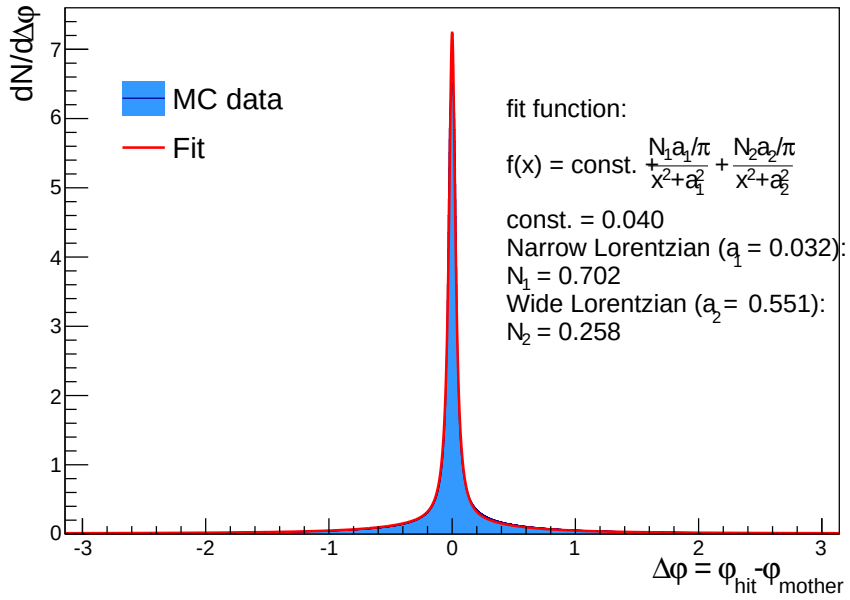

Figure 8.16: Difference in azimuthal angle of where particles are detected on the FMD, compared to the φ-angle of the original mother particle. Simulated using HIJING with GEANT3 as transport code.

a large spread has a direct impact on the observed flow values, with higher harmonics being increasingly sensitive to this kind of 'blurring' of the distribution. Finally, the azimuthal angle of the last 4.0% of the particles hitting the FMD contains no remaining correlation with the original primary particle. That kind of background affects all harmonics equally.

Before looking into a full detector simulation with a model containing flow. A toy model is set up to study what happens with a flow signal with v_1 to v_9 all equal to 0.05, when a smearing of the φ-coordinate according to the distribution in Fig. 8.16 is added to the flow signal. The result is shown in Fig. 8.17, where the signal is increasingly suppressed for higher harmonics. It can be shown that the reduction in the signal for v_n is related of the Fourier coefficients of the smearing function, $f(\varphi)$ [138]:

$$\frac{v_n^{obs}}{v_n^{true}} = \sqrt{\left(\int_{-\pi}^{\pi} f(\varphi)\cos(n\varphi)d\varphi\right)^2 + \left(\int_{-\pi}^{\pi} f(\varphi)\sin(n\varphi)d\varphi\right)^2}. \tag{8.6}$$

This calculation is shown as the black line in Fig. 8.17. The conclusion is that in order to perform a flow measurement on the FMD data, it is necessary to apply a direct MC-driven correction in order to remove effects from secondary particles. This correction is discussed further in Section 8.7, but as the secondary particles also contain non-flow-like correlations, which will *enhance* the signal for two-particle measurements and needs to be removed before applying the correction for the suppression, the non-flow correction is discussed first. Similarly, the VZERO is also affected by the secondary particles, as it is placed near the FMD.

8.6 Non-Flow Estimation

In Section 2.4 the various sources of non-flow contributing to the two-particle-measurements were discussed. Above it was shown that, additionally, a large number of secondary particles affect the signal and that these contain non-flow. Thus, it is necessary to apply a non-flow

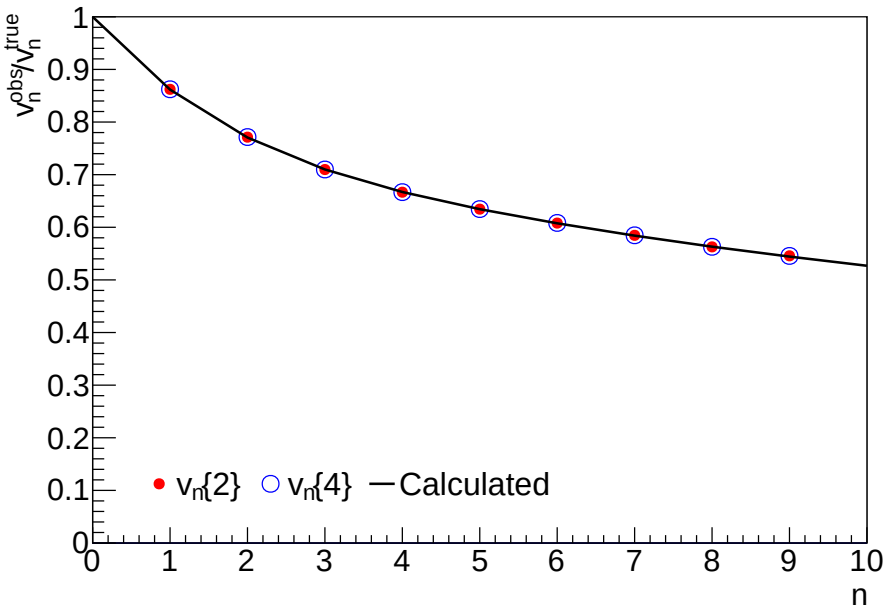

Figure 8.17: Toy model estimating the effect of φ-scattering on different harmonics, using the distribution in Fig. 8.16 as the smearing function. The reduction can also be calculated directly using Eq. (8.6). The signal is found to be increasingly suppressed in higher harmonics.

correction to the measurements to remove the standard non-flow as well as the non-flow in the secondary particles. In addition, the reconstructed signals of the MC used for the secondary particle correction contains the same non-flow bias as the real data and therefore also needs to be non-flow corrected. The ordering of the MC correction and the non-flow correction is important; first the non-flow correction is applied to data and MC and then the MC correction is applied to the data.

The non-flow correction can be either based on a HIJING simulation or by using the measurements from pp collisions at the same energy, both of which are assumed to only contain non-flow correlations. The non-flow corrections can be rescaled according to the multiplicity dependence found in Section 3.4.5, which is necessary when using pp collisions:

$$c_n\{2\}^{nf\text{-}corr} = c_n\{2\}^{obs} - \frac{M^{nf}}{M^{obs}}\delta_n, \tag{8.7}$$

$$d_n\{2\}^{nf\text{-}corr} = d_n\{2\}^{obs} - \frac{M^{nf}}{M^{obs}}\delta'_n, \tag{8.8}$$

where superscript *nf-corr* implies the *non-flow corrected* measurement, superscript *obs* is the observed signal in either data or a MC model containing flow and δ_n and δ'_n are non-flow corrections derived from either HIJING or pp collisions. In the case of the rapidity-gap method using three correlators (see Section 3.4.3), there are two different $d_n\{2\}$ terms and each is corrected for non-flow separately, if the gap is not large enough to remove all the non-flow correlations.

Since some of the non-flow observed is coming from secondary particles, the non-flow correction depends on what material is in front of the detector. Consequently, the corrections to the differential measurements have a vertex dependence, see Fig. 8.18 for an example of the correction to δ'_2 in the 70–80% central events according to HIJING. The vertex dependence is clearly observed. The reference flow is taken over an entire detector, in which case the effect

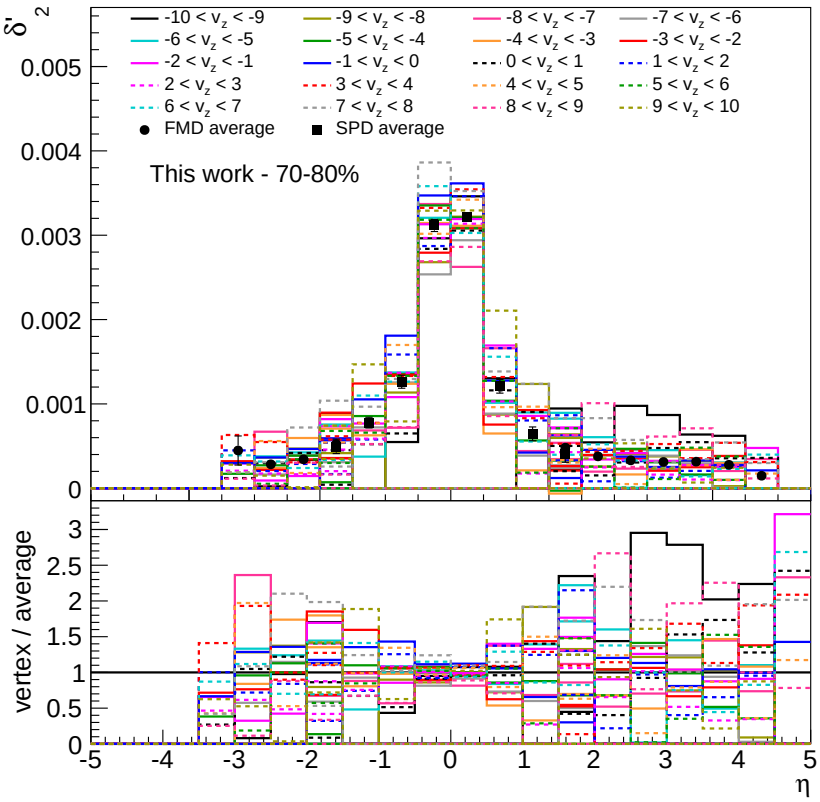

Figure 8.18: Non-flow correction to $v_2\{2\}$ per vertex for the 70–80% central events for the FMD and SPD, obtained from HIJING. The vertex dependence is seen as the systematic variation of the distributions. Statistical errors are not shown due to readability, but they are smaller than the vertex variations. The bottom plot is a ratio to the corrections averaged over all vertices. It is seen that the non-flow changes significantly with vertex (more than a factor of 2).

of shifting material is negligible and the non-flow correction is averaged over all vertices. The non-flow correction for the reference flow is seen in Fig. 8.19a for the TPC-only tracks. The vertex average of the differential non-flow correction to $v_2\{2\}$ is shown in Fig. 8.19b. The differential non-flow corrections to $v_3\{2\}$ and $v_4\{2\}$ are shown in Appendix C.4 and are very similar in shape to the correction for $v_2\{2\}$. Since most of the non-flow from secondary particles is removed due to using the tracks for the reference flow, this is very similar to the non-flow distribution of the primary particles in HIJING, except for a multiplicity scaling. The reason for using rapidity-gaps in many analyzes to remove non-flow is also apparent from the figure. The non-flow contributions fall off quickly away from mid-rapidity, which corresponds to an increase in η-separation between the reference particles (from TPC) and the particles of interest (in SPD or FMD).

8.7 Monte Carlo Correction

For this analysis an effective MC-based correction derived from a simulation containing flow is applied to the data, such that:

$$v'^{corr}_n = \frac{v'^{MC,prim}_n}{v'^{MC,obs}_n} v'^{data,obs}_n \tag{8.9}$$

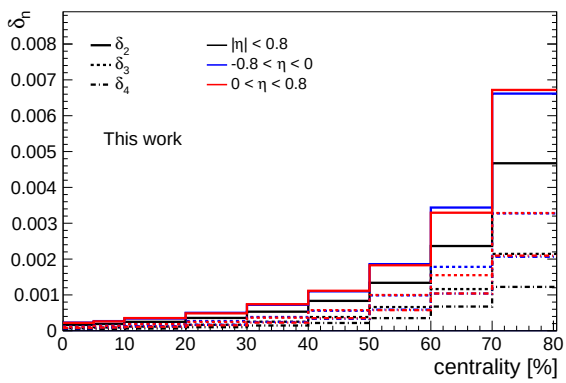

(a) Non-flow correction to reference flow for $v_n\{2\}$ to the TPC-only tracks obtained from HIJING.

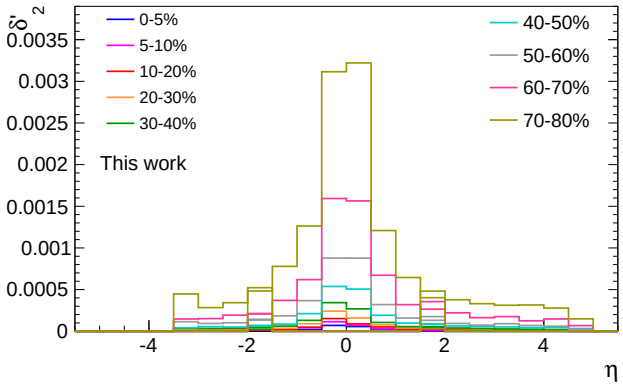

(b) Non-flow correction to differential flow for $v_2\{2\}$ in the FMD and SPD obtained from HIJING.

Figure 8.19: Centrality dependence of non-flow corrections obtained from HIJING. Statistical errors are not shown due to readability.

where $v'^{MC,prim}_n$ is the result of the flow analysis on primary tracks from the primary particles in a simulation, $v'^{MC,obs}_n$ is the results from the full detector simulation and response in the same MC, finally $v'^{data,obs}_n$ is the measurement from real collision data, and v'^{corr}_n is the final result - which is the best estimate of the collective flow of the primary particles in the actual collision. In the equation, *all* of the input values have already had a non-flow correction applied. This equation assumes linearity, which is verified by the fact that the (non-flow corrected) corrections are centrality independent, even though v_n is not.

The corrections are made for each vertex, but averaged over centrality to reduce statistical uncertainties. It is found that in order to get statistically stable results, at least 100k events in a single centrality bin is required for centralities $< 50\%$. More events are necessary for the more peripheral events. Running a full simulation with an event-generator and a transport code including all of the ALICE detector systems requires massive amounts of CPU resources. Thus, these simulations are made centrally on the ALICE grid network. Yet even there, resources are limited. Consequently, there are only two available simulations containing flow for this analysis to use for the MC correction. One of the simulations is an AMPT simulation with 100k events available in each of nine centrality bins ranging from 0–5% to 70–80%. With the exception of the 40–50% bin, which contains 500k events. The second available simulation is an AliGenTunedOnPbPb simulation where 500k events are available for the 0–5% centrality bin and one million events available for the 40–50% centrality bin, but with only those two centralities available.

The fact that there are two different simulations available allows for an important systematic check on any model dependence the MC correction might have, see Section 9.2. However, another key point sets the two simulations apart. The AMPT simulation was produced in the beginning of 2012, while the AliGenTunedOnPbPb simulation was produced in the summer of 2014. Due to known issues with the description of the ALICE detectors in AliRoot (see Section 7.6), the geometry used for the AMPT simulation is known to underestimate the secondary particle production by about 10–15% in the regions around $|\eta| = 2$. In order to obtain the best possible result, the AliGenTunedOnPbPb simulation is used for the actual results, while the AMPT simulation is considered for systematic checks.

Since the AliGenTunedOnPbPb simulation only contains two centralities, it is vital that the non-flow correction removes any centrality dependence, as suggested in Section 8.6. This is best tested in the AMPT production, as a much wider centrality range is available in that simulation.

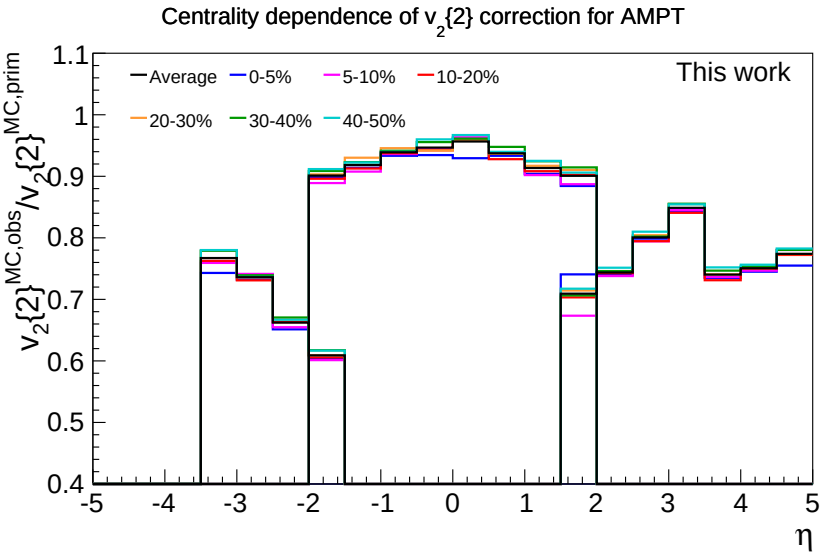

Figure 8.20: AMPT-based correction over a wide range of centralities. After non-flow correction, no significant centrality dependence is observed.

The correction factor, $v'^{MC,prim}_n/v'^{MC,obs}_n$ for a range of centralities where statistically stable results are available is shown in Fig. 8.20. No centrality dependence is observed. For the actual corrections applied to the data from AliGenTunedOnPbPb, the correction factors for each of the two centralities are shown in Appendix C.5 for v_2, v_3 and v_4 for both the two- and four-particle cumulant. The centrality averaged corrections are shown in Fig. 8.21. It is important to note that the corrections for $v_n\{2\}$ are identical to those for $v_n\{4\}$. This suggests that after the non-flow corrections, the effect of secondaries depends on v_n only. In addition, the shape of the $dN/d\eta$-distribution of the secondary particles shown in Fig. 8.15 is easily recognizable in the shape of the correction factors of all the flow observables. Finally, the average corrections appear to be consistent with the predictions from the toy-model above.

In all of the above figures the correction factors are also averaged over vertex. This is done for visual purposes only. In the actual analysis, the correction factors are calculated for each vertex-bin, as the different material that is traversed at different vertices make the correction factors vertex dependent - just as was the case for the non-flow correction to the differential flow.

An equation for estimating the magnitude of the MC correction was given in Eq. (8.6). By estimating the $\Delta\varphi$-distributions like in Fig. 8.16, but in η-bins, it is possible to calculate the contribution to the effective MC correction coming directly from the φ-scattering. Since the effective MC corrections also contain effects from detector segmentation it is necessary to factor in this effect to do a comparison. The effects from detector segmentation are discussed in Sections 3.4.8 and 8.8. Taking both of these effects into account, in Fig. 8.22 the η-dependent MC corrections are calculated and compared to the effective corrections. With the exception of a single point in the $v_4\{2\}$ correction, there is agreement within 10%. For SPD it is closer to 5%. The calculated values only take the φ-scattering and the detector segmentation into account. This means that e.g. η-scattering is not taken into account. Due to the η-dependence of the flow, this likely to explain some of the discrepancies away from mid-rapidity.

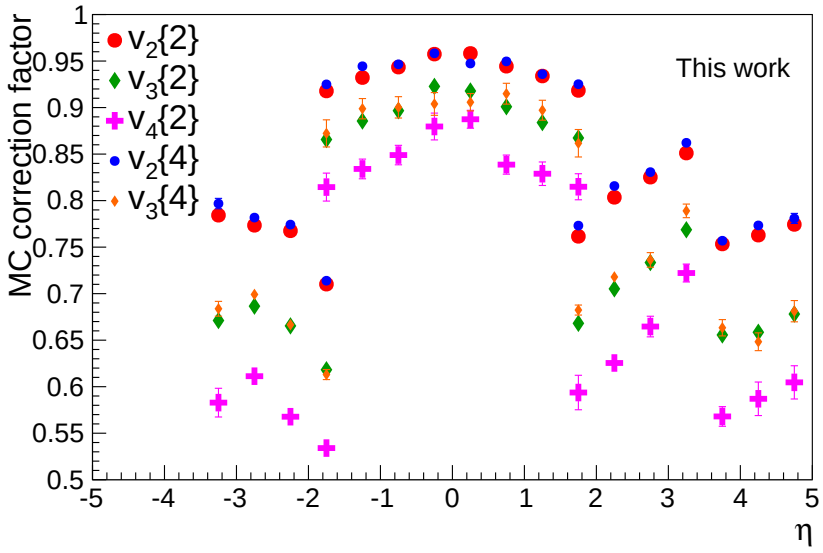

Figure 8.21: Vertex- and centrality-averaged MC corrections based on AliGenTunedOnPbPb. In the analysis the applied corrections are not vertex-averaged.

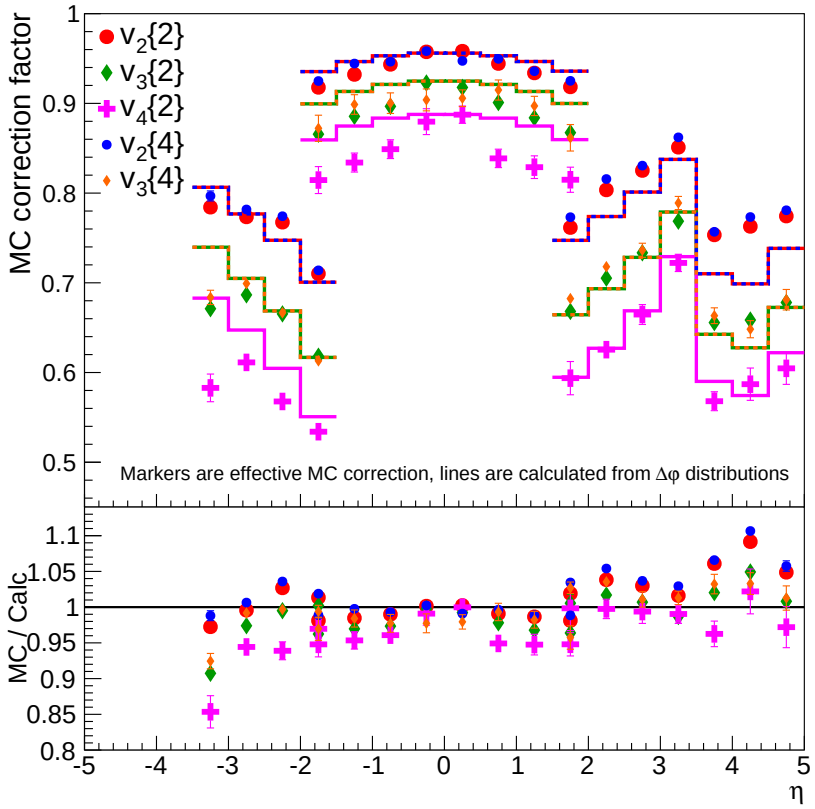

Figure 8.22: Comparison between effective MC corrections derived from AliGenTunedOnPbPb and a calculated MC corrections based on $\Delta\varphi$-distributions from MC, using Eq. (8.6) and taking into account the reduction of the signal caused by detector segmentation.

8.8 Detector Segmentation

Detector segmentation is important to consider in the case of the FMD (20 φ-sectors) and the VZERO (8 φ-sectors). For the FMD Eq. (3.129) can be used, as flow harmonics of v_{10} and higher can safely be assumed to be zero [139]. The calculations show that the observed values of v_2 are *suppressed* by 1.64%. Similarly the bias is 3.66% for v_3 and 6.45% for v_4. For VZERO elliptic and triangular flow can still be estimated approximately from Eq. (3.129) as $v_2 \gg v_6$ and $v_3 \gg v_5$. In particular $v_3 \gg v_5$ is not completely true, but near enough to get a rough estimate. This yields a bias of 10% and 22% for v_2 and v_3 respectively. For $v_4\{2\}$ it is necessary to use Eq. (3.130), which for $n = N/2$ is:

$$E\left[\langle 2\rangle_{N/2}\right] = 2 \cdot v_{N/2}^2 \frac{\sin^2\left(\frac{(N/2)}{N}\pi\right)}{\left(\frac{(N/2)}{N}\pi\right)^2} \Rightarrow$$
$$E\left[\langle v_{N/2}\rangle\right] = \sqrt{2} \cdot v_{N/2} \frac{\sin\left(\frac{\pi}{2}\right)}{\frac{\pi}{2}} = v_{N/2}\frac{2\sqrt{2}}{\pi}, \tag{8.10}$$

yielding a suppression of 10% for the v_4 measurement in the VZERO detector. While it is possible to approximately calculate these corrections, in the actual analysis the correction for detector segmentation is applied together with the MC correction for secondary particles. This is due to the construction of the MC correction factors in Eq. (8.9). In the correction factor, $v'^{MC,obs}_n$ is biased from detector segmentation, while $v'^{MC,prim}_n$ is not due to the high precision information available on MC particles. Consequently, the segmentation correction is actually built into the MC correction, without the need for explicit calculations such as the above.

8.9 Trending

The choice of dataset and event selection was discussed in Section 8.1. When combining data over a period of running it is important to study if the detector performance is constant over the entire period. The integrated flow values of $v_2\{2\}$ and $v_2\{4\}$ for the Pb–Pb runs in the LHC10h period analyzed here is shown vs. run number in so-called *trending-plots* in Figs. 8.23a and 8.23b. In the figures the measurements are averaged over the 0–80% centrality range and fitted with a constant function. The reduced χ^2 is given in the legend. For all detectors a constant performance over the entire period is observed.

8.10 Results

Applying the non-flow corrections as well as the MC corrections shown in Fig. 8.21 to the data allows for a first look at the results. In the final results, the overlap of the SPD and FMD coverage in the regions $1.75 < |\eta| < 2.0$ are calculated as a weighted average between the two detectors. However, in Fig. 8.15 it is found that for the FMD in these regions there are more secondary particles than primary particles. For the SPD there is only about 10% the amount of secondaries as there are primaries. This means that before the MC correction is applied the two detectors observe different values for the flow. This is shown in Fig. 8.25. After all the corrections are applied there is a much better agreement between the two detectors, shown for the 30–40% central events in Fig. 8.24. Plots for two more centralities are available in Appendix C.6. This strongly suggests that the biases are well understood and properly corrected for in this analysis. An overview of all the centralities analyzed here is shown in Fig. 8.26, although only statistical errors are shown, as systematic uncertainties are only calculated in the next chapter. The results shown here use TPC-only tracks for reference flow and FMD and SPD clusters for the differential

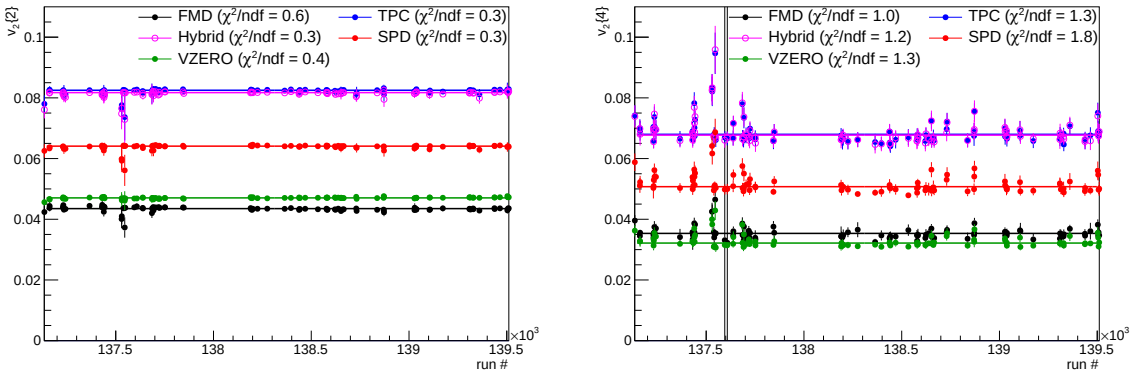

(a) Trending plots for integrated $v_2\{2\}$ in LHC10h.

(b) Trending plots for integrated $v_2\{4\}$ in LHC10h.

Figure 8.23

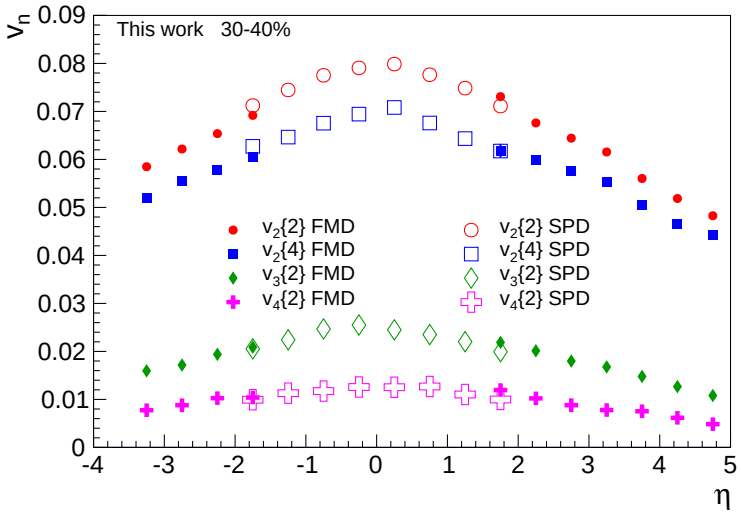

Figure 8.24: Overlap between FMD and SPD after all corrections for 30–40% central events. A good agreement is observed.

flow. For the analyzes with other setups, including hybrid tracks or the VZERO as well as those employing rapidity-gaps, see Chapters 9 and 10.

For $v_2\{2\}$ and $v_3\{2\}$ all centrality-bins in the range 0–80% are shown and yield statistically stable results. For $v_4\{2\}$ only results up to 60% in centrality are statistically stable. The reason for the 60–80% results being unstable for v_4 only can be attributed to the fact that the signal is so much smaller than v_2 and v_3, which, combined with the very low multiplicities of peripheral events, does not yield a high enough resolution for a v_4 estimate. Similarly, multi-particle measurements require many more particles to obtain a decent resolution. Thus, only $v_2\{4\}$ is statistically stable, and even that only up to 50% in centrality. It should be noted that in the AliGenTunedOnPbPb simulation it is possible to get statistically stable results for $v_3\{4\}$ as is shown in Fig. 8.21. This is due to the simplicity of the flow signal in that particular simulation, as it does not contain multiplicity and flow fluctuations it is easier to get statistically stable results.

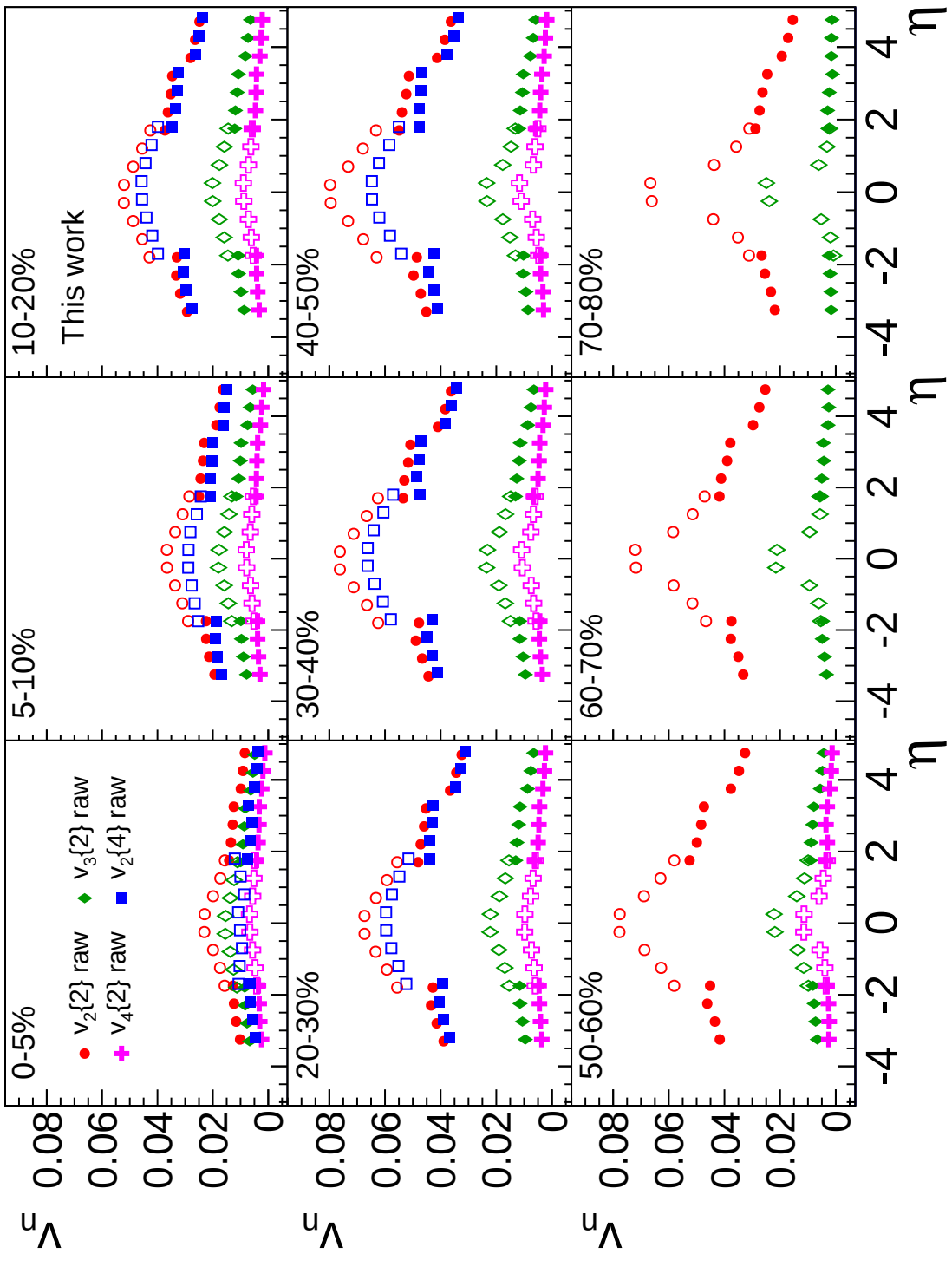

Figure 8.25: Raw measurements for $v_2\{2\}$, $v_3\{2\}$, $v_4\{2\}$ and $v_2\{4\}$ obtained with TPC-only tracks for reference flow and SPD (open markers) and FMD (full markers) clusters for differential flow. Neither non-flow nor MC correction has been applied.

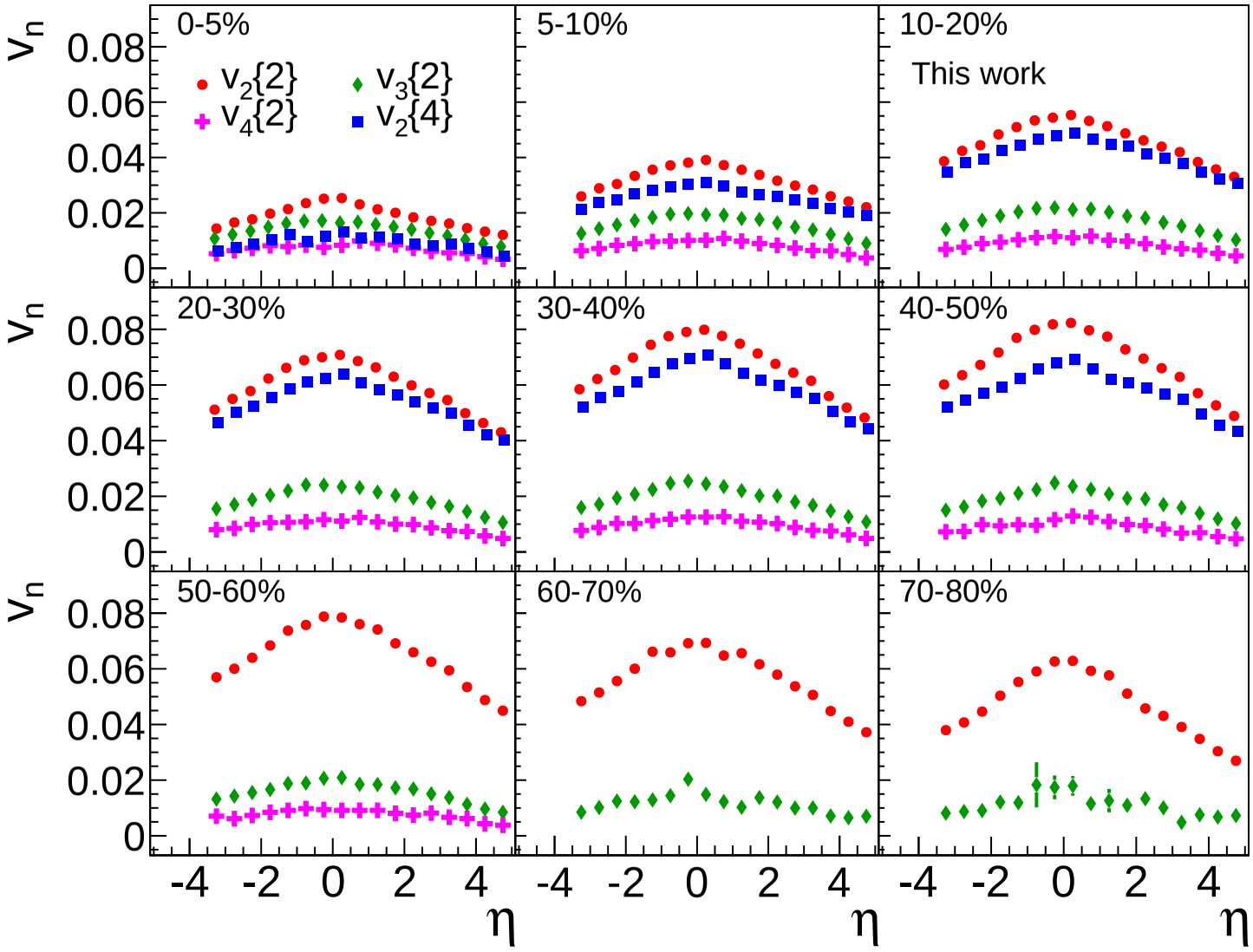

Figure 8.26: Corrected results for $v_2\{2\}$, $v_3\{2\}$, $v_4\{2\}$ and $v_2\{4\}$ obtained with TPC-only tracks for reference flow and SPD and FMD clusters for differential flow. Only statistical errors are shown. For centrality bins where one or more observable is missing, the corresponding observable is not found to be statistically stable.

Chapter 9

Systematic Uncertainties

There are four sources of systematic uncertainties for the two-particle measurements and three sources for the four-particle measurement. The sources are:

Track selection In this analysis tracks are only used for reference flow. To test how sensitive the results are to the choice of reference particles, a cross-check using hybrid tracks is performed.

Model dependence of MC correction The MC correction should only depend on the effect of the secondary particle production on the flow signal. To verify this, a correction derived from an AMPT simulation is compared to the AliGenTunedOnPbPb-based correction.

Material description Also with respect to the MC correction, the amount of material, or the density of the material, traversed by the particles plays an important role. To test how sensitive the MC correction is to the density of the material, two HIJING productions with $\pm 7\%$ material density, respectively, are applied with a flow afterburner, and the differences in the measured flow is tested.

Non-flow correction The non-flow correction is obtained from subtracting non-flow measured with HIJING. This is cross-checked using pp collision data to subtract the flow and by comparing with results from an analysis with a large rapidity gap.

This chapter only describes cross-checks that contribute to the total systematic uncertainty. For other comparisons, e.g. with using the VZERO detector instead of the FMD, see Chapter 10. First, the contribution to the systematic uncertainties from each of the four sources is described in detail. Then, at the end of the chapter, the values are all combined in tables and the total systematic uncertainty is calculated.

9.1 Track Selection

For the results presented here TPC-only tracks are used. To estimate the dependence of the result on the choice of reference particles, an analysis is made where hybrid tracks are used instead. See Section 6.6 for a definition of the different track types. The cuts on the tracks are described in Section 8.2.4. A direct comparison is shown on the top of Fig. 9.1. Open markers are using hybrid tracks, while full markers use TPC-only tracks. The ratio is shown in the bottom of the figure. There are three sets of dashed lines representing three different systematic uncertainties. The inner set of dashed lines ranging from 5–80% is the systematic uncertainty assigned to v_2 and v_3 for centralities larger than 5% and for v_4 for centralities larger than 30% (2% systematic uncertainty). The next set is for v_2 and v_3 with centrality in the range 0–5% (4% systematic uncertainty). The outer set is for the maximum value for the v_4 uncertainty in

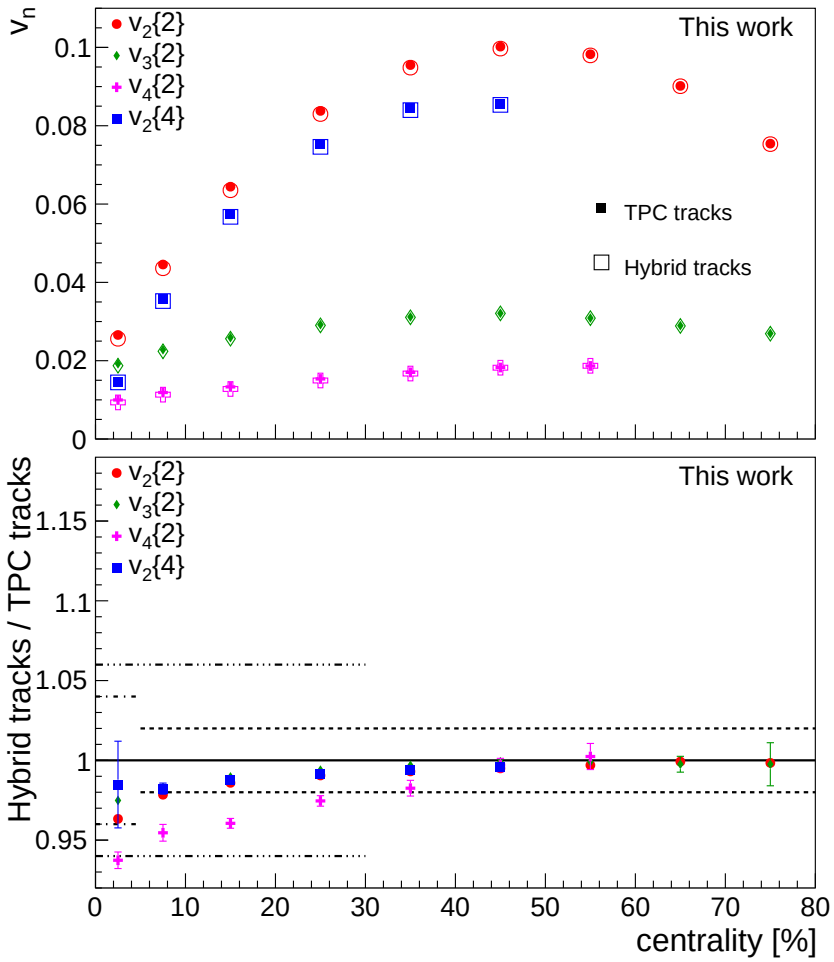

Figure 9.1: Different choice of tracks for the reference flow. Systematic uncertainties assigned: v_2 and v_3: 0–5% central: 4%, 5–80% central: 2%. v_4: 0–30% central: 3%–6%, 30–60% central: 2%.

the centrality range 0–30% (3%–6% systematic uncertainty). The uncertainties are the same for the track selections for both FMD and SPD.

9.2 Model Dependence

The correction for secondary particles is only feasible if it is not dependent on the underlying flow. After the non-flow correction is applied, it should only depend on how the secondary particles suppress the flow signal. To test this two different models are compared. The AliGenTunedOnPbPb-based correction that is used for the final results is compared to one based on an AMPT simulation. One thing to note is that the two simulation were run two years apart. During that time, the geometry description of ALICE in the software improved significantly. Particularly the ITS and support structures were updated, which affects the FMD correction around $|\eta| \approx 2$. This means that deviation in those regions are more likely to be caused by a shifting or addition of material, than a strong dependence on the underlying model. A comparison between the two corrections is shown in Fig. 9.2. In the figure a large discrepancy of up to 15% is observed around $|\eta| \approx 2$. Away from these regions, the difference is within 5% for $v_2\{2\}$ and $v_2\{4\}$ (inner dashed lines) and within 7% for $v_3\{2\}$ and $v_4\{2\}$ (outer dashed lines). These values are assigned as the systematic uncertainties on the model dependence. It should

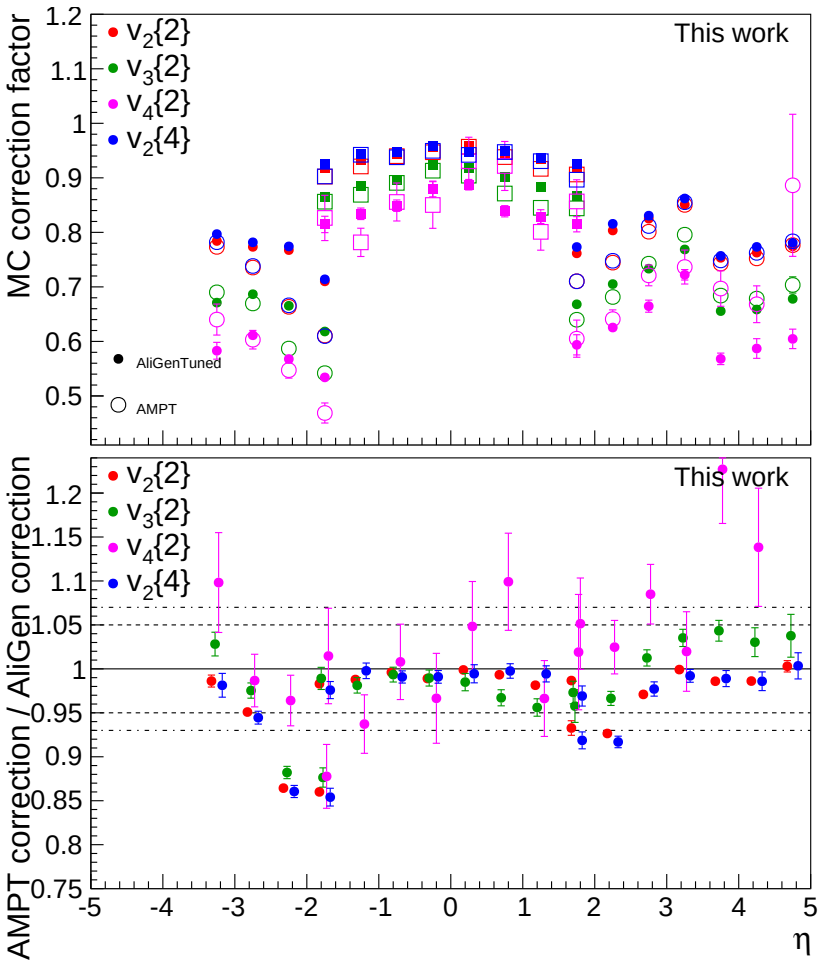

Figure 9.2: Comparison of MC correction for secondary particles derived with AMPT and AliGenTunedOnPbPb. The corrections shown here have been averaged over centrality and then vertex. For the actual analysis the corrections are done for each vertex. Systematic uncertainties assigned: $v_2\{2\}$ and $v_2\{4\}$: 5%, $v_3\{2\}$ and $v_4\{2\}$: 7%.

be noted that the corrections in the figure are averaged over all vertices, while they are applied per vertex to the actual analysis results. This is done for visual purposes only, as the variations remain the same as with the corrections calculated per vertex.

The systematic uncertainty assigned to the model dependence ignores the 15% variation as the geometry in AliGenTunedOnPbPb simulation is known to be better than the one in the AMPT simulations. Similarly, in Fig. 8.24 it was shown that using the correction from AliGenTunedOnPbPb there is a good agreement between the FMD and SPD in the overlap regions, suggesting that the description used for the AliGenTunedOnPbPb results is close to the true geometry.

9.3 Material Description

The largest correction applied in this analysis stems from the secondary particles hitting the detectors (see Fig. 8.15). Consequently there is a strong dependence on a correct description of the experiment in the software used for simulations. However, it is known that the current description is not perfect, although much improved in recent years. To estimate the sensitivity of

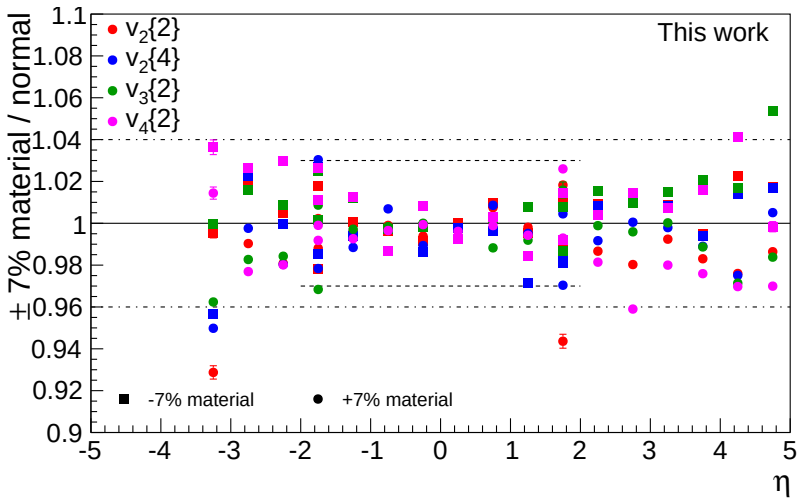

Figure 9.3: Sensitivity of the analysis to different material densities. HIJING simulations with flow added after particle production. Very little sensitivity is found. Long dotted lines: systematic uncertainty for the FMD: 4%. Short dotted lines: systematic uncertainty for the SPD: 3%. Statistical errors shown, but mostly smaller than marker size.

the analysis to the amount of material in front of the detectors, three HIJING simulations with: normal, +7% material density and −7% material density, respectively, are utilized. In this case, to introduce flow in the events, an *afterburner* is applied to the tracks, MC particles and track references from particle hits in the FMD and SPD (see Section 7.5.1). The results are shown in Fig. 9.3, where it is seen that the analysis is in fact not very sensitive to *density variations* in the material. In the figure, there are separate systematic uncertainties for the SPD and FMD, as the FMD is affected more than the SPD due to the much larger number of secondary particles hitting it. The assigned systematics for the detectors are 4% and 3% respectively.

This is in slight contradiction with what was seen in Fig. 9.2, where the big differences around $|\eta| \approx 2$ were attributed to a change in the geometry between the two productions. This can be understood as the analysis having a larger sensitivity to the *position of the material*, but less so to the *density*. This is not entirely intuitive, but as flow analysis is a measure of *relative* multiplicities it does provide an explanation. The agreement between the SPD and FMD after all the corrections are applied suggests that this issue is under control.

9.4 Non-Flow Correction

Since only the two-particle measurements are affected by non-flow, the non-flow related systematics discussed here only apply to those results. In general, the non-flow correction is the largest contributor to the systematic uncertainties. For this cross-check an analysis is used, where a rapidity-gap of $|\Delta\eta| > 2.0$ is used. The method is the three-sub-event method discussed in Section 3.4.3. A problem with this approach is that the rapidity-gap analysis does not select a large number of particles, which results in statistically unstable result for centralities where the track-based results are still stable. In fact v_4 is not even statistically stable with this method. As a further cross-check, measurements from pp collisions at $\sqrt{s} = 2.76$ TeV is also used. For the pp-based correction, the multiplicity scaling of non-flow is used. This also makes it applicable for all centralities. The results are shown in Figs. 9.4 to 9.6. For the v_2 results inner dotted lines are for systematic uncertainties in the range 0–60%, outer dotted lines are for 60–80%. For v_3 and v_4 all centralities have the same systematic uncertainty.

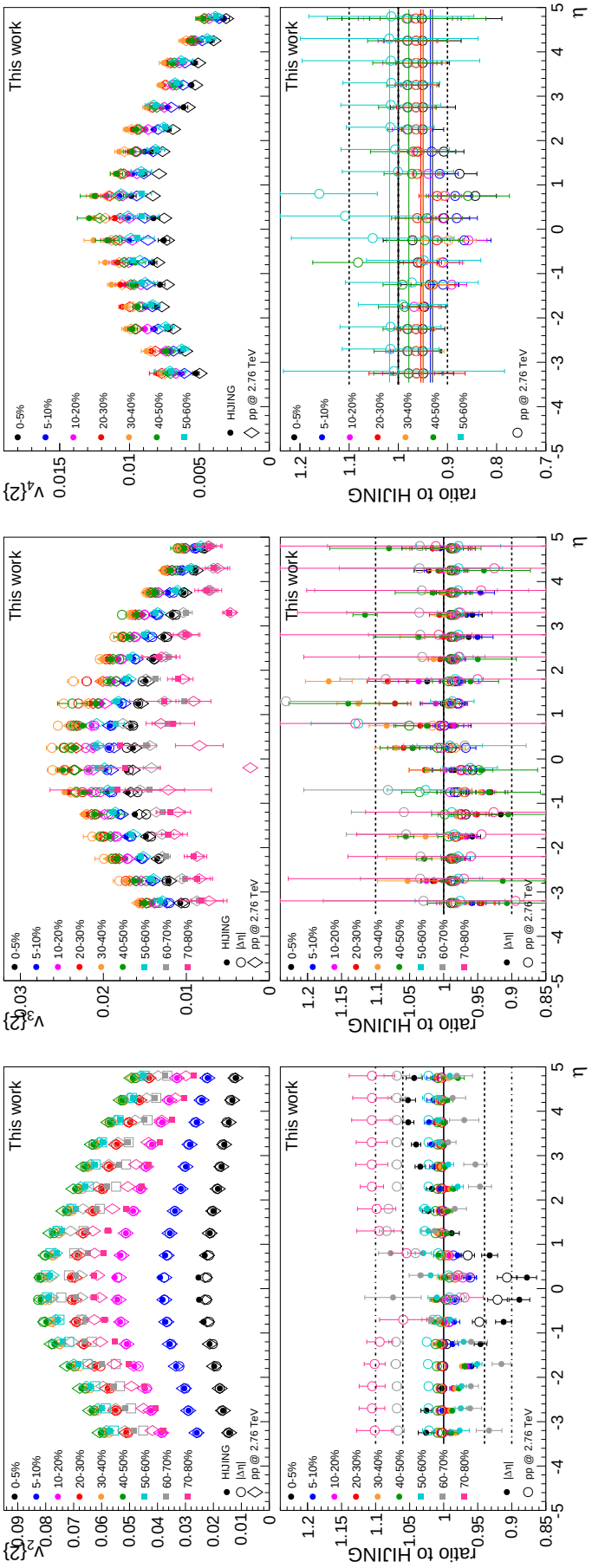

Figure 9.4: $v_2\{2\}$ with non-flow removed using HIJING compared to $v_2\{2, |\Delta\eta| > 2.0\}$ and using pp collisions. Systematic uncertainties assigned: 0–60% central: 6%, 60–80% central: 10%.

Figure 9.5: $v_3\{2\}$ with non-flow removed using HIJING compared to $v_3\{2, |\Delta\eta| > 2.0\}$ and using pp collisions. Systematic uncertainties assigned: 10%.

Figure 9.6: $v_4\{2\}$ with non-flow removed using HIJING compared to using pp collisions. Linear fits are added to guide the eyes. Systematic uncertainties assigned: 10%.

9.5 Summary of Systematic Uncertainties

All the above uncertainties are assumed to be independent. In this section they are summarized and added in quadrature. In principle, the HIJING simulation used to correct for non-flow also depends on the material used, leading to some degree of correlation between the non-flow correction uncertainty and the material description uncertainty. However, it is difficult to estimate exactly how big this correlations is. If it is assumed to be 100%, the effect would be largest for $v_2\{2\}$, where it would change the total systematic uncertainty to 9% for the FMD (down from 10%). Since the net effect is small, and it is unlikely that the two uncertainties are actually 100% correlated, it is assumed that the two uncertainties are uncorrelated (giving the slightly larger net uncertainty).

9.5.1 $v_2\{2\}$

Source	Centrality	SPD	FMD
Reference track choice	0–5%	4%	4%
	5–80%	2%	2%
Model dependence	All	5%	5%
Material description	All	3%	4%
Non-flow correction	0–60%	6%	6%
	60–80%	10%	10%
Total	0–5%	9%	10%
	5–60%	9%	9%
	60–80%	12%	12%

9.5.2 $v_3\{2\}$

Source	Centrality	SPD	FMD
Reference track choice	0–5%	4%	4%
	5–80%	2%	2%
Model dependence	All	5%	5%
Material description	All	3%	4%
Non-flow correction	All	10%	10%
Total	0–5%	12%	13%
	5–80%	12%	13%

9.5.3 $v_4\{2\}$

Source	Centrality	SPD	FMD
Reference track choice	0–5%	6%	6%
	5–10%	5%	5%
	10–20%	4%	4%
	20–30%	3%	3%
	30–60%	2%	2%
Model dependence	All	7%	7%
Material description	All	3%	4%
Non-flow correction	All	10%	10%
Total	0–5%	14%	14%
	5–10%	14%	14%
	10–20%	13%	13%
	20–30%	13%	13%
	30–60%	13%	13%

9.5.4 $v_2\{4\}$

Source	Centrality	SPD	FMD
Reference track choice	0–5%	4%	4%
	5–50%	2%	2%
Model dependence	All	5%	5%
Material description	All	3%	4%
Total	0–5%	7%	8%
	5–50%	6%	6%

Chapter 10

Results

In this chapter the final results are presented with the systematic uncertainties applied. The results are compared to other ALICE measurements for a final consistency check. This analysis is also compared to results from other experiments at LHC and at RHIC at lower energies. Finally, comparisons to the AMPT model is presented. For all plots presented here, the thin errors bars represent 1σ statistical errors and the wide error bars with faded colors are 1σ systematic error bars, unless otherwise noted.

10.1 Complete Results

In Fig. 10.1 the results from Fig. 8.26 are shown with the systematic uncertainties found in Section 9.5 applied. It is observed that the shape of v_n vs. η is extremely similar between the harmonics measured here. The ratios v_3/v_2, v_4/v_2 and v_4/v_3 are shown in Fig. 10.3, where all three harmonics appear to have the same η-dependence. Similarly, the relative η-dependence does not change significantly between the most central events (0–5%) and more peripheral (50–60%), this is shown in Fig. 10.4. As expected from the calculations of the fluctuation bias to the two- and four-particle cumulants, $v_2\{2\}$ (enhanced by fluctuations) is found to be consistently larger than $v_2\{4\}$ (suppressed by fluctuations). Each of the centrality-bins considered here are shown in a larger version in Appendix D.1. Taking into account that it is a symmetric collision system, calculating $v_n(\eta)$ as the weighted average from negative and positive η may improve the measurement. The results, using the symmetry around $\eta = 0$ is shown in Fig. 10.2, where slightly more smooth distributions are seen.

10.2 Comparison to Other ALICE Measurements

This section contains comparisons to other ALICE measurements. Some are from published results using TPC-only tracks. Others are also part of this analysis, but utilizing other detectors for either the reference or differential flow measurement.

10.2.1 Comparison to TPC Published Results

Many flow results have been published using TPC-only tracks. One of the arguments for using the tracks for the reference flow in this analysis is that the flow in the TPC-only tracks is well known from other analyses. Thus, the results obtained here should also be consistent with the published values. The reference flow obtained with TPC-only tracks in this analysis is compared to the two-particle cumulant results presented in Ref. [140] and the four-particle results presented in Ref. [74]. The measurements are compared in Fig. 10.5 and a good agreement is observed.

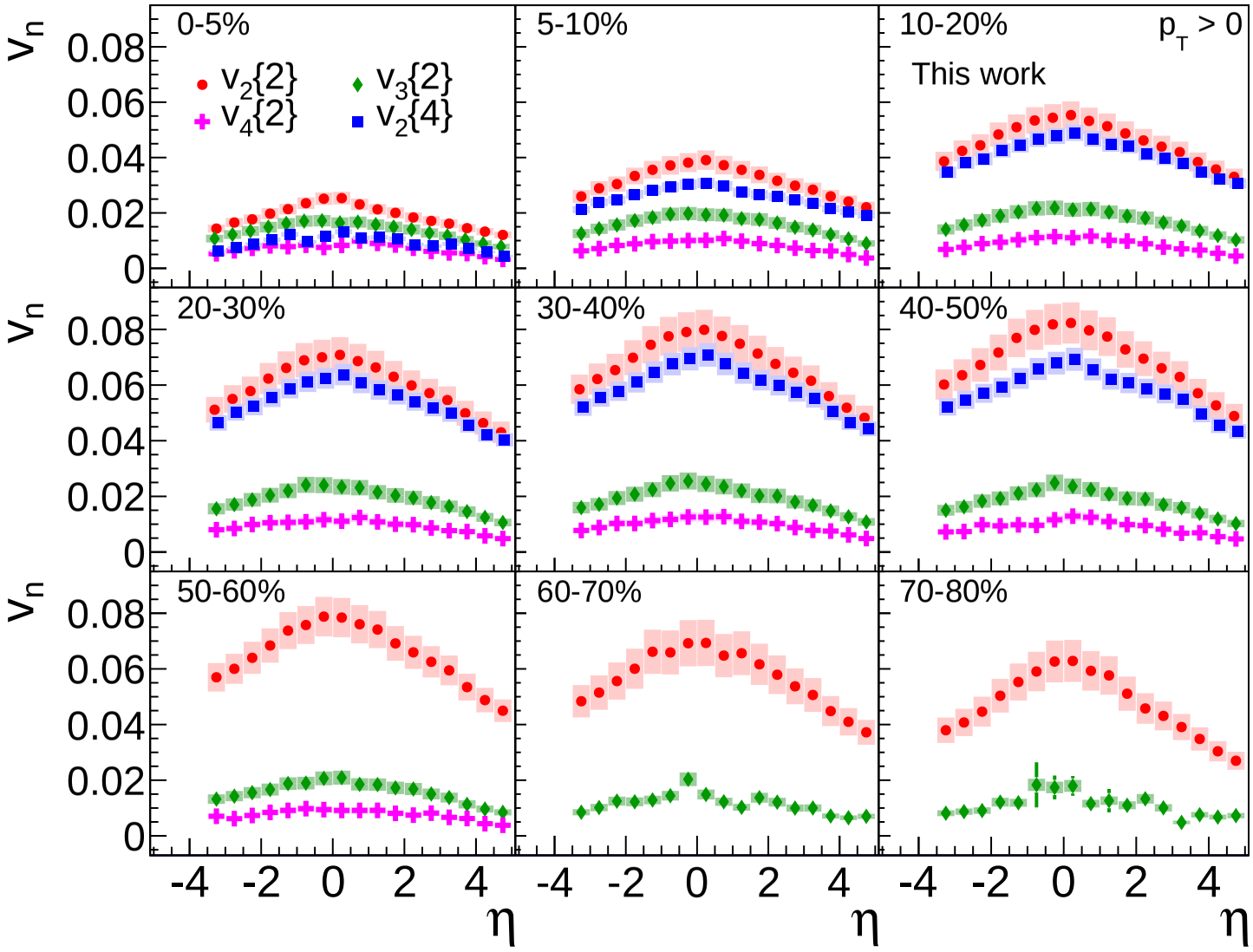

Figure 10.1: Overview of final results including systematic uncertainties. Statistical errors are shown as thin error bars, systematic uncertainties as thick lines.

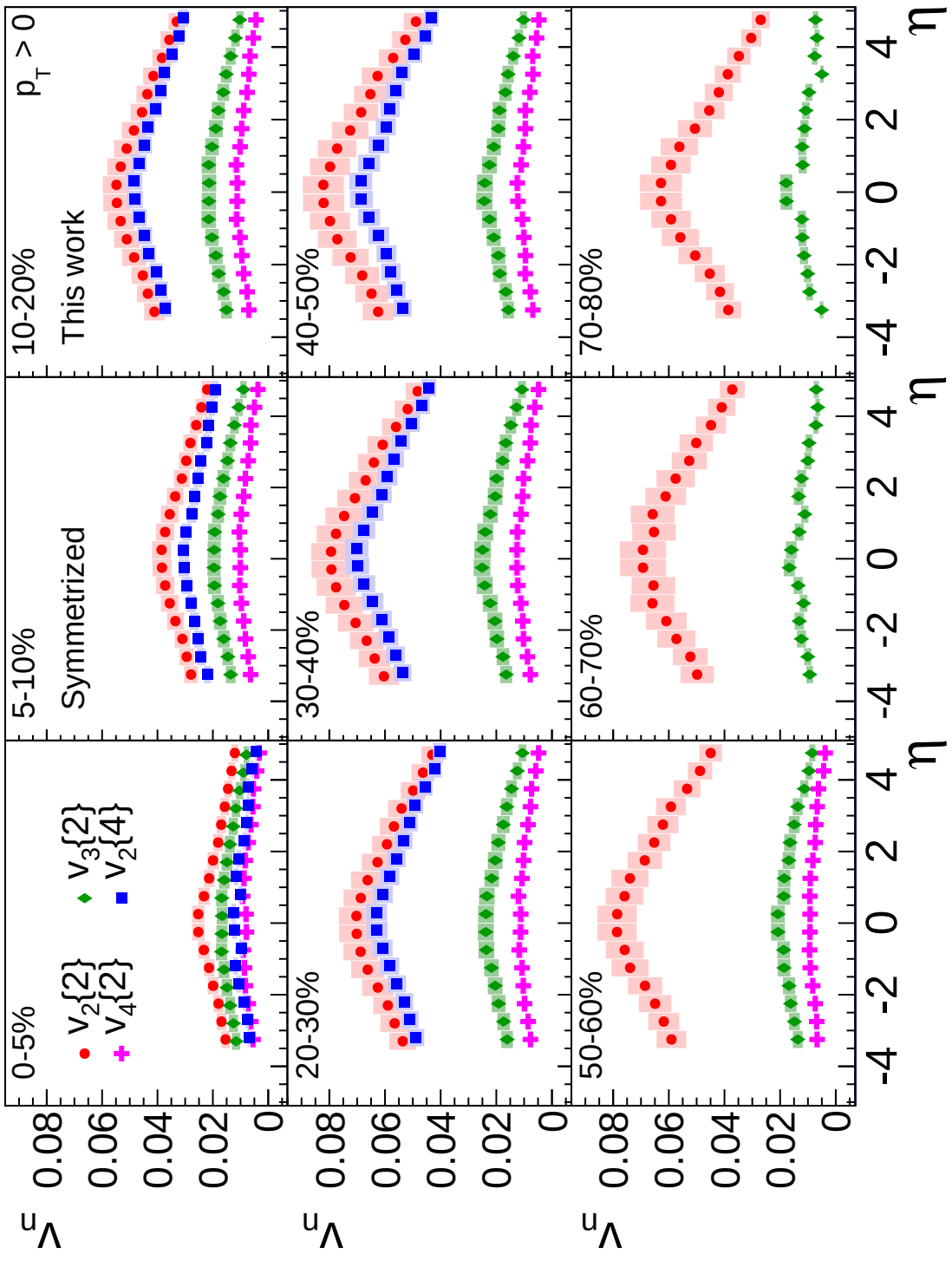

Figure 10.2: Overview of final results where the regions with coverage in both η and $-\eta$ are made symmetrical. Including systematic uncertainties. Statistical errors are shown as thin error bars, systematic uncertainties as thick lines.

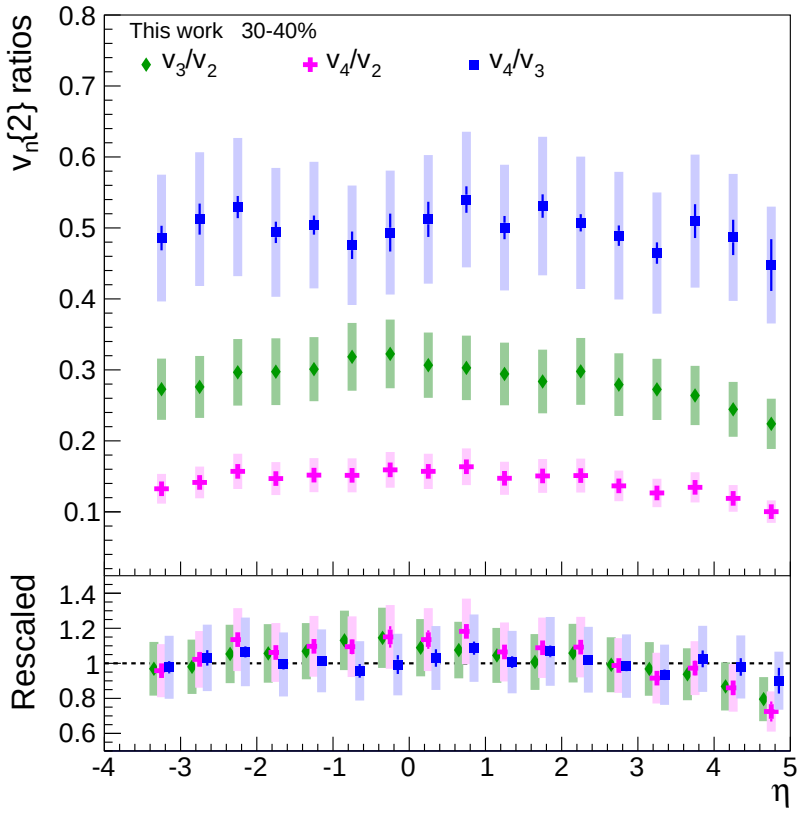

Figure 10.3: Ratios of v_3/v_2, v_4/v_2 and v_4/v_3 show that the η-dependence for all three harmonics is very similar. In the bottom plot all three ratios are rescaled for better comparison. Shown here for 30–40% central events, other centralities yield similar results.

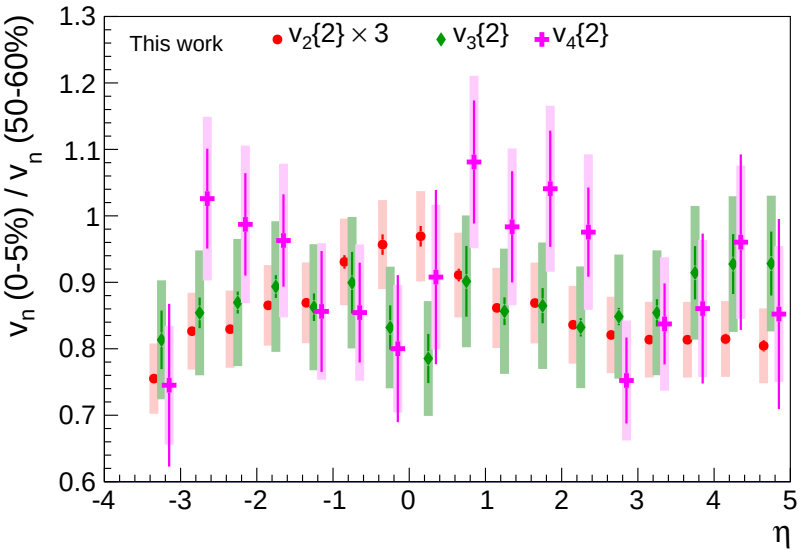

Figure 10.4: Ration between very central events (0–5%) and more peripheral (50–60%) reveal that the relative η-dependence of all the observables does not change significantly with centrality. The $v_2\{2\}$ results are rescaled by a factor 3 for better comparison between the harmonics.

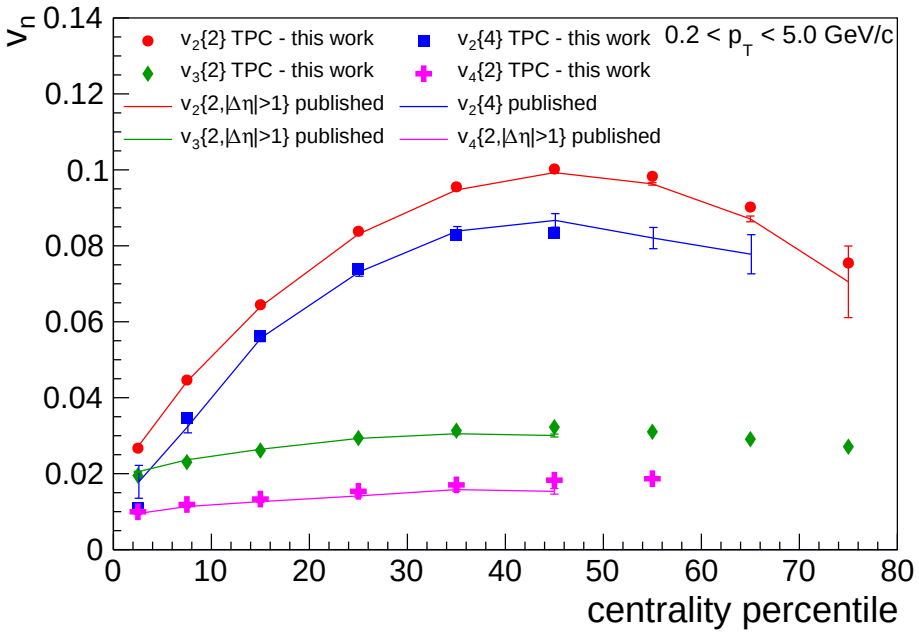

Figure 10.5: $v_2\{2\}$, $v_3\{2\}$, $v_4\{2\}$ and $v_2\{4\}$ of the reference flow measured using TPC-only tracks for this analysis compared to previously published results [74, 140]. With transverse momentum cut $0.2 < p_{\mathrm{T}} < 5.0$ GeV/c. Only statistical errors are shown. A good agreement is observed.

The TPC-only tracks are measured in the range $0.2 < p_{\mathrm{T}} < 5.0$ GeV/c. These values can be extrapolated to 0 GeV/c and then compared to the SPD results from this analysis at mid-rapidity. This is done using fits to the charged particle spectra results from ALICE. The TPC results for $v_2\{EP, |\Delta\eta| > 2\}$, $v_3\{EP, |\Delta\eta| > 2\}$, and $v_2\{4\}$ are obtained from the event plane analysis in Ref. [141]. The $v_4\{2, |\Delta\eta| > 1\}$ results are the two-particle cumulant results from Ref. [140], which unfortunately only contains results in two centrality bins for the p_{T}-dependence, which is necessary for the extrapolation. For the differential flow, a plot of v_n vs. centrality is shown in Fig. 10.6, where a very good agreement is observed between this analysis and the extrapolated TPC-only results. A more detailed look is available in Figs. 10.7a, 10.7b, 10.8a and 10.8b, which gives a consistent picture. Overall, this suggests that the results at mid-rapidity are consistent within ALICE.

10.2.2 Using the VZERO at Forward Rapidity

The VZERO is the only other detector to cover approximately the same η-region as the FMD, making it the only choice for an independent cross-check of the forward-rapidity region. A ratio between using the VZERO and using the FMD is shown for a representative centrality (10–20%) in Fig. 10.9. An overview of the measurement for all centralities is shown in Appendix D.2. One of the rings is completely off, by almost a factor 2. This is not fully understood, but appears to be a VZERO issue, as the flow in that ring is consistently larger than in all the others. Considering that the VZERO results are obtained with only eight φ-segments and a simple gain-matching algorithm applied to the signal, the agreement is quite good for the other seven rings. This is an important cross-check for the FMD results, where other comparisons are not possible. The fact that the two measurements are mostly consistent is a very significant result.

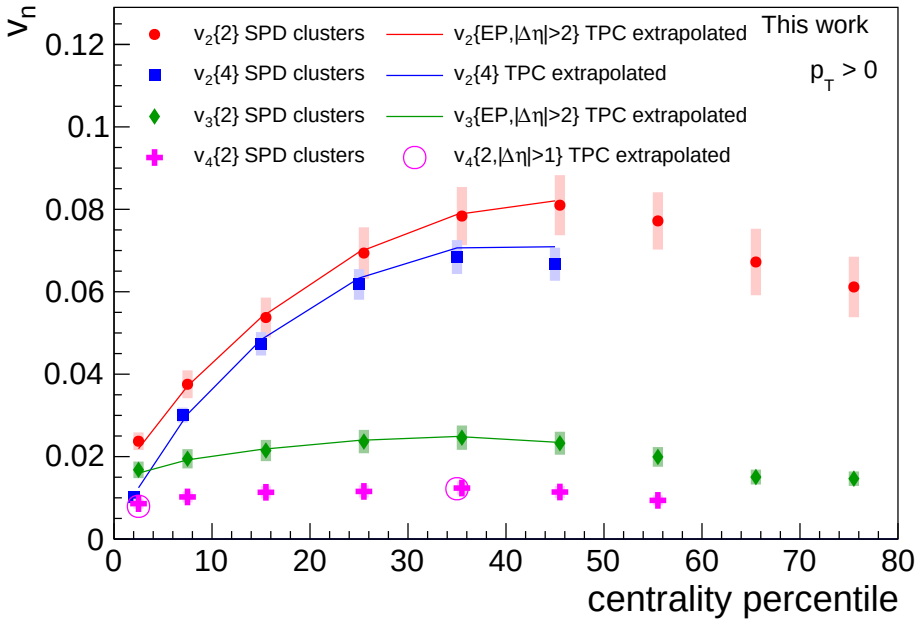

Figure 10.6: $v_2\{2\}$, $v_3\{2\}$, $v_4\{2\}$ and $v_2\{4\}$ integrated for $|\eta| < 1.0$ including systematic uncertainties, compared to published TPC track results extrapolated to $p_{\mathrm{T}} = 0$ GeV/c.

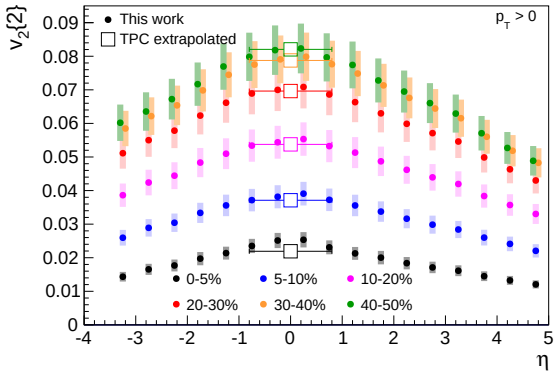

(a) $v_2\{2\}$ vs. η compared to extrapolated TPC-only track results. A good agreement is observed for all centralities.

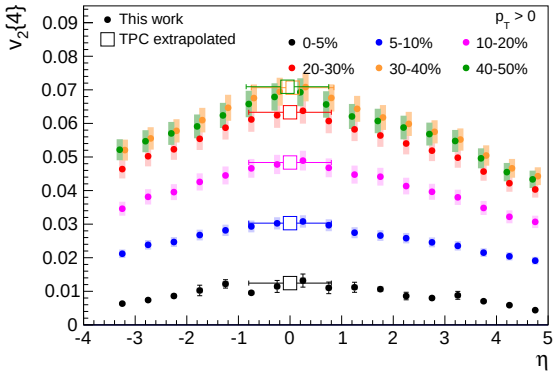

(b) $v_2\{4\}$ vs. η compared to extrapolated TPC-only track results. A good agreement is observed.

Figure 10.7

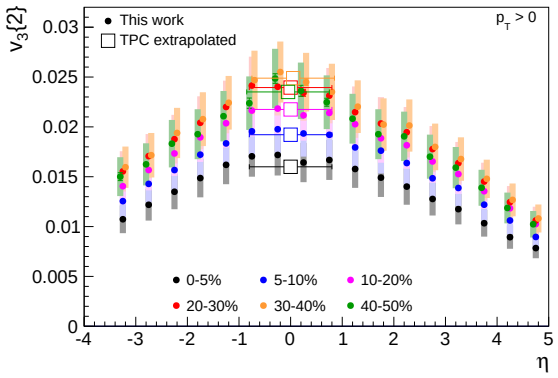

(a) $v_3\{2\}$ vs. η compared to extrapolated TPC-only track results. A good agreement is observed for all centralities.

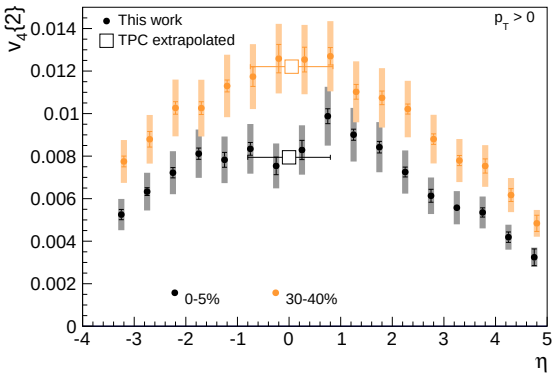

(b) $v_4\{2\}$ vs. η compared to extrapolated TPC-only track results. A good agreement is observed for the 30–40% centrality bin. A jump is observed for 0–5%, but there is still agreement in the overlap region.

Figure 10.8

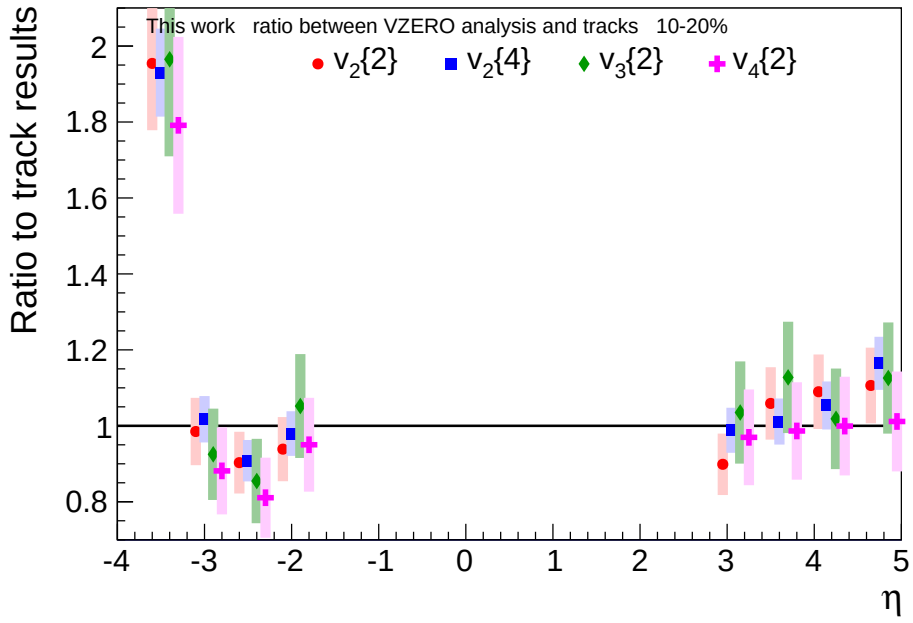

Figure 10.9: Ratio between using the VZERO and the FMD in the forward regions. Here shown for the 10–20% most central events. The ratios between the measurements are similar in all centralities.

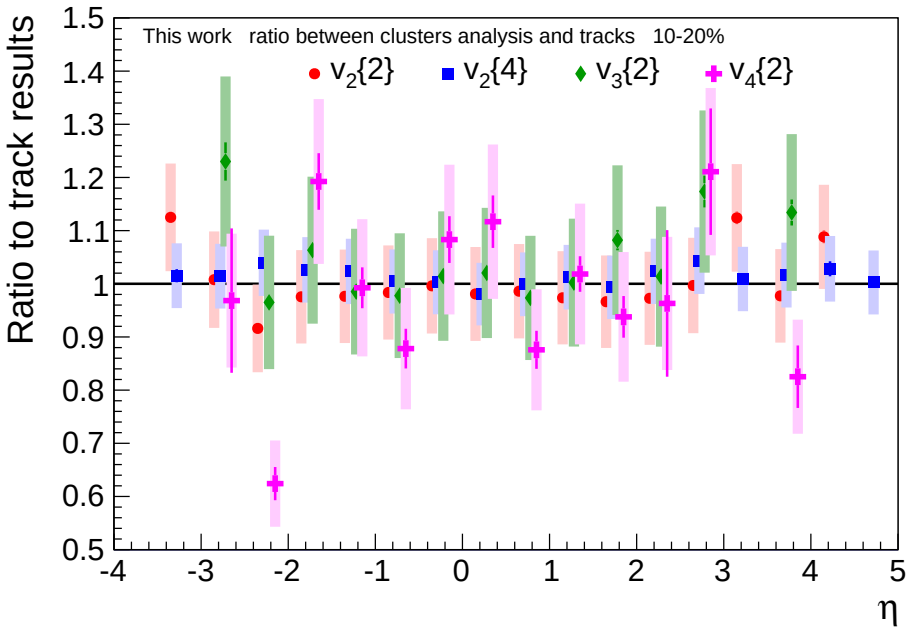

Figure 10.10: Ratio between using clusters and TPC tracks for the reference flow. Here shown for the 10–20% most central events. The agreement between the measurements is similar in all centralities, except for $v_4\{2\}$ where there is a larger discrepancy in more peripheral events.

10.2.3 Changing the Reference Detector

While using tracks from mid-rapidity for the reference flow measurement has many advantages, also using them for the reference measurement at forward-rapidities does make the analysis susceptible to effect from symmetry plane fluctuations (see Section 3.4.10). While the bias to the Q-cumulants method from symmetry plane fluctuations has not yet been studied in detail (Section 3.4.11), if they are significant in this analysis, they might be observed by changing the detector used for the reference flow. In this case, instead of using tracks, the SPD clusters are used for both reference flow and differential flow in the SPD region. Similarly, the FMD is used for both reference and differential flow in the FMD regions. If symmetry plane fluctuations cause a significant bias, the effect should be most clearly seen in the FMD, where the results using tracks should be systematically lower. The ratio between the measurements for the 10–20% most central events is presented in Fig. 10.10, where a very good agreement is observed. This is similar for all centralities, except for $v_4\{2\}$ where the discrepancy becomes slightly larger in more peripheral events. An overview of the measurement for all centralities is shown in Appendix D.3. This suggests that symmetry plane fluctuations, if present, are not significant enough to bias the results in this analysis. It should be noted that due to the smallness of v_4, especially at forward-rapidities, the results obtained using only the FMD are not statistically significant, except in the most central events.

10.2.4 Applying a Rapidity-Gap

The analysis utilizing a rapidity-gap was used to estimate the systematic uncertainty arising from the non-flow correction in Chapter 9. In Fig. 10.11 all the results are presented and compared to the final results of the analysis obtained using HIJING to remove non-flow. As the systematic uncertainties are assigned with the use of the $v_n\{2, |\Delta\eta| > 2.0\}$ measurements, the agreement between the two measurements does not contain any new information. Yet it is still

an interesting result. Most significantly, the analysis using a rapidity-gap has a slightly weaker η-dependence at mid-rapidity.

10.2.5 Forward-Backward Symmetry

As the collisions system is symmetric around $\eta = 0$, the results are also expected to be symmetric. However, as the amount of secondary particles hitting the detectors is not symmetric around $\eta = 0$ (see Fig. 8.15), mirroring the results as $\eta \to -\eta$ allows for a check of the MC correction for secondary particles and the non-flow correction. The ratios between the forward-rapidity and backward-rapidity results are shown for all centralities in Figs. 10.12a to 10.12d. The direct comparisons are shown in Appendix D.4 for three different centralities. The forward-backward results are consistent within the systematic uncertainties. This further suggests that the bias to anisotropic flow from secondary particles is under control.

10.3 Comparison to Other Experiments

At the LHC, other measurements of v_n vs. η cut off at $|\eta| = 2.5$. With the exception of a v_2 measurement by CMS [87] and a v_2 measurement by ATLAS [142], they are also all done in narrow p_{T} regions, which makes comparison to these results difficult. An overview of the LHC results was presented in Section 4.1.5. In general, ATLAS and CMS both find a very weak η-dependence at mid-rapidity, one that is slightly weaker than what is observed here. Although the results of this analysis using a rapidity-gap is less peaked at mid-rapidity. In Fig. 10.13 a direct comparison to the CMS results reported in Ref. [87] is shown. The results are presented for three centralities: 2.5%–15%, 15–25% and 25–50%. The CMS results are extrapolated down to $p_{\mathrm{T}} = 0$ GeV/c, making the direct comparison possible. These results are found to be in agreement with the CMS results for all three centralities.

The PHOBOS experiment at RHIC published results on elliptic flow vs. η with p_{T} cuts consistent with this analysis. At RHIC, elliptic flow was found to have a strong pseudorapidity dependence. As discussed above, at the LHC, v_2 appear to have a slightly weaker pseudorapidity dependence at mid-rapidity. A comparison to the top RHIC energy is shown in Fig. 10.14. The figure shows that the slopes at forward rapidity look very similar between RHIC and LHC. In Fig. 10.15 the PHOBOS results are rescaled to agree with the magnitude of v_2 in this analysis at mid-rapidity. From this figure it is clear that while v_2 appear to have a weaker pseudorapidity dependence at mid-rapidity at the LHC, taking into account the systematic uncertainties, it can also be said to be consistent with the results from PHOBOS at RHIC.

The slope of v_2 vs. η was studied extensively at RHIC, and it was found that it scaled nicely with $\eta - y_{beam}$ - so-called longitudinal scaling. At $\sqrt{s_{\mathrm{NN}}} = 2.76$ TeV the beam-rapidity is 7.99. Shifting these results by 7.99 on the η-axis, and plotting them together with the PHOBOS results presented in Ref. [75] shows that longitudinal scaling for v_2 also holds at LHC energy. The result is shown in Fig. 10.16, where v_2 is calculated vs. $|\eta|$ as $v_2(|\eta|) = 0.5 \cdot (v_2(-\eta) + v_2(\eta))$. This is consistent with what CMS and ATLAS found in Ref. [87,142]. For this result, the measurement is presented for the 0–40% most central events. However, unlike the other results presented here, which utilize the multiplicity weights defined in Section 3.4, this result is event weighted. This means that the analysis was first performed in bins of 0–5%, 5–10%, 10–20%, 20–30% and 30–40% using multiplicity weights, and then the event weighted average over the five bins was calculated. This is similar to what PHOBOS did in their paper, and so it is also done here in order to do a direct comparison. The difference between the event weighted approach shown here and using the usual multiplicity weights is on the order of a few percent.

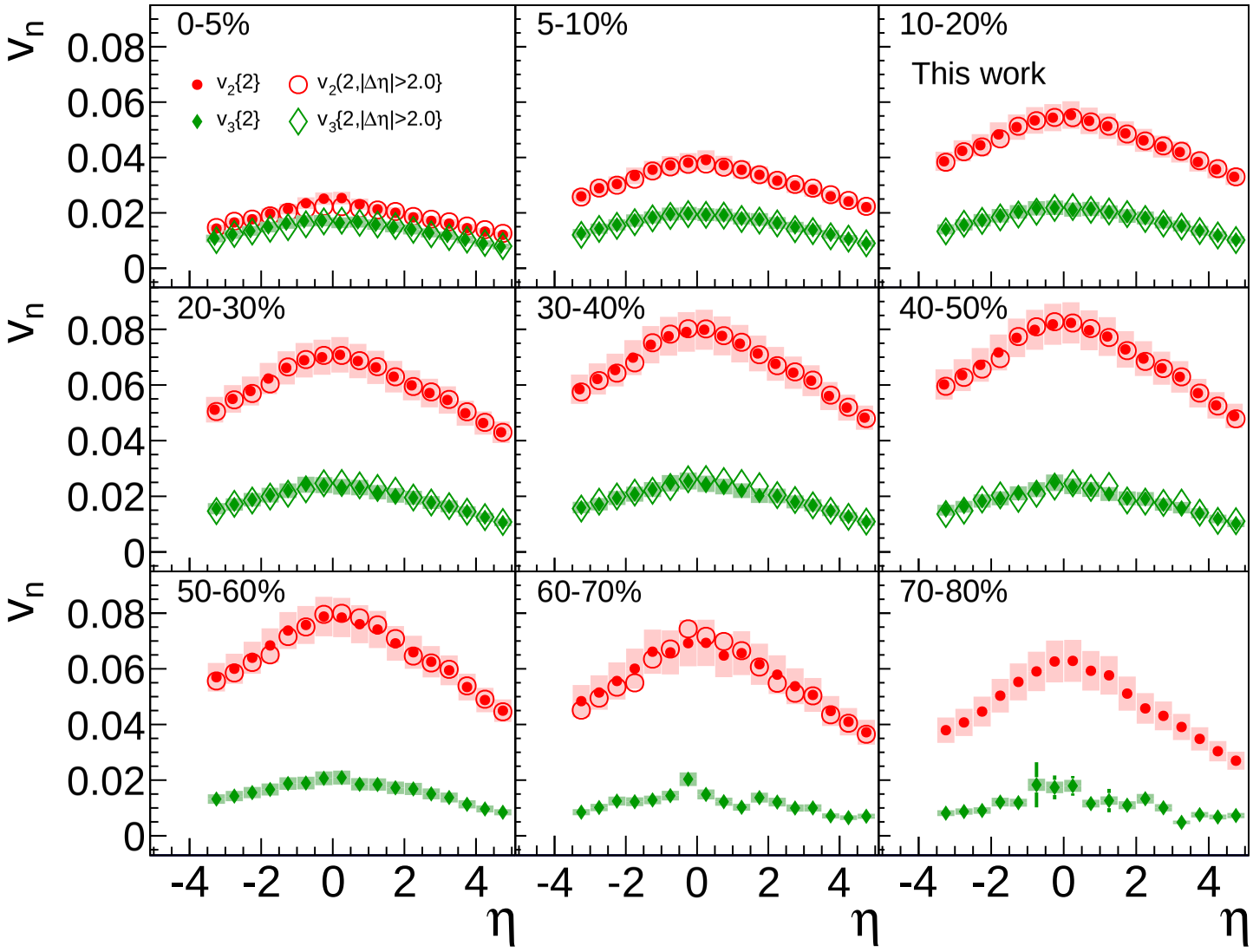

Figure 10.11: $v_2\{2\}$ and $v_3\{2\}$ comparison between using a large rapidity gap and removing the non-flow using HIJING. A good agreement is observed, although the η-gap results are not as statistically stable due to the smaller number of particles selected as RPs.

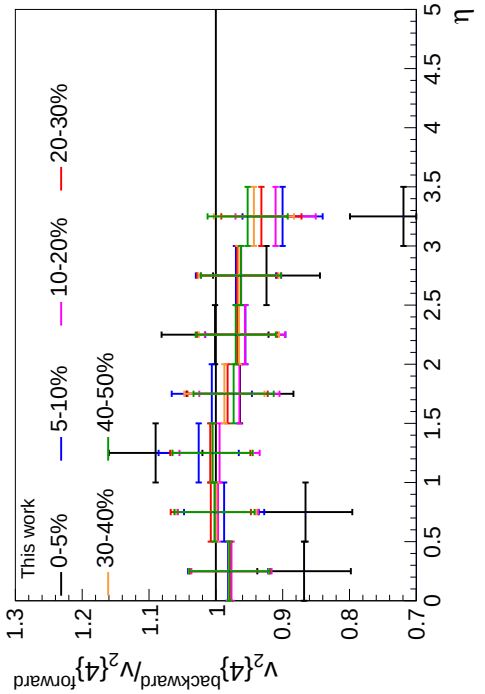

(a) Ratio of $v_2\{2\}(-\eta)/v_2\{2\}(\eta)$ for all centralities. Thin error bars represent 1σ systematic uncertainty.

(b) Ratio of $v_2\{4\}(-\eta)/v_2\{4\}(\eta)$ for all centralities. Thin error bars represent 1σ systematic uncertainty.

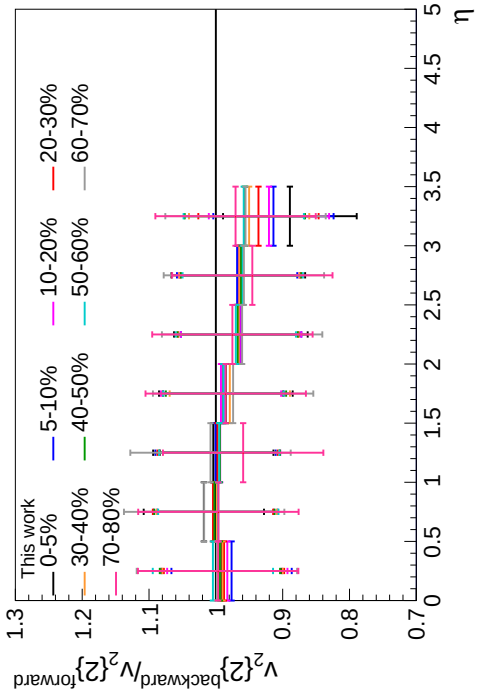

(c) Ratio of $v_3\{2\}(-\eta)/v_3\{2\}(\eta)$ for all centralities. Thin error bars represent 1σ systematic uncertainty.

(d) Ratio of $v_4\{2\}(-\eta)/v_4\{2\}(\eta)$ for all centralities. Thin error bars represent 1σ systematic uncertainty.

Figure 10.12

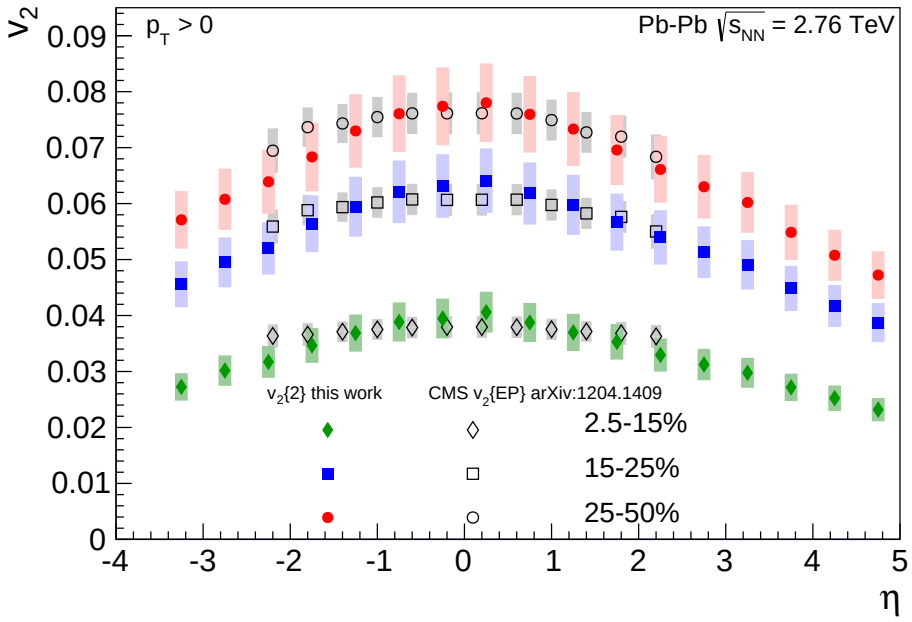

Figure 10.13: Elliptic flow vs. η comparison to CMS [87].

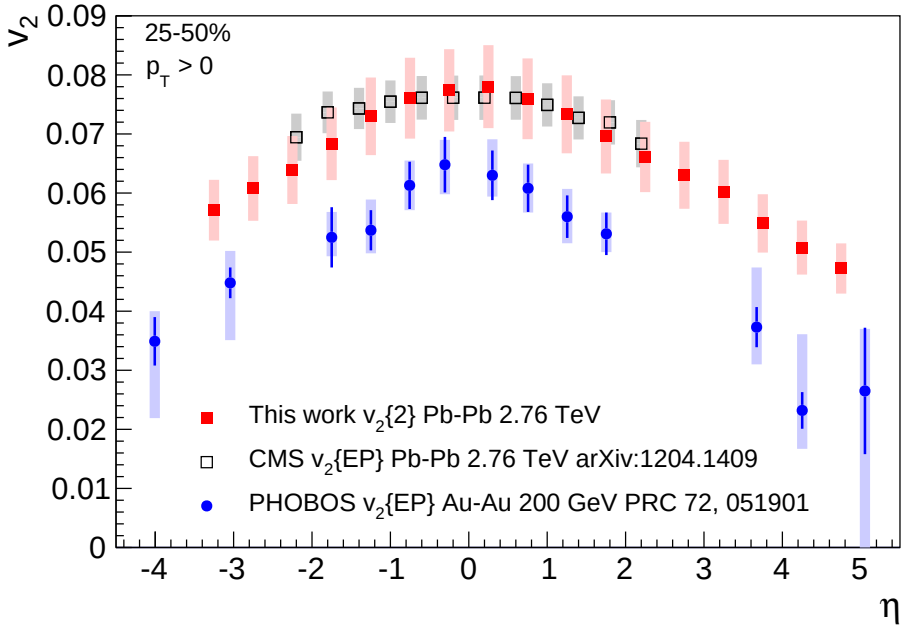

Figure 10.14: Shape of v_2 vs. η between top RHIC energy, and LHC energy. Other experiments are CMS [87] and PHOBOS [143]. Thick error bars for the PHOBOS results represent 90% C.L. systematic uncertainties.

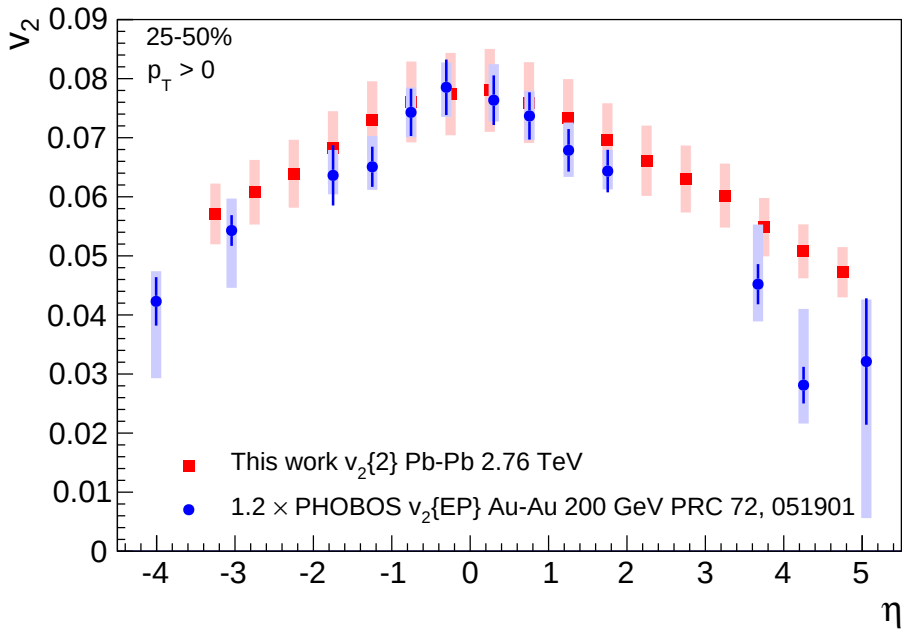

Figure 10.15: v_2 vs. η between top RHIC energy, and LHC energy. The PHOBOS [143] results have been rescaled to match the results of this analysis at mid-rapidity. Taking into account the systematic errors on both measurements, it is not possible to conclude that v_2 has a different shape at the LHC. Thick error bars for the PHOBOS results represent 90% C.L. systematic uncertainties.

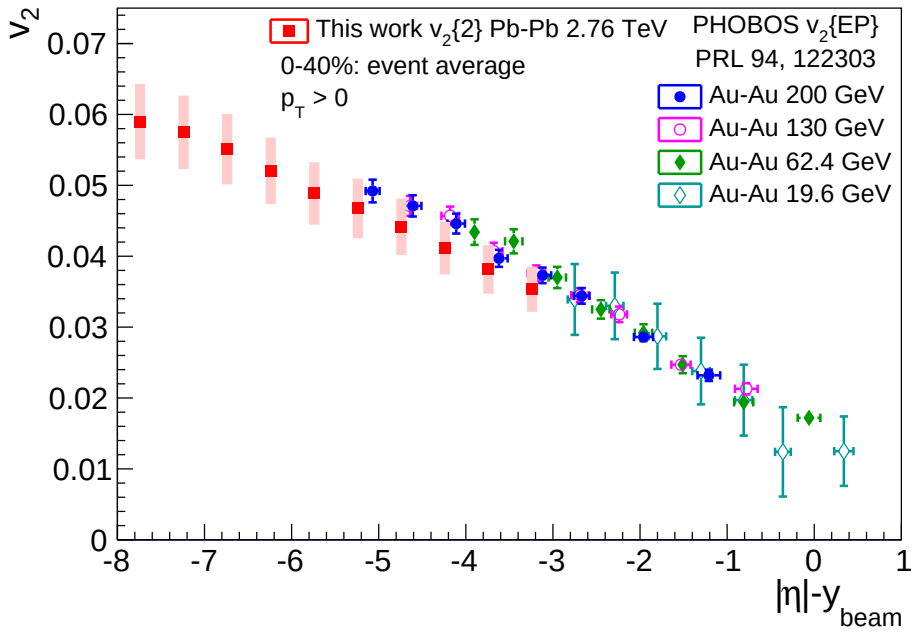

Figure 10.16: $v_2\{2\}$ vs. $|\eta| - y_{beam}$ comparison to PHOBOS [75]. Only statistical errors are shown for the PHOBOS results.

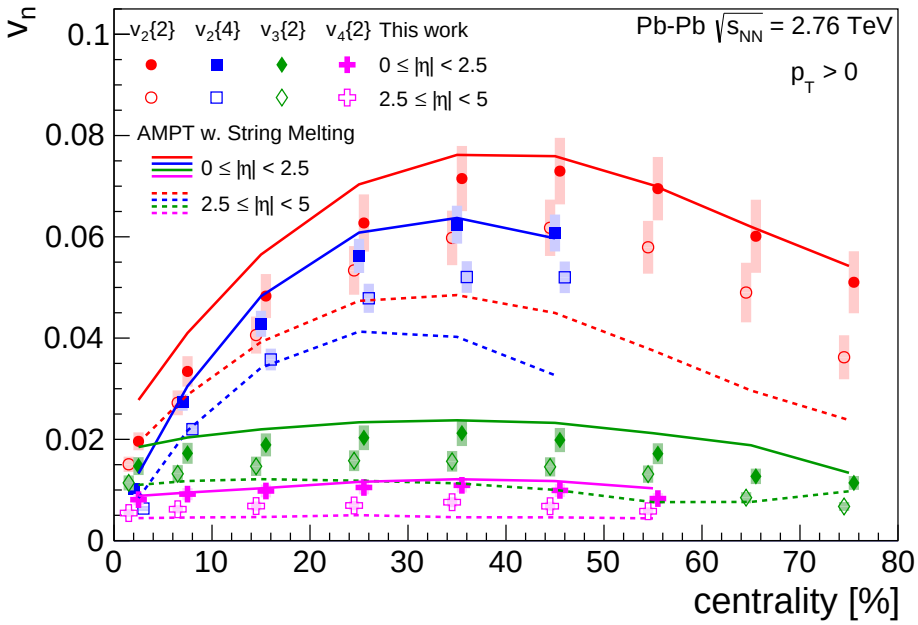

Figure 10.17: Centrality-dependence of the results of this analysis compared to an AMPT simulation with parameters tuned to LHC results at mid-rapidity [127] for the 40–50% central events.

10.4 Model Comparisons

The AMPT model [125] with parameters tuned to mid-rapidity LHC results for semi-central events [127] gives a good description of $v_2\{2\}$, $v_2\{4\}$, $v_3\{2\}$ and $v_4\{2\}$ at mid-rapidity, see Fig. 10.17. At forward rapidity AMPT generally underestimates the flow, this is particularly evident for v_2. The figure also shows, for the first time at the LHC, that the centrality dependence at forward-rapidity is similar to the centrality dependence at mid-rapidity for all of the observables discussed here.

Further comparisons to AMPT is shown in Figs. 10.18 and 10.19, where the 5–10% centrality-bin and the 40–50% centrality-bin, respectively, are shown. For the 40–50% central results there is a very good agreement over the entire rapidity range for v_3 and v_4, even though AMPT is only tuned to mid-rapidity results of v_2 and v_3 in this centrality range. For v_2, AMPT slightly underestimates the flow at forward rapidity. For the most central events, AMPT overestimates the flow, as can also be observed in Fig. 10.17, but the rapidity dependence is still very consistent with what is observed.

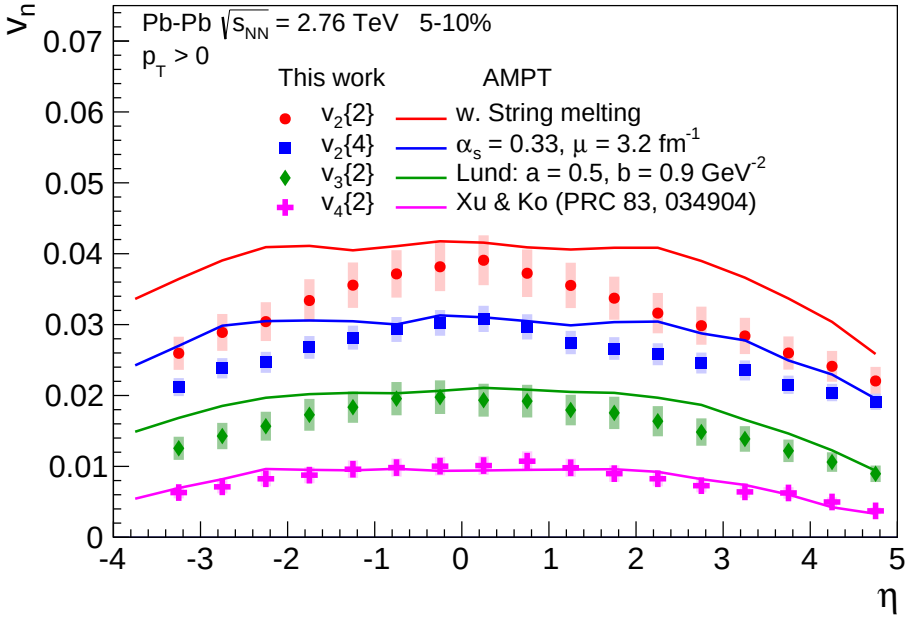

Figure 10.18: η-dependence of the 5–10% central results, compared to AMPT tuned to LHC results a mid-rapidity. For this centrality AMPT overestimates the flow. In particular the elliptic flow.

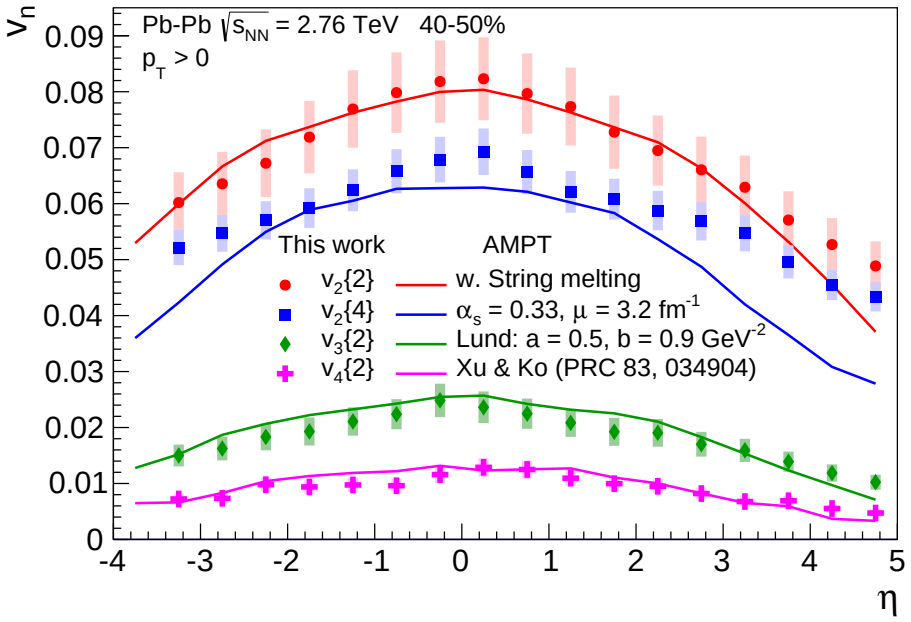

Figure 10.19: η-dependence of the 40–50% central results, compared to AMPT tuned to LHC results a mid-rapidity. This is the rapidity AMPT was tuned to, and a good agreement is observed over the entire range for v_3 and v_4. v_2, however, is underestimated at forward rapidities.

Chapter 11

Conclusions and Outlook

For the analysis presented here, data from the Forward Multiplicity Detector (FMD), the Silicon Pixel Detector (SPD) and Time Projection Chamber of the ALICE experiment were used (Chapter 5). Combining the FMD and SPD coverage yields an η-coverage of more than eight units of pseudorapidity ($-3.5 < \eta < 5$). Results for $v_2\{2\}$, $v_2\{4\}$, $v_3\{2\}$ and $v_4\{2\}$ were presented for up to nine different centralities. The lack of tracking capabilities over much of the covered pseudorapidity-range makes this analysis susceptible to issues that are not normally present in flow analyses. Due to the massive amount of secondary particles hitting the FMD, the effect these particles have on the flow signal has been studied extensively (Chapter 8). In the end, an effective MC-based correction was applied successfully.

These results greatly extend the η-coverage of flow results from the LHC (Chapter 10). It was found that at mid-rapidity the flow has a weak pseudorapidity dependence, perhaps slightly weaker than what was observed at lower energy at the RHIC experiments. Although with a direct comparison it was clear that within the systematic uncertainties the distributions at RHIC and LHC can also be considered consistent. The η-dependence observed by ATLAS and CMS is slightly weaker than what was found here, but also consistent within the systematic uncertainties. In addition, by plotting v_2 vs. $\eta - y_{beam}$, the longitudinal scaling observed by PHOBOS for $\sqrt{s_{\mathrm{NN}}} = 19.6$–$200$ GeV was found to hold up to $\sqrt{s_{\mathrm{NN}}} = 2.76$ TeV. This was previously also observed to be true for $dN/d\eta$ and directed flow, v_1. A paper containing the results of this thesis is currently in progress.

There is still plenty to be done in the future of this analysis. In 2015 the LHC will collide lead–ions at $\sqrt{s_{\mathrm{NN}}} = 5.1$ TeV and there is no reason not to apply the analysis framework developed here to those data. While flow analysis is moving towards event-by-event observables, it seems that the event-by-event fluctuations of secondary particles will make such analysis extremely difficult with the FMD - at least with the currently available methods. However, there are many other observables where the unique η-coverage might prove very valuable. The most obvious example is that of symmetry plane fluctuations. If Ψ_n depends on η, the FMD should be able to measure it. In parallel to this, some of the newly proposed "standard-candles" should be observable with the FMD as well, as they essentially build on the Q-cumulants framework. Although in this context it should be noted that the only statistically stable four-particle cumulant found in this thesis was that of elliptic flow. Consequently, the standard candles may turn out to be too weak to be measured precisely with the FMD.

The field of anisotropic azimuthal flow analysis is characterized by many different approaches to measure the flow harmonics, v_n. Here, the most common methods have been presented and discussed (Chapter 3). Each method has its own strengths and weaknesses. In particular the Q-cumulants method, which was also applied in the analysis of this work, was described in great detail. It is very important to understand the weaknesses of the methods applied. To that end, new calculations on the bias to Q-cumulants from flow fluctuations, non-flow

and particle selection criteria have been presented, and recently published in [60]. There are, however, still some unresolved issues to be worked out. Of particular note are effects from non-uniform azimuthal acceptance (NUA). Here it was shown that a cross-harmonic bias exists, and needs to be taken into account when correcting for NUA, but only calculations for the two-particle cumulant were presented. These calculations should be extended to include multi-particle correlations.

Another hot topic, covered only briefly in this thesis is the observations of collective behaviour in p–Pb collisions, as well as correlation signals in high-multiplicity pp collisions similar to those observed in larger systems. The jury is still out on what to make of these observations. Due to strong non-flow and multiplicity fluctuations, it is not clear if the bias to current methods is fully understood in the case of p–Pb collisions.

Fortunately, heavy-ion physics is a field that is rapidly evolving. Precision measurements and event-by-event observables as well as a new understanding of the role of initial-state fluctuations have resulted in a wealth of new observables and methods. Some of these new observables have been presented in this thesis (Chapter 4). Measurements of v_n per event and observables sensitive to non-linear responses in hydrodynamics seem particularly promising and interesting.

The objective of high-energy heavy-ion physics is to find and study the state of matter known as the quark-gluon plasma (QGP). So far a strongly interacting system has been found and studied (the sQGP). Current observations of the sQGP can be described with models containing relativistic hydrodynamical calculations, suggesting collectivity and a strong interactions (Chapter 2). The anisotropic flow results presented in this thesis are in agreement with the previous observations of a strongly interacting system being formed.

Bibliography

[1] ALICE Collaboration, A. Hansen, "Study of pseudorapidity dependence of the anisotropic flow with ALICE at the LHC," *Nucl.Phys.* **A904-905** (2013) pp. 523c–526c, [arXiv:1210.7095 [nucl-ex]].

[2] BRAHMS Collaboration, I. Arsene *et al.*, "Quark gluon plasma and color glass condensate at RHIC? The Perspective from the BRAHMS experiment," *Nucl.Phys.* **A757** (2005) pp. 1–27, [arXiv:nucl-ex/0410020 [nucl-ex]].

[3] B. Back, M. Baker, M. Ballintijn, D. Barton, B. Becker, *et al.*, "The PHOBOS perspective on discoveries at RHIC," *Nucl.Phys.* **A757** (2005) pp. 28–101, [arXiv:nucl-ex/0410022 [nucl-ex]].

[4] STAR Collaboration, J. Adams *et al.*, "Experimental and theoretical challenges in the search for the quark gluon plasma: The STAR Collaboration's critical assessment of the evidence from RHIC collisions," *Nucl.Phys.* **A757** (2005) pp. 102–183, [arXiv:nucl-ex/0501009 [nucl-ex]].

[5] PHENIX Collaboration, K. Adcox *et al.*, "Formation of dense partonic matter in relativistic nucleus-nucleus collisions at RHIC: Experimental evaluation by the PHENIX collaboration," *Nucl.Phys.* **A757** (2005) pp. 184–283, [arXiv:nucl-ex/0410003 [nucl-ex]].

[6] B. Martin and G. Shaw, "Particle Physics," Wiley, 2nd ed., 2005.

[7] R. K. Ellis, W. J. Stirling, and B. R. Webber, "QCD and Collider Physics," vol. 8 of *Camb.Monogr.Part.Phys.Nucl.Phys.Cosmol.*, Cambridge Univ. Press, 2003. Photography by S. Vascotto.

[8] B. L. Ioffe, V. S. Fadin, and L. N. Lipatov, "Quantum chromodynamics: perturbative and nonperturbative aspects," vol. 30 of *Camb.Monogr.Part.Phys.Nucl.Phys.Cosmol.*, Cambridge Univ. Press, 2010.

[9] E. V. Shuryak, "Quantum Chromodynamics and the Theory of Superdense Matter," *Phys.Rept.* **61** (1980) pp. 71–158.

[10] T. Lee and G. Wick, "Vacuum Stability and Vacuum Excitation in a Spin 0 Field Theory," *Phys.Rev.* **D9** (1974) pp. 2291–2316.

[11] E. V. Shuryak, "Theory of Hadronic Plasma," *Sov.Phys.JETP* **47** (1978) pp. 212–219.

[12] G. Baym, "RHIC: From dreams to beams in two decades," *Nucl.Phys.* **A698** (2002) pp. XXIII–XXXII, [arXiv:hep-ph/0104138 [hep-ph]].

[13] J. Rafelski and J. Birrell, "Traveling Through the Universe: Back in Time to the Quark-Gluon Plasma Era," [arXiv:1311.0075 [nucl-th]].

[14] J. Letessier and J. Rafelski, "Hadrons and quark-gluon plasma," vol. 18 of *Camb.Monogr.Part.Phys.Nucl.Phys.Cosmol.*, Cambridge Univ. Press, 2002.

[15] R. Snellings, "Collective Expansion at the LHC: selected ALICE anisotropic flow measurements," [arXiv:1408.2532 [nucl-ex]].

[16] X.-N. Wang and M. Gyulassy, "HIJING: A Monte Carlo model for multiple jet production in p p, p A and A A collisions," *Phys.Rev.* **D44** (1991) pp. 3501–3516.

[17] M. Gyulassy and X.-N. Wang, "HIJING 1.0: A Monte Carlo program for parton and particle production in high-energy hadronic and nuclear collisions," *Comput.Phys.Commun.* **83** (1994) p. 307, [arXiv:nucl-th/9502021 [nucl-th]].

[18] ALICE Collaboration, K. Aamodt *et al.*, "Centrality dependence of the charged-particle multiplicity density at mid-rapidity in Pb-Pb collisions at $\sqrt{s_{\rm NN}} = 2.76$ TeV," *Phys.Rev.Lett.* **106** (2011) p. 032301, [arXiv:1012.1657 [nucl-ex]].

[19] M. Petran, J. Letessier, J. Rafelski, and G. Torrieri, "SHARE with CHARM," *Comput.Phys.Commun.* **185** (2014) pp. 2056–2079, [arXiv:1310.5108 [hep-ph]].

[20] S. Wheaton and J. Cleymans, "THERMUS: A Thermal model package for ROOT," *Comput.Phys.Commun.* **180** (2009) pp. 84–106, [arXiv:hep-ph/0407174 [hep-ph]].

[21] A. Andronic, P. Braun-Munzinger, and J. Stachel, "Thermal hadron production in relativistic nuclear collisions: The Hadron mass spectrum, the horn, and the QCD phase transition," *Phys.Lett.* **B673** (2009) pp. 142–145, [arXiv:0812.1186 [nucl-th]].

[22] H. Satz, "QCD and QGP: A Summary," [arXiv:hep-ph/9706342 [hep-ph]].

[23] ATLAS Collaboration, G. Aad *et al.*, "Observation of a Centrality-Dependent Dijet Asymmetry in Lead-Lead Collisions at $\sqrt{s_{\rm NN}} = 2.76$ TeV with the ATLAS Detector at the LHC," *Phys.Rev.Lett.* **105** (2010) p. 252303, [arXiv:1011.6182 [hep-ex]].

[24] T. Matsui and H. Satz, "J/ψ Suppression by Quark-Gluon Plasma Formation," *Phys.Lett.* **B178** (1986) p. 416.

[25] H. Satz, "Probing the States of Matter in QCD," *Int.J.Mod.Phys.* **A28** (2013) p. 1330043, [arXiv:1310.1209 [hep-ph]].

[26] NA50 Collaboration, M. Abreu *et al.*, "Evidence for deconfinement of quarks and gluons from the J / psi suppression pattern measured in Pb + Pb collisions at the CERN SPS," *Phys.Lett.* **B477** (2000) pp. 28–36.

[27] PHENIX Collaboration, A. Adare *et al.*, "J/ψ Production vs Centrality, Transverse Momentum, and Rapidity in Au+Au Collisions at $\sqrt{s_{\rm NN}} = 200$ GeV," *Phys.Rev.Lett.* **98** (2007) p. 232301, [arXiv:nucl-ex/0611020 [nucl-ex]].

[28] R. L. Thews, M. Schroedter, and J. Rafelski, "Enhanced J/ψ production in deconfined quark matter," *Phys.Rev.* **C63** (2001) p. 054905, [arXiv:hep-ph/0007323 [hep-ph]].

[29] ALICE Collaboration, B. B. Abelev *et al.*, "Centrality, rapidity and transverse momentum dependence of J/Ψ suppression in Pb-Pb collisions at $\sqrt{s_{\rm NN}} = 2.76$ TeV," *Phys.Lett.* **B734** (2014) pp. 314–327, [arXiv:1311.0214 [nucl-ex]].

[30] STAR Collaboration, L. Adamczyk *et al.*, "Dielectron Mass Spectra from Au+Au Collisions at $\sqrt{s_{\rm NN}} = 200$ GeV," *Phys.Rev.Lett.* **113** (2014) p. 022301, [arXiv:1312.7397 [hep-ex]].

[31] B. Alver and G. Roland, "Collision geometry fluctuations and triangular flow in heavy-ion collisions," *Phys.Rev.* **C81** (2010) p. 054905, [arXiv:1003.0194 [nucl-th]].

[32] CMS Collaboration, S. Chatrchyan *et al.*, "Multiplicity and transverse momentum dependence of two- and four-particle correlations in pPb and PbPb collisions," *Phys.Lett.* **B724** (2013) pp. 213–240, [arXiv:1305.0609 [nucl-ex]].

[33] CMS Collaboration, S. Chatrchyan *et al.*, "Multiparticle correlations in pPb," 2014. Analysis note: CMS-HIN-14-006.

[34] CMS Collaboration, S. Chatrchyan *et al.*, "Long-range and short-range dihadron angular correlations in central PbPb collisions at a nucleon-nucleon center of mass energy of 2.76 TeV," *JHEP* **1107** (2011) p. 076, [arXiv:1105.2438 [nucl-ex]].

[35] CMS Collaboration, S. Chatrchyan *et al.*, "Observation of long-range near-side angular correlations in proton-lead collisions at the LHC," *Phys.Lett.* **B718** (2013) pp. 795–814, [arXiv:1210.5482 [nucl-ex]].

[36] CMS Collaboration, V. Khachatryan *et al.*, "Observation of Long-Range Near-Side Angular Correlations in Proton-Proton Collisions at the LHC," *JHEP* **1009** (2010) p. 091, [arXiv:1009.4122 [hep-ex]].

[37] "CMS - Unexplained long-range correlations observed in pPb collisions." http://cms.web.cern.ch/news/unexplained-long-range-correlations-observed-ppb-collisions. [Online; accessed 16-Aug-2014].

[38] "Quark Matter 2014: Proceedings." http://inspirehep.net/record/1305330. [Online; accessed 17-Sep-2014].

[39] J.-Y. Ollitrault, "Relativistic hydrodynamics for heavy-ion collisions," *Eur.J.Phys.* **29** (2008) pp. 275–302, [arXiv:0708.2433 [nucl-th]].

[40] U. W. Heinz, "Early collective expansion: Relativistic hydrodynamics and the transport properties of QCD matter," [arXiv:0901.4355 [nucl-th]].

[41] T. Hirano, N. van der Kolk, and A. Bilandzic, "Hydrodynamics and Flow," *Lect.Notes Phys.* **785** (2010) pp. 139–178, [arXiv:0808.2684 [nucl-th]].

[42] C. Gale, S. Jeon, and B. Schenke, "Hydrodynamic Modeling of Heavy-Ion Collisions," *Int.J.Mod.Phys.* **A28** (2013) p. 1340011, [arXiv:1301.5893 [nucl-th]].

[43] H. Petersen, "Anisotropic flow in transport+hydrodynamics hybrid approaches," [arXiv:1404.1763 [nucl-th]].

[44] M. L. Miller, K. Reygers, S. J. Sanders, and P. Steinberg, "Glauber modeling in high energy nuclear collisions," *Ann.Rev.Nucl.Part.Sci.* **57** (2007) pp. 205–243, [arXiv:nucl-ex/0701025 [nucl-ex]].

[45] L. McLerran, "Gluon Saturation and the Formation Stage of Heavy Ion Collisions," [arXiv:0807.4095 [hep-ph]].

[46] W. Israel, "Nonstationary irreversible thermodynamics: A Causal relativistic theory," *Annals Phys.* **100** (1976) pp. 310–331.

[47] W. Israel and J. Stewart, "Transient relativistic thermodynamics and kinetic theory," *Annals Phys.* **118** (1979) pp. 341–372.

[48] G. Denicol, T. Kodama, T. Koide, and P. Mota, "Stability and Causality in relativistic dissipative hydrodynamics," *J.Phys.* **G35** (2008) p. 115102, [arXiv:0807.3120 [hep-ph]].

[49] J. M. Maldacena, "The Large N limit of superconformal field theories and supergravity," *Int.J.Theor.Phys.* **38** (1999) pp. 1113–1133, [arXiv:hep-th/9711200 [hep-th]].

[50] M. Luzum and J.-Y. Ollitrault, "Eliminating experimental bias in anisotropic-flow measurements of high-energy nuclear collisions," *Phys.Rev.* **C87** (2013), no. 4 p. 044907, [arXiv:1209.2323 [nucl-ex]].

[51] S. Voloshin and Y. Zhang, "Flow study in relativistic nuclear collisions by Fourier expansion of Azimuthal particle distributions," *Z.Phys.* **C70** (1996) pp. 665–672, [arXiv:hep-ph/9407282 [hep-ph]].

[52] A. M. Poskanzer and S. Voloshin, "Methods for analyzing anisotropic flow in relativistic nuclear collisions," *Phys.Rev.* **C58** (1998) pp. 1671–1678, [arXiv:nucl-ex/9805001 [nucl-ex]].

[53] STAR Collaboration, C. Adler *et al.*, "Elliptic flow from two and four particle correlations in Au+Au collisions at $\sqrt{s_{\rm NN}}$ = 130 GeV," *Phys.Rev.* **C66** (2002) p. 034904, [arXiv:nucl-ex/0206001 [nucl-ex]].

[54] J.-Y. Ollitrault, A. M. Poskanzer, and S. A. Voloshin, "Effect of flow fluctuations and nonflow on elliptic flow methods," *Phys.Rev.* **C80** (2009) p. 014904, [arXiv:0904.2315 [nucl-ex]].

[55] N. Borghini, P. M. Dinh, and J.-Y. Ollitrault, "A New method for measuring azimuthal distributions in nucleus-nucleus collisions," *Phys.Rev.* **C63** (2001) p. 054906, [arXiv:nucl-th/0007063 [nucl-th]].

[56] N. Borghini, P. M. Dinh, and J.-Y. Ollitrault, "Flow analysis from multiparticle azimuthal correlations," *Phys.Rev.* **C64** (2001) p. 054901, [arXiv:nucl-th/0105040 [nucl-th]].

[57] N. Borghini, P. M. Dinh, and J.-Y. Ollitrault, "Flow analysis from cumulants: A Practical guide," [arXiv:nucl-ex/0110016 [nucl-ex]].

[58] A. Bilandzic, "Anisotropic Flow Measurements in ALICE at the Large Hadron Collider,". PhD thesis, Utrecht University, (2012).

[59] A. Bilandzic, R. Snellings, and S. Voloshin, "Flow analysis with cumulants: Direct calculations," *Phys.Rev.* **C83** (2011) p. 044913, [arXiv:1010.0233 [nucl-ex]].

[60] A. Bilandzic, C. H. Christensen, K. Gulbrandsen, A. Hansen, and Y. Zhou, "Generic framework for anisotropic flow analyses with multi-particle azimuthal correlations," *Phys.Rev.* **C89** (2014) p. 064904, [arXiv:1312.3572 [nucl-ex]].

[61] I. Selyuzhenkov and S. Voloshin, "Effects of non-uniform acceptance in anisotropic flow measurement," *Phys.Rev.* **C77** (2008) p. 034904, [arXiv:0707.4672 [nucl-th]].

[62] R. S. Bhalerao, M. Luzum, and J.-Y. Ollitrault, "Determining initial-state fluctuations from flow measurements in heavy-ion collisions," *Phys.Rev.* **C84** (2011) p. 034910, [arXiv:1104.4740 [nucl-th]].

[63] J. Jia and P. Huo, "A method for studying the rapidity fluctuation and decorrelation of harmonic flow in heavy-ion collisions," [arXiv:1402.6680 [nucl-th]].

[64] U. Heinz, Z. Qiu, and C. Shen, "Fluctuating flow angles and anisotropic flow measurements," *Phys.Rev.* **C87** (2013), no. 3 p. 034913, [arXiv:1302.3535 [nucl-th]].

[65] R. Bhalerao, N. Borghini, and J. Ollitrault, "Genuine collective flow from Lee-Yang zeroes," *Phys.Lett.* **B580** (2004) pp. 157–162, [arXiv:nucl-th/0307018 [nucl-th]].

[66] R. Bhalerao, N. Borghini, and J. Ollitrault, "Analysis of anisotropic flow with Lee-Yang zeroes," *Nucl.Phys.* **A727** (2003) pp. 373–426, [arXiv:nucl-th/0310016 [nucl-th]].

[67] N. Borghini, R. Bhalerao, and J. Ollitrault, "Anisotropic flow from Lee-Yang zeroes: A Practical guide," *J.Phys.* **G30** (2004) pp. S1213–S1216, [arXiv:nucl-th/0402053 [nucl-th]].

[68] A. Bilandzic, N. van der Kolk, J.-Y. Ollitrault, and R. Snellings, "Event-plane flow analysis without non-flow effects," *Phys.Rev.* **C83** (2011) p. 014909, [arXiv:0801.3915 [nucl-ex]].

[69] P. Naselsky, C. Christensen, P. Christensen, P. Damgaard, A. Frejsel, *et al.*, "Morphology of High-Multiplicity Events in Heavy Ion Collisions," *Phys.Rev.* **C86** (2012) p. 024916, [arXiv:1204.0387 [hep-ph]].

[70] ATLAS Collaboration, G. Aad *et al.*, "Measurement of the distributions of event-by-event flow harmonics in lead-lead collisions at = 2.76 TeV with the ATLAS detector at the LHC," *JHEP* **1311** (2013) p. 183, [arXiv:1305.2942 [hep-ex]].

[71] ATLAS Collaboration, G. Aad *et al.*, "Measurement of the azimuthal anisotropy for charged particle production in $\sqrt{s_{\rm NN}}$ = 2.76 TeV lead-lead collisions with the ATLAS detector," *Phys.Rev.* **C86** (2012) p. 014907, [arXiv:1203.3087 [hep-ex]].

[72] CMS, S. Chatrchyan *et al.*, "Studies of azimuthal dihadron correlations in ultra-central PbPb collisions at $\sqrt{s_{\rm NN}}$ = 2.76 TeV," *JHEP* **1402** (2014) p. 088, [arXiv:1312.1845 [nucl-ex]].

[73] J.-Y. Ollitrault, "Anisotropy as a signature of transverse collective flow," *Phys.Rev.* **D46** (1992) pp. 229–245.

[74] ALICE Collaboration, K. Aamodt *et al.*, "Elliptic flow of charged particles in Pb-Pb collisions at 2.76 TeV," *Phys.Rev.Lett.* **105** (2010) p. 252302, [arXiv:1011.3914 [nucl-ex]].

[75] PHOBOS Collaboration, B. Back *et al.*, "Energy dependence of elliptic flow over a large pseudorapidity range in Au+Au collisions at RHIC," *Phys.Rev.Lett.* **94** (2005) p. 122303, [arXiv:nucl-ex/0406021 [nucl-ex]].

[76] C. Gale, S. Jeon, B. Schenke, P. Tribedy, and R. Venugopalan, "Event-by-event anisotropic flow in heavy-ion collisions from combined Yang-Mills and viscous fluid dynamics," *Phys.Rev.Lett.* **110** (2013) p. 012302, [arXiv:1209.6330 [nucl-th]].

[77] M. Luzum and J.-Y. Ollitrault, "Extracting the shear viscosity of the quark-gluon plasma from flow in ultra-central heavy-ion collisions," *Nucl.Phys.* **A904-905** (2013) pp. 377c–380c, [arXiv:1210.6010 [nucl-th]].

[78] C. Nonaka and S. A. Bass, "Space-time evolution of bulk QCD matter," *Phys.Rev.* **C75** (2007) p. 014902, [arXiv:nucl-th/0607018 [nucl-th]].

[79] B. Schenke, S. Jeon, and C. Gale, "Elliptic and triangular flow in event-by-event (3+1)D viscous hydrodynamics," *Phys.Rev.Lett.* **106** (2011) p. 042301, [arXiv:1009.3244 [hep-ph]].

[80] STAR Collaboration, J. Adams *et al.*, "Azimuthal anisotropy at RHIC: The First and fourth harmonics," *Phys.Rev.Lett.* **92** (2004) p. 062301, [arXiv:nucl-ex/0310029 [nucl-ex]].

[81] F. Cooper and G. Frye, "Comment on the Single Particle Distribution in the Hydrodynamic and Statistical Thermodynamic Models of Multiparticle Production," *Phys.Rev.* **D10** (1974) p. 186.

[82] PHENIX Collaboration, A. Adare *et al.*, "Deviation from quark-number scaling of the anisotropy parameter v_2 of pions, kaons, and protons in Au+Au collisions at $\sqrt{s_{\rm NN}} = 200$ GeV," *Phys.Rev.* **C85** (2012) p. 064914, [arXiv:1203.2644 [nucl-ex]].

[83] ALICE Collaboration, B. B. Abelev *et al.*, "Elliptic flow of identified hadrons in Pb-Pb collisions at $\sqrt{s_{\rm NN}} = 2.76$ TeV," [arXiv:1405.4632 [nucl-ex]].

[84] CMS Collaboration, S. Chatrchyan *et al.*, "Measurement of higher-order harmonic azimuthal anisotropy in PbPb collisions at a nucleon-nucleon center-of-mass energy of 2.76 TeV," [arXiv:1310.8651 [nucl-ex]].

[85] STAR Collaboration, J. Adams *et al.*, "Azimuthal anisotropy in Au+Au collisions at $\sqrt{s_{\rm NN}} = 200$ GeV," *Phys.Rev.* **C72** (2005) p. 014904, [arXiv:nucl-ex/0409033 [nucl-ex]].

[86] E. B. Johnson, "Rapidity dependence of elliptic flow at RHIC," *AIP Conf.Proc.* **842** (2006) pp. 137–139, [arXiv:nucl-ex/0601010 [nucl-ex]].

[87] CMS Collaboration, S. Chatrchyan *et al.*, "Measurement of the elliptic anisotropy of charged particles produced in PbPb collisions at nucleon-nucleon center-of-mass energy = 2.76 TeV," *Phys.Rev.* **C87** (2013) p. 014902, [arXiv:1204.1409 [nucl-ex]].

[88] I. Selyuzhenkov, "Charged particle directed flow in Pb-Pb collisions at $\sqrt{s_{\rm NN}} = 2.76$ TeV measured with ALICE at the LHC," *J.Phys.* **G38** (2011) p. 124167, [arXiv:1106.5425 [nucl-ex]].

[89] ALICE Collaboration, E. Abbas *et al.*, "Centrality dependence of the pseudorapidity density distribution for charged particles in Pb-Pb collisions at $\sqrt{s_{\rm NN}} = 2.76$ TeV," *Phys.Lett.* **B726** (2013) pp. 610–622, [arXiv:1304.0347 [nucl-ex]].

[90] PHOBOS Collaboration, B. Alver *et al.*, "Event-by-Event Fluctuations of Azimuthal Particle Anisotropy in Au + Au Collisions at $\sqrt{s_{\rm NN}} = 200$ GeV," *Phys.Rev.Lett.* **104** (2010) p. 142301, [arXiv:nucl-ex/0702036 [nucl-ex]].

[91] S. A. Voloshin, A. M. Poskanzer, A. Tang, and G. Wang, "Elliptic flow in the Gaussian model of eccentricity fluctuations," *Phys.Lett.* **B659** (2008) pp. 537–541, [arXiv:0708.0800 [nucl-th]].

[92] L. Yan, J.-Y. Ollitrault, and A. M. Poskanzer, "Eccentricity distributions in nucleus-nucleus collisions," *Phys.Rev.* **C90** (2014) p. 024903, [arXiv:1405.6595 [nucl-th]].

[93] H. Niemi, G. Denicol, H. Holopainen, and P. Huovinen, "Event-by-event distributions of azimuthal asymmetries in ultrarelativistic heavy-ion collisions," *Phys.Rev.* **C87** (2013) p. 054901, [arXiv:1212.1008 [nucl-th]].

[94] P. Huo, J. Jia, and S. Mohapatra, "Elucidating the event-by-event flow fluctuations in heavy-ion collisions via the event shape selection technique," [arXiv:1311.7091 [nucl-ex]].

[95] F. G. Gardim, F. Grassi, M. Luzum, and J.-Y. Ollitrault, "Breaking of factorization of two-particle correlations in hydrodynamics," *Phys.Rev.* **C87** (2013), no. 3 p. 031901, [arXiv:1211.0989 [nucl-th]].

[96] ATLAS Collaboration, G. Aad *et al.*, "Measurement with the ATLAS detector of multi-particle azimuthal correlations in p+Pb collisions at $\sqrt{s_{\rm NN}} = 5.02$ TeV," *Phys.Lett.* **B725** (2013) pp. 60–78, [arXiv:1303.2084 [hep-ex]].

[97] ALICE Collaboration, B. B. Abelev *et al.*, "Long-range angular correlations of pi, K and p in p–Pb collisions at $\sqrt{s_{\rm NN}} = 5.02$ TeV," *Phys.Lett.* **B726** (2013) pp. 164–177, [arXiv:1307.3237 [nucl-ex]].

[98] K. Werner, M. Bleicher, B. Guiot, I. Karpenko, and T. Pierog, "Evidence for flow in pPb collisions at 5 TeV from v2 mass splitting," *Phys.Rev.Lett.* **112** (2014) p. 232301, [arXiv:1307.4379 [nucl-th]].

[99] J. Schukraft, A. Timmins, and S. A. Voloshin, "Ultra-relativistic nuclear collisions: event shape engineering," *Phys.Lett.* **B719** (2013) pp. 394–398, [arXiv:1208.4563 [nucl-ex]].

[100] D. Teaney and L. Yan, "Non linearities in the harmonic spectrum of heavy ion collisions with ideal and viscous hydrodynamics," *Phys.Rev.* **C86** (2012) p. 044908, [arXiv:1206.1905 [nucl-th]].

[101] F. G. Gardim, F. Grassi, M. Luzum, and J.-Y. Ollitrault, "Mapping the hydrodynamic response to the initial geometry in heavy-ion collisions," *Phys.Rev.* **C85** (2012) p. 024908, [arXiv:1111.6538 [nucl-th]].

[102] ATLAS Collaboration, G. Aad *et al.*, "Measurement of event-plane correlations in $\sqrt{s_{\rm NN}} =$ 2.76 TeV lead-lead collisions with the ATLAS detector," [arXiv:1403.0489 [hep-ex]].

[103] ALICE Collaboration, K. Aamodt *et al.*, "The ALICE experiment at the CERN LHC," *JINST* **3** (2008) p. S08002.

[104] C. Holm Christensen, "ALICE Forward Multiplicity Detector,". PhD thesis, Niels Bohr Institute, Copenhagen University, (2007).

[105] ALICE Collaboration, P. Cortese *et al.*, "ALICE technical design report on forward detectors: FMD, T0 and V0," tech. rep., (2004).

[106] ALICE Collaboration, G. Dellacasa *et al.*, "ALICE technical design report of the inner tracking system (ITS)," tech. rep., (1999).

[107] ALICE Collaboration, G. Dellacasa *et al.*, "ALICE: Technical design report of the time projection chamber," tech. rep., (2000).

[108] ALICE Collaboration, L. Musa and K. Safarik, "Letter of Intent for the Upgrade of the ALICE Experiment," Tech. Rep. CERN-LHCC-2012-012. LHCC-I-022, CERN, Geneva, (Aug 2012).

[109] ALICE Collaboration, "Upgrade of the ALICE Inner Tracking System," Tech. Rep. CERN-LHCC-2013-024. ALICE-TDR-017, CERN, Geneva, (Nov 2013).

[110] ALICE Collaboration, "Upgrade of the ALICE Time Projection Chamber," Tech. Rep. CERN-LHCC-2013-020. ALICE-TDR-016, CERN, Geneva, (Oct 2013).

[111] ALICE Collaboration, "Addendum to the Letter Of Intent for the Upgrade of the ALICE Experiment : The Muon Forward Tracker," Tech. Rep. CERN-LHCC-2013-014. LHCC-I-022-ADD-1, CERN, Geneva, (Aug 2013).

[112] ALICE Collaboration, "Upgrade of the ALICE Readout &; Trigger System," Tech. Rep. CERN-LHCC-2013-019. ALICE-TDR-015, CERN, Geneva, (Sep 2013).

[113] H. H. Dalsgaard, "Pseudorapidity Densities in p+p and Pb+Pb collisions at LHC measured with the ALICE experiment,". PhD thesis, Niels Bohr Institute, Copenhagen University, (2011).

[114] C. Nygaard, "Charged particle multiplicity distributions into forward pseudorapidities in pp and PbPb collisions at the LHC,". PhD thesis, Niels Bohr Institute, Copenhagen University, (2011).

[115] ALICE Collaboration, E. Abbas *et al.*, "Performance of the ALICE VZERO system," *JINST* **8** (2013) p. P10016, [arXiv:1306.3130 [nucl-ex]].

[116] ALICE Collaboration, R. Santoro, "Status of the ALICE silicon pixel detector," *Nucl.Instrum.Meth.* **A581** (2007) pp. 330–334.

[117] J. F. Grosse-Oetringhaus, "Measurement of the Charged-Particle Multiplicity in Proton-Proton Collisions with the ALICE Detector,". PhD thesis, University of Munster, (2009).

[118] P. Billoir, "Progressive track recognition with a Kalman like fitting procedure," *Comput.Phys.Commun.* **57** (1989) pp. 390–394.

[119] ALICE Collaboration, B. Alessandro *et al.*, "ALICE: Physics performance report, volume II," *J.Phys.* **G32** (2006) pp. 1295–2040.

[120] B. Alver, M. Baker, C. Loizides, and P. Steinberg, "The PHOBOS Glauber Monte Carlo," [arXiv:0805.4411 [nucl-ex]].

[121] T. Sjostrand, S. Mrenna, and P. Z. Skands, "PYTHIA 6.4 Physics and Manual," *JHEP* **0605** (2006) p. 026, [arXiv:hep-ph/0603175 [hep-ph]].

[122] H.-U. Bengtsson and T. Sjostrand, "The Lund Monte Carlo for Hadronic Processes: Pythia Version 4.8," *Comput.Phys.Commun.* **46** (1987) p. 43.

[123] T. Sjostrand, "The Lund Monte Carlo for Jet Fragmentation and e+ e- Physics: Jetset Version 6.2," *Comput.Phys.Commun.* **39** (1986) pp. 347–407.

[124] ALICE Collaboration, K. Aamodt *et al.*, "Charged-particle multiplicity density at mid-rapidity in central Pb-Pb collisions at $\sqrt{s_{\rm NN}} = 2.76$ TeV," *Phys.Rev.Lett.* **105** (2010) p. 252301, [arXiv:1011.3916 [nucl-ex]].

[125] Z.-W. Lin, C. M. Ko, B.-A. Li, B. Zhang, and S. Pal, "A Multi-phase transport model for relativistic heavy ion collisions," *Phys.Rev.* **C72** (2005) p. 064901, [arXiv:nucl-th/0411110 [nucl-th]].

[126] B. Zhang, "ZPC 1.0.1: A Parton cascade for ultrarelativistic heavy ion collisions," *Comput.Phys.Commun.* **109** (1998) pp. 193–206, [arXiv:nucl-th/9709009 [nucl-th]].

[127] J. Xu and C. M. Ko, "Pb-Pb collisions at $\sqrt{s_{\rm NN}} = 2.76$ TeV in a multiphase transport model," *Phys.Rev.* **C83** (2011) p. 034904, [arXiv:1101.2231 [nucl-th]].

[128] L.-W. Chen and C. M. Ko, "System size dependence of elliptic flows in relativistic heavy-ion collisions," *Phys.Lett.* **B634** (2006) pp. 205–209, [arXiv:nucl-th/0505044 [nucl-th]].

[129] B.-A. Li and C. M. Ko, "Formation of superdense hadronic matter in high-energy heavy ion collisions," *Phys.Rev.* **C52** (1995) pp. 2037–2063, [arXiv:nucl-th/9505016 [nucl-th]].

[130] J. Xu and C. M. Ko, "Triangular flow in heavy ion collisions in a multiphase transport model," *Phys.Rev.* **C84** (2011) p. 014903, [arXiv:1103.5187 [nucl-th]].

[131] J. Xu and C. M. Ko, "Higher-order anisotropic flows and dihadron correlations in Pb-Pb collisions at $\sqrt{s_{\rm NN}} = 2.76$ TeV in a multiphase transport model," *Phys.Rev.* **C84** (2011) p. 044907, [arXiv:1108.0717 [nucl-th]].

[132] R. Brun, F. Carminati, and S. Giani, "GEANT Detector Description and Simulation Tool," 1994. CERN Program Library Long Writeup.

[133] GEANT4, S. Agostinelli *et al.*, "GEANT4: A Simulation toolkit," *Nucl.Instrum.Meth.* **A506** (2003) pp. 250–303.

[134] "AliROOT - The ALICE Off-line Project." http://aliweb.cern.ch/Offline/. [Online; accessed 24-Sep-2014].

[135] "ROOT - A Data Analysis Framework." http://root.cern.ch/. [Online; accessed 24-Sep-2014].

[136] "ALICE TWiki - Trigger Coordination." https://twiki.cern.ch/twiki/bin/viewauth/ALICE/TriggerCoordination. [Online; ALICE users only; accessed 07-Sep-2014].

[137] ALICE Collaboration, B. Abelev *et al.*, "Centrality determination of Pb-Pb collisions at $\sqrt{s_{\rm NN}} = 2.76$TeV with ALICE," *Phys.Rev.* **C88** (2013), no. 4 p. 044909, [arXiv:1301.4361 [nucl-ex]].

[138] K. Gulbrandsen. Private Communication.

[139] ALICE Collaboration, K. Aamodt *et al.*, "Harmonic decomposition of two-particle angular correlations in Pb-Pb collisions at $\sqrt{s_{NN}} = 2.76$ TeV," *Phys.Lett.* **B708** (2012) pp. 249–264, [arXiv:1109.2501 [nucl-ex]].

[140] ALICE Collaboration, K. Aamodt *et al.*, "Higher harmonic anisotropic flow measurements of charged particles in Pb-Pb collisions at $\sqrt{s_{\rm NN}} = 2.76$ TeV," *Phys.Rev.Lett.* **107** (2011) p. 032301, [arXiv:1105.3865 [nucl-ex]].

[141] ALICE Collaboration, B. Abelev *et al.*, "Anisotropic flow of charged hadrons, pions and (anti-)protons measured at high transverse momentum in Pb-Pb collisions at $\sqrt{s_{\rm NN}} = 2.76$ TeV," *Phys.Lett.* **B719** (2013) pp. 18–28, [arXiv:1205.5761 [nucl-ex]].

[142] ATLAS Collaboration, G. Aad *et al.*, "Measurement of the centrality and pseudorapidity dependence of the integrated elliptic flow in lead-lead collisions at $\sqrt{s_{\rm NN}} = 2.76$ TeV with the ATLAS detector," [arXiv:1405.3936 [hep-ex]].

[143] PHOBOS Collaboration, B. Back *et al.*, "Centrality and pseudorapidity dependence of elliptic flow for charged hadrons in Au+Au collisions at $\sqrt{s_{\rm NN}} = 200$ GeV," *Phys.Rev.* **C72** (2005) p. 051901, [arXiv:nucl-ex/0407012 [nucl-ex]].

Appendices

Appendix A

Detailed Derivations of Bias to Differential Flow Caused by Flow Fluctuations

This appendix contains detailed calculations of the results presented in Section 3.4.4 regarding bias from flow fluctuations caused by different particle selection criteria. Subscript n on flow harmonics is suppressed in all equations for simplicity. It was shown that for reference flow:

$$v\{2\} = \langle v \rangle + \frac{1}{2}\frac{\sigma_v^2}{\langle v \rangle}, \tag{A.1}$$

$$v\{4\} = \langle v \rangle - \frac{1}{2}\frac{\sigma_v^2}{\langle v \rangle}, \tag{A.2}$$

where $\langle v \rangle$ is the mean value of the flow harmonic of interest and σ_v^2 is the variance of that flow harmonic. This can be obtained by assuming $\sigma_v^2/\langle v \rangle^2 \ll 1$ and using [58]:

$$\langle f(x) \rangle \equiv E[f(x)] \approx f(\mu_x) + \frac{\sigma_x^2}{2} f''(\mu_x), \tag{A.3}$$

where $E[x]$ is the expectation value of a random variable x, $f(x)$ is any function, μ_x is the mean of x, and σ_x is the standard deviation of x. Below the same calculations are done for the two- and four-particle differential cumulants.

A.1 $v'\{2\}$

The differential two-particle cumulant estimate, $v'\{2\}$, is obtained by [56]:

$$v'\{2\} = \frac{\langle v'v \rangle}{\sqrt{\langle v^2 \rangle}}, \tag{A.4}$$

where v is the flow harmonic of the reference particles (RPs) and v' is the differential flow harmonic of the particles of interest (POIs). Inserting Eq. (A.1) for $\sqrt{\langle v^2 \rangle}$ and again assuming $\sigma_v^2/\langle v \rangle^2 \ll 1$ yields:

$$v'\{2\} \approx \frac{\langle v'v \rangle}{\langle v \rangle}\left(1 - \frac{1}{2}\frac{\sigma_v^2}{\langle v \rangle^2}\right). \tag{A.5}$$

The main issue is then to determine $\langle v'v \rangle$. In general:

$$\langle v'v \rangle = \langle v' \rangle \langle v \rangle + \rho\, \sigma_{v'} \sigma_v, \tag{A.6}$$

where ρ is the correlation coefficient between the reference flow and the differential flow and is defined in the range $[-1, 1]$, where specifically $\rho = 1$ in the case where v and v' are perfectly correlated, $\rho = 0$ when they are uncorrelated and $\rho = -1$ when they are anti-correlated. $\sigma_{v'}$ is the standard deviation of the flow harmonic for POIs. This means:

$$v'\{2\} \approx \langle v' \rangle \left(1 + \rho \frac{\sigma_{v'}\sigma_v}{\langle v' \rangle \langle v \rangle} - \frac{1}{2}\frac{\sigma_v^2}{\langle v \rangle^2}\right), \tag{A.7}$$

from which it is clearly seen that $v'\{2\}$ can be either *suppressed* or *enhanced* by flow fluctuations depending on the value of ρ.

A.2 $v'\{4\}$

The differential four-particle cumulant estimate, $v'\{4\}$, is obtained by [56]:

$$v'\{4\} = \frac{-\langle v'v^3 \rangle + 2\langle v'v \rangle \langle v^2 \rangle}{(v\{4\})^3}. \tag{A.8}$$

Using Eq. (A.2) this becomes:

$$v'\{4\} = \frac{-\langle v'v^3 \rangle + 2\langle v'v \rangle \langle v^2 \rangle}{\langle v \rangle^3} \left(1 + \frac{3}{2}\frac{\sigma_v^2}{\langle v \rangle^2}\right). \tag{A.9}$$

$-\langle v'v^3 \rangle + 2\langle v'v \rangle \langle v^2 \rangle$ must now be estimated. By using:

$$\begin{aligned} Var\left[f(x)\right] &\equiv E[f(x)^2] - E[f(x)]^2 \\ &\approx \left(f'\left(\mu_x\right)\right)^2 Var[x], \end{aligned} \tag{A.10}$$

then

$$\begin{aligned} \langle v'v^3 \rangle &= \langle v' \rangle \langle v^3 \rangle + \rho' \sigma_{v'} \sigma_{v^3} \\ &\approx \langle v' \rangle \left(\langle v \rangle^3 + 3\sigma_v^2 \langle v \rangle\right) + \rho \sigma_{v'} 3 \langle v \rangle^2 \sigma_v \\ &= \langle v' \rangle \langle v \rangle^3 + 3\langle v' \rangle \langle v \rangle \sigma_v^2 + 3\rho \langle v \rangle^2 \sigma_{v'} \sigma_v, \end{aligned} \tag{A.11}$$

where Eq. (A.3) was also used for $\langle v^3 \rangle$. ρ' is the correlation between $\sigma_{v'}$ and σ_{v^3}, applying the approximation in Eq. (A.10) to get to σ_v yields the correlation between $\sigma_{v'}$ and σ_v, which is ρ to first order. The next term to be estimated:

$$\begin{aligned} 2\langle v'v \rangle \langle v^2 \rangle &= 2\left(\langle v' \rangle \langle v \rangle + \rho \sigma_{v'} \sigma_v\right)\left(\sigma_v^2 + \langle v \rangle^2\right) \\ &= 2\langle v' \rangle \langle v \rangle \sigma_v^2 + 2\langle v' \rangle \langle v \rangle^3 + 2\rho \langle v \rangle^2 \sigma_v \sigma_{v'} + 2\rho \sigma_{v'} \sigma_v^3 \end{aligned} \tag{A.12}$$

The last term in Eq. (A.12) is of order $\mathcal{O}(\sigma_v^3 \sigma_{v'})$ and can be neglected. Inserting these results into Eq. (A.9) it is seen that flow fluctuations bias $v'\{4\}$ in the following way:

$$\begin{aligned} v'\{4\} &\approx \frac{\langle v' \rangle \langle v \rangle^3 - \langle v' \rangle \langle v \rangle \sigma_v^2 - \rho \langle v \rangle^2 \sigma_{v'} \sigma_v}{\langle v \rangle^3} \left(1 + \frac{3}{2}\frac{\sigma_v^2}{\langle v \rangle^2}\right) \\ &= \langle v' \rangle \left(1 - \frac{\sigma_v^2}{\langle v \rangle^2} - \rho \frac{\sigma_{v'}\sigma_v}{\langle v' \rangle \langle v \rangle}\right)\left(1 + \frac{3}{2}\frac{\sigma_v^2}{\langle v \rangle^2}\right) \\ &\approx \langle v' \rangle \left(1 - \rho \frac{\sigma_{v'}\sigma_v}{\langle v' \rangle \langle v \rangle} + \frac{1}{2}\frac{\sigma_v^2}{\langle v \rangle^2}\right), \end{aligned} \tag{A.13}$$

which once again can lead to either *suppression* or *enhancement* of flow fluctuations. In general one can write:

$$v'\{^2_4\} \approx \langle v' \rangle \left(1 \pm \rho \frac{\sigma_{v'}\sigma_v}{\langle v' \rangle \langle v \rangle} \mp \frac{1}{2}\frac{\sigma_v^2}{\langle v \rangle^2}\right), \tag{A.14}$$

showing that the bias to the two- and four-particle cumulants is similar but opposite.

Appendix B

Detailed Derivations of Bias From Other Harmonics When Correcting for Non-Uniform Acceptance

This appendix contains detailed calculation of the results presented in Section 3.4.7 regarding bias from other harmonics when dealing with a non-uniform acceptance (NUA). The goal is to evaluate the following five integrals in the case of NUA:

$$\textcircled{1} = \int_0^{2\pi} d\bar{\Psi} \int_{\varphi_a}^{\varphi_b} d\varphi_i \int_{\varphi_a}^{\varphi_b} d\varphi_j e^{in(\varphi_i - \varphi_j)} \cdot 1, \tag{B.1}$$

$$\textcircled{2} = \int_0^{2\pi} d\bar{\Psi} \int_{\varphi_a}^{\varphi_b} d\varphi_i \int_{\varphi_a}^{\varphi_b} d\varphi_j e^{in(\varphi_i - \varphi_j)} \cdot 2\sum_n v_n \cos(n(\varphi_i - \Psi_n)), \tag{B.2}$$

$$\textcircled{3} = \int_0^{2\pi} d\bar{\Psi} \int_{\varphi_a}^{\varphi_b} d\varphi_i \int_{\varphi_a}^{\varphi_b} d\varphi_j e^{in(\varphi_i - \varphi_j)} \cdot 2\sum_m v_m \cos(m(\varphi_j - \Psi_m)), \tag{B.3}$$

$$\textcircled{4} = \int_0^{2\pi} d\bar{\Psi} \int_{\varphi_a}^{\varphi_b} d\varphi_i \int_{\varphi_a}^{\varphi_b} d\varphi_j e^{in(\varphi_i - \varphi_j)} \cdot 4\sum_k v_k^2 \cos(k(\varphi_i - \Psi_k))\cos(k(\varphi_j - \Psi_k)), \tag{B.4}$$

$$\textcircled{5} = \int_0^{2\pi} d\bar{\Psi} \int_{\varphi_a}^{\varphi_b} d\varphi_i \int_{\varphi_a}^{\varphi_b} d\varphi_j e^{in(\varphi_i - \varphi_j)} \cdot 4\sum_{\substack{j,l \\ j\neq l}} v_j v_l \cos(j(\varphi_i - \Psi_j))\cos(l(\varphi_j - \Psi_l)). \tag{B.5}$$

In the case of a detector with NUA, either $\varphi_a \neq 0$ or $\varphi_b \neq 2\pi$. Both may also be true, and in case the detector used has more than one hole it is possible to do:

$$\int_0^{2\pi} d\bar{\Psi} \int_{\varphi_a}^{\varphi_b} d\varphi_i \int_{\varphi_a}^{\varphi_b} d\varphi_j \to \sum_\alpha \left(\int_0^{2\pi} d\bar{\Psi} \int_{\varphi_{a,\alpha}}^{\varphi_{b,\alpha}} d\varphi_i \int_{\varphi_{a,\alpha}}^{\varphi_{b,\alpha}} d\varphi_j \right), \tag{B.6}$$

for simplicity, the summation is not explicitly written below. In this case $\textcircled{1} \neq 0$:

$$\textcircled{1} = \int_0^{2\pi} d\bar{\Psi} \int_{\varphi_a}^{\varphi_b} d\varphi_i \int_{\varphi_a}^{\varphi_b} d\varphi_j e^{in(\varphi_i - \varphi_j)} = \frac{2\pi 4 \sin^2\left(\frac{n(\varphi_b - \varphi_a)}{2}\right)}{n^2}, \tag{B.7}$$

note that the integral is not normalized. Using $e^{in(\varphi_i - \varphi_j)} = e^{in\varphi_i} e^{-in\varphi_j}$ it is seen that using Q-vectors it can be evaluated as :

$$\textcircled{1}_{norm} = \langle\langle\cos(n\varphi_1)\rangle\rangle\langle\langle\cos(n\varphi_2)\rangle\rangle + \langle\langle\sin(n\varphi_1)\rangle\rangle\langle\langle\sin(n\varphi_2)\rangle\rangle. \tag{B.8}$$

This term is the correction derived in Ref. [58]. Using Matlab to solve the real and imaginary parts of (2) separately yields a number of terms proportional to:

$$f(n(2\pi - \varphi_i)) - f(n\varphi_i), \tag{B.9}$$

where φ_i is either φ_a or φ_b and $f(x)$ is either $\cos(x)$ or $\sin(x)$ in which case Eq. (B.9) is 0. Furthermore, (2) = 0. (3) = 0 can be shown using the same approach. The fourth integral is divided into two separate cases. One in which $n = k$ and one in which $n \neq k$. Once again using Matlab so solve the equation and doing some algebra, for $n = k$:

$$(4a) = 2\pi v_n^2 \left((\varphi_a - \varphi_b)^2 + \frac{4\sin^2\left(\frac{2n(\varphi_b - \varphi_a)}{2}\right)}{(2n)^2} \right) + \varphi_a(\ldots) + \varphi_b(\ldots), \tag{B.10}$$

here the sine term is similar to that of Eq. (B.7). The φ_a and φ_b terms can be shown to be 0 by using the same approach as for (2) and (3). Normalizing and expressing the sine term in Q-vectors, the event average of (4a) is:

$$(4a)_{norm} = v_n^2 \left(1 + \langle\langle\cos(2n\varphi_1)\rangle\rangle\langle\langle\cos(2n\varphi_2)\rangle\rangle + \langle\langle\sin(2n\varphi_1)\rangle\rangle\langle\langle\sin(2n\varphi_2)\rangle\rangle\right). \tag{B.11}$$

For $n \neq k$ Matlab will give a large number of terms. Some of them are 0, in the same way as in the previous integrals, but there are also a few terms that are not 0. Collecting these terms and normalizing yields:

$$(4b)_{norm} = \sum_{\substack{k \\ k\neq n}} v_k^2 \left(\frac{4\sin^2\left(\frac{(k-n)(\varphi_b - \varphi_a)}{2}\right)}{(k-n)^2(\varphi_b - \varphi_a)^2} + \frac{4\sin^2\left(\frac{(k+n)(\varphi_b - \varphi_a)}{2}\right)}{(k+n)^2(\varphi_b - \varphi_a)^2} \right). \tag{B.12}$$

And in terms of Q-vectors following the same principles as before:

$$\begin{aligned}(4b)_{norm} = \sum_{\substack{k \\ k\neq n}} v_k^2 (&\langle\langle\cos((k-n)\varphi_1)\rangle\rangle\langle\langle\cos((k-n)\varphi_2)\rangle\rangle \\ &+\langle\langle\sin((k-n)\varphi_1)\rangle\rangle\langle\langle\sin((k-n)\varphi_2)\rangle\rangle \\ &+\langle\langle\cos((k+n)\varphi_1)\rangle\rangle\langle\langle\cos((k+n)\varphi_2)\rangle\rangle \\ &+\langle\langle\sin((k+n)\varphi_1)\rangle\rangle\langle\langle\sin((k+n)\varphi_2)\rangle\rangle).\end{aligned} \tag{B.13}$$

This is a quite important term. It demonstrates how other coefficient than the one being measured will introduce a bias when there is a NUA. Furthermore, the magnitude of the bias is on the same order as the measurement, i.e. $c_n\{2\}$ measures v_n^2 and the bias is on the order of v_k^2. So when $v_k > v_n$ this bias can be quite significant. Finally, (5) = 0 by use of Eq. (B.9) once more. In conclusion, the sum of integrals (1) to (5) is:

$$\begin{aligned}\langle\langle e^{in(\varphi_1 - \varphi_2)}\rangle\rangle = v_n^2 &+ \langle\langle\cos(n\varphi_1)\rangle\rangle\langle\langle\cos(n\varphi_2)\rangle\rangle + \langle\langle\sin(n\varphi_1)\rangle\rangle\langle\langle\sin(n\varphi_2)\rangle\rangle \\ &+ v_n^2\big[\langle\langle\cos(2n\varphi_1)\rangle\rangle\langle\langle\cos(2n\varphi_2)\rangle\rangle + \langle\langle\sin(2n\varphi_1)\rangle\rangle\langle\langle\sin(2n\varphi_2)\rangle\rangle\big] \\ &+ \sum_{\substack{k \\ k\neq n}} v_k^2\big[\langle\langle\cos((k-n)\varphi_1)\rangle\rangle\langle\langle\cos((k-n)\varphi_2)\rangle\rangle \\ &+ \langle\langle\sin((k-n)\varphi_1)\rangle\rangle\langle\langle\sin((k-n)\varphi_2)\rangle\rangle \\ &+ \langle\langle\cos((k+n)\varphi_1)\rangle\rangle\langle\langle\cos((k+n)\varphi_2)\rangle\rangle \\ &+ \langle\langle\sin((k+n)\varphi_1)\rangle\rangle\langle\langle\sin((k+n)\varphi_2)\rangle\rangle\big].\end{aligned} \tag{B.14}$$

The equations for how to correct for all of these biases are presented in Section 3.4.7.

Appendix C

Additional Figures with Cuts and Corrections

This appendix contains additional plots for the discussion in Chapter 8.

C.1 Agreement Between Reconstructed and Track References

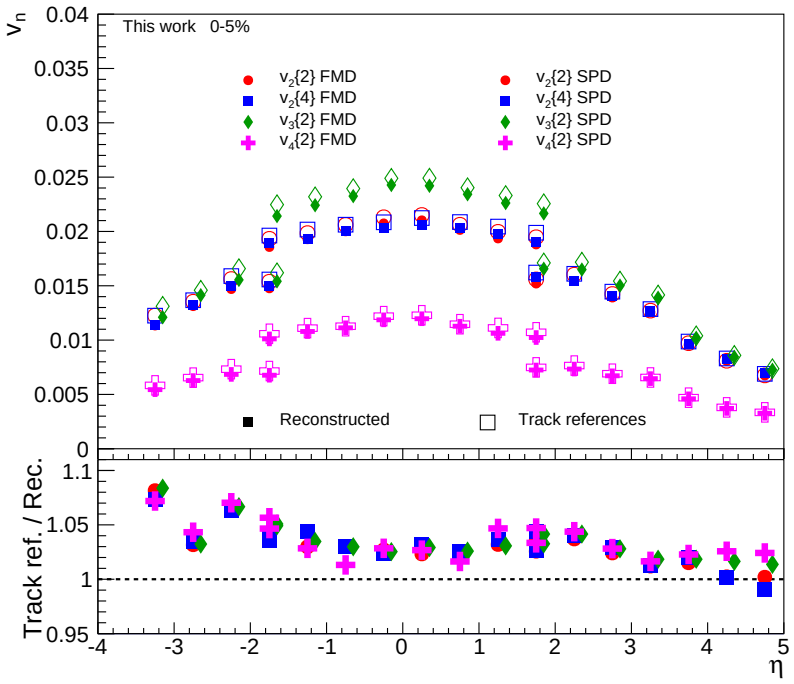

Figure C.1: Comparison between simulated detector response with cuts applied and using track reference information from the MC generator. MC generator is AliGenTunedOnPbPb with GEANT3 transport code and 0–5% central events. A good agreement is observed.

C.2 'Hot Spots' in the FMD

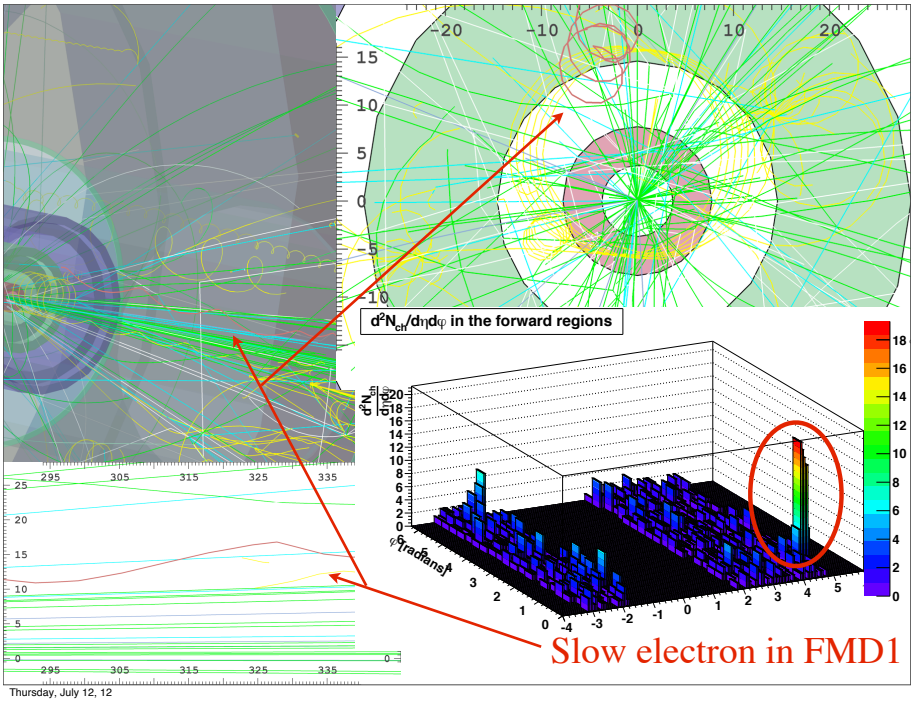

Figure C.2: Several views of an event where a large signal in the FMD is caused by one slow moving electron. The bottom right corner shows a very large signal confined to a few strips of the FMD. Looking at event-displays, it is possible to identify the particle responsible for the signal as being a slow electron. In the bottom plot a small kink in the electron trajectory is seen where it impinges on FMD1 and produces the signal.

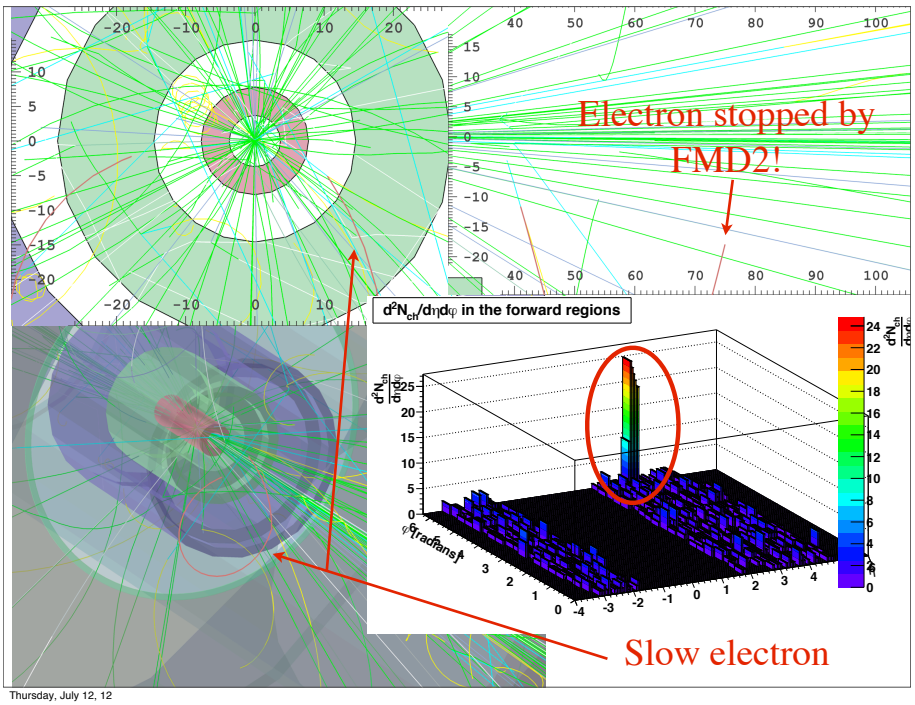

Figure C.3: Another event, similar to the above. Here the large signal is in FMD2 and the electron is completely stopped by FMD2 (top right plot).

C.3 FMD and SPD Acceptance Plots

This appendix contains the acceptance profiles of the FMD and SPD in vertex-bins with a width of 2 cm, in the range -10 cm $< v_z < 10$ cm. For all figures blue colors are FMD3 inner and outer, black is SPD, green are FMD2 inner and outer, and red is FMD1

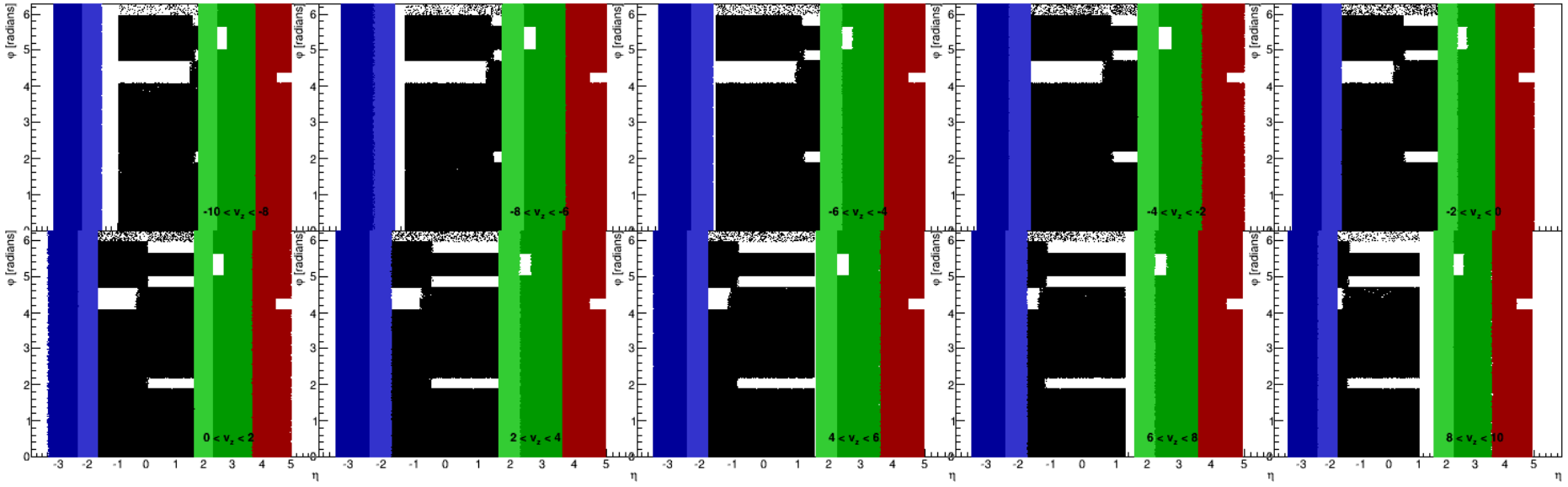

Figure C.4: Acceptance shifts in vertex-bins with a width of 2 cm. Colors are explained in the text.

C.4 Additional Non-Flow Correction Plots

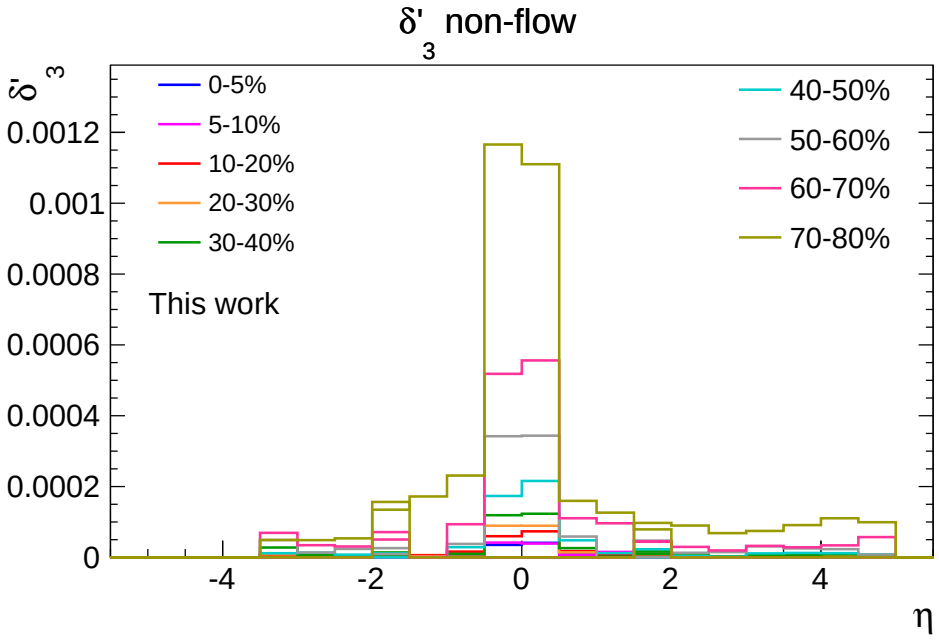

Figure C.5: Non-flow correction to differential flow for $v_3\{2\}$ in the FMD and SPD obtained from HIJING.

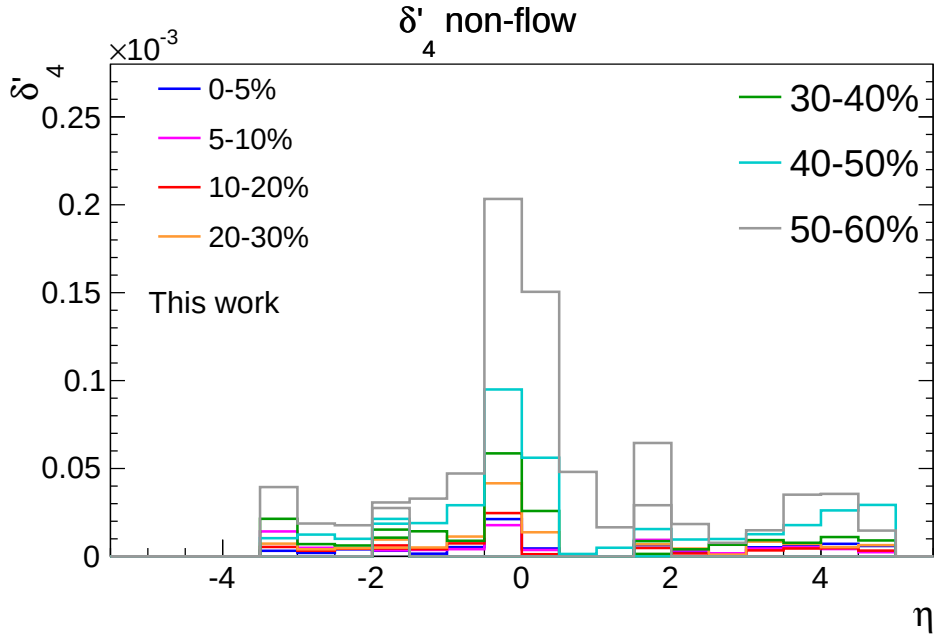

Figure C.6: Non-flow correction to differential flow for $v_4\{2\}$ in the FMD and SPD obtained from HIJING.

C.5 Additional Secondary Particle MC Correction Plots

This section contains extra plots for the applied MC corrections. The MC correction derived from AliGenTunedOnPbPb is shown for the two available centralities as well as the centrality averaged correction. All plots are averaged over all vertices. Errors are suppressed for visual purposes.

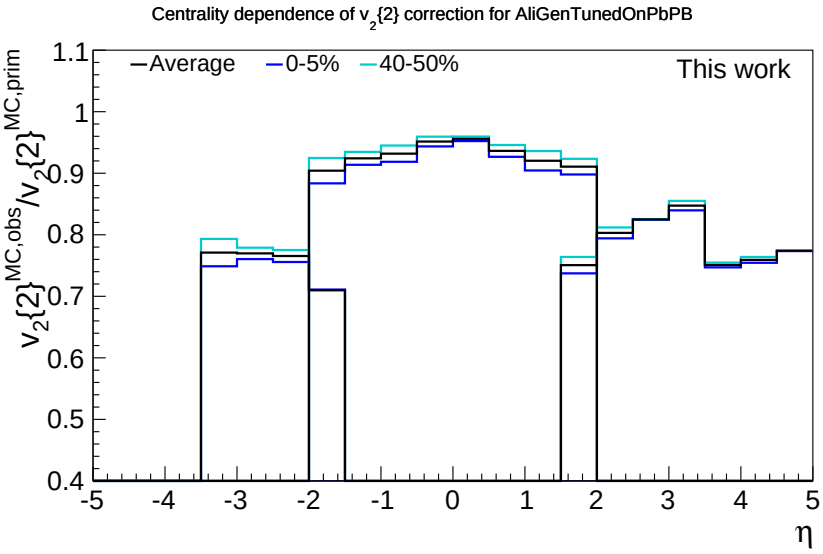

Figure C.7: Vertex-averaged MC correction using AliGenTunedOnPbPb for $v_2\{2\}$ for the two centralities and the centrality average.

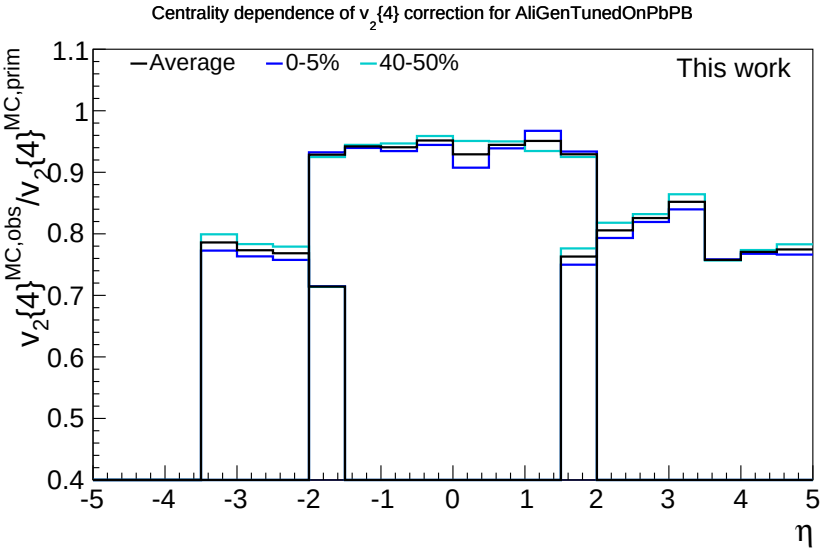

Figure C.8: Vertex-averaged MC correction using AliGenTunedOnPbPb for $v_2\{4\}$ for the two centralities and the centrality average.

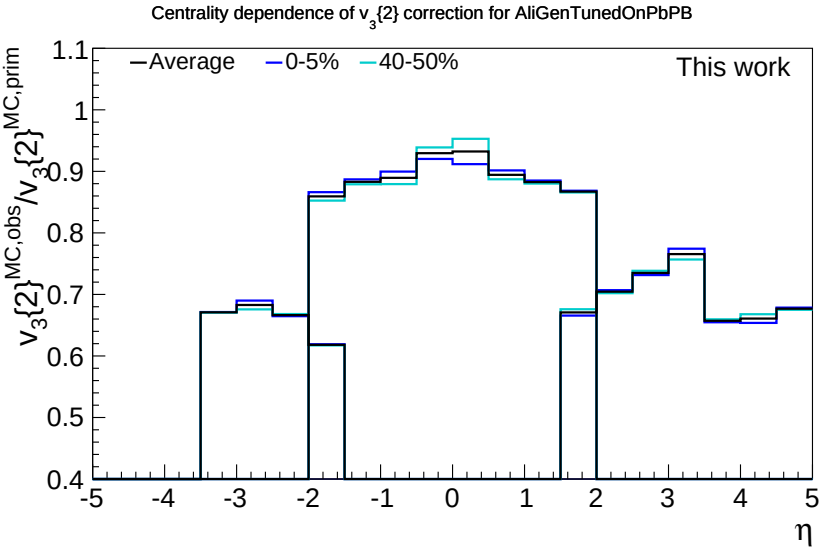

Figure C.9: Vertex-averaged MC correction using AliGenTunedOnPbPb for $v_3\{2\}$ for the two centralities and the centrality average.

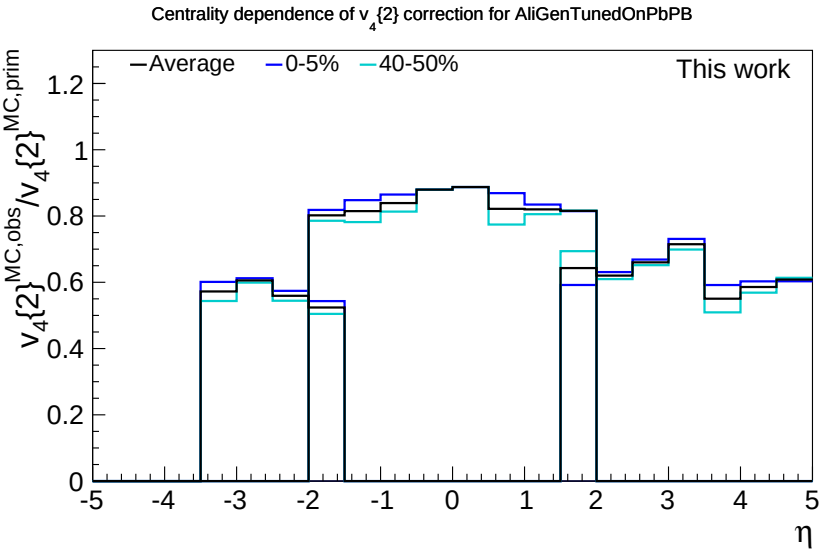

Figure C.10: Vertex-averaged MC correction using AliGenTunedOnPbPb for $v_4\{2\}$ for the two centralities and the centrality average.

C.6 Overlap Between FMD and SPD After All Corrections

Extra centralities for the agreement between the FMD and SPD measurements after all corrections are applied.

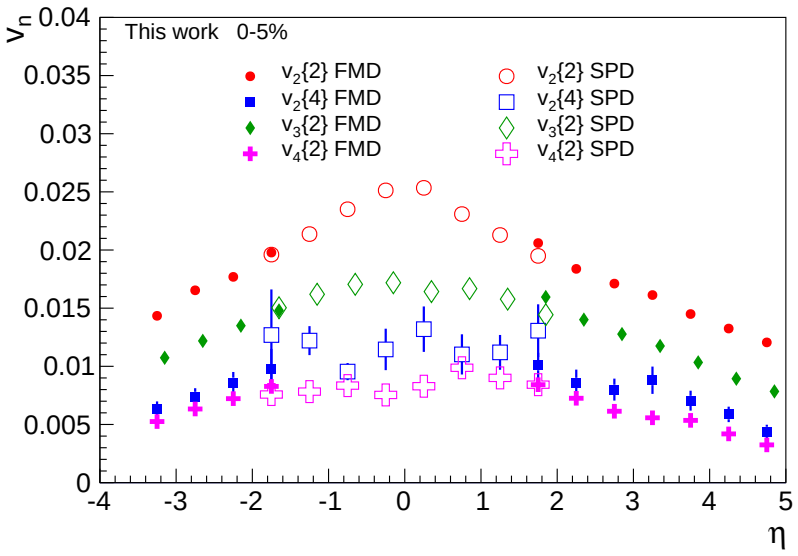

Figure C.11: Overlap between FMD and SPD after all corrections for 0–5% central events. A good agreement is observed.

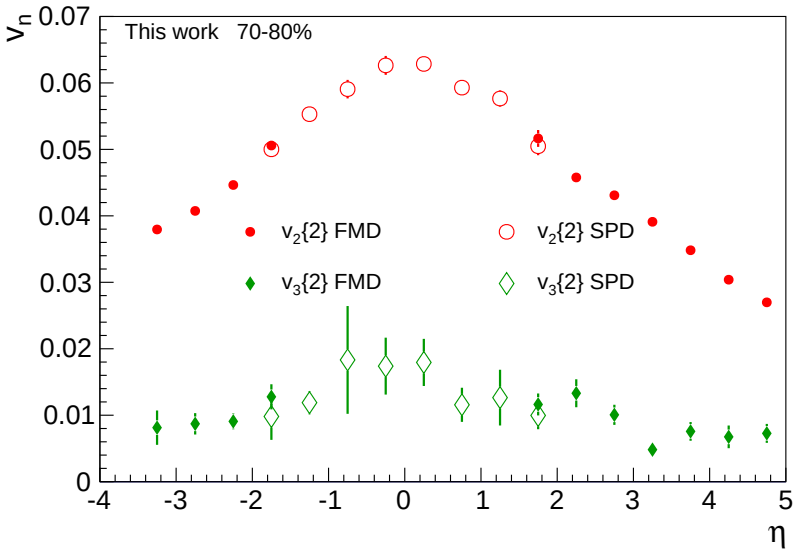

Figure C.12: Overlap between FMD and SPD after all corrections for 70–80% central events. A good agreement is observed.

Appendix D

Additional Look at the Results

This appendix contains extra plots of the results and comparisons shown in Chapter 10

D.1 Final Results in Individual Centrality Bins

This appendix contains the final results of this thesis. Here each centrality-bin is shown in a larger version for those who wish to study them in more detail. Statistical errors represent 1σ and are shown as thin error bars. Systematic uncertainties are also for 1σ and shown as thick errors bars. In many cases the statistical errors are smaller than the marker size.

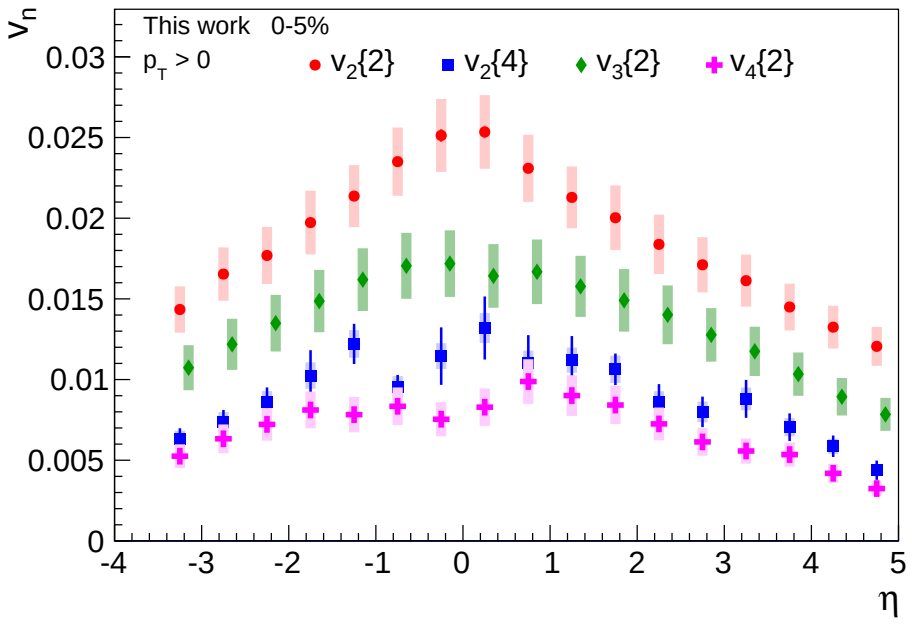

Figure D.1: Final results with flow in FMD and SPD clusters, using TPC tracks for reference flow. 0–5% central events.

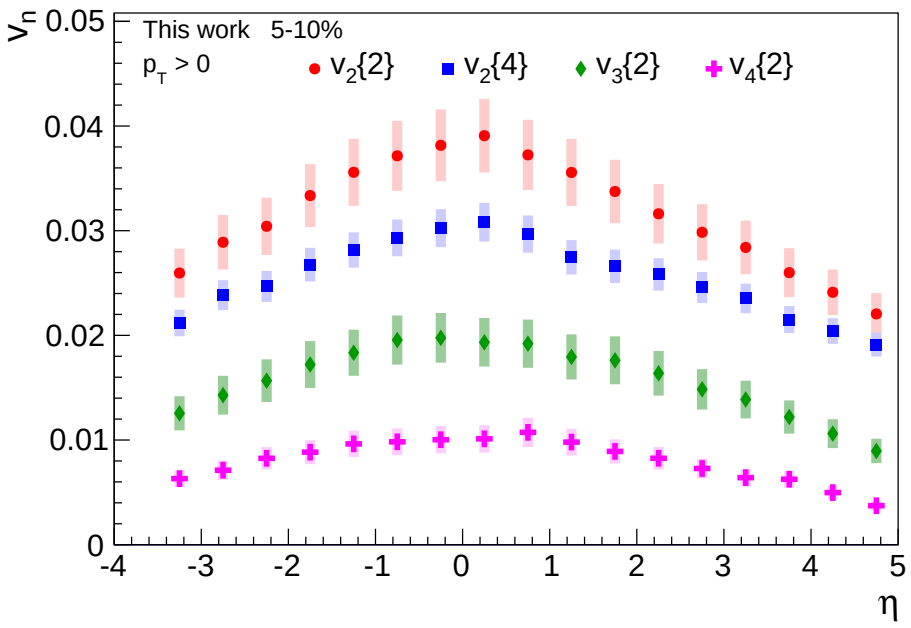

Figure D.2: Final results with flow in FMD and SPD clusters, using TPC tracks for reference flow. 5–10% central events.

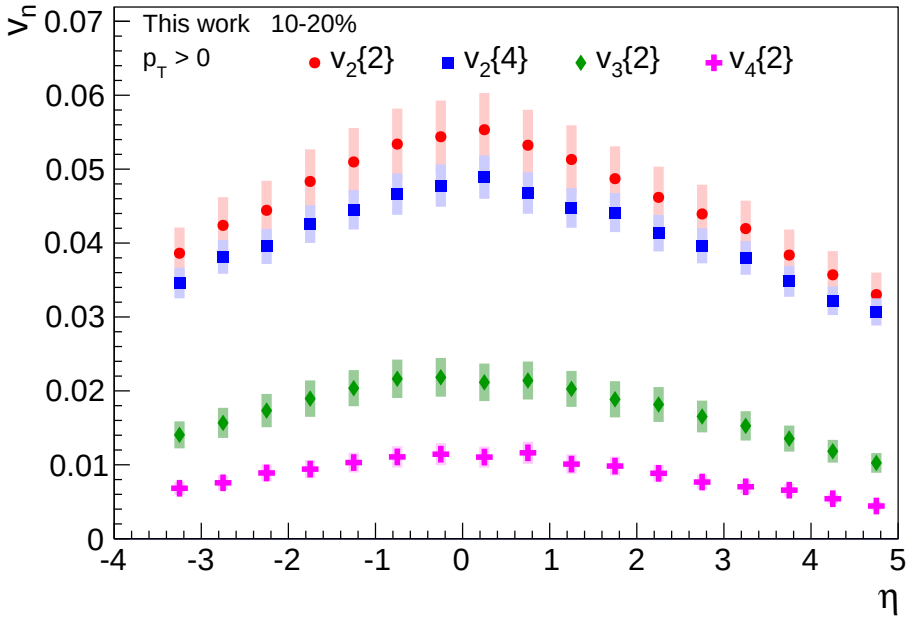

Figure D.3: Final results with flow in FMD and SPD clusters, using TPC tracks for reference flow. 10–20% central events.

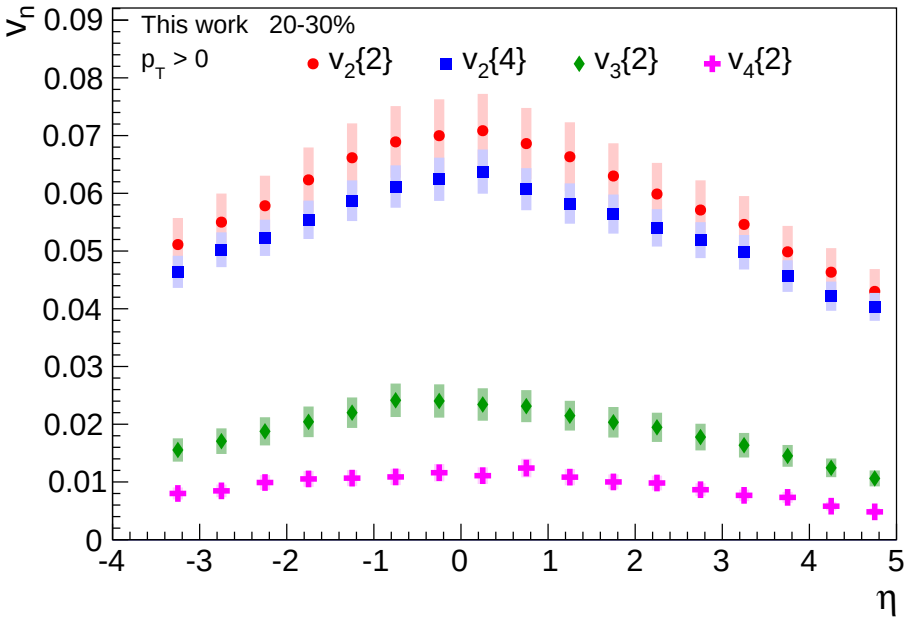

Figure D.4: Final results with flow in FMD and SPD clusters, using TPC tracks for reference flow. 20–30% central events.

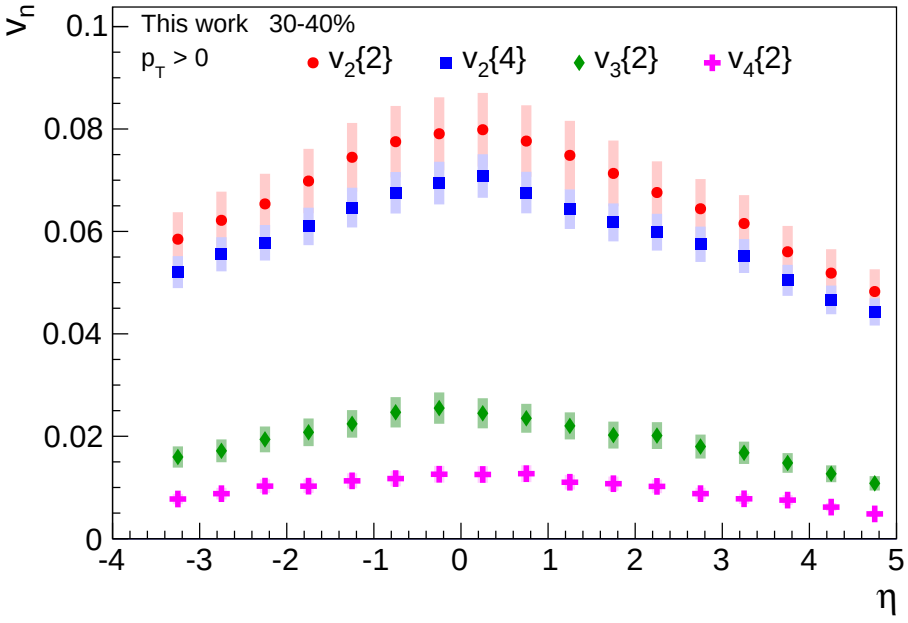

Figure D.5: Final results with flow in FMD and SPD clusters, using TPC tracks for reference flow. 30–40% central events.

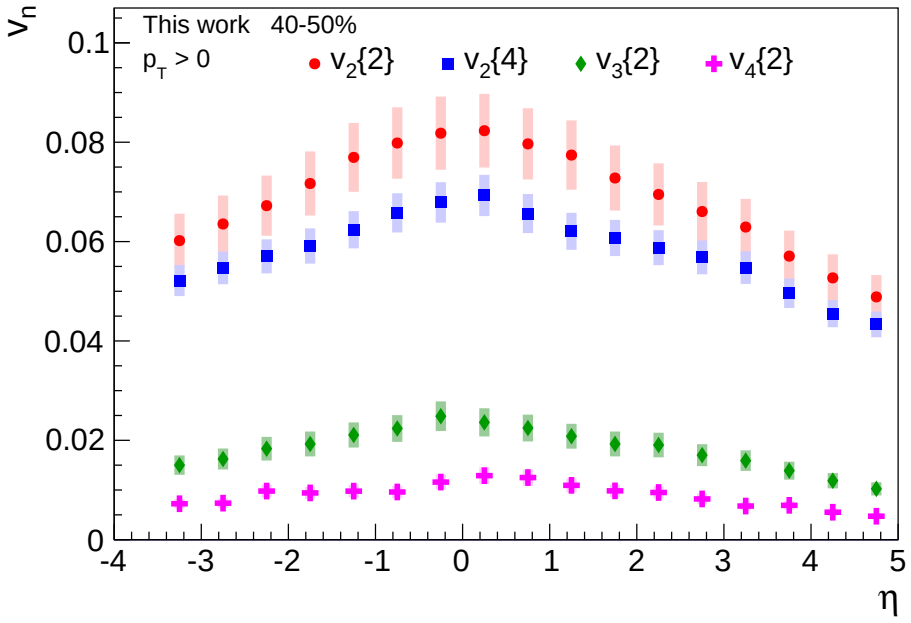

Figure D.6: Final results with flow in FMD and SPD clusters, using TPC tracks for reference flow. 40–50% central events.

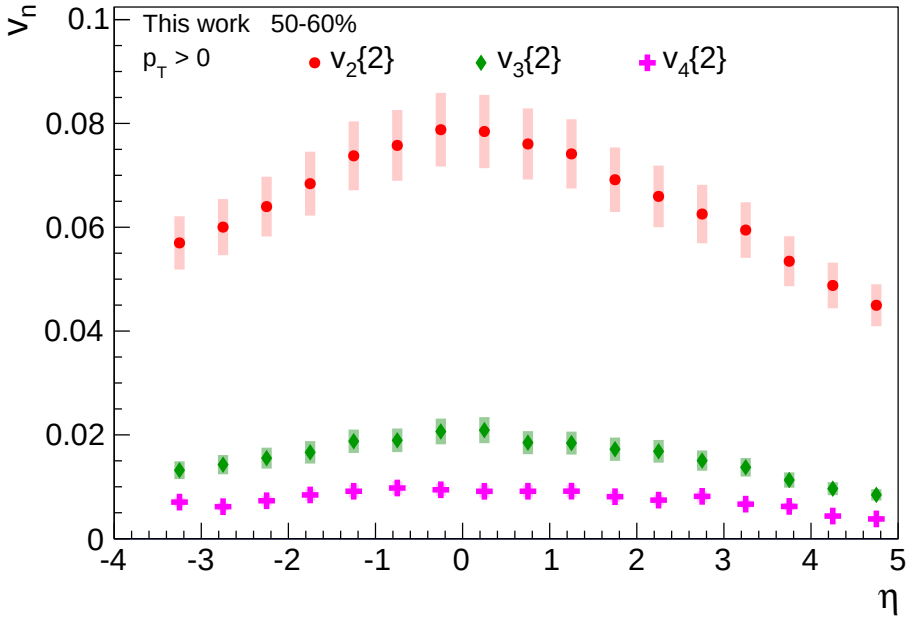

Figure D.7: Final results with flow in FMD and SPD clusters, using TPC tracks for reference flow. 50–60% central events.

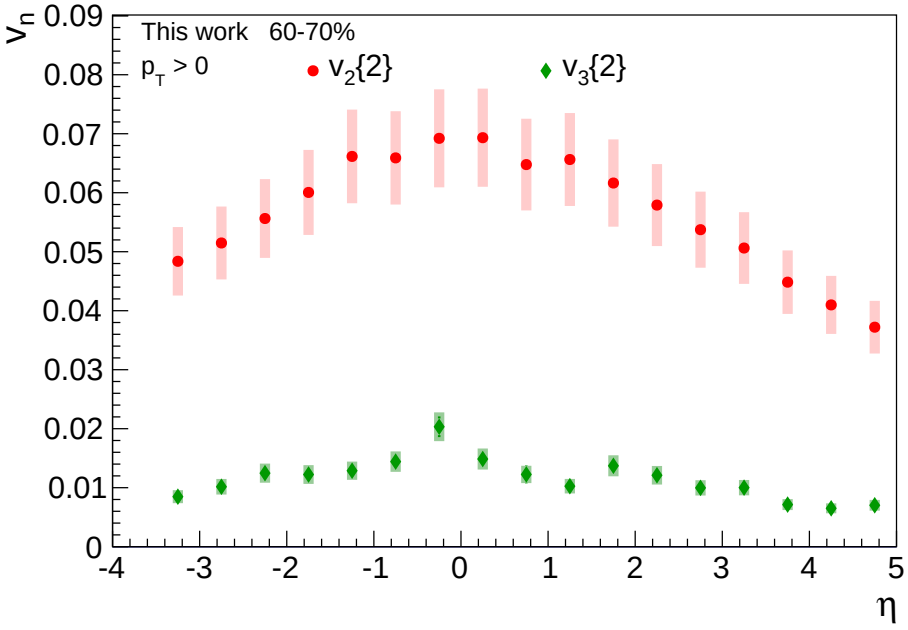

Figure D.8: Final results with flow in FMD and SPD clusters, using TPC tracks for reference flow. 60–70% central events.

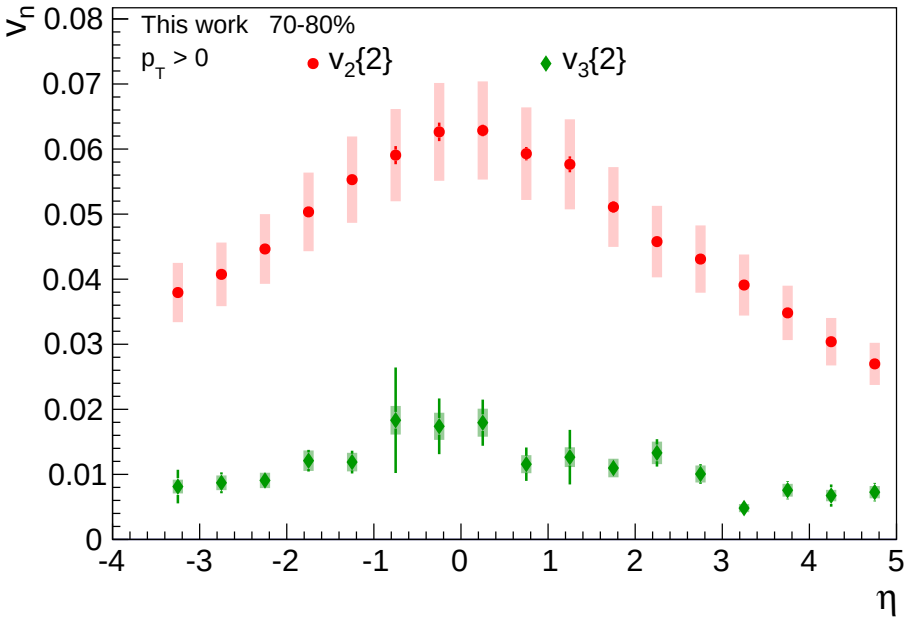

Figure D.9: Final results with flow in FMD and SPD clusters, using TPC tracks for reference flow. 70–80% central events.

D.2 Comparison to VZERO

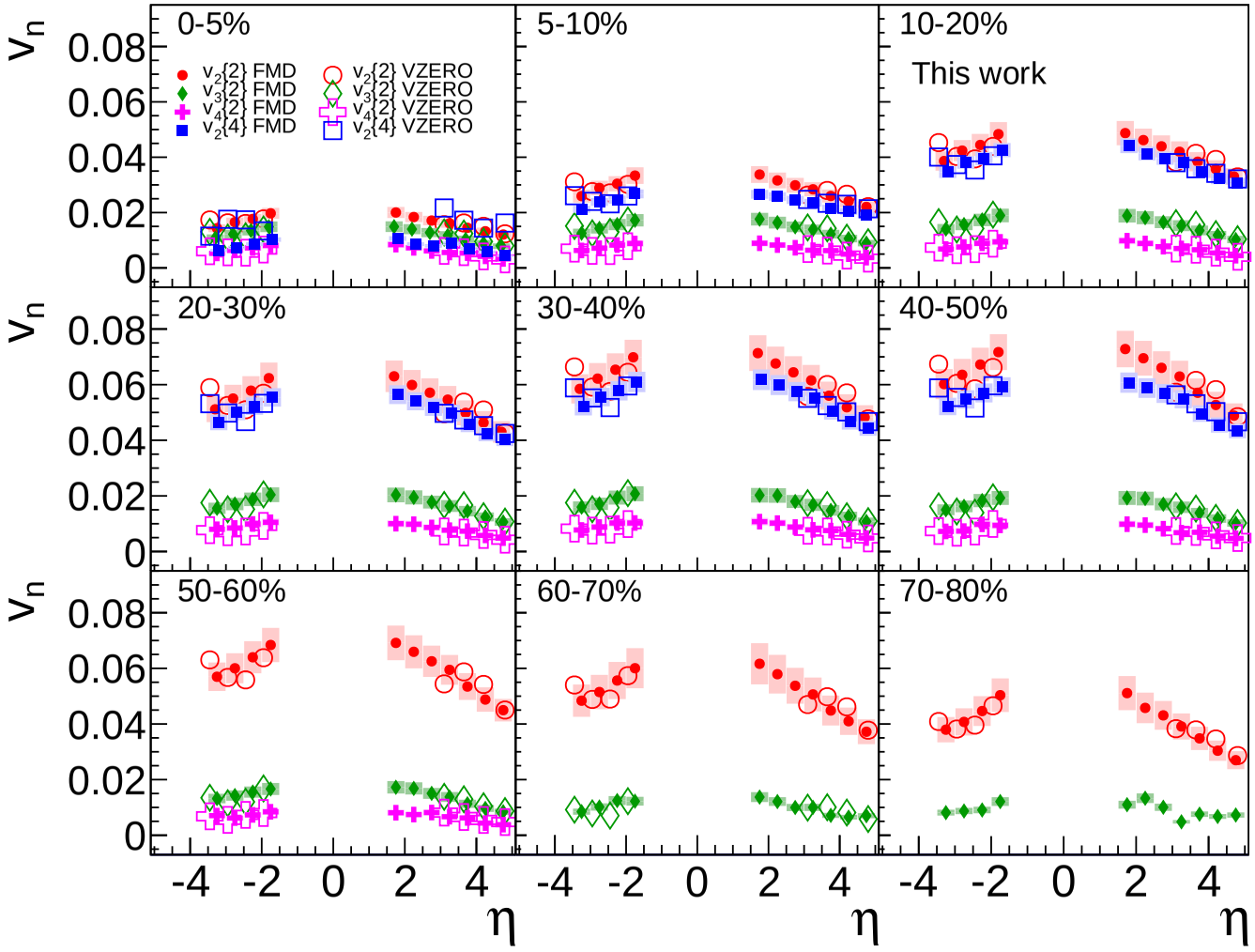

Figure D.10: $v_2\{2\}$, $v_3\{2\}$, $v_4\{2\}$ and $v_2\{4\}$ comparison between using the FMD and the VZERO away from mid-rapidity. The results agree within the systematic uncertainties (thick errors bars).

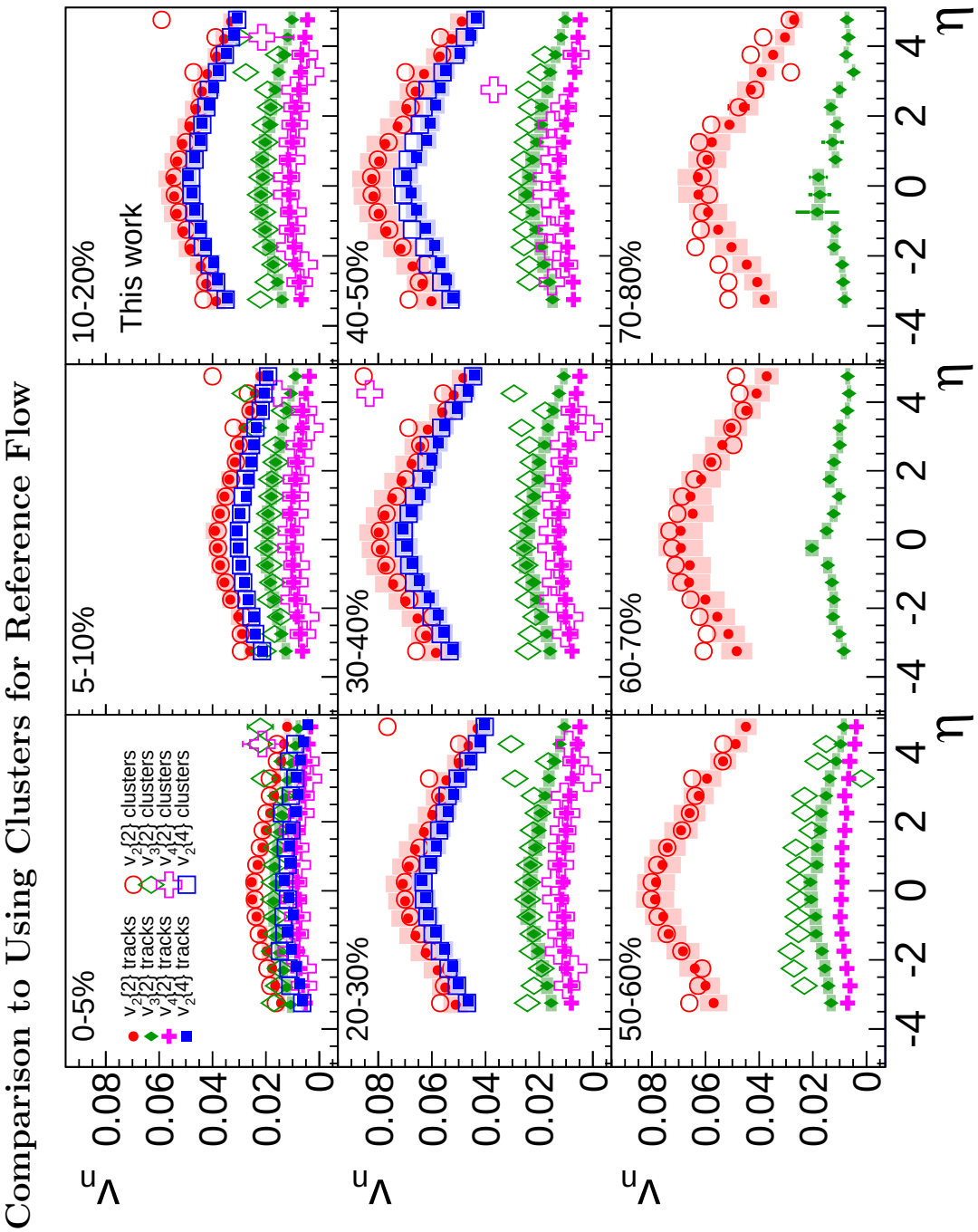

Figure D.11: $v_2\{2\}$, $v_3\{2\}$, $v_4\{2\}$ and $v_2\{4\}$ comparison between using clusters and tracks for the reference flow. The results agree within the systematic uncertainties (thick errors bars).

D.4 Forward-Backward Symmetry Plots

Here plots are shown with the results mirrored around $\eta = 0$ for three different centralities to estimate the symmetry of the measurements.

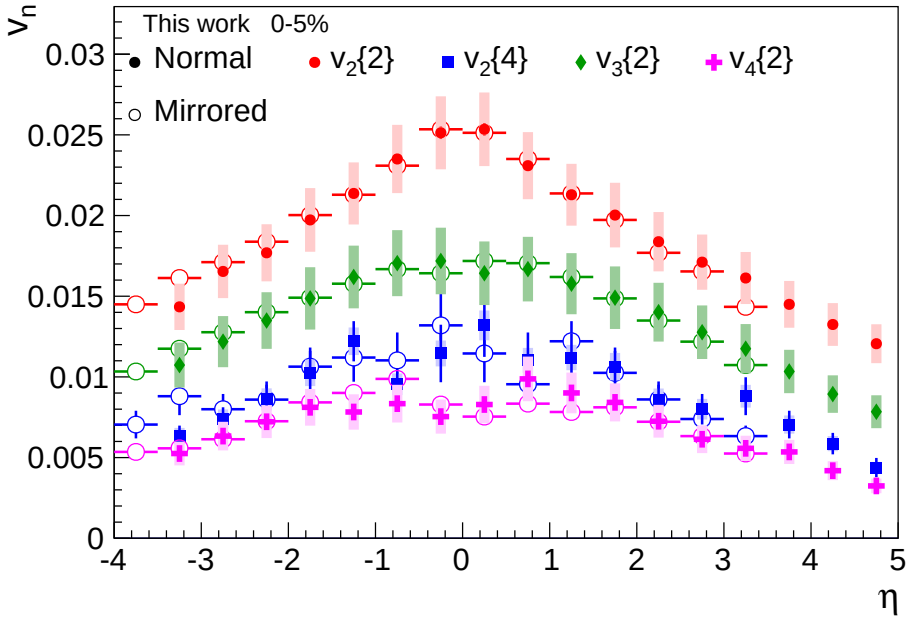

Figure D.12: Results mirrored around $\eta = 0$ for 0–5% central events. Open markers are mirrored points. A good agreement is observed.

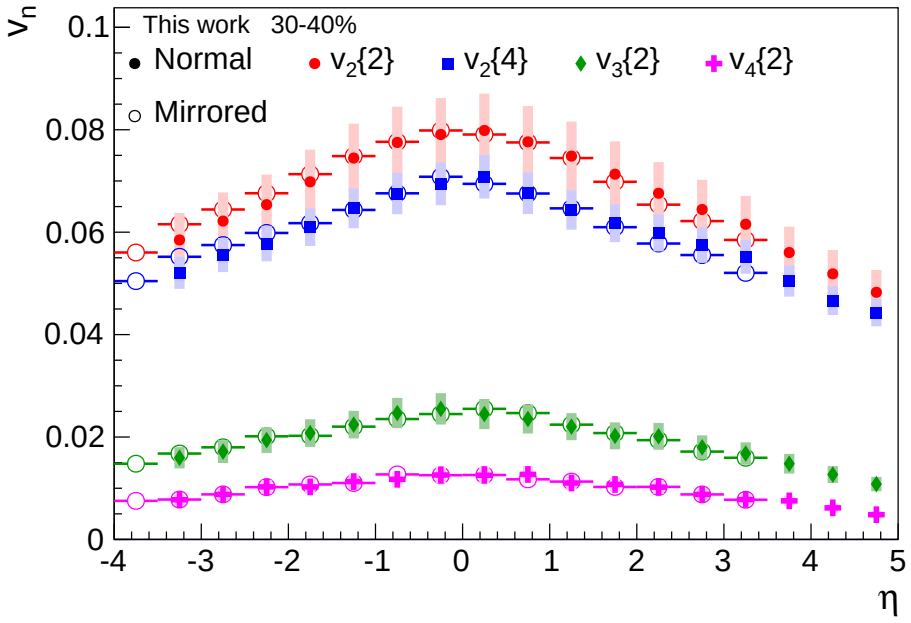

Figure D.13: Results mirrored around $\eta = 0$ for 30–40% central events. Open markers are mirrored points. A good agreement is observed.

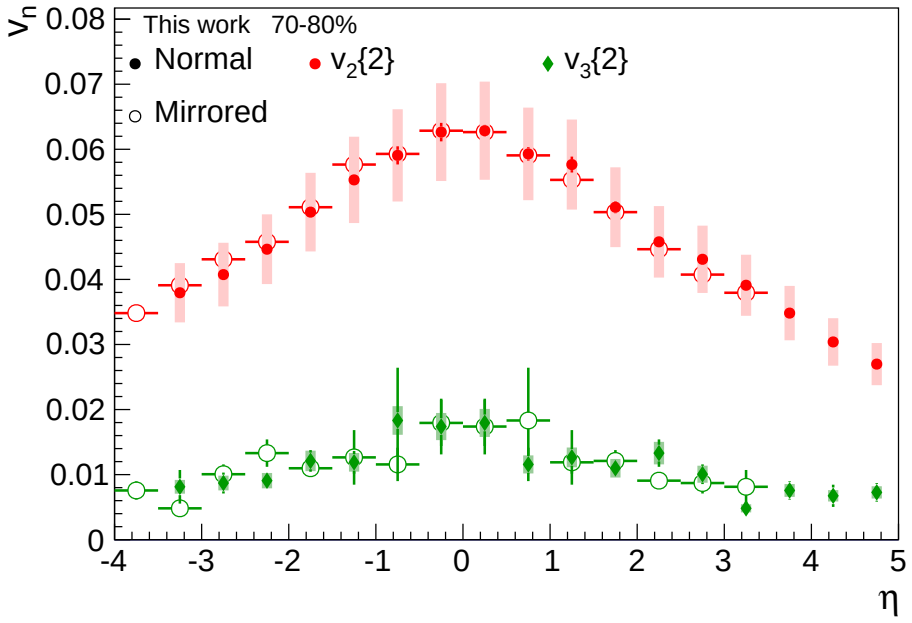

Figure D.14: Results mirrored around $\eta = 0$ for 70–80% central events. Open markers are mirrored points. A good agreement is observed.

Summary

In ultra-relativistic heavy-ion collisions a new state of matter known as the *strongly interacting quark-gluon plasma* (sQGP) is produced. A key observable in the study of sQGP is anisotropic azimuthal flow. Traditionally, the anisotropies are described by a Fourier decomposition of the azimuthal yields. The flow is then quantified as the magnitude of the corresponding Fourier coefficients, or *flow harmonics*, v_n.

One of the most significant results from the Relativistic Heavy Ion Collider (RHIC) was that the observed *elliptic flow*, v_2, was well described by models using relativistic hydrodynamics. This was considered strong evidence of a strongly interacting, thermalized system having formed. At the CERN Large Hadron Collider (LHC) collisions of lead-ions take place at center-of-mass energies 14 times higher than at RHIC. Previous measurements at the LHC support the observations made at RHIC concerning a sQGP being formed.

Measuring anisotropic flow is not a simple matter. Many methods exist, of particular importance to this thesis is the Q-cumulants method. Here it is employed to measure flow through two- and four-particle correlations, $v_n\{2\}$ and $v_n\{4\}$, respectively. The Q-cumulants allow for direct and efficient estimates of the flow harmonics, avoiding bias from auto-correlations and interpolation that previous methods suffered from. Here it is shown that in the case of detectors having a non-uniform azimuthal acceptance, it is necessary to apply a correction. This correction depends not only on terms of the same flow harmonic, but also terms from other harmonics. One of the advantages of the Q-cumulants is the possibility to estimate the flow harmonics differentially, in narrow regions of phase-space (e.g. in pseudorapidity, η), by making use of a reference flow measurements. Here it is shown that this method is susceptible to an extra bias from flow fluctuations.

The main result of this thesis is an analysis of the η-dependence of v_2, v_3 and v_4 over a wide kinematic range: $-3.5 < \eta < 5.0$ in Pb–Pb collisions at $\sqrt{s_{\mathrm{NN}}} = 2.76$ TeV. The analysis is performed using the ALICE Forward Multiplicity Detector and Silicon Pixel Detector at the CERN Large Hadron Collider. The results are compared to other LHC experiments, as well as previous measurements in ALICE. In all cases a good agreement is observed. The results for v_2 are also compared to previous heavy-ion experiments at lower collision energy. It is found that, while v_2 has increased at the LHC, the general shape of v_2 vs. η is consistent with what is observed at lower energy. Finally, by plotting v_2 as observed from the rest frame of one of the colliding nuclei, it is found that the *longitudinal scaling* observed at lower energies holds up to LHC energy, i.e. it spans two orders of magnitude in collision energy, from $\sqrt{s_{\mathrm{NN}}} = 19.6$ GeV to 2.76 TeV.

Resumé (in Danish)

I ultra-relativistiske tung-ions kollisioner bliver der skabt en ny form for stof, kendt som den *stærkt vekselvirkende kvark-gluon plasma* (sKGP). En af de vigtigste observable når man studerer sKGP er det anisotrope azimutale "flow". Det anisotrope flow karakteriseres ved at konstruere en Fourierrække af den azimutale partikelproduktion. Flowet måles på størrelsen af Fourierkoefficienterne, v_n.

En af de mest signifikante resultater fra "Relativistic Heavy Ion Collider" (RHIC) eksperimenterne var at det observerede elliptiske flow (v_2) kunne beskrives med modeller indeholdende relativistisk hydrodynamik. Dette blev set som et signifikant bevis på at et stærkt vekselvirkende termodynamisk system var blevet produceret. Ved CERN's "Large Hadron Collider" (LHC) bliver blykerner kollideret ved energier der er 14 gange højere end ved RHIC. Tidligere målinger ved LHC understøtter observationerne fra RHIC.

Det er ikke simpelt at måle det anisotrope flow. Der eksisterer mange forskellige metoder til at måle det, den vigtigste metode i forhold til denne afhandling er Q-kumulant metoden. Denne metode bruges her til at måle to- og firepartikel korrelationer: $v_n\{2\}$ og $v_n\{4\}$. Q-kumulanterne gør det muligt at bestemme flow koefficienterne direkte og på en effektiv måde, hvorved bias fra autokorrelationer og interpolationer undgås, hvilket ellers har været et problem for ældre metoder. Her vises det at hvis man bruger en detektor med ufuldkommen azimutal dækning er det nødvendigt at lave en korrektion. Denne korrektion afhænger ikke bare af led fra samme flow koefficienter, men også led fra andre koefficienter. En af fordelene ved Q-kumulanterne er muligheden for at bestemme flowet differentielt i små områder af faserummet (f.eks. pseudorapiditet, η), ved at gøre brug af en reference flow måling. Her vises det at denne metode er følsom overfor en ekstra bias fra flow fluktuationer.

Hovedresultatet i denne afhandling er en analyse af η-afhængigheden af v_2, v_3 og v_4 over en stor vinkel: -3,5 $< \eta <$ 5,0 i bly–bly kollisioner ved 2,76 TeV energi per nukleonpar. Analysen er udført ved brug af "Forward Multiplicity Detektoren" og "Silicon Pixel Detektoren" i ALICE ved LHC. Resultaterne sammenlignings med resultater fra de andre LHC eksperimenter og tidligere målinger med ALICE. Ved alle sammenligningerne findes en god enighed mellem tidligere resultater og resultaterne præsenteret her. Resultaterne for v_2 sammenlignes også med tidligere tung-ions eksperimenter ved lavere kollisionsenergier. I disse sammenligninger ses det at mens v_2 er større ved LHC, så er den generelle form af v_2 som funktion af η konsistent med hvad der blev set ved lavere energier. Ved at plotte v_2 som funktion af η set fra en af blykernernes hvilesystem findes det at den *longitudinale skalering* set ved lavere energier holder helt op til LHC energi. Dvs. den spænder over to størrelsesordner i kollisionsenergi: fra 19,6 GeV til 2,76 TeV per nukleonpar.